Acta Physica Hungarica

VOLUME 56, NUMBERS 1–4, 1984

Akadémiai Kiadó, Budapest

ACTA PHYS HUNG APAHAQ 56 (1-4) 1-260 (1984) HU ISSN 0231-4428

ACTA PHYSICA HUNGARICA

A JOURNAL OF THE HUNGARIAN ACADEMY OF SCIENCES

EDITED BY

I. KOVÁCS

Acta Physica publishes original papers on subjects in physics. Papers are accepted in English, French, German and Russian.

Acta Physica is published in two yearly volumes (4 issues each) by

AKADÉMIAI KIADÓ
Publishing House of the Hungarian Academy of Sciences
H-1054 Budapest, Alkotmány u. 21

Subscription information

Orders should be addressed to

KULTURA Foreign Trading Company
1389 Budapest P.O. Box 149

or to its representatives abroad.

Acta Physica is indexed in Current Contents, in Physics Abstracts and in Current Papers in Physics.

ACTA PHYSICA HUNGARICA

VOLUME 56

AKADÉMIAI KIADÓ, BUDAPEST
1984

CONTENTS

Volume 56

FLUIDS, PLASMAS AND ELECTRIC DISCHARGES

CONDENSED MATTER

ASTROPHYSICS

CONTENTS

FLUIDS, PLASMAS AND ELECTRIC DISCHARGES

CONDENSED MATTER

ASTROPHYSICS

Manuscript received by Akadémiai Kiadó: 27. July 1983
Manuscript received by the Printers: 26. August 1983
Date of publication: 29 March 1985

PRINTED IN HUNGARY
Akadémiai Kiadó és Nyomda, Budapest

Acta Physica Hungarica 56 (1—4), pp 3—8 (1984)

POTENTIAL ENERGY CURVES AND DISSOCIATION ENERGY OF THE DIATOMIC SELENIUM MOLECULE

P. SAMBASIVA RAO

Physics Department, J. N. Technological University College of Engineering, Anantapur-515002, India

R. RAMAKRISHNA REDDY

Physics Department K.S.R.M. College of Engineering, Cuddapah-516001, India

and

T. V. RAMAKRISHNA RAO

Institut des Sciences Exactes Université de Constantine, Constantine, Algeria

(Received 26 August 1982)

The experimental potential energy curves for $X_1{}^3\Sigma_g^-$, $X_2{}^3\Sigma_g^-$, $B_1{}^3\Sigma_u^-$, $B_2{}^3\Sigma_u^-$, $C_1{}^3\Sigma_u^-$ and E states of the diatomic selenium molecule have been constructed using the method of Lakshman and Rao and also by Jarmain's method. The dissociation energy for the ground state of the molecule has been estimated to be 3.31 eV by the method of curve fitting using the electronegativity potential function of Szőke and Baitz. Also the first ionization potential of the Se_2 molecule is found to be 8.68 eV.

Introduction

The construction of experimental potential energy curves for the atomic interactions is of fundamental importance in chemical physics for the understanding of various physical problems arising in astrophysics, gas kinetics and molecular spectra. Also a knowledge of the exact values of the dissociation energies (D_0) of diatomic molecules is necessary in thermo-chemistry. The present paper mainly deals with the construction of potential energy curves for $X_1{}^3\Sigma_g^-$, $X_2{}^3\Sigma_g^-$, $B_1{}^3\Sigma_u^-$, $B_2{}^3\Sigma_u^-$, $C_1{}^3\Sigma_u^-$ and E states of the Se_2 molecule using the method of Lakshman and Rao [1] and theoretical estimation of D_0 of the molecule by the method of curve fitting. The molecular constants required for the present work have been taken from Huber and Herzberg [2].

Potential energy curves

The method of Lakshman and Rao is a modified form of Rydberg–Klein–Rees method [3] in which f and g terms are written in a simplified form. Chakraborty and Pan [4] had mentioned in their review paper that the method of Lakshman and Rao is

reliable and accurate. As the present method was successfully verified [5–9] for several states belonging to different diatomic molecules, and because the full details of the said method were reported in literature [1] only the results of the present work are given in Table I. The turning points of the vibrational motion, obtained by the method of Jarmain [10] are also presented in Table I, for comparison.

Dissociation energy

An accurate estimation of the dissociation energy (D_e) requires an empirical potential function which gives the best reproduction of the experimental potential energy curve. Various attempts to get such empirical functions have been reported in literature. A critical evaluation of the more important of these functions was given by Steele et al [11] and they have shown that the potential function of Hulburt and Hirschfelder [12] and the Lippincott potential function [13] fit well with the RKR curves of a large number of diatomic molecules. In the present investigation, it is observed that the electronegativity potential function proposed by Szőke and Baitz [14] has given the best reproduction of the experimental potential energy curves of Se_2. Also, it has been found by Singh et al [15] that the Szőke and Baitz potential function fit well with the RKR curves of the molecules built from like atoms, such as I_2, N_2, O_2, etc.

The function used is of the form

$$U(r)=D_e\left[1-\exp\left(\frac{\gamma\Delta r^2}{2r}\right)\right]\times\left[1-a\left(\frac{b^2\gamma}{2r}\right)^{1/2}\Delta r\exp\left\{-\left(\frac{b^2\gamma}{2r_e}\right)^{1/2}\Delta r\right\}\right], \quad (1)$$

where $\gamma=de/D_e^{1/2}$. d is obtained from the expression $k_e=d(e_1e_2D_e)^{1/2}r_e^{-1}$, b is considered a constant (~ 1.065) and $a=0.35e^{1/2}$ where $e=(e_1e_2)^{1/2}$, e_1 and e_2 being the electronegativities (Pauling scale) of the atoms constituting the molecules. The turning points of the ground state of Se_2 are used in the Szőke and Baitz potential function and for a particular value of D_e, the observed energy values of U are compared with the calculated energy values $[U(r)]$. This procedure is repeated for different values of D_e, and the D_e value (3.33 eV) for which the best fit of the energy values $[U(r)]$ is observed is taken as the dissociation energy (D_e) of the molecule.

Results and discussion

The turning points obtained for ninety-two observed vibrational levels of six electronic states of the Se_2 molecule are presented in Table I.

It is obvious from Table II that the best fitting of the energy values is achieved for $D_e=3.33$ eV (26875 cm^{-1}) since the average percentage deviation in this case is

Table I

The turning points of the potential energy curves of the Se_2 molecule

v	U [cm^{-1}]	$U+T_e$ [cm^{-1}]	Lakshman and Rao method		Jarmain method	
			r_{min} [nm]	r_{max} [nm]	r_{min} [nm]	r_{max} [nm]
	X_1 state	$T_e=0$		$r_e=0.2166$ nm		
0	192.4	192.4	0.2121	0.2215	0.2121	0.2215
2	957.2	957.2	0.2069	0.2280	0.2069	0.2280
4	1714.3	1714.3	0.2039	0.2323	0.2039	0.2323
6	2463.5	2463.5	0.2017	0.2359	0.2017	0.2359
8	3204.9	3204.9	0.1998	0.2391	0.1999	0.2392
10	3938.5	3938.5	0.1982	0.2421	0.1983	0.2421
12	4664.1	4664.1	0.1968	0.2449	0.1969	0.2450
14	5381.8	5381.8	0.1956	0.2476	0.1956	0.2477
16	6091.5	6091.5	0.1944	0.2501	0.1945	0.2503
18	6793.1	6793.1	0.1934	0.2526	0.1935	0.2528
20	7486.7	7486.7	0.1924	0.2550	0.1925	0.2552
22	8172.2	8172.2	0.1915	0.2574	0.1916	0.2576
24	8849.5	8849.5	0.1906	0.2597	0.1908	0.2600
	X_2 state	$T_e=510.0$		$r_e=0.2163$ nm		
0	193.3	703.3	0.2118	0.2211	0.2118	0.2211
2	967.9	1471.9	0.2066	0.2276	0.2066	0.2276
4	1722.7	2232.7	0.2037	0.2320	0.2037	0.2320
6	2475.8	2985.8	0.2015	0.2356	0.2015	0.2356
8	3221.2	3731.2	0.1996	0.2888	0.1996	0.2888
10	3958.9	4468.9	0.1981	0.2418	0.1981	0.2418
12	4688.8	5198.8	0.1967	0.2446	0.1967	0.2447
14	5411.1	5921.1	0.1954	0.2473	0.1955	0.2474
16	6125.6	6635.6	0.1943	0.2499	0.1944	0.2500
18	6832.5	7342.5	0.1933	0.2524	0.1933	0.2525
20	7531.6	8041.6	0.1923	0.2548	0.1924	0.2549
22	8223.0	8733.0	0.1914	0.2572	0.1915	0.2573
24	8565.8	9075.8	0.1910	0.2584	0.1911	0.2585
26	9582.7	10092.7	0.1898	0.2619	0.1899	0.2620
28	10250.9	10760.9	0.1891	0.2642	0.1892	0.2643
	B_1 state	$T_e=25980.4$		$r_e=0.2447$ nm		
0	122.9	26103.3	0.2391	0.2508	0.2391	0.2508
2	609.3	26589.7	0.2328	0.2592	0.2328	0.2592
4	1087.2	27067.6	0.2293	0.2650	0.2293	0.2650
6	1556.5	27536.8	0.2267	0.2698	0.2267	0.2698
8	2016.7	27997.1	0.2245	0.2742	0.2245	0.2743
10	2467.7	28448.1	0.2227	0.2783	0.2227	0.2784
12	2909.2	28889.5	0.2211	0.2822	0.2212	0.2823
14	3340.9	29321.2	0.2197	0.2860	0.2198	0.2861
	B_2 state	$T_e=26058.6$		$r_e=0.2440$ nm		
0	122.9	26181.5	0.2385	0.2503	0.2385	0.2503
2	608.4	26666.0	0.2328	0.2592	0.2328	0.2592
4	1084.1	27142.7	0.2297	0.2655	0.2297	0.2655

Table I. *(cont.)*

v	U [cm^{-1}]	$U+T_e$ [cm^{-1}]	Lakshman and Rao method		Jarmain method	
			r_{min} [nm]	r_{max} [nm]	r_{min} [nm]	r_{max} [nm]
	C_1 state	$T_e=53220.5$		$r_e=0.2089$ nm		
0	213.7	53434.2	0.2047	0.2136	0.2047	0.2136
2	1062.4	54282.9	0.1998	0.2198	0.1998	0.2198
4	1901.3	55121.8	0.1970	0.2239	0.1970	0.2239
6	2730.5	55950.9	0.1949	0.2274	0.1949	0.2275
8	3549.9	56770.4	0.1932	0.2305	0.1932	0.2306
	E state	$T_e=54752.5$		$r_e=0.2137$ nm		
0	210.6	54954.1	0.2093	0.2184	0.2093	0.2184
2	1001.6	55754.1	0.2043	0.2249	0.2043	0.2249
4	1791.2	56543.7	0.2014	0.2292	0.2014	0.2292

Table II

Comparison of the observed and calculated energy values

r [nm]	U [cm^{-1}]	Calculated energy values $U(r)$		
		$D_e=3.29$ eV	$D_e=3.33$ eV	$D_e=3.38$ eV
0.2121	192.4	192.4	192.3	192.3
0.2215	192.4	192.3	192.3	192.4
0.2039	1714.3	1710.4	1708.9	1707.3
0.2323	1714.3	1714.8	1716.8	1718.8
0.1998	3204.9	3197.1	3193.3	3189.6
0.2391	3204.9	3200.6	3206.0	3211.4
0.1968	4664.1	4646.8	4640.4	4634.1
0.2449	4664.1	4652.7	4662.9	4672.9
0.1944	6091.5	6067.8	6058.6	6049.6
0.2501	6091.5	6061.9	6078.0	6093.8
0.1924	7486.7	7454.9	7442.8	7430.9
0.2550	7486.7	7429.3	7452.3	7474.9
0.1906	8849.5	8816.0	8800.8	8786.0
0.2597	8849.5	8748.0	8779.1	8809.5
Average percentage deviation:		0.35	0.33	0.37

minimum. Hence the dissociation energy for the ground state of Se_2 is 3.33 eV and the value as measured from the lowest vibrational level is $D_0=3.31$ eV. But from the predissociations in B_1 state, observed by Barrow et al [16] the dissociation limits are fixed at 27508 cm^{-1} and 29 498 cm^{-1}. From these dissociation limits three possible spectroscopic values i.e. 3.4105, 3.1638, 3.0964 eV for D_0 can be derived depending on the assumed atomic states at the observed predissociation limits. Barrow et al [16]

prefer $D_0 = 3.164$ eV. But the present value of D_0 (3.31 eV) is slightly higher. Yet this estimated value is reliable because both photoionization and thermochemical studies [2] strongly favour a higher value of $D_0 = 3.411$ eV.

Also, the dissociation energy (D_e) for B_1 state of the molecule has been established at 1.19 eV (9625 cm^{-1}) using Eq. (1).

The lowest state of atomic selenium [17] in $^3P_2$ and the Wigner–Witmer correlation rules [18] show that two normal atoms ($^3P_2 + {}^3P_2$) can give, among other types $^3\Sigma_g^-$ but not $^3\Sigma_u^-$. The ground state, $X_1\,{}^3\Sigma_g^-$, should therefore dissociate to normal atoms Se ($^3P_2$) + Se ($^3P_2$) but the upper state $B_1\,{}^3\Sigma_u^-$ must go to a different pair of products.

From the relation

$$D_e(B_1) + T_e = D_e(X_1) + E_A \tag{2}$$

the atomic excitation energy (E_A) is evaluated from the estimated D_e values of the excited (B_1) and ground (X_1) states and the electronic term (T_e).

Since the T_e value for the $B_1 - X_1$ system is 25980.36 cm^{-1}, $E_A = 9625 + 25980.36 - 26875 = 8730.36$ cm^{-1}. As this value of atomic excitation energy is close to the atomic state energy (9576 cm^{-1}) of $^1D_2$ for selenium atom [17], the upper state, $B_1\,{}^3\Sigma_u^-$, may dissociate into Se ($^3P_2$) + Se ($^1D_2$).

Knowing the D_0 value of Se_2 and the D_0 value of Se_2^+ [18] and the first ionization potential of selenium atom [17], the first ionization potential of Se_2 can be evaluated. The difference between Se_2 and Se_2^+ bond energies is given by the relation

$$D_0(Se_2^+) - D_0(Se_2) = I(Se) - I(Se_2) = 1.07 \text{ eV} \tag{3}$$

which is consistent with the ionization of an antibonding electron. It expresses that Se_2^+ has one antibonding electron less than Se_2 and so one would expect $D_0(Se_2^+)$ to be larger than $D_0(Se_2)$.

So, from Eq. (3) the ionization potential of the Se_2 molecule is given by

$$I(Se_2) = I(Se) + D_0(Se_2) - D_0(Se_2^+)$$
$$= 9.75 + 3.31 - 4.38 = 8.68 \text{ eV},$$

which is in good agreement with the value of 8.88 eV recommended by Huber and Herzberg [2].

Acknowledgements

The authors are grateful to Professors S. V. J. Lakshman and S. V. Subrahmanyam for their encouragement.

References

1. S. V. J. Lakshman and T. V. Ramakrishna Rao, J. Phys. *B4*, 269, 1971.
2. K. P. Huber and G. Herzberg, Molecular Spectra and Molecular Structure: IV. Constants of Diatomic Molecules, Van Nostrand Reinhold, New York, 1979.
3. A. L. G. Rees, Proc. Phys. Soc., *59A*, 998, 1947.
4. B. Chakraborty and Y. K. Pan, Appl. Spectrosc.Rev., *7(2)*, 283, 1973.
5. T. V. Ramakrishna Rao, R. Ramakrishna Reddy and P. Sambasiva Rao, Physica, *106C*, 445, 1981.
6. T. V. Ramakrishna Rao, R. Ramakrishna Reddy and P. Sambasiva Rao, Curr. Sci., *50*, 567, 1981.
7. P. Sambasiva Rao and T. V. Ramakrishna Rao, Nat. Acad. Sci. Letters, *4*, 253, 1981.
8. P. Sambasiva Rao and T. V. Ramakrishna Rao, JQSRT, *27*, 207, 1982.
9. P. Sambasiva Rao and T. V. Ramakrishna Rao, Acta Ciencia Indica, 1982 (in press).
10. W. R. Jarmain, Can. J. Phys., *38*, 217, 1960.
11. D. Steele, E. R. Lippincott and J. T. Vanderslice, Rev. Mod. Phys., *34*, 239, 1962.
12. H. M. Hulburt and J. O. Hirschfelder, J. Chem. Phys. *9*, 61, 1941; ibid. *35*, 1901, 1961.
13. D. Steele and E. R. Lippincott, J. Chem. Phys., *35*, 2065, 1961.
14. S. Szőke and E. Baitz, Can. J. Phys., *46*, 2563, 1968.
15. J. Singh, K. P. R. Nair and D. K. Rai, J. Mol. Struc., *5*, 492, 1970.
16. R. F. Barrow, G. G. Chandler and C. B. Meyer, Phil. Trans. Roy. Soc. London, Ser. *A260*, 395, 1966.
17. A. G. Gaydon, Dissociation Energies and Spectra of Diatomic Molecules, Chapman and Hall, London, 1968.
18. G. Herzberg, Molecular Spectra and Molecular Structure: I. Spectra of Diatomic Molecules, Van Nostrand, New York, 1950.

Acta Physica Hungarica 56 (1—4), pp 9—20 (1984)

ON QUARK AND COLOUR CONFINEMENT

C. v. WESTENHOLZ

*D-45 Osnabrück—Dodesheide, FRG**

(Received 21 September 1982)

The problem of quark confinement is re-investigated in terms of a structural analysis of the Wilson loop confinement criterion.

Within a suitably chosen gauge-geometrical framework it is shown that the topological structure of the vacuum underlies the mechanism of confinement. The non-existence of free coloured particles within this approach confirms that the problem of quark confinement becomes that of colour confinement

1. Introduction

A description of hadronic matter leads to the question: Why are quarks permanently trapped within hadrons? This problem of quark confinement, where strongly interacting hadrons show signs of an inner structure deals with the status of quarks as the fundamental constituents of all hadrons within the framework of some non-abelian gauge theory. The basic dynamical and topological aspects which are derived from such a gauge geometry are intimately related to some interaction energy, $E(R)$, between a heavy quark-antiquark $(q\bar{q})$-pair, imbedded in a gluon soup, separated by a distance R for a time T. A model where confinement occurs when $E(R)$ grows with R, $R\to\infty$, i.e. when $E(R)>0$, or, alternatively, where pair-produced quarks will repel, when $E(R)<0$, can be of the type which refers to *Wilson's confinement criterion.* The interaction energy of massive quarks, which appear as an effect of a spontaneously broken gauge symmetry (cf. Section 3), can be calculated by evaluating the vacuum expectation value of the ordered exponential of the line integral of the corresponding gauge field $\omega^1 = A_\mu\, dx^\mu$ (in the $A_0=0$ gauge) about a loop c_1 of spatial extent R and time extent T, such that

$$W(c_1) = <\text{vac}\,|\,\text{Tr}\,P\exp\left(i\int_{c_1}\omega^{1)}\right)|\,\text{vac}> \underset{T\to\infty}{\to} \exp\left[-E(R)T\right]. \tag{1}$$

Note that for large T the vacuum expectation value (1) behaves like

$$W(c_1) \# \exp(\text{-const. } A) \tag{2}$$

* Address: Eibenweg 6, D-45 Osnabrück—Dodesheide, FRG

(in certain cases), where A is the minimal area enclosed by the Wilson loop $c_1 := c_1(R \times T)$ in space-time.

The aim of this paper is a structural analysis of Wilson's confinement criterion, in terms of a relativistic field theory on space-time M^4, the base of a gauge-invariant structure $P(M^4, G)$ with symmetry G, the colour-gauge transformations. The fields are pairs

$$(\omega^p, c_p), \quad \omega^p \in F^p(M^4) \quad \text{(vector space of } p\text{-forms on } M^4) \tag{3}$$
$$c_p \in C_p(M^4) \quad \text{(space of } p\text{-chains on } M^4); \; p = 0, 1, 2, 3, 4$$

such that the the chains and loops $c_1 \in C_1(M^4)$ are associated with a gas of closed continuous loops, replacing the conventional discrete lattice gauge theoretical approach to confinement. I.e. we consider a statistical system in a lattice-independent description in the sense of Samuel [1]. Within such an approach to quark confinement in terms of the geometrical fields (3), the structure of the observed hadrons, i.e. matter arises from the physical properties of the "empty" space, the QCD vacuum. This ground state will enjoy statistical properties similar to those of a quantum liquid state.

2. Dynamical and topological aspects of quark confinement

The fields (3) are assumed to derive from a principal fibre bundle $P = P(M^4, G)$ over space-time $M^4 = (M^4, ds^2)$ with structure group G [2]. Let α be a connection form, $\Omega = (\Omega_\alpha^\beta)$ the curvature form of this connection and (e_i) be a frame in G', the Lie algebra of G. The potential A and the Yang–Mills field F associated with α are given by virtue of a local cross section $s: U \to P$, $U \subset M^4$, in terms of the pull-backs by s:

$$s^*\alpha = A = A^i_\mu \, dx^\mu e_i \qquad \text{defined by} \qquad A_\mu = \emptyset \wedge \partial_\mu \emptyset + \emptyset a_\mu, \tag{4}$$
$$s^*\Omega = F = F^i_{\mu\nu} \, dx^\mu \wedge dx^\nu \, e_i;$$
$$F^i_{\mu\nu} = A^i_{\nu\mu} - A^i_{\mu\nu} + c^i_{jk} \, A^j_\mu A^k_\nu \Rightarrow F_{\mu\nu} = \partial_\mu \emptyset \wedge \partial_\nu \emptyset + \emptyset(\partial_\mu a_\nu - \partial_\nu a_\mu), \tag{5}$$

where (c^i_{jk}) are the structure constants of G and (x^μ) a system of local coordinates in U. Denote by $E = E(M^4, V, G, P)$ the bundle associated with P with standard fibre V, a vector space. The Higgs field $\emptyset$ which determines the potential (4) and the field strengths (5) is the pull-back of the map $\varphi: P \to O \subset V$, O an orbit of G, by a section s, such that

$$\emptyset = s^*\varphi = \varphi_0 s: U \subset M^4 \to V, \tag{6}$$

$$\nabla\emptyset = s^*\nabla\varphi = \nabla_\mu \emptyset^i dx^\mu e_i; \qquad \nabla_\mu \emptyset^i = \emptyset^i_{,\mu} + c^i_{jk} A^j_\mu \emptyset^k, \tag{7}$$

whenever $V = G'$. $\nabla\emptyset$ stands for the covariant derivative of $\emptyset$.

The *dynamics of the quark confinement* as well as the corresponding "observables" related to colour charge screening derive from a Lagrange density of a variational

principle. This Lagrangian L is invariant under G-colour gauge transformations and is obtained from P by the following construction: Let g be an Ad-invariant metric on G', $g_{ij}=g(e_i, e_j)$, and $\| \varphi \| = h_{ij}\varphi^i\varphi^j$ an invariant metric on V, then

$$\lambda = g_{ij} {}^*\Omega^i \wedge \Omega^j + h_{ij} {}^*V\varphi^i \wedge V\varphi^j + V(\| \varphi \|)\eta_h ; \quad \Omega = \Omega^i e_i \quad ({}^*\Omega \text{ the dual form of } \Omega) \tag{8}$$

which is an invariant 4-form under the action of G, such that $\omega^4 = s^*\lambda$ (cf. (9)) will embody the dynamics with respect to the oriented Riemannian space with volume element $\eta = dx^0 \wedge dx^1 \wedge dx^2 \wedge dx^3$ (η_h is a horizontal form). Hence we may classify all the fields, dynamical and topological "observables" relevant to the problem of quark confinement as follows:

$$(\omega^4, c_4) \to I = \int_{c_4} \omega^4 ;$$

$$\omega^4 = L\eta = -\frac{1}{4} F \wedge {}^*F + V\emptyset \wedge {}^* V\emptyset + U(\| \emptyset \|)\eta \in F^4(M^4), \quad c_4 \in C_4(M^4); \tag{9}$$

$$(\omega^3, c_3) \to Q_c = \int_{c_3} \omega^3 ;$$

$$\omega^3 = j_0 \, dx^1 \wedge dx^2 \wedge dx^3 ; \quad d\omega^3 = 0 \quad (d : F^p \to F^{p+1} \text{ ext. derivative}) \tag{10}$$

$$(\omega^2, c_2) \to 4\pi g = \int_{c_2} \omega^2 ; \quad \omega^2 = \tfrac{1}{2}\varepsilon_{ijk}\emptyset^i \frac{\partial \emptyset^j}{\partial x^l} \frac{\partial \emptyset^k}{\partial x^m} dx^l \wedge dx^m , \tag{11}$$

$$(\omega^1, c_1) \to l(c_1, c_1') = \int_{c_1} \omega^1 = n \in \mathbb{Z}; \quad \omega^1 = H_i dx^i ;$$

$$\vec{H} = \frac{-1}{4\pi} \int_{c_1'} \frac{(x-y) \wedge dy}{\| x-y \|^3}, \quad [1], [2] \tag{12}$$

$$(\omega^{1'}, c_1) \to \Delta S/\hbar = 1/\hbar \int_{c_1} dS = e/\hbar c \int_{c_1} A_i \, dx^i = e/\hbar c \Phi_c ;$$

$$\omega^{1'} = \frac{e}{c} A_i \, dx^i = dS \in F^1(M); \tag{13}$$

$$(\omega^0, c_0) \to \int_{c_0} \omega^0 = \sum_{i=1}^{2} g_i S(P_i) = S(P_2) - S(P_1), \quad \omega^0 = S : M^4 \to \mathbb{R} ;$$

$$c_0 = \Sigma g_i P_i = P_2 - P_1 \in C_0(M^4). \tag{14}$$

The integral observable (9) stands for the action integral. The "observable" (10), the colour charge Q_c, is related to some conserved current e.g.

$$d^*F = 4\pi\omega^3, \quad \omega^3 = \varepsilon_{\mu\nu\gamma\delta} j^\delta \, dx^\mu dx^\nu dx^\gamma, \quad d\omega^3 = 0 . \tag{15}$$

(* is the Hodge star operator). The observable associated with the Yang–Mills–Higgs-2-field (11) is the magnetic flux through the closed surface c_2. The total magnetic charge g related to (11) may also be interpreted in terms of (14). Let

$$I: C_0(M^4) \to \mathbb{R}; \quad I(c_0) = \sum_i g_i = Q \qquad [2] \tag{16}$$

be Kronecker's Index, which is a linear map which associates with each 0-chain $c_0 = \sum_i g_i P_i \in C_0(M^4)$ the quantity (16). If the coefficients g_i are regarded as a discrete magnetic charge distribution $g_1, g_2, \ldots, g_k$ over the points $P_1, P_2, \ldots, P_k$, then (16) equals the total magnetic charge $Q = g$. Relation (14) assumes $g_1 = 1$ and $g_2 = \bar{g}_1 = -1$ as unit charges for a quark-antiquark pair. The action for a line of quantized flux, i.e. a string terminating at such quark monopoles is $\omega^0 = S$, hence (ω^0, c_0) yielding the observable (13). The observable (12), $l(c_1, c_1') = n$ is a linkage property and arises as follows: Let c_1' be a vortex solution of the Lagrangian (9). If its linking number with a Wilson loop c_1 is $l(c_1, c_1')$, then one may express the contribution for several vortices with positive and negative linkages, n_+ and n_-, respectively, to Wilson's vacuum expectation value (1) in terms of

$$\hat{g}(c_1', x_0, x_1) = P \exp\left(i \int_{c_1} A_k dx^k\right) = e^{i\Phi} = \exp\left[\frac{i2\pi g}{e}(n_+ - n_-)\right] \in G, \tag{17}$$

where

$$\emptyset(x_1, c_1) = D[\hat{g}(c_1, x_1, x_0)]\emptyset(x_0); \quad \emptyset(x_0) \in G/H \quad \text{(cf. Section 3)}, \tag{18}$$

P being the Dyson ordering operator alon the loop c_1. As shown in [1], an evaluation of the vacuum expectation value $W(c_1)$ in terms of the linkage property (12) yields, on account of a quantal vortex field $\emptyset$:

$$W(c_1) \# \exp\left[-\left(\frac{2\pi g}{e}\right)^2 \emptyset_t \int H^2 d^3x\right], \quad \vec{H} = -1/4\pi \int \frac{(y-x) \wedge dy}{\| y-x \|^3} \quad [2], [1] \tag{19}$$

$$\int H^2 d^3x \# (1/4\pi)^2 \, 2T \ln(R/R_0); \quad R_0 = \text{const.} \quad [1] \tag{20}$$

for any Wilson loop which is homotopic to a "rectangle" $R \times T$ for large T. $\emptyset_t$ denotes some trial solution.

On the other hand, assume $M^4 = S^3 \times \mathbb{R}$. If $y \neq x$ are regular values of a differentiable map $\emptyset: S^3 \to S^2$, the linkig number of the closed curves $\emptyset^{-1}(x)$ and $\emptyset^{-1}(y)$ equals the Hopf invariant $H(\emptyset)$ [3], [4], given by

$$H(\emptyset) = l(\emptyset^{-1}(x), \ \emptyset^{-1}(y)) = \int_{S^3} A \wedge dA,$$

$$dA = 1/2\varepsilon_{ijk} \emptyset^i \frac{\partial \emptyset^j}{\partial x^l} \frac{\partial \emptyset^k}{\partial x^m} dx^l \wedge dx^m, \quad A = A_i dx^i. \tag{21}$$

This relation refers to the following geometrical set-up: Let c_2 be some closed connected 2-chain (2-cycle) in S^3 with boundary $\phi^{-1}(x) \cong c_1$ then, by virtue of (21) we may count the number of times $\phi^{-1}(y) \cong c_1'$ intersects the surface c_2. Since the 2-form dA is used for a representation of $H(\phi)$, i.e. $H(\phi)$ and the linking number follow from the topological structure of the vacuum-Higgs-manifold $M_0 = S^2$, the Hopf charge holds true no matter what action principle determines the dynamics of the Higgs field ϕ^i.

3. Spontaneous symmetry breakdown and quark confinement

By virtue of the spontaneously broken colour-gauge symmetry G the previously massless gauge mesons acquire a mass. This spontaneous symmetry breaking relates to the following geometrical set-up [5]: Let $H := \{g \in G : D(g)\phi_0 = \phi_0\}$ be the isotropy subgroup of G at ϕ_0, $D : G \times V \to V$ a representation of G in V. Let $M_0 = G/H$ be the homogeneous space of G. On account of the Higgs field (6), $\varphi : P \to M_0 \subset V$, we have the subbundle $P' = \{p \in P : \varphi(p) = \phi_0\}$ of P over space-time M^4 with structure group H. M_0 is the vacuum manifold, i.e. the set of all vacua, obtained from ϕ_0 by $M_0 = D(G)\,\phi_0$, where ϕ_0 is a field configuration which minimizes the energy $U(\phi)$ in (9). Note that by the converse, a given reduction P' of a principal fibre bundle P to a subgroup H of its structure group G defines a Higgs field $\varphi : P \to M_0 = G/H$ by $\varphi(p) = \phi_0 \in M_0$ whenever $p \in P'$. Let now $\phi : S^3 \to S^2$ which determines the Hopf invariant $H(\phi)$ in (21). For any fixed t and $M^4 = S^3 \times \mathbb{R}$ we consider a Higgs field over the trivial bundle $P = S^2 \times G$, with the choice of $G = SO(3)$ [5]:

$$\varphi : P(S^2, SO(3)) = S^2 \times SO(3) \to S^2 \subset \mathbb{R}^3, \quad \varphi(\phi, g) = g^{-1}\phi\,;$$

$$M_0 = SO(3)/SO(2) = S^2, \tag{22}$$

$$P' = \{p \in P / \varphi(p) = \phi_0 \in S^2\} = P'(S^2, SO(2))\,. \tag{23}$$

This set-up corresponds to the *monopole vortex solutions of the 't Hooft-Polyakov type*. In fact, under the condition that the structure group G is reducible to H and if $\nabla_\mu \phi = 0$, a connection of $P(M^4, G)$ is reducible to a connection of $P'(M^4, H)$. Otherwise stated: A connection form α on P, restricted to P', defines an H-connection iff it is H'-valued, i.e. iff $\nabla\Phi = 0$. In the case of the associated bundle $E(S^2, SO(3)/SO(2), SO(3), P)$ with fibre $G/H = SO(3)/SO(2)$, the condition that the principal fibre bundle P is reducible to $P'(S^2, SO(2))$ is satisfied [2]. The geometry of $P'(S^2, SO(2))$ may be regarded as the geometrical structure of a $U(1)$-monopole, since $SO(2) \cong U(1)$. In fact, by (4) and (5), i.e. the definition of the Yang–Mills connection and curvature, respectively, the $U(1)$-curvature of the structure P' is given by

$$F' = g'/\|\phi\|^3\, \varepsilon_{ijk}\phi^i \frac{\partial \phi^j}{\partial x^\mu} \cdot \frac{\partial \phi^k}{\partial x^\nu}\, dx^\mu \wedge dx^\nu + (\partial_\mu a_\nu - \partial_\nu a_\mu) dx^\mu \wedge dx^\nu := F_1 + F_2\,;\; g' = g/2\,, \tag{24}$$

where, by (11), $F_1 = g\omega^2$. F_1 induces the magnetic flux described in Section 2:

$$4\pi g = \frac{1}{2e \| \Phi \|^3} \int_{c_2} \varepsilon_{ijk} \phi^i \frac{\partial \phi^j}{\partial x^l} \frac{\partial \phi^k}{\partial x^m} dx^l dx^m , \tag{25}$$

which admits a Homology classification of Higgs fields and monopoles as given in [5]. Moreover, the 2-form F' yields, via F_1, the relation (21) between the Hopf invariant $H(\phi)$ and the *linkage property* between a Wilson loop and vortex solutions. Hence *the proposed framework of a non-abelian gauge theory for an analysis of the problem of quark confinement admits a description of hadronic matter with monopole-antimonopole-configurations.* Quantization of charge in the presence of the colour gauge group $SO(3) = SU(2)/Z(2)$ can now be derived from the gauge structure $P'(S^2, SO(2))$.

Proposition 1. Let $P' = P'(M, SO(2))$ (e.g. $M = S^2$) be a principal fibre bundle over a 2-dimensional oriented Riemannian space M. Let the curvature 2-form of a connection in P' be determined by (24), i.e. $\Omega' = \Pi^* F'$. F' admits the quantum condition $g = n/2e$, $n \in \mathbb{Z}$, where g is given by (25), iff $eF'/2/2\pi$ represents an integral cohomology class (integrality condition).

Proof: If we identify $SO(2)$ with $U(1)$ and regard P' as a bundle with structure group $U(1)$, then the characteristic class of P' is represented by $eF'/2\pi$, whereby M^4, for any fixed t and $r > 0$, may be chosen as S^2. The integrality condition, following which the cohomology class F' is integral, amounts to

$$\int_{c_2} eF'/2\pi = n \in \mathbb{Z} \; \forall c_2 . \tag{26}$$

Since $M = S^2$ is compact, then

$$\int_M \Omega' = 2\chi(M) , \quad (\chi(M) \text{ is the Euler characteristic of } M) , \tag{27}$$

i.e.

$$\int_{S^2} \Omega' = 4\pi , \quad \chi(S^2) = 2 . \tag{28}$$

Now, $\Omega' = \pi^* \omega^2$, i.e. $F' = g\omega^2$, and

$$\omega^2 = 1/\| \phi \|^3 (\phi^1 d\phi^2 \wedge d\phi^3 + \phi^2 d\phi^3 \wedge d\phi^1 + \phi^3 d\phi^1 \wedge d\phi^2) ,$$

then

$$\int_{c_2} \frac{e}{2\pi} F' = n \Rightarrow \frac{ge}{2\pi} \int \Omega' = n \Leftrightarrow g = \frac{n}{2e} . \tag{29}$$

This 't Hooft–Polyakov monopole-quantum condition differ in its internal structure from monopoles which have a point singularity, in that 't Hooft–Polyakov monopoles enjoy a smooth internal structure satisfying the $SO(3)$ gauge theory equations without the need for external sources. The Higgs field in the adjoint representation of the full

colour gauge symmetry group before symmetry breaking would yield a structure of the topological quantum numbers which is characterized in terms of the Poincaré group $\Pi_1(SO(3)) = Z_2$, the cyclic group of order two. However, integral topological charge which is consistent with the 't Hooft–Polyakov model, i.e. with proposition 1, derives from the vacuum manifold $M_0 = S^2$, which corresponds to the 2nd homotopy group

$$\Pi_2(SO(3)/SO(2)) = \Pi_2(S^2) = Z\,, \quad [2], \tag{30}$$

i.e.

$$\Pi_2(SO(3)/SO(2)) = \Pi_1(SO(2)) \qquad \Pi_2(G/H) = \Pi_1(H) \tag{31}$$

which expresses the structure of the topological quantum numbers involved in terms of the exact gauge symmetry group $H = SO(2)$ only, i.e. the symmetry, which is "directly observable". The relations (30) through (31) relate to the following

Proposition 2 [5]: There exists a 2-field of the type (3) and a nondegenerate bilinear map β

$$\beta : H^2(S^2) \times H_2(S^2) \to \mathbb{R};\ (\omega^2, c_2) \to n = \deg(\hat{\emptyset}) = 1/4\pi \int_{S^2} \hat{\Phi}^* \omega^2\,, \tag{32}$$

where $\omega^{2\prime} = \hat{\Phi}^* \omega^2$; $\omega^2 = 1/\| \emptyset \|^3 (\emptyset^1 d\emptyset^2 \wedge d\emptyset^3 + \emptyset^2 d\emptyset^3 \wedge d\emptyset^1 + \emptyset^3 d\emptyset^1 \wedge d\emptyset^2)$, and where $\hat{\emptyset} : S^2_\gamma \to S^2$ is defined by $\hat{\emptyset}(x) = \emptyset(x)/\| \emptyset(x) \|$.

For a proof refer to [5]. Note that the cohomology class $[\omega^2] \in H^2(S^2)$ (the second de Rham group of the unit sphere S^2) is integral, i.e. $\langle \omega^2, c_2 \rangle \in \mathbb{Z}\ \forall c_2$. This is consistent with proposition 1. On account of (25) and (29) the monopole condition $g = n/2e$ may be recasted as

$$n = \frac{1}{4\pi \| \emptyset \|^3} \int_{c_2} \varepsilon_{ijk} \emptyset^i \frac{\partial \emptyset^j}{\partial x^m} \frac{\partial \emptyset^k}{\partial x^l} dx^m dx^l\,, \tag{33}$$

which is the number of times $\emptyset(x)$ covers the sphere M_0, as x covers $S^2(r)$. The number (33) originates from the form dA (relation (21)), which in turn determines the Hopf invariant $H(\emptyset)$ and via the linking number $l(\emptyset^{-1}(x), \emptyset^{-1}(y))$ *determines quark confinement* by virtue of the relations (19)–(21).

Discussion: The map $\hat{\emptyset} : S^2(r) \to S^2$ (proposition 2) represents a smooth normalized Higgs-vector field, which, by proposition 2, admits a classification of monopoles relevant to the *problem of quark confinement* in terms of 't Hooft's $SO(3)$ gauge tensor field

$$F_{\mu\nu} = \hat{\emptyset}^i G^i_{\mu\nu} - \frac{1}{e} \varepsilon_{ijk} \hat{\emptyset}^i \nabla_\mu \hat{\emptyset}^j \cdot \nabla_\nu \hat{\emptyset}^k \tag{34}$$

or, in terms of a more simplified version in the use of the field strength (5). Obviously, the reasonings are not different. In the case of the tensor (34), the Hopf invariant (21) will be determined by the 2-form

$$\omega^2 = 1/2\, \varepsilon_{ijk} \hat{\emptyset}^i \nabla \hat{\emptyset}^j \wedge \nabla \hat{\emptyset}^k\,; \qquad \nabla \hat{\emptyset}^j = \nabla_\mu \hat{\emptyset}^j\, dx^\mu\,. \tag{21}$$

This monopole-classification refers to the set of isolated zeros of the Higgs field $\emptyset$ (the vector field $\emptyset$ has an isolated 0 at some point x, if $\emptyset(x)=0$, but $\emptyset(x')\neq 0$ for $x'\neq x$ in a neighbourhood of x). The integer n of (32) arises as follows: There is a linear isomorphism $I:=\int_{S^2}: H^2(S^2)\to\mathbb{R}$ which determines a unique linear map $f^*:\mathbb{R}\to\mathbb{R}$ such that the diagram

$$\begin{array}{ccc} H^2(S^2) & \xleftarrow{\hat{\emptyset}^*} & H^2(S^2)\,, \\ I_1\downarrow & & \downarrow I_2 \qquad (D) \qquad \text{(cf. [2])} \\ \mathbb{R} & \xleftarrow{f^*} & \mathbb{R} \end{array}$$

commutes. Since $f^*\in L(\mathbb{R},\mathbb{R})$, this map is of the form $f^*: t\to kt$, $k\in\mathbb{R}$. Moreover, since $f^*\circ I_2 = I_1\circ\hat{\emptyset}^*$ and if ω^2 belongs to the class $[\omega^2]\in H^2(S^2)$ then

$$\int_{S^2}\hat{\emptyset}^*\omega^2 = k\int_{S^2}\omega^2 = \deg(\hat{\emptyset})\int_{S^2}\omega^2 \qquad \text{with} \quad \deg(\hat{\emptyset})=f^*(1)\,. \tag{32}$$

The degree of the mapping $\hat{\emptyset}$ is called the index $I(\hat{\emptyset})$, i.e. $\deg(\hat{\emptyset})\overset{\text{def}}{=}I(\hat{\emptyset})$ [3]. This Kronecker index whose general integral representation is

$$I(\hat{\emptyset}) = \frac{1}{A_{n-1}}\int\hat{\Phi}^*\omega = \frac{1}{A_{n-1}}\int_M \frac{1}{\|\Phi\|^u}\varepsilon_{i_1\ldots i_u}\Phi^{i_1}\,d\Phi^{i_2}\wedge\ldots\wedge d\Phi^{i_u}\,;$$

$$\omega = \sum_{i=1}^{u}(-1)^{i-1}\frac{\Phi^i}{\|\Phi\|^u}d\Phi^1\ldots d\hat{\Phi}^i\ldots d\Phi^u \tag{35}$$

admits a classification of the breakdown configurations of the models of Nielson–Olesen, 't Hooft–Polyakov, Salam–Weinberg and Georgi–Glashow, as exhibited by [6]. In the case of a *vortex*-1 field (ω^1, c_1) in $\mathbb{R}^2$, where

$$\omega^1 = d\vartheta = -\emptyset^2 d\emptyset^1 + \emptyset^1 d\emptyset^2 \in F^1(\mathbb{R}^2) \qquad \text{and} \qquad c_1\in C_1(\mathbb{R}^2) \tag{36}$$

we have

$$\hat{\emptyset}: S^1_r\to S^1, \quad \hat{\emptyset}(re^{i\vartheta}) = \emptyset(re^{i\vartheta})/\|\emptyset(re^{i\vartheta})\|\,; \quad re^{i\vartheta}\in S^1_r\,,$$

hence

$$(\omega^1, c_1)\to I(\hat{\emptyset}) = \deg(\hat{\emptyset}) = \frac{1}{2\pi}\int_{S^1}\hat{\emptyset}^*d\vartheta = \frac{1}{2\pi}\int_0^{2\pi}d\vartheta = +1\,. \tag{37}$$

Vortex fields are therefore singularities of index $I=1$.

4. Quantummechanical aspects of quark confinement

The question of quark confinement does not arise if we are treating the monopoles of Section 3 classically. Monopole–antimonopole systems, i.e. meson-like systems in a superconducting medium with string like magnetic flux connecting them are considered in this paper in terms of the observables (13) and (14) and display quantummechanical aspects. Since vortices are singularities of index one, they carry, by (29), a unit of magnetic flux $g=1/2e$, where, in conformity with (13) we may write

$$4\pi g = \int_{c_1} A_i dx^i \# S \# g \int_{c_2} \frac{\emptyset^1 d\emptyset^2 \wedge d\emptyset^3 + \emptyset^2 d\emptyset^3 \wedge d\emptyset^1 + \emptyset^3 d\emptyset^1 \wedge d\emptyset^2}{\| \emptyset \|^3}, \tag{38}$$

i.e. $dS = e/c\, A_\mu dx^\mu$ is the action differential of the action for a line of quantized flux which, by (13), ensures a kind of quantized Meissner flux confining effect. The right-hand side of (38) holds true by the following reasoning: Consider the 2-form F_1 in relation (24). This closed curvature form enjoys the property $F_1 = dA$ (locally for some A):

$$F_1 = dA = dx^1 \wedge dx^2, \quad A = (1+x^1)dx^2, \quad \text{Rank} \quad F = 2 \text{ (cf. [4])},$$

by virtue of Darboux's theorem [2]. Let now $\tilde{C}_1 : \tau \to x^\mu(\tau), \tau \in [0, 1]$ be a closed curve in M^4, which induces a closed curve c_1 in M^2, which by assumption satisfies the boundary property $c_1 - c_1' = \partial c_2$ for some c_1' and some 2-chain c_2. Then

$$\beta \int_{\tilde{c}_1} A_\mu \, dx^\mu = \beta \int_{c_2} \sqrt{g}\, du^1 du^2 = \beta \int_{c_2} \omega_1 \wedge \omega_2 = \beta \int_{c_2} \Omega = S$$

$$\beta := e/c \qquad g := \det (g_{ij})$$

on account of the choice $c_2 \subseteq S^2$ with respect to the differential forms $\omega^1 = dx^1$ and $\omega^2 = dx^2$ that diagonalize the first fundamental form of the local surface c_2, i.e.

$$ds^2 = g_{ij} du^i du^j = (du^1 du^2) \begin{pmatrix} g_{11} & g_{12} \\ g_{21} & g_{22} \end{pmatrix} \begin{pmatrix} du^1 \\ du^2 \end{pmatrix} = (\omega_1 \omega_2) \begin{pmatrix} 1 & 0 \\ 0 & 1 \end{pmatrix} \begin{pmatrix} \omega_1 \\ \omega_2 \end{pmatrix}$$

and

$$\Omega = \sin \varphi \, d\vartheta \wedge d\varphi = \emptyset^1 d\emptyset^2 \wedge d\emptyset^3 + \emptyset^2 d\emptyset^3 \wedge d\emptyset^1 + \emptyset^3 d\emptyset^1 \wedge d\emptyset^2 \quad \text{on} \quad S^2.$$

Consider now two vortex solutions terminating at monopoles g and $-g$. These solutions (c_1, g) and $(\bar{c}_1, -g)$, which enjoy the property (14), whenever this meson-like system of string like magnetic fluxes connects g and $-g$, is one-one correspondence with the elements $(I, -I)$ of Z_2, the group of integers modulo 2. This means, that in terms of the colour group $SO(3)$ this quantummechanical aspect shows that the topological quantum numbers have the structure of the Poincaré group

$$\Pi_1(SO(3)) = \Pi_1(SU(2)/Z_2) = Z_2. \tag{39}$$

In theories with $G=SU(3)/Z_3$ three-monopole systems, as well as monopole-antimonopole systems are physically realizable. The general case is the local invariance group $SU(n)$, such that the universal covering group is $\bar{G}$, $\bar{G}/C=G$, C denotes the center of G. In this case

$$G=SU(n)/Z_n\,;\quad \Pi_1(SU(n)/Z_n)=Z_n\,. \tag{40}$$

The Higgs fields are chosen in the adjoint representation of $SU(n)$ and a classification of vortices, which are physical objects exhibiting homotopic conservation laws, is obtained in terms of (40). The factor $P\exp i\int_{C^1} A_k dx^k$) (Eq. (17)) belongs to C.

5. Quark confinement and colour confinement

All quarks carry a hidden quantum number "colour". Hadrons are "white", i.e. they are always formed of combinations of quarks that are colour neutral. Theories that are invariant under G-colour gauge transformations should then admit the configurations $q\bar{q}$ and qqq as the simplest colourless structures, corresponding to mesons and baryons, respectively. Since these colourless or colour singlet-combinations of quarks have the quantum number of normal hadrons, the *problem of quark confinement becomes that of colour confinement.* The meaning of the conjectured "colour charge screening" is that all physical states carry the colour charge (cf. (10))

$$Q_c=\int_{c_3}\omega^3=\int_{c_3} j_c^c\, dx^1dx^2dx^3=0,\qquad d\omega^3=0\,. \tag{41}$$

A dynamics of quark confinement characterized in terms of fields (3) such that the action integral is obtained from (9) admits a representation of quarks, which are in one-to-one correspondence with monopole–antimonopole systems, whenever these quarks are internal vectors ψ_α of the internal vector space V of $E=E(M^4, V, G, P)$, which are transferred in parallel around a loop c_1. This parallel transport induces a linear transformation U. Thus quark–monopole systems are given by the properties

$$c_1\to\psi_\alpha(x)=U_\alpha^\beta(x)\psi_\beta(x)\,;\ U_\alpha^\beta=\delta_\alpha^\beta+\frac{1}{2}\Omega_{\alpha\mu\nu}^\beta\, dx^\mu dx^\nu\in H_x\,,\ \Omega_{\alpha\mu\nu}^\beta=F_{\mu\nu}^i(I_i)_\alpha^\beta\,;\ I_i\in G\,; \tag{42}$$

$$(\omega^1, c_1)\to l(c_1, c_1')=\int_{c_1}\omega^1\,;\quad \omega^1=H_i dx^i=n\in\mathbb{Z}\quad \text{(Eq. (12)) [2]}\,, \tag{43}$$

$$\Phi^i=4\pi g_i=\int_{c_2} {}^*F_{\mu\nu}^i\, dx^\mu\wedge dx^\nu=4\pi\int_{c_3}\omega^3=4\pi\int_{c_3} j_0 dx^1\, dx^2dx^3\,,\quad \text{(by (15))}\,. \tag{44}$$

Within this framework, it is only by virtue of the linkage property (43) that the transformations (42) represent quarks with monopole charges (44). The flux quantities (44) are given in terms of

$$P \exp i \int_{c_1} A_\mu^k I_k \cdot dx^\mu = \exp i\Phi^k I^k \in G\,. \tag{45}$$

The bundle curvatures (Ω_α^β), which are the generators of the internal holonomy group H_x [2] contribute to these fluxes via (44) in terms of the net effect of transporting an internal vector field about an unknotted circuit c_1 which amounts to a change of phase by the amount (44). Colour confinement is now obtained as follows: $Q = \Sigma\, g_i = I(c_0) = 0$ for $c_0 = \sum_i g_i P_i = P_2 - P_1$ (Eqs (14) and (16)). Now $I(c_0) = 0 \Leftrightarrow c_0 = \partial c_1$. Hence

$$(\omega^0, c_0) \to \int_{c_0} \omega^0 = \int_{c_0} S = \int_{\partial c_1} S = \int_{c_1} dS = \Delta S = S(P_2) - S(P_1)\,; \quad I(c_0) = 0\,, \tag{46}$$

which, by (13) and (14) yields quantized flux. Since magnetic charge does not originate in dynamics, but rather follows from the topological structure of M_0, one may choose a dynamics (9), where L depends on the quark field ψ_α (42) through $L_1(A, \psi_\alpha) = -1/4 F_{\mu\nu}^i F_i^{\mu\nu} + \sum_\alpha \psi_\alpha (i\not{\nabla} - m_\alpha)\psi_\alpha$, such that L is G-invariant. On account of a judicious choice of $c_3 \in C_3(M^4)$, $M^4 = S^3 \times \mathbb{R}$, colour confinement follows from the reasoning as was emphasized above by (46):

$$Q_c = \Sigma g_i = \int_{c_3} j_0 dx^1\, dx^2 dx^3 = \int_{c_3} \omega^3 = I(c_3 \cdot c_0) = 0\,, \tag{47}$$

where, by definition: $P \cdot c_3 = P$ if $P \in c_3$ (or 0 if $P \notin c_3$). (The operation "dot" differs from the set-theoretical intersection in that the orientation of chains is taken into account). The relation (47) uses the index-property

$$I(c_3 \cdot c_0) = \int_{c_3} \omega^3 \cdot$$

If the choice of the dynamical field $(\omega^4 \cdot c_4)$ admits a Hopf-invariant-type of current (cf. [4]), then the linkage property (21) equals zero, which amounts to the absence of interaction, i.e. the non-existence of free coloured particles, as a special case of (47).

Acknowledgments

The author takes pleasure in thanking Professor A. Salam for his invation to the International Centre for Theoretical Physics in Trieste. He also wishes to thank Professor N. S. Cragie for his discussions on the question of quark confinement.

References

1. A. Samuel, Nuclear Physics *B154*, 62, 1979.
2. C. v. Westenholz, Differential Forms in Mathematical Physics, North Holland, Amsterdam, 1980.
3. J. Milnor, Topology from the Differentiable Viewpoint, The University Press of Virginia, Charlottesville, 1965.
4. C. v. Westenholz, C. R. Acad. Sc. Paris, *288*, 885, 1979.
5. C. v. Westenholz, Acta Phys. Hung., *48*, 213, 1980.
6. C. Montonen, Nuclear Physics, *B140*, 333, 1978.

Acta Physica Hungarica 56 (1—4), pp 21—25 (1984)

STUDY OF THE STRUCTURE OF SOME ALKALINE EARTHS PHOSPHATE AND BORATE GLASSES BY MÖSSBAUER EFFECT

N. A. EISSA, E. E. SHAISHA and A. A. BAHGAT

Department of Physics, Faculty of Science, Al-Azhar University
Cairo, Egypt

(Received in revised form 25 November 1982)

Mössbauer spectra were measured for a series of alkaline earth phosphate and borate glasses with mole % composition (100-X) P_2O_5 + X MeO + SnO_2 (where Me = Mg, Ca, Sr or Ba and X = 20, 24 or 28). The results were analyzed as a function of glass composition and tin atoms valence state. The decrease in the isomer shift (IS) value with the increase of the alkaline earth oxide content was attributed to an increase in the ionic strength of bonds around the tin ions. The increase of the quadrupole splitting (QS) and line width (LW) values with the gradual increase of alkaline earth oxide content were attributed to be due to an asymmetric and irregular distribution of alkaline earth ions around the tin ions. The asymmetry in the absorption peak is due to Goldanskii effect. The tin was found only in the quadrivalent state.

Introduction

Mössbauer measurements have become a major tool for the investigation of the electronic properties, structure and bonding in glass. Virtually all previous Mössbauer work with phosphate glasses has dealt with either iron in alkaline earth phosphate glasses [1] or in alkali phosphate glasses [2, 3]. The only work on the sodium phosphate glasses containing tin was done by Evstropev et al [4]. The present work is an extension for a work done by the authors on both borate [5] and phosphate [6] glasses, containing tin using ME to study the valence state, coordination number and the symmetry of the immediate environment of the tin atoms. An explanation was suggested for the dependence of the ratio of the various valence and coordination structural states of the tin in the phosphate and borate glasses on the amount and nature of the alkaline earth ions.

Experimental technique

The method of preparation of the glass samples is based on the mole% composition mentioned above. Mössbauer spectra were measured at room temperature using a constant acceleration driving system coupled to a 256 multichannel

analyzer. The source used was 5 mCi Sn^{119} in Ba, Sn, O. The absorber contained nearly 1 mg Sn^{119}/cm^2. The measured ME spectra had simple shapes and were analyzed on the basis of the known Lorentzian line shape.

Results and discussion

The outstanding feature common to the Mössbauer spectra of all the glasses studied was a well resolved two peaks spectrum as shown in Figs 1, 2 and 3. Spectra in Fig. 1 are arranged according to the variation of MgO content while in Fig. 2 in order to compare the different cation effects in phosphate glasses. In Fig. 3 effects of the type of cations are studied in borate glasses. All the values obtained for the Mössbauer

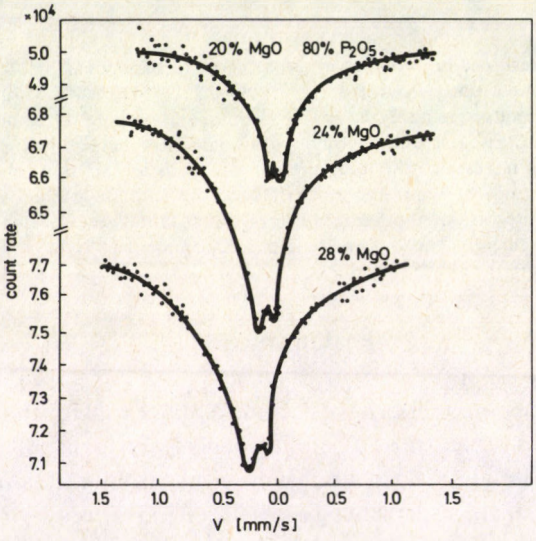

Fig. 1. Effect of alkaline earth content in phosphate glasses

parameters are presented in Table I. The general features of the isomeric shift (IS) results are their decrease as the ionic size of the MeO increases. The interpretation of this trend depends on the fact that there is a mutual polarization interaction between the Me cations and the neighbouring oxygen ions bound to the Sn^{4+} ion. This polarizing power is measured quantitatively by the charge/radius ratio which decreases in the Mg—Ca—Sr—Ba direction. Also the valence electrons of oxygen have to spend more time in the Mg—O than in the Sn—O bond and vice versa in the case of barium glasses. Consequently, the IS decreases in the direction of the increase of the ionic size. On the other hand the IS values decrease upon increasing the MeO content. This

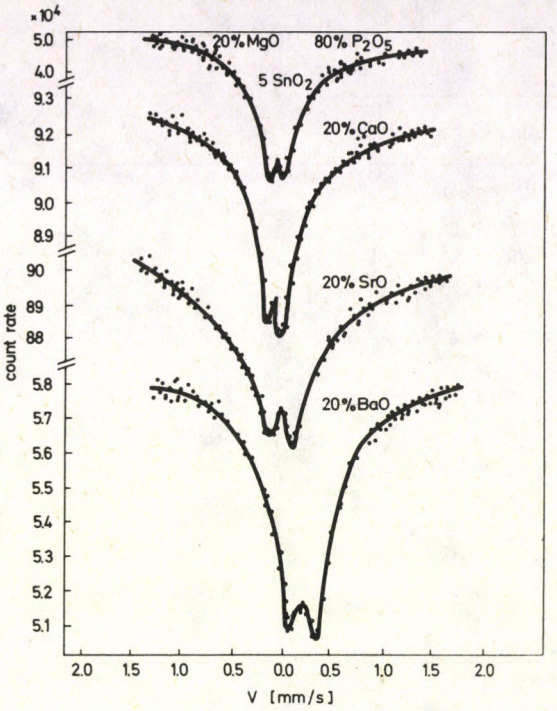

Fig. 2. Effect of alkaline earth type in phosphate glasses

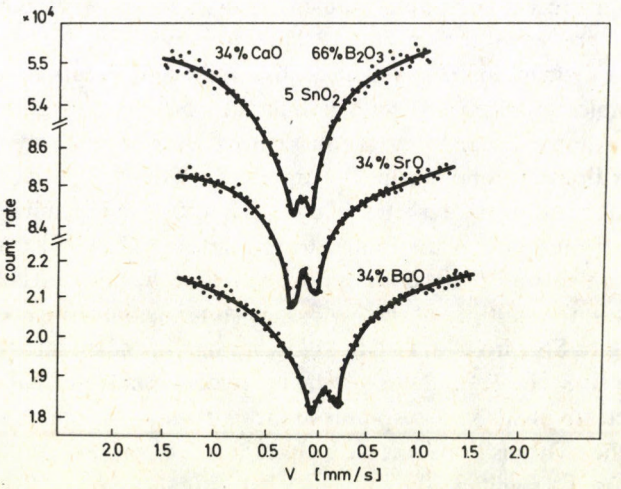

Fig. 3. Effect of alkaline earth type in borate glasses

Table I

Mössbauer parameters

Composition of glass	I. S.* [mm/s]	Q. S. [mm/s]	L. W. [mm/s]
Effect of MeO content			
20% $MgO + 80\% P_2O_5 + 5SnO_2$	2.57	0.11	0.5
24% $MgO + 76\% P_2O_5 + 5SnO_2$	2.72	0.20	0.66
28% $MgO + 72\% P_2O_5 + 5SnO_2$	2.82	0.28	0.80
Effect of MeO type			
a) Phosphate glasses			
20% $MgO + 80\% P_2O_5 + 5SnO_2$	2.57	0.11	0.5
20% $CaO + 80\% P_2O_5 + 5SnO_2$	2.52	0.16	56
20% $SrO + 80\% P_2O_5 + 5SnO_2$	2.45	0.26	0.75
20% $BaO + 80\% P_2O_5 + 5SnO_2$	2.30	0.33	0.89
b) Borate glasses			
34% $CaO + 66\% B_2O_3 + 5SnO_2$	2.72	0.2	0.66
34% $SrO + 66\% B_2O_3 + 5SnO_2$	2.60	0.27	0.6
34% $BaO + 66\% B_2O_3 + 5SnO_2$	2.45	0.36	0.76

* I. S. are measured relative to β-tin.

increase in the values of IS suggests an increase of covalency in the glass samples with increasing the MeO content.

The increase of the quadrupole splitting (QS) with the increase of the MeO content can also be interpreted on the basis of this covalency mentioned above. As known from the theory [7], the spherically asymmetric charge distribution of valence *P*-electrons will produce a large field gradient at the nucleus. Furthermore, when all three *P*-orbitals are equally populated, their superposition forms a spherically symmetric charge distribution. Thus the QS observed due to the increase of covalency in the glass samples is associated with unbalanced $5P$ electron density. Generally speaking, this splitting of the Sn^{4+} spectrum is caused by the non-equivalency of the Sn bonds in the coordination polyhedron. The amplitude of the Sn^{4+} ion vibrations along the nonequivalent bonds will clearly be different. Therefore the asymmetry of the Sn^{4+} quadrupole spectrum which is attributed to Goldanskii effect [8] can naturally be explained by the anisotropy of the dynamic properties of the SnO_6 structural group. In the studied glasses, the splitting of the Sn^{4+} spectrum has the nature as in crystalline SnO_2. According to Shapiro et al [9], in SnO_2 the sign of the quadrupole interaction constant is positive i.e. $E \pm 3/2 > E \pm 1/2$. Therefore the right hand line in the quadrupole spectrum of Sn^{4+} corresponds to the -transition, while the left hand line corresponds to the -transition. It is clear that the force constant of the Sn—O bond along the *Z*-axis is significantly smaller than in the perpendicular direction. Consequently, the two oxygen ions lying on the *Z*-axis in the SnO_6 group are at a

greater distance from the Sn^{4+} than the rest. This clearly causes the splitting and the asymmetry of the Sn^{4+} spectrum. Thus, we can come to the conclusion that there is a direct connection between the value of the QS and the anisotropy of the probability of the Mössbauer factor f.

The increase in the line width LW with the gradual increase of MeO content may be due to the increase of non-uniformity of sites in this direction. Also the disorder of the Me atoms causes great variations in the intensities of the molecular electric fields which in its turn causes a certain broadening in the absorption peak.

The tin was observed only in the quadrivalent state which has an octahedral coordination with respect to oxygen.

References

1. C. Hirayama, J. G. Castle, Jr. and M. Kuriyama, Phys. Chem. Glasses, *9*, 109, 1968.
2. C. R. Kurkjian and E. A. Sigety, Phys. Chem. Glasses, *9*, 73, 1968.
3. C. K. Lewis, Jr., and H. G. Drickamer, J. Chem. Phys., *49, 3785, 1968.*
4. K. S. Evstropev, V. G. Bezrodnyi, P. P. Seregin and V. T. Shipatov, Leningrad Gos. Univ. im Zhdanova Leningrad, USSR, Izv. Akad. Nauk, SSR, Neorg. Mater., *6*, 781, 1970.
5. N. A. Eissa, E. E. Shaisha and A. L. Hussein, J. of non-Cryst. Solids, *16*, 206, 1974.
6. N. A. Eissa, E. E. Shaisha and A. A. Bahgat "Mössbauer and IR spectra of tin in alkali phosphate glasses", Paper presented at the Fifth Conference of the Egyptian Solid State Society at Assiut University, Feb. 1982.
7. M. C. Hayes, J. Inorg. Nucl. Chem., *26, 915, 1964.*
8. V. I. Goldanskii, G. M. Gorodinskii, S. V. Karyagin, L. A. Korytko, L. M. Krizhanskii, E. F. Makarov, I. F. Suzdalev and V. V. Kharpov, Dokl. Akad. Nauk SSSR, *156*, 400, 1964.
9. V. G. Shapiro and V. S. Shpinel, Zh. Eksp. Teor. Fiz., *46*, 160, 1964.

Acta Physica Hungarica 56 (1—4), pp 27—30 (1984)

GÁSPÁR UNIVERSAL POTENTIAL WITH CORRELATION CORRECTION

J. GLEMBOCKIS

Institute of Physics of the Academy of Sciences of the Lithuanian SSR, Vilnius, USSR

and

J. PETKEVIČIUS

Institute of Mathematics and Cybernetics of the Academy of Sciences of the Lithuanian SSR, Vilnius, USSR

(Received 28 January 1983)

A method is suggested for completing the Gáspár universal potential with the correlation term. Calculations are performed for the sulphur and silver atoms in the ground configurations.

Gáspár [1] suggested a universal potential and a universal function which were broadly and successfully used by many authors for calculating one-electron eigenvalues and wave functions as well as for establishing other atomic magnitudes and properties. In [2] the original Gáspár potential (for neutral atoms) using a simplified Fermi–Amaldi type correction [3] was modified for ions. Both the original and modified Gáspár potentials have very simple analytical forms, are convenient for calculations, give an orthonormal set of one-electron wave functions and well approximate Hartree—Fock functions. The Gáspár universal potential consists of the generalization of the Hartree field and statistical approximation of the exchange terms. In this paper an attempt is made to complete the Gáspár universal potential with a correlation term.

In the statistical theory of the atom [3] correlation energy is evaluated by a correlation function. In [4] a new expression for the correlation function was established which has a very simple form and gives rather good results:

$$g(\rho^{1/3}) = \frac{\gamma}{z^{1/3}} \rho^{1/3}, \tag{1}$$

where $\gamma = 0.04846\ e^2 a^{-1}$ and ρ is electronic density. Applying the Gáspár procedure and his universal function [1]

$$\rho^{1/3} = z^{2/3} \frac{Ce^{-\alpha x}}{1 + Ax}, \tag{2}$$

where

$$C=3.1a_0^{-1}, \quad \alpha=0.04, \quad A=9, \quad x=\frac{r}{\mu}, \quad \mu=\frac{0.8853a_0}{z^{1/3}},$$

for the correlation potential we get the expression

$$\frac{4\gamma C}{3e} z^{1/3} \frac{e^{-\alpha x}}{1+Ax}. \tag{3}$$

Then the modified Gáspár universal potential for an ion with $N-a$ electrons is given by (in a.u.)

$$V_x=\frac{\mu \Delta I}{x}+\frac{Z-\Delta I}{2Z}\left\{\frac{2Z\mu}{x}\cdot\frac{e^{-\lambda_0 x}}{1+A_0 x}+2\left(2.3928+\frac{0.1570}{Z^{1/3}}\right)\frac{e^{-\alpha x}}{1+Ax}\right\}, \qquad x\leq x_0 \tag{4a}$$

$$V_x=\frac{\mu I}{x}, \qquad x>x_0, \tag{4b}$$

where x_0 is the value of x, when the values of (4a) and (4b) are equal and $I=a+1$, $\lambda_0=0.1837$, $A_0=1.05$, Δ is the empirical parameter.

In order to get one-electron wave functions we solve the following Schrödinger equation

$$\frac{d^2P}{dx^2}+\left[2V_x-\frac{l(l+1)}{x^2}-\varepsilon\right]P=0 \tag{5}$$

with necessary boundary conditions. The eigenvalue parameter is given by $\varepsilon=2E\mu^2e^{-2}a_0^{-1}$ and E is the one-electron energy parameter of the nontransformed Schrödinger equation. For solving Eq. (5) the program of Bogdanovich [5] was adjusted. For example, we have solved the equations for the sulphur and silver atoms in the ground configurations both with and without correlation correction taking $I=0$ and $\Delta=0$ (the original Gáspár universal potential). These cases were investigated by Gáspár himself [6, 7] (without correlation correction) and that gives us a possibility to compare and verify the results obtained by program [5].

The one-electron eigenvalues are given in Table I for the sulphur atom and in Table II for the silver atom, where they are compared with the original Gáspár data

Table I

One-electron eigenvalues of the sulphur atom in the ground configuration (in a.u.)

	1s	2s	2p	3s	3p
Gáspár [6]	−90.28	−7.85	−5.89	−0.588	−0.233
Gáspár (here)	−90.3726	−7.8585	−5.8955	−0.5888	−0.2326
Gáspár + corr.	−90.5419	−7.9048	−5.9450	−0.6011	−0.2425
Empirical data	−91.2	−8.5	−6.25	−0.77	−0.43

and with the empirical data (Landolt–Börnstein) both taken from [6, 7]; for the state 5*s* (the lower values in Table II) the equations were solved taking $I = 1$ and $\Delta = 0$ (as in [7]) as well. It follows from the Tables that one-electron eigenvalues with correlation correction become large (in absolute value) and are in better agreement with the empirical data.

Table II

One-electron eigenvalues of the silver atom in the ground configuration (in a.u.)

	1*s*	2*s*	2*p*	3*s*	3*p*
Gáspár [7]	−915.95	−130.82	−122.65	−23.26	−19.70
Gáspár (here)	−917.124	−131.072	−122.768	−23.308	−19.717
Gáspár + corr.	−917.450	−131.211	−122.918	−23.362	−19.776
Empirical data	−939.67	−140.21	−126.65	−26.49	−21.68

	3*d*	4*s*	4*p*	4*d*	5*s*
Gáspár [7]	−12.65	−3.22	−2.12	−0.375	−0.214 −0.244
Gáspár (here)	−12.660	−3.2231	−2.1243	−0.3757	−0.2149 −0.2450
Gáspár + corr.	−12.721	−3.2414	−2.1450	−0.3904	−0.2206 −0.2487
Empirical data	−13.67	−3.57	−2.14	−0.195	−0.278

The correlation correction in the Gáspár universal potential shifts one-electron wave functions towards the nucleus. This shift can be illustrated by calculating the diamagnetic susceptibilities for which we use the formula [3]:

$$\chi = -A_N \frac{e^2}{6mc^2} \sum_{nl} N_{nl} \int_0^\infty P^2(nl/r) r^2 dr, \tag{6}$$

where A_N is the Avogadro's number, N_{nl} is the number of electrons in the nl shell and summing is extended on all shells of the investigated configuration.

In Table III the data on the diamagnetic susceptibilities (gram-atom) for the Ag^+ ion are given. These diamagnetic susceptibilities were calculated using the one-electron wave functions of neutral silver atom (as in [7]). It follows from the Table that the correlation correction leads to larger changes in outer shells and improves the value of diamagnetic susceptibility which is in better agreement with the experimental data $-24 \cdot 10\ 10^{-6}$ cm^3 taken from [7].

It follows from Eq. (4) that the influence of correlation decreases when increasing the atomic number, as $Z^{-1/3}$, which is in accordance with the physical situation.

Table III

Contribution of electronic shells to the diamagnetic susceptibility χ of the Ag^+ ion in the ground configuration (10^{-6} cm^3)

	$1s^2$	$2s^2$	$2p^6$	$3s^2$	$3p^6$
Gáspár (here)	−0.0022	−0.0361	−0.0811	−0.2626	−0.7640
Gáspár + corr.	−0.0022	−0.0361	−0.0811	−0.2623	−0.7630

	$3d^{10}$	$4s^2$	$4p^6$	$4d^{10}$	Ag^+
Gáspár (here)	−1.1454	−1.6755	−5.9389	−20.4143	−30.3201
Gáspár + corr.	−1.1429	−1.6711	−5.9166	−20.1203	−29.9956

Investigations on the subject of correlation correction to the Gáspár universal potential in a broader scope are in progress and are supposed to be published in subsequent papers.

The authors wish to acknowledge with thanks the aid of Dr. P. Bogdanovich in adjusting his program to performing the required calculations.

References

1. R. Gáspár, Acta Phys. Hung., *3*, 263, 1954.
2. A. Jucys, J. Glembockis and R. Gáspár, Acta Phys. Hung., *23*, 425, 1967.
3. See, e.g., P. Gombás, Die statistische Theorie des Atoms und ihre Anwendungen, Springer-Verlag, Wien, 1949.
4. И. И. Глембоцкий, И. Ю. Петкявичюс, Лит. физ. сбор., *22*, N4, 28, 1982.
5. П. О. Богданович, Программа численного решения уравнений Хартри-Фока, Ин-ут Физики АН Лит. ССР, Вильнюс, 1978.
6. R. Gáspár, Acta Phys. Hung., *12*, 171, 1960.
7. R. Gáspár and K. Molnár-Ivanecsko, Acta Phys. Hung., *6*, 105, 1956.

Acta Physica Hungarica 56 (1—4), pp 31—38 (1984)

CALCULS DES COEFFICIENTS DE DILATATION DE MODELES SIMPLES A L'AIDE DE LA MECANIQUE QUANTIQUE

Y. THOMAS

Institut de Recherches Scientifiques et Techniques
49045 Angers Cedex (France)

(Reçu 31 janvier 1983)

Les interactions entre phonons rendent compte de la dilatation thermique des solides, leur traitement est effectué par la méthode de la fonction thermodynamique de Green. L'expression du coefficient de dilatation thermique est retrouvée par cette méthode pour une chaîne linéaire d'atomes et pour le solide d'Einstein.

Le champ phonique est un champ de vecteurs obéissant à une équation d'onde linéaire et homogène du second degré par rapport aux coordonnées de l'espace et du temps. Il présente une superposition d'ondes planes caractérisées par une relation de dispersion.

Pour de petites vibrations, un oscillateur harmonique monodimensionnel a pour hamiltonien:

$$H = \frac{p^2}{2m} + \frac{1}{2} m\omega_0^2 u^2 \quad \text{avec} \quad [up] = i\hbar$$

où $p = -i\hbar \dfrac{\partial}{\partial u}$ est le moment, u le déplacement, m la masse et ω_0 la fréquence angulaire. En résolvant l'équation de Schrödinger $H\psi_n = E_n\psi_n$ on montre, qu'étant donné une solution quelconque ψ_n relative à la valeur propre $e_n = \dfrac{E_n}{\hbar\omega_0}$, il est toujours possible d'en tirer une solution ψ_{n+1} correspondant à la valeur propre e_{n+1} et une solution ψ_{n-1} correspondant à e_{n-1} (si ψ_n n'est pas l'état fondamental). L'opérateur $\left(\dfrac{\partial}{\partial y} - y\right)$, où $y = \left(\dfrac{m\omega_0}{\hbar}\right)^{1/2} u$, est l'opérateur création b^+ qui permet de passer d'un état d'énergie $E_n = \hbar\omega_0\left(n + \dfrac{1}{2}\right)$ à un état E_{n+1}; l'opérateur $\left(\dfrac{\partial}{\partial y} + y\right)$, permettant de passer d'un état $|n\rangle$ à un état $|n-1\rangle$, est l'opérateur annihilation b:

$$b = \frac{1}{\sqrt{2\hbar}}\left(\sqrt{m\omega_0 u} + \frac{i}{\sqrt{m\omega_0}}p\right),$$

$$b^+ = \frac{1}{\sqrt{2\hbar}}\left(\sqrt{m\omega_0 u} - \frac{i}{\sqrt{m\omega_0}}p\right).$$

Si l'on résoud ce système en fonction des opérateurs p et u l'hamiltonien devient:

$$H = \frac{\hbar\omega_0}{2}(b^+b + bb^+) = \hbar\omega_0\left(b^+b + \frac{1}{2}\right).$$

Considérons un solide qui est un système mécanique à N degrés de liberté. Son énergie potentielle est minimale dans l'état d'équilibre. En première approximation, pour de petits écarts par rapport à sa position d'équilibre, on peut adopter l'hamiltonien harmonique:

$$H = \sum_k \frac{p_k^2}{2m_k} + \frac{1}{2}\sum_l^N G_{kl}u_k u_l$$

où la matrice G_{kl} est symétrique. Il est transformable en une somme de N parties indépendante en considérant un ensemble de N vecteurs orthonormés B_{lj} définis comme les vecteurs propres de la matrice symétrique dite dynamique:

$$D_{kl} = \frac{G_{kl}}{\sqrt{m_k m_l}}.$$

Si ω_j^2 est la valeur propre: $D \cdot \vec{B}_j = \omega_j^2 \vec{B}_j$.

En développant: $\sum_l D_{kl}B_{lj} = \omega_j^2 B_{kj}$.

De même que précédemment, les opérateurs b_j et b_j^+ peuvent être définis à l'aide des vecteurs propres B_{kj}:

$$b_j = \frac{1}{\sqrt{2\hbar}}\sum_k B_{kj}^*\left(\sqrt{m_k\omega_j}u_k + i\frac{p_k}{\sqrt{m_k\omega_j}}\right),$$

$$b_j^+ = \frac{1}{\sqrt{2\hbar}}\sum_k B_{kj}\left(\sqrt{m_k\omega_j}u_k - i\frac{p_k}{\sqrt{m_k\omega_j}}\right).$$

Ils peuvent être résolus afin de tirer les opérateurs hermitiens:

$$u_k = \sum_j \left(\frac{\hbar}{\sqrt{2m_k\omega_k}}\right)^{1/2}(b_j B_{kj} + b_j^+ B_{kj}^*),$$

$$p_k = \frac{1}{i}\sum_j \left(\frac{\hbar m_k\omega_k}{2}\right)^{1/2}(b_j B_{kj} - b_j^+ B_{kj}^*), \qquad (1)$$

d'où l'hamiltonien, somme de N oscillateurs harmoniques indépendants:

$$H = \sum_j \hbar\omega_j \left(b_j^+ b_j + \frac{1}{2} \right).$$

Etudions les vibrations d'un cristal en considérant le cas le plus simple d'une chaîne monoatomique de N atomes, équidistants de x et interagissant par des forces harmoniques entre plus proches voisins.

Soit une chaîne d'atomes fixée à ses extrémités, des forces agissent sur les extrémités en plus des interactions. Si G est la constante de rappel de la force, l'hamiltonien s'écrit:

$$H = \sum_{n=1}^{N} \frac{p_n^2}{2m} + \frac{1}{2} G \sum_{1}^{N-1} (u_n - u_{n-1})^2 + \frac{1}{2} G(u_1^2 + u_N^2).$$

Si l'on considère une chaîne monoatomique cyclique où tous les atomes jouent le même rôle, on doit ajouter le terme $-Gu_1 u_N$:

$$H = \sum_{n=1}^{N} \frac{p_n^2}{2m} + \frac{1}{2} G \sum_{1}^{N-1} (u_n - u_{n-1})^2 + \frac{1}{2} G(u_N - u_1)^2,$$

$$H = \sum_n \frac{p_n^2}{2m} + \frac{1}{2} \Sigma \{ G_{n,n} u_n^2 + G_{n+1,n} u_{n+1} u_n + G_{n,n-1} u_n u_{n-1} \} + \frac{1}{2} G(u_N - u_1)^2.$$

Par rapport au cas précédent, les termes G_{kl} sont nuls sauf si $k = l$ ou si $k - l = \pm 1$. Tous les atomes étant identiques:

$$D_{kl} = \frac{G_{kl}}{m} = 0 \,(\text{si } k \neq l) = \frac{2G}{m} \,(\text{si } k = l) = -\frac{G}{m} \,(\text{si } k - l = \pm 1).$$

L'égalité: $\sum_j D_{nl} B_{lj} = \omega_j^2 B_{nj}$ se réduit à:

$$D_{n,n-1} B_{n-1,j} + D_{n,n} B_{nj} + D_{n,n+1} B_{n+1,j} = \omega_j^2 B_{nj},$$

$$-\frac{G}{m} B_{n-1,j} + \frac{2G}{m} B_{n,j} - \frac{G}{m} B_{n+1,j} = \omega_j^2 B_{nj},$$

$$-B_{n-1,j} + 2B_{n,j} - B_{n+1,j} = \frac{\omega_j^2}{\omega_0^2} B_{nj} \quad \text{si} \quad \omega_0 = \left(\frac{G}{m} \right)^{1/2}.$$

On prend comme solution une combinaison linéaire arbitraire des solutions fondamentales $B_n = \exp(\pm iqnx)$ avec $\exp(iqNx) = 1$ d'où les vecteurs propres

$$B_{Nq} = \frac{1}{\sqrt{N}} \exp(iqnx). \tag{2}$$

La relation de dispersion est [1]:

$$\frac{\omega_q^2}{\omega_0^2} = 2(1-\cos qx) \qquad \text{où} \quad \omega_q = 2\omega_0 \sin\frac{qx}{2} \qquad \text{avec} \quad q = \frac{2\pi}{Nx}s$$

(où s est l'un des N entiers pairs compris entre $\pm N/2$ correspondant aux N coordonnées indépendantes de la série de Fourier de réseau).

On obtient de même:

$$H = \frac{p^2}{2mN} + \sum_{j\neq 0} \hbar\omega_j \left(b_j^+ b_j + \frac{1}{2} \right).$$

Mais cette approximation harmonique, assemblage de modes normaux quantifiés en phonons, ne permet pas d'expliquer la dilatation pour laquelle on doit aller au-delà du second degré dans le développement de l'énergie potentielle afin de tenir compte des interactions phonons–phonons.

Soit une chaîne d'atomes à l'équilibre (a) et déplacés par des vibrations longitudinales selon l'axe des x (b):

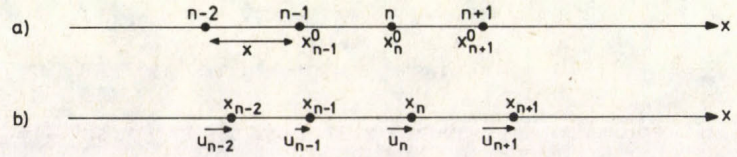

Hors d'équilibre, la distance x varie et devient $x' = x_n - x_{n-1} = (x_n^0 + u_n) - (x_{n-1}^0 + u_{n-1})$ $= x + u_n - u_{n-1}$. La variation de la distance due au mouvement thermique entre deux atomes consécutifs est $dx = u_n - u_{n-1}$.

L'énergie potentielle entre deux atomes est une fonction de leur écart et peut être développée en puissance de dx, l'Hamiltonien anharmonique de la chaîne est:

$$H = \sum_{n=1}^{H} \frac{p_n^2}{2m} + \frac{a}{2}\sum_{n=1}^{N}(u_n - u_{n-1})^2 + \frac{b}{6}\sum_{1}^{N}(u_n - u_{n-1})^3 + \frac{c}{24}\sum_{1}^{N}(u_n - u_{n-1})^4 + \ldots$$

où a, b, c sont les constantes harmonique, cubique et du quatrième ordre respectivement, des forces entre plus proches voisins.

Le déplacement atomique peut être exprimé à l'aide des opérateurs création et annihilation de phonons, pour cela portons l'équation (2) dans l'équation (1):

$$u_n = \sum_k \left(\frac{\hbar}{2mN\omega_k} \right)^{1/2} (b_k e^{iqnx} + \underline{b}_k^+ e^{iqnx})$$

or $qx = \dfrac{2\pi s}{N} = k$ valeurs permises par la condition cyclique aux limites $(u_{n+N} = u_n)$

$$u_n = \left(\frac{\hbar}{2mN} \right)^{1/2} \sum_k \frac{e^{ikn}}{\omega_k^{1/2}} (b_k + \underline{b}_k^+) \tag{3}$$

où ω_k est la fréquence des modes normaux du réseau non perturbé [1]:

$$\omega_k = 2\omega_0 \sin\frac{qx}{2} = \left(\frac{4a}{m}\right)^{1/2} \sin\frac{k}{2}.$$

A l'aide de l'équation (3), l'expression de l'hamiltonien en seconde quantification avec $B_k = (b_k + \underline{b}_k^+) \ldots$ est [2]:

$$H = \sum_k \hbar\omega_k \left(b_k^+ b_k + \frac{1}{2}\right) + \sum_{k_1 k_2 k_3} V^3_{k_1 k_2 k_3} B_{k_1} B_{k_2} B_{k_3} + \sum_{k_1 \ldots k_4} V^4_{k_1 \ldots k_4} B_{k_1} \ldots B_{k_4} + \ldots .$$

D'après l'équation (3):

$$u_{n-1} = \left(\frac{\hbar}{2mN}\right)^{1/2} \sum_k \frac{e^{ik(n-1)}}{\omega_k^{1/2}} (b_k + \underline{b}_k^+)$$

d'où la moyenne:

$$\langle dx \rangle = \langle u_n - u_{n-1} \rangle = \left(\frac{\hbar}{2mN}\right)^{1/2} \sum_k \frac{e^{ikn} - e^{ik(n-1)}}{\omega_k^{1/2}} \langle b_k + \underline{b}_k^+ \rangle$$

$$= 2i \left(\frac{\hbar}{2mN}\right)^{1/2} \sum_k \frac{\sin k/2}{\omega_k^{1/2}} e^{-i\frac{k}{2}} e^{ikn} \langle b_k + \underline{b}_k^+ \rangle .$$

Il faut évaluer la moyenne thermodynamique $\langle B_k \rangle$, cet opérateur satisfait à l'équation suivante de mouvement [2]:

$$i\frac{\partial}{\partial t}(b_k + \underline{b}_k^+) = \omega_k B_k + 6 \sum_{k_1 k_2} V^3_{k_1, k_2, -k} B_{k_1} B_{k_2} + 8 \sum_{k_1 k_2 k_3} V^4_{k_1, k_2, k_3, -k} B_{k_1} B_{k_2} B_{k_3} + \ldots \quad (4)$$

La valeur thermique moyenne de l'observable A est la trace (Tr) de ρA où ρ est l'opérateur densité et H l'hamiltonien du système:

$$\langle A \rangle = \mathrm{Tr}\, \rho \cdot A = \mathrm{Tr} \frac{e^{-H/kT}}{\mathrm{Tr}\, e^{-H/kT}} \cdot A .$$

En explicitant l'opérateur à l'aide de ses états propres $|n\rangle$:

$$\langle A_t \rangle = \frac{1}{Z} \sum_n e^{-En/kT} \langle n | A_t | n \rangle$$

où $Z = \mathrm{Tr}\, e^{-H/kT}$ est la fonction de partition, or, $A_t = e^{iHt} A_0 e^{-iHt}$, d'où:

$$\langle A_t \rangle = \frac{1}{Z} \sum_n e^{-En/kT} \langle n | A_0 | n \rangle$$

indépendant du temps t soit: $\dfrac{d}{dt} \langle A_t \rangle = 0$.

Prenons la moyenne thermodynamique de l'équation (4)

$$0=\omega_k\langle B_k\rangle+6\sum_{k_1k_2}V^3_{k_1,k_2,-k}\langle B_{k_1}B_{k_2}\rangle+8\sum_{k_1,k_2,k_3}V^4_{k_1,k_2,k_3,-k}\langle B_{k_1}B_{k_2}B_{k_3}\rangle+\ldots.$$

En se limitant au premier terme anharmonique:

$$\langle B_k\rangle=-6\sum_{k_1k_2}V^3_{k_1k_2-k}\cdot\frac{1}{\omega_k}\langle B_{k_1}B_{k_2}\rangle$$

avec [2]:

$$\langle B_{k_1}B_{k_2}\rangle=N_{k_1}\delta_{k_1k_2}=\coth\frac{\omega_{k_1}}{2kT}\delta_{k_1k_2}.$$

La moyenne est:

$$\langle dx\rangle=2i\left(\frac{\hbar}{2mN}\right)^{1/2}\sum_k\frac{\sin k/2}{\omega_k^{1/2}}e^{-i\frac{k}{2}}e^{ikn}.\ (-6)\sum_q V^3_{q,-q,-k}\frac{1}{\omega_k}\coth\frac{\omega q}{2kT}.$$

D'où [2, 3]:

$$V^3=\frac{-ib}{\sqrt{288}a^{3/2}N^{1/2}}\Delta_{q,-q,-k}\omega_q\omega_k^{1/2},$$

$$\langle dx\rangle=\frac{-b\hbar}{2m^{1/2}a^{3/2}N}\sum_{kq}\frac{\sin k/2\,e^{-i\frac{k}{2}}e^{ikn}}{\omega_k^{3/2}}\omega_q\omega_k^{1/2}N_q\Delta_k$$

$$=\frac{-4b\hbar}{m^2N}\sum_{kq}\frac{\sin^2\frac{q}{2}\sin\frac{k}{2}}{\omega_k^2\omega_q}N_q\Delta_k e^{ikn}$$

$$=\frac{-b\hbar}{4a^2N}\sum_q\omega_qN_q$$

$$=\frac{-b}{4a^2N}\sum_q\hbar\omega_q\coth\frac{\omega_q}{2kT}.$$

L'énergie moyenne d'un oscillateur dans l'approximation harmonique est:

$$\langle E\rangle=\langle H\rangle=\mathrm{Tr}\,\rho H=-\frac{\partial}{\partial\frac{1}{kT}}\log Z=\frac{1}{2}\hbar\omega+\frac{\hbar\omega}{e^{\frac{\hbar\omega}{kT}}-1}$$

$$=\frac{1}{2N}\hbar\omega\coth\frac{\hbar\omega}{2kT}$$

(soit kT à haute température)

$$\langle dx\rangle=-\frac{b}{2a^2}\langle E\rangle,$$

le coefficient de dilatation linéaire est:

$$\alpha_T = \frac{1}{x}\frac{\partial}{\partial T}\langle dx\rangle = -\frac{b}{2a^2x}\frac{d\bar{E}}{dT} = -\frac{b}{2a^2x}C_{v_T}$$

si C_{v_T} est la chaleur spécifique par atome. Il existe une similitude avec l'analyse de Kittel [5], l'expression moyenne de l'énergie, selon la mécanique quantique, remplaçant la valeur classique kT. Ce résultat a aussi été obtenu par une méthode très différente [4].

L'Hamiltonien d'un solide d'Einstein est [6]:

$$H = \frac{p^2}{2m} + \frac{a}{2}x^2 + \frac{b}{6}x^3 + \frac{c}{24}x^4$$

où x est le déplacement de l'atome par rapport à sa position d'équilibre.

L'équation de mouvement est:

$$-m\frac{d^2x}{dt^2} = ax + \frac{b}{2}x^2 + \frac{c}{6}x^3,$$

sa moyenne thermodynamique est:

$$0 = a\langle x\rangle + \frac{b}{a}\langle x^2\rangle$$

en négligeant le dernier terme, soit:

$$\langle x\rangle = -\frac{b}{2a}\langle x^2\rangle.$$

Comme l'énergie est la moyenne thermique de l'hamiltonien: $E = \langle H\rangle$:

$$\langle x^2\rangle = \frac{e^{-\frac{1}{kT}(n+\frac{1}{2})\hbar\omega}\langle n|x^2|n\rangle}{\sum_n e^{-\frac{1}{kT}(n+\frac{1}{2})\hbar\omega}} = \frac{1}{m\omega_0^2}\frac{\hbar\omega}{2}\cdot\coth\frac{\hbar\omega}{2kT} = \frac{\bar{E}}{a}$$

en fonction de l'énergie interne du solide. $\langle x\rangle = -\frac{b}{2a^2}\bar{E}$. Le résultat de Kittel [5] à haute température est ainsi retrouvé très rapidement.

La méthode de la fonction thermodynamique de Green a permis de retrouver élégamment l'expression du coefficient de dilatation linéaire. Cette illustration sur deux exemples simples laisse entrevoir la fécondité de la méthode pour l'étude de la dilatation thermique des solides à laquelle jusqu'ici elle ne semble pas avoir été appliquée.

References

1. R. A. Levy, Principles of Solid State Physics, Academic Press Inc., New York, 1965.
2. K. N. Pathak, Phys. Rev., *139*,5A, 1569, 1965.
3. A. A. Maradudin et al., Ann. of Physics, *15*, 337, 1961.
4. G. Liebfried et W. Ludwig, Solid State Physics, *12*, 275, 1960.
5. C. Kittel, Introduction to Solid State Physics, Wiley, New York, 1956.
6. Y. Thomas, Physics Letters, *66A* 2, 131, 1978; Acta Phys. Hung., *48*, 397, 1980.

Acta Physica Hungarica 56 (1—4), pp 39—45 (1984)

ON SEMI-SIMPLICITY OF SUPERALGEBRAS

NGUYEN AI VIET

Institute of Physics, Nghia do, Tu liem, Ha noi, Viet nam

(Received in revised form 30 January 1983)

Superalgebras can become semi-simple, if one constraint in the analysis of Haag, Lopuszánsky and Sohnius [1] is ignored. A complete analysis for reconstruction of all possible superalgebras is shown in this case. The self-consistent conditions which the superalgebras must satisfy are derived. Finally, we classify those models and give new possibilities of unified theories. Using those models we can look for the prospect of irreducible multiplets of particles with different masses. In certain models, we would have superunified theories with arbitrary internal symmetry groups. As a minor result, the Coleman–Mandula's theorem is also given in weaker form.

1. Introduction

Up to now the superalgebras used in superunified theories have based on the analysis of Haag, Lopuszánsky and Sohnius [1]. In that paper the authors showed a complete analysis on all possible generators of supersymmetry of S-matrix with three assumptions:

(i) they commute with S-matrix;

(ii) they act additively on the states of several incoming particles. (This requirement can be expressed most conveniently in the following way: Let G denote the possible generator, $\mathbf{a}_{i,r}^{(in)}(p)$ denote the creation operator of an incoming particle of type i with momentum p and spin orientation r, and $a_{i,r}^{(in)}(p)$ the corresponding destruction operator. Then:

$$G = \sum_{i,j,r,s} \int d^3p d^3p' \mathbf{a}_{i,r}^{(in)}(p) K(p, p') a_{j,s}^{(in)}(p') ,$$

where K is a c number kernel);

(iii) they connect only particles with the same mass.

As the result, a GLA which has been used widely up to now in superunified theories, is obtained. It can be considered as a non-trivial unification of Poincaré algebra and the internal symmetry algebra.

Let us restrict with the generators $M_{\mu\upsilon}$, P_ρ, Q_α^L, $\bar{Q}_\beta^M$ and B_l only, this GLA has the following form:

$$[M_{\mu\upsilon}, M_{\rho\sigma}] = g_{\mu\rho} M_{\upsilon\sigma} + g_{\upsilon\sigma} M_{\mu\rho} - g_{\upsilon\rho} M_{\mu\sigma} - g_{\mu\sigma} M_{\upsilon\rho} , \tag{1.1}$$

$$[M_{\mu\nu}, P_\rho] = i(g_{\mu\rho}P_\nu - g_{\nu\rho}P_\mu), \tag{1.2}$$

$$[P_\mu, P_\nu] = 0, \tag{1.3}$$

$$[M_{\mu\nu}, Q_\alpha^L] = \frac{1}{2}\cdot(\sigma_{\mu\nu})_\alpha^\beta Q_\beta^L, \tag{1.4}$$

$$[M_{\mu\nu}, B_l] = 0, \tag{1.5}$$

$$[B_l, B_m] = i\sum_k c_{lm}^k B_k, \tag{1.6}$$

$$\{Q_\alpha^L, \bar{Q}_\beta^M\} = c^{iM}\sum_u (\sigma_\mu)_{\alpha\beta}P^\mu, \tag{1.7}$$

$$\{Q_\alpha^L, Q_\beta^M\} = c_{\alpha\beta}\sum_l a_l^{LM}B_l, \tag{1.8}$$

$$[B_l, Q_\alpha^L] = \sum_M s_l^{LM}Q_\alpha^M, \tag{1.9}$$

$$[P_\mu, B_l] = 0, \tag{1.10}$$

$$[P_\mu, Q_\alpha^L] = 0. \tag{1.11}$$

($\mu, \nu, \rho = 1, 2, 3, 0$; Minkowski indices, l, m: internal indices α, β spinor indices, $L, M = 1, 2, \ldots, N$: unified indices).

The numerical matrices c^{LM}, a_l^{LM}, s_l^{LM} must satisfy certain self-consistent constraints. The vanishing matrices $c=0$, $a_l=0$, $s_l=0$ are the trivial solutions of the system of self-consistent conditions. So, in some GLAs those numerical matrices can vanish. In [1] the authors affirmed that the c matrix is different from zero, and then c^{LM} can be normalized to δ^{LM} in any case of GLA. But in fact there is no argument for it. In our previous paper [2] we showed that with reparametrization of superspace we can get such a GLA, in which $c=0$. In such models we have more degrees of freedom for the internal symmetry groups as it will be shown in Section 4.

It is worth noting that all above GLAs have the commutative ideal $\{P_\rho\}$. In this study we also discuss the possibility of the existence of semi-simple superalgebras, when we ignore the assumption (iii) of Haag, Lopuszánsky and Sohnius. Mathematically, we must have the system of self-conditions of the semi-simple superalgebras. Using the semi-simple superalgebras P^2 is no longer Casimir operator. So, we come to two possibilities:

1. Interacting multiplets: In an irreducible multiplet we would have composite particles and elementary particles together. Their bare masses are the same, but new sources would appear to give corrections to mass. After a certain procedure of renormalization the physical masses can be different.

2. Free multiplets: In this case operator P^2 is the mass operator. So, we have particles with different masses in an irreducible multiplet.

Of course all these possibilities can be realized only on concrete models.

2. Analysis

First, we preserve Poincaré algebra and the internal symmetry algebra, so we come to (1.1), (1.2), (1.3) and (1.5). Let us assume that P_ρ belongs to (1/2, 1/2) representation, Q_α^L belongs to (1/2, 0) representation, $\bar{Q}_\beta^M$ belongs to (0, 1/2) representation, B_l belongs to (0, 0) representation of Lorentz group, we come to (1.4) and (1.6)

The case of the commutator $\{Q_\alpha^L, \bar{Q}_\beta^M\}$:

Generally speaking, $\{Q_\alpha^L, Q_\beta^M\}$ belongs to the $(1/2, 0)\times(1/2, 0)=(1, 0)\oplus(0, 0)$ representation of Lorentz group. Let us restrict with $M_{\mu\nu}, P_\rho, Q_\alpha^L, Q_\beta^M$ and B_l generators only. There is no operator belonging to the (1, 0) representation in our analysis. So the coefficient of this component in the above expansion equals zero and the coefficients of (0, 0) are a_l^{LM} (because zero belongs to every representation, a_l^{LM} can vanish in some models). So, we come to (1.8).

The case of the commutator $\{Q^L, \bar{Q}_\beta^M\}$:

The commutator $\{Q_\alpha^L, \bar{Q}_\beta^M\}$ belongs to the $(1/2, 0)\times(0, 1/2)=(1/2, 1/2)$ representation, so we come to (1.7).

Naturally, c^{LM} can be chosen as zero in some specific models. And there is no argument to identify it with δ^{LM} in the general case as it had been done in [1].

The case of the commutator $[B_l, Q_\alpha^L]$:

The commutator $[B_l, Q_\alpha^L]$ belongs to the $(0, 0)\times(1/2)=(1/2, 0)$ representation of Lorentz group. So we come to (1.9). Like the case of a_l and c, the s_l matrices can vanish, too, in some specific GLAs.

If we do not require assumption (iii), we can replace (1.10) and (1.11) commutators by more general ones. We continue to use the standard technique to find the possible forms of $[P_\mu, B_l]$ and $[P_\mu, Q_\alpha^L]$ without the assumption (iii).

The case of the commutator $[P_\mu, B_l]$:

The commutator $[P_\mu, B_l]$ belongs to $(1/2, 1/2)\times(0, 0)=(1/2, 1/2)$ representation. Hence, the most general form of it is determined by the following formula:

$$[P_\mu, B_l]=\Sigma(b_l)_\mu^\nu P_\nu\,. \tag{2.1}$$

The case of the commutator $[P_\mu, Q_\alpha^L]$:

The commutator $[P_\mu, Q_\alpha^L]$ belongs to the $(1/2, 1/2)\times(1/2, 0)=(1, 1/2)\oplus(0, 1/2)$ representation of Lorentz group. Hence the most general form of it is:

$$P_\mu, Q_\alpha^L] = \Sigma d^{LM}(\sigma_\mu)_\alpha^\beta \bar{Q}_\beta^M , \tag{2.2}$$

because there is no generator (1, 1/2) in our analysis.

The matrices b_l and d can vanish too as well as the matrices a_l, s_l and c in some specific GLAs. With non-trivial d we have the ideal $\{P_\mu\}$ no longer, the algebra becomes semi-simple.

Generally, $\{P_\mu, B_l, Q_\alpha^L, \bar{Q}_\beta^M\}$ form a non-commutative ideal of this algebra, so our algebra cannot be simple. We need more generators to get a simple GLA.

3. Self-consistent conditions

We must satisfy the Jacobi identities for the generators. Only in this case the previous commutators would form a GLA. These identities would impose constraints on the numerical matrices.

First, let us consider the Jacobi identity (P_μ, B_l, B_m). We come to:

$$b_l \cdot b_m - b_m \cdot b_l = i\Sigma c_{lm}^k \cdot b_k , \tag{3.1}$$

where b_k are 4×4 matrices. So, b_k matrices form a 4-dimensional representation of the generators of the internal symmetry group. The condition of using the models with $b_k \neq 0$ is that the internal symmetry group has 4-dimensional representations. Then we can speak about Lie extension of Poincaré algebra and the internal symmetry algebra. This algebra is not a trivial extension. However, we always want to have an internal symmetry group with arbitrarily big size. In the following discussion we choose $b_k \equiv 0$.

The Jacobi identity (P_μ, B_l, Q_α^L) gives:

$$\sum_M (s_l^{LM} d^{MN} + d^{LM} \cdot \mathbf{s}_l^{MN}) = 0 \tag{3.2}$$

in the matrix form

$$s_l \cdot d = -d \cdot \mathbf{s}_l .$$

The Jacobi identity $(B_l, Q_\alpha^L, \bar{Q}_\beta^M)$ gives:

$$\sum_N (\mathbf{s}_l^{MN} \cdot c^{LN} + c^{NM} \cdot s_l^{LN}) = 0 \tag{3.3}$$

in the matrix form

$$c \cdot s_l = -s_l \cdot c .$$

The Jacobi identity (P_μ, P_ν, Q) gives:

$$\Sigma d^{LM} \cdot \mathbf{d}^{MN} = 0 , \tag{3.4}$$

in the matrix form

$$d \cdot \mathbf{d} = 0 .$$

The Jacobi identity (B_l, B_m, Q_α^L) gives:

$$\sum_N (s_l^{LN} \cdot s_m^{NM} - s_m^{LN} \cdot s_l^{NM}) = i\Sigma c_{lm}^k s_k^{LM} \tag{3.5}$$

in the matrix form

$$[s_l, s_m] = i\Sigma c_{lm}^k s_k .$$

The Jacobi identity $(B_l, Q_\alpha^L, Q_\beta^M)$ gives:

$$s_l \cdot a_k^c - a_k \cdot s_l^c = i\Sigma c_{lm}^k a_m . \tag{3.6}$$

The Jacobi identity $(Q_\gamma^L, Q_\alpha^M, \bar{Q}_\beta^N)$ gives

$$\text{when } \alpha = \gamma \qquad d^{LE} \cdot c^{MN} = d^{ME} \cdot c^{LN}, \tag{3.7}$$

$$\text{when } \alpha \neq \gamma \qquad \Sigma \mathbf{s}_l^{NE} \cdot a_l^{LM} = 0 . \tag{3.8}$$

The Jacobi identity $(Q_\alpha^L, Q_\beta^M, Q_\gamma^N)$ gives us:

$$\Sigma (a_l)^{KL} \cdot s_l^{NM} = \Sigma a_l^{LN} \cdot s_l^{KM}. \tag{3.9}$$

Other Jacobi identities satisfy trivially.

From the conjungation, we have two relations:

$$a_l^{LM} = -a_l^{ML} \qquad \text{(antisymmetric)} \tag{3.10}$$

and

$$c^{ML} = \mathbf{c}^{LM} \qquad \text{(hermitic)}. \tag{3.11}$$

So, generally matrix elements of s_l, a_l, c_l, $d(b_k \equiv 0)$ must satisfy ten of the above self-consistent conditions.

4. Classification and discussion

The case of $b_k \neq 0$: As it was quoted in the previous point, with $M_{\mu\nu}$, P_ρ, B_l generators, we have a non-semi-simple Lie algebra with the Abelian ideal $\{P_\mu\}$. However, it is not the trivial extension of the external and the internal symmetry group. The extended group is not simply the direct product of the geometrical symmetry group and the internal symmetry group. So, if the internal symmetry is big enough not to have 4-dimensional representation, the unification is impossible. From the viewpoint of the Lie algebra theory, we come to a weaker form of the Coleman–Mandula's theorem, when we ignore the assumption (iii). (According to the Coleman–Mandula's theorem [3] with the three above assumptions the unification of Poincaré algebra and the internal symmetry algebra is trivial).

In GLA models, for the arbitrariness of the internal symmetry group we choose $b_k=0$ with any k.

Non semi-simple models had been reviewed in [1] with $d=0$.

In the models with $d\neq 0$, the operator P^2 is no longer a Casimir operator. We have two possibilities:

1. Free representation

We have this possibility if we can assign free elementary particles into an irreducible representation of such models. Because P^2 is the mass operator then, if we would succeed in searching for another Casimir operator $K=K(P^2, G_i)$ where G_i are the generators of the considered GLA, the mass would not be constant in each irreducible representation. And we would come to a mass-formula without symmetry breaking. In this case, as expected, the internal degrees of freedom and fermion charges would give corrections to mass.

2. Interacting representation

We have this possibility if we can assign elementary particles and composite particles together into an irreducible multiplet. In this case P^2 is not mass operator indeed. The bare masses of particles in an irreducible representation can be the same. But the field equation is inhomogeneous. It means that new sources will appear to give corrections to mass. After a certain procedure of renormalization the physical mass in an irreducible representation is not constant too.

The above situations give us the prospect to search for a mass-splitting mechanism on exact symmetry. It is worth studying because, as we know, up to now no symmetry breaking has been found in superunified theories.

With $c=0$, we have the *Tsp* models studied in [2]. We can get those models from the usual models with $c^{LM}=\delta^{LM}$ when we replace Q_α^L by $Tsp_\alpha^L=Q^L+i\bar{Q}_{\dot{\beta}}^L(\sigma_\mu)_\alpha^{\dot{\beta}}P^\mu$. In these models the superfields are determined uniquely, the superspace will be vectorspace, the supertranslation group will be Abelian. It is worth noting that in this case (3.3) satisfy automatically. So s_l can be chosen more arbitrarily. We can speak about the $SU(N)$ superunified theories.

With $c\neq 0$, we have the models of Haag, Lopuszánsky and Sohnius. These models have been considered in [1]. Note that if in these models we choose $c^{LM}=\delta^{LM}$, from (3.3) we come to $\bar{s}_l=-s_l$ hence we have only the orthogonal supergravity. To have other internal groups ($SU(N)$ for instance) in superunified theories we must choose $c=0$ or at least must keep it in general form.

With $a_l=0$, we have the models without central charges, which can be used as well as the models with central charges [1].

It is worth examining the models with $s_l=0$. The algebra will have the ideal $\{B_l\}$. Without central charges this extension is trivial. So with $s_l=0$ the non-trivial unified theories must be the models with central charges.

5. Conclusion

Using the semi-simple superalgebras we would unify the particles with different masses into an irreducible multiplet. The mechanism of mass splitting would be studied only on the concrete models satisfying conditions (3.2)–(3.11). The choice of these models will be decided only by the physical conditions. We will revert to this point again in the nearest future.

Acknowledgements

Thanks are due to Professor Dao Vong Duc for many helpful discussions. Without his help the discussion of the above results is uncompleted.

I am also indebted to my master Professor I. Lovas, who introduced me to elementary particle physics in first steps.

References

1. R. Haag, J. T. Lopuszánsky and M. Sohnius, Nuclear Physics, *B88*, 257, 1975.
2. Nguyen Ai Viet, Acta Phys. Hung., *54*, 353, 1983.
3. S. Coleman and J. Mandula, Phys. Rev., *159*, 1251, 1967.

Acta Physica Hungarica 56 (1—4), pp 47—53 (1984)

THERMOSOLUTAL CONVECTIVE INSTABILITY IN A STELLAR ATMOSPHERE

R. C. SHARMA* and K. N. SHARMA

Department of Mathematics, Himachal Pradesh University
Simla-171005, India

(Received 3 February 1983)

Thermal-convective instability in a stellar atmosphere is considered to include the effect of a stable solute gradient. A criterion for monotonic instability is derived. The thermosolutal convective instability problem in the presence of magnetic field and rotation is also studied. The criterion derived for monotonic instability of the stellar atmosphere is found to hold good, both in the presence of magnetic field as well as rotation, on the thermosolutal-convective instability.

1. Introduction

The instability in which motions are driven by buoyancy forces, of a thermally unstable atmosphere has been termed as "thermal-convective instability". Defouw [1] has generalized the Schwarzschild criterion for convection to include departure from adiabatic motion and has shown that a thermally unstable atmosphere is also convectively unstable, irrespective of the atmospheric temperature gradient.

Defouw [1] has found that an inviscid stellar atmosphere is unstable if

$$D = \frac{1}{C_p}(L_T - \rho\alpha L_\rho) + \kappa k^2 < 0\,, \tag{1}$$

where L is the energy lost minus the energy gained per gram per second and α, ρ, κ, k, L_T, L_ρ denote respectively the coefficient of thermal expansion, the density, the coefficient of thermometric conductivity, the wave number of the perturbation, the partial derivative of L with respect to temperature $T$and the partial derivative of L with respect to density ρ, both evaluated in the equilibrium state. In general, the instability due to inequality (1) may be either oscillatory or monotonic. Defouw [1] has also studied the effects of a uniform rotation and a uniform magnetic field on thermal-convective instability of a stellar atmosphere and has found that inequality (1) is a sufficient condition for monotonic instability.

The conditions under which convective motions are important in stellar atmospheres are usually far removed from the consideration of a single component

* Present address: Department of Physics, University of Alberta, Edmonton, Canada T6G 2J1

fluid and rigid boundaries and therefore it is desirable to consider two component fluid and free boundaries. In the case of a two component fluid buoyancy forces can arise not only from density differences due to variations in temperature but also from those due to variations in solute concentrations. Veronis [4] has considered the problem of thermohaline convection in a layer of fluid heated from below and subjected to a stable salinity gradient. The thermohaline convection in a horizontal layer of viscous fluid heated from below and salted from above has been studied by Nield [2].

In the present paper we consider the thermal-convective instability of a stellar atmosphere in the presence of a stable solute gradient. We also study the thermosolutal-convective instability problem in the presence of rotation and magnetic field. In many situations of astrophysical interest such as interstellar gas, interior of stars etc. the gases may not be composed of a single component fluid but may be subjected to the concentration gradient of another component fluid. The motivation of this study is due to the importance in astrophysics of thermal-convective instability problem in the presence of solute gradient.

2. Perturbation equations

Here we consider an infinite horizontal fluid layer of thickness d heated from above and subjected to a stable solute concentration gradient so that the temperature and concentrations at the bottom surface $z=0$ are T_0 and C_0 and at the upper surface $z=d$ are T_1 and C_1 respectively, z-axis being taken as vertical. This layer is acted on by gravity force $\mathbf{g}(0, 0, -g)$. Then the equations governing the motion of the fluid, following Boussinesq approximation, are

$$\frac{\partial \mathbf{v}}{\partial t} + (\mathbf{v}\cdot\nabla)\mathbf{v} = -\frac{1}{\rho_0}\nabla p + \nu\nabla^2\mathbf{v} + \mathbf{g}\left(1+\frac{\delta\rho}{\rho_0}\right), \tag{2}$$

$$\nabla\cdot\mathbf{v}=0, \tag{3}$$

$$\frac{\partial C}{\partial t} + (\mathbf{v}\cdot\nabla)C = \kappa'\nabla^2 C, \tag{4}$$

$$\rho = \rho_0[1-\alpha(T-T_0)+\alpha'(C-C_0)]. \tag{5}$$

Eqs (2)–(4) express the conservation of momentum, mass and solute mass concentration, respectively. Eq. (5) represents the equation of state. The suffix zero refers to values at the reference level $z=0$. $\mathbf{v}(u, v, w)$, g, ρ, p, T, C, α and α' stand for velocity, gravitational acceleration, density, pressure, temperature, concentration, thermal coefficient of expansion and an analogous solvent coefficient, respectively. The kinematic viscosity ν, the thermal diffusivity κ and the solute diffusivity κ' are each assumed to be constant.

The steady state solution is

$$\mathbf{v}=0, \quad T=T_0+\beta z, \quad C=C_0-\beta' z, \quad \rho=\rho_0(1-\alpha\beta z-\alpha'\beta' z),$$

where

$$\beta=\frac{T_1-T_0}{d} \qquad \text{and} \qquad \beta'=\frac{C_0-C_1}{d}$$

are the magnitudes of uniform temperature and concentration gradients. $\beta\left(=\frac{dT}{dz}\right)$ is positive as the temperature increases upwards whereas $\beta'\left(=-\frac{dC}{dz}\right)$ is positive as the concentration decreases upwards.

We now consider a small perturbation on the steady state solution and let $\mathbf{v}$, $\delta\rho$, δp, θ and γ denote the perturbations in velocity, density, pressure, temperature and concentration, respectively, so that the change in density $\delta\rho$, caused by the perturbations θ and γ in temperature and concentration, is given by

$$\delta\rho=-\rho_0(\alpha\theta-\alpha'\gamma).$$

Then Eqs (2)–(4) on linearization give

$$\frac{\partial\mathbf{v}}{\partial t}=-\frac{1}{\rho_0}\nabla\delta p+\nu\nabla^2\mathbf{v}-\mathbf{g}(\alpha\theta-\alpha'\gamma), \tag{6}$$

$$\nabla\cdot\mathbf{v}=0, \tag{7}$$

$$\frac{\partial\gamma}{\partial t}-\kappa'\nabla^2\gamma=\beta' w. \tag{8}$$

The first law of thermodynamics can be written as

$$C_v\frac{dT}{dt}=-L+\frac{K}{\rho}\nabla^2 T+\frac{p}{\rho^2}\frac{d\rho}{dt}, \tag{9}$$

where p is pressure, K is thermal conductivity, C_v is specific heat at constant volume, T is temperature and t is time.

Following Defouw [1], the linearized perturbation form of Eq. (9) is

$$\frac{\partial\theta}{\partial t}+\frac{1}{C_p}(L_T-\alpha\rho L_\rho)\theta-\kappa\nabla^2\theta=-\left(\beta+\frac{g}{C_p}\right)w. \tag{10}$$

Here we consider the case in which both boundaries are free as well as perfect conductors of both heat and solute concentration. The density changes arise principally from thermal effects. The case of two free boundaries is the most appropriate for stellar atmospheres (Spiegel, [3]). The boundary conditions appropriate for the problem are

$$w=\partial^2 w\,|\,\partial z^2=\theta=\gamma=0. \tag{11}$$

3. Dispersion relation and discussion

Analyzing in terms of normal modes, we seek solutions whose dependence on x, y, z and t is of the form

$$\exp(ik_x x + ik_y y + nt)\sin k_z z\,, \tag{12}$$

where n is the growth rate and $k_z = s\pi/d$, s being any integer and d is the thickness of the layer and $k(=\sqrt{k_x^2+k_y^2+k_z^2})$ is the wave number of the perturbation.

Eqs (6)–(8) and (10) give

$$\frac{\partial}{\partial t}(\nabla^2 w) = g\left(\frac{\partial^2}{\partial x^2}+\frac{\partial^2}{\partial y^2}\right)(\alpha\theta-\alpha'\gamma)+\nu\nabla^4 w\,, \tag{13}$$

$$\left(\frac{\partial}{\partial t}+D\right)\theta = -\left(\beta+\frac{g}{C_p}\right)w\,, \tag{14}$$

$$\left(\frac{\partial}{\partial t}-\kappa'\nabla^2\right)\gamma = \beta' w\,. \tag{15}$$

Eliminating θ, γ from Eqs (13)–(15) and using (12), we obtain the dispersion relation

$$n^3+[D+(\nu+\kappa')k^2]n^2+\left[k^2\{(\nu+\kappa')D+\nu\kappa' k^2\}+\Gamma\left(\beta+\frac{g}{C_p}\right)+\Gamma'\beta'\right]n$$

$$+\left[\nu\kappa' k^4 D+\kappa' k^2\Gamma\left(\beta+\frac{g}{C_p}\right)+\Gamma'\beta' D\right]=0\,, \tag{16}$$

where

$$\Gamma = \frac{g\alpha(k_x^2+k_y^2)}{k^2} \quad \text{and} \quad \Gamma' = \frac{g\alpha'(k_x^2+k_y^2)}{k^2}\,.$$

When

$$D<0 \quad \text{and} \quad |(\nu\kappa' k^4+\Gamma'\beta')D| > \Gamma\left(\beta+\frac{g}{C_p}\right)\kappa' k^2\,, \tag{17}$$

the constant term in Eq. (16) is negative. Eq. (16), therefore involves one change of sign and hence contains one positive real root. The occurrence of positive root implies monotonic instability.

We thus obtain a criterion that a stellar atmosphere in the presence of stable solute concentration gradient is unstable if

$$D<0 \quad \text{and} \quad |(\nu\kappa' k^4+\Gamma'\beta')D| > \Gamma\left(\beta+\frac{g}{C_p}\right)\kappa' k^2\,.$$

4. Effect of magnetic field

Here we consider an infinite horizontal viscous and finitely conducting fluid layer subjected to a stable solute concentration gradient and acted on by a uniform vertical magnetic field $\mathbf{H}(0, 0, H)$ and gravity force $\mathbf{g}(0, 0, g)$. This layer is heated such that a steady temperature gradient $\beta(=dT/dz)$ is maintained. The linearized perturbed equations of motion and Maxwell's equations are

$$\frac{\partial \mathbf{v}}{\partial t} = -\frac{1}{\rho_0} \nabla \delta p + \nu \nabla^2 \mathbf{v} - \mathbf{g}(\alpha\theta - \alpha'\gamma) + \frac{\mu_e}{4\pi\rho_0} (\nabla \times \mathbf{h}) \times \mathbf{H}, \tag{18}$$

$$\nabla \cdot \mathbf{h} = 0, \tag{19}$$

$$\frac{\partial \mathbf{h}}{\partial t} = (\mathbf{H} \cdot \nabla)\mathbf{v} + \eta \nabla^2 \mathbf{h}, \tag{20}$$

where μ_e, η and $\mathbf{h}$ denote respectively the magnetic permeability, the resistivity and the perturbation in magnetic field $\mathbf{H}$. Eqs (7), (8) and (10) remain unaltered. Eqs (7), (8), (10) and (18)–(20) give

$$\left(\frac{\partial}{\partial t} - \nu\nabla^2\right)\nabla^2 w = g\alpha\left(\frac{\partial^2\theta}{\partial x^2} + \frac{\partial^2\theta}{\partial y^2}\right) - g\alpha'\left(\frac{\partial^2\gamma}{\partial x^2} + \frac{\partial^2\gamma}{\partial y^2}\right) + \frac{\mu_e H}{4\pi\rho_0} \nabla^2 \frac{\partial h_z}{\partial z}, \tag{21}$$

$$\left(\frac{\partial}{\partial t} - \eta\nabla^2\right) h_z = H \frac{\partial w}{\partial z}, \tag{22}$$

$$\left(\frac{\partial}{\partial t} + D\right)\theta = -\left(\beta + \frac{g}{C_p}\right) w, \tag{23}$$

$$\left(\frac{\partial}{\partial t} - \kappa'\nabla^2\right)\gamma = \beta' w. \tag{24}$$

Eliminating θ, γ and h_z from Eqs (21)–(24) and using (12), we obtain

$$\begin{aligned} &n^4 + [k^2(\nu + \eta + \kappa') + D]n^3 + \Big[\kappa' k^2 D + \nu\eta k^4 + k^2(\nu + \eta)(D + \kappa' k^2) \\ &+ \Gamma\left(\beta + \frac{g}{C_p}\right) + \Gamma'\beta' + k_z^2 V_A^2\Big] n^2 + \Big[\kappa' k^4 (\nu + \eta) D + (\nu\eta k^4 + k_z^2 V_A^2)(D + \kappa' k^2) \\ &+ k^2(\kappa' + \eta)\Gamma\left(\beta + \frac{g}{C_p}\right) + \Gamma'\beta'(D + \eta k^2)\Big] n + \Big[\nu\eta\kappa' k^6 D \\ &+ \kappa'\eta k^4 \Gamma\left(\beta + \frac{g}{C_p}\right) + \eta k^2 D\, \Gamma'\beta' + \kappa' k^2 V_A^2 k_z^2 D\Big] = 0, \end{aligned} \tag{25}$$

where

$$V_A^2 = \frac{\mu_e H^2}{4\pi\rho_0}.$$

When the inequalities (17) are satisfied, the constant term in Eq. (25) is negative. This means that Eq. (25) has one positive real root, meaning thereby monotonic instability. The criterion for monotonic instability (17), thus, holds good in the presence of magnetic field on thermosolutal-convective instability in a stellar atmosphere.

5. Effect of rotation

Here also we consider an infinite horizontal viscous fluid layer heated from above and solute concentrated from below acted on by a uniform rotation $\boldsymbol{\Omega}$ $(0, 0, \Omega)$ and gravity force $\mathbf{g}(0, 0, -g)$. The linearized perturbed equation of motion becomes

$$\frac{\partial \mathbf{v}}{\partial t} = -\frac{1}{\rho_0} \nabla \delta p + \nu \nabla^2 \mathbf{v} - \mathbf{g}(\alpha\theta - \alpha'\gamma) + 2(\mathbf{v} \times \boldsymbol{\Omega}) . \tag{26}$$

Eqs (7), (8) and (10) remain unaltered.

Eqs (7), (8), (10) and (26) give

$$\frac{\partial}{\partial t} \nabla^2 w - \nu \nabla^4 w = g\alpha \left(\frac{\partial^2 \theta}{\partial x^2} + \frac{\partial^2 \theta}{\partial y^2} \right) - g\alpha' \left(\frac{\partial^2 \gamma}{\partial x^2} + \frac{\partial^2 \gamma}{\partial y^2} \right) - 2\Omega \frac{\partial \zeta}{\partial z} , \tag{27}$$

$$\frac{\partial \zeta}{\partial t} - \nu \nabla^2 \zeta = 2\Omega \frac{\partial w}{\partial z} , \tag{28}$$

where $\zeta = \dfrac{\partial v}{\partial x} - \dfrac{\partial u}{\partial y}$ denotes the z-component of vorticity. Eqs (14) and (15) remain the same. Eliminating θ, γ and ζ from Eqs (14), (15) (27) and (28) and using (12), we obtain

$$\begin{aligned} & n^4 + [D + k^2(2\nu + \kappa')] n^3 + \left[\nu^2 k^4 + \kappa' k^2 D + 2\nu k^2 (D + \kappa' k^2) \right. \\ & \left. + \Gamma \left(\beta + \frac{g}{C_p} \right) + \Gamma' \beta' + \frac{4\Omega^2 k_z^2}{k^2} \right] n^2 + \left[2\nu\kappa' k^4 D + \nu^2 k^4 (D + \kappa' k^2) \right. \\ & + k^2 (\nu + \kappa') \Gamma \left(\beta + \frac{g}{C_p} \right) + \Gamma' \beta' (D + \nu k^2) + \frac{4\Omega^2 k_z^2}{k^2} (D + \kappa' k^2) \Big] n \\ & + \left[\nu k^2 \left\{ (\nu\kappa' k^4 + \Gamma' \beta') D + \kappa' k^2 \Gamma \left(\beta + \frac{g}{C_p} \right) \right\} + 4\Omega^2 k_z^2 \kappa' D \right] = 0 . \end{aligned} \tag{29}$$

When (17) is satisfied, the constant term in Eq. (29) is negative, which means that this equation has a positive real root, leading to monotonic instability. The criterion for monotonic instability, thus, holds good in the presence of rotation on thermosolutal-convective instability in a stellar atmosphere.

6. Discussion

The stellar chromospheres, coronas and the interstellar medium may exhibit thermal-convective instability. The Schwarzschild criterion is applicable in the interior of a star, where the photon mean free path is small, the assumption that the motion is adiabatic is justified. The departure from adiabatic motion may be significant in the outer layers of a stellar atmosphere, where the effective heat transfer is no longer prevented by opacity. The conditions under which convective motions are important in stellar atmospheres are usually far removed from the consideration of a single component fluid. We therefore consider the two component fluid, i.e. one fluid acted on by mass concentration gradient of another fluid. Keeping in mind such astrophysical situations, we study the thermal-convective instability of a stellar atmosphere in the presence of a stable solute concentration gradient. A criterion for monotonic instability of the stellar atmosphere has been derived. The criterion has been found to hold good for thermosolutal-convective instability in the presence of magnetic field and rotation.

References

1. R. J. Defouw, Astrophys. J., *160*, 659, 1970.
2. D. A. Nield, J. Fluid Mech., *29*, 545, 1967.
3. E. A. Spiegel, Astrophys. J., *141*, 1068, 1965.
4. G. Veronis, J. Marine Res., *23*, 1, 1965.

Acta Physica Hungarica 56 (1—4), pp 55—65 (1984)

AXISYMMETRIC STATIONARY GRAVITATIONAL AND MAXWELL FIELDS IN THE GENERAL SCALAR TENSOR THEORY

T. SINGH and TARKESHWAR SINGH

Applied Mathematics Section, Institute of Technology, Banaras Hindu University Varanasi — 221 005, India

(Received 3 February 1983)

It is shown that the axisymmetric stationary gravitational and Maxwell fields in the general scalar tensor theory can be obtained from the axisymmetric stationary Einstein — Maxwell fields. The scalar-tensor analogue of the Kerr–Newman solution has been obtained by this method.

1. Introduction

Within the framework of the general scalar tensor (ST) theory of gravitation [1], [2], [3], [4] one can allow the parameter ω to be an arbitrary function of the scalar field Φ. Recently Barker [2] proposed a special case of the general class of scalar tensor theories where the Newtonian gravitational constant G does not vary with time. Also Schwinger [5] and Kimball and Yee [6] have formulated a ST theory which is a member of the general class of ST theories.

Owing to the highly non-linear character of these field equations, there is a relative scarcity of their exact solution which is an obstacle to a better understanding of the physical implications of this theory. Hence a substantial increase in the number of exact solutions would be a useful first step. Recently some authors [7], [8], [9] discussed methods of generating solutions of these equations.

In this paper we establish a procedure to obtain solutions to the stationary axially symmetric general ST field coupled to non-null source-free Maxwell fields. We show that starting from any solution to the Einstein — Maxwell field equations one can generate a class of solutions to the general ST field equations including Maxwell fields. The method is applied to the Kerr–Newman solution. Thus we have generalized the result of Singh and Rai [10] for a stationary, axially symmetric electrovac in Brans–Dicke theory [11] of gravitation where $\omega = \text{constant}$.

2. Field equations

We start by considering a stationary, axially symmetric space-time whose metric is of the form

$$ds^2 = e^{2u}(dt + \Omega d\varphi)^2 - e^{2k-2u}[(dx^1)^2 + (dx^2)^2] - h^2 e^{-2u} d\varphi^2 , \tag{2.1}$$

where u, Ω, k and h are functions of x^1 and x^2 only. The Nordvedt–Maxwell equations to be solved are

$$R_{ij} = -\frac{8\Pi}{\Phi} E_{ij} - \frac{\omega}{\Phi^2} \Phi_{,i}\Phi_{,j} - \frac{\Phi_{,i;j}}{\Phi} + \frac{g_{ij}(\Phi_{,k}\Phi^{,k})}{2(2\omega+3)\Phi} \frac{d\omega}{d\Phi}, \tag{2.2}$$

$$\Box\Phi = \Phi^{;i}_{;i} = -\frac{\Phi_{,i}\Phi^{,i}}{(2\omega+3)} \frac{d\omega}{d\Phi}, \tag{2.3}$$

$$\text{(a)} \quad F^{ij}_{;j} = 0, \qquad \text{(b)} \quad F_{[ij;k]} = 0, \tag{2.4}$$

where comma and semicolon followed by an index denote partial and covariant derivatives, respectively.

The electromagnetic energy momentum tensor E_{ij} is given by

$$E_{ij} = -F_{i\alpha}F^{\alpha}_{j} + \frac{1}{4} g_{ij} F_{\alpha\beta} F^{\alpha\beta} .$$

Also $F_{ij} = A_{i,j} - A_{j,i}$ are the components of the electromagnetic field tensor, A_i being the electromagnetic four-potential. For the metric (2.1) the surviving equations from the field equations (2.2)–(24) are

$$\begin{aligned} 2[u_2^2 - u_1^2] + \frac{2k_1h_1}{h} - \frac{2k_2h_2}{h} + \frac{e^{4u}}{2h^2}(\Omega_1^2 - \Omega_2^2) \\ + \frac{1}{h}(h_{22} - h_{11}) = \frac{8\Pi e^{2u-p}}{h^2}[2\Omega(\psi_2\chi_2 - \psi_1\chi_1) \\ -(\psi_2^2 - \psi_1^2) - (\Omega^2 - h^2e^{-4u})(\chi_2^2 - \chi_1^2)] - (\omega+1)(p_2^2 - p_1^2) \\ -(p_{22} - p_{11}) - 2(k_1 - u_1)p_1 + 2(k_2 - u_2)p_2 , \end{aligned} \tag{2.5}$$

$$\begin{aligned} 2u_1u_2 - \frac{k_2h_1}{h} - \frac{k_1h_2}{h} - \frac{e^{4u}}{2h^2}\Omega_1\Omega_2 + \frac{h_{12}}{h} \\ = \frac{8\Pi e^{2u-p}}{h^2}[\Omega(\psi_1\chi_2 + \psi_2\chi_1) - \psi_1\psi_2 - (\Omega^2 - h^2e^{-4u})\chi_1\chi_2] \\ -(\omega+1)p_1p_2 - p_{12} + (k_2 - u_2)p_1 + (k_1 - u_1)p_2 , \end{aligned} \tag{2.6}$$

$$\Omega_{11} + \Omega_{22} - \frac{1}{h}(\Omega_1h_1 + \Omega_2h_2) + 4(u_1\Omega_1 + u_2\Omega_2)$$

$$= \frac{8\Pi e^{2u-p}}{h^2}[\Omega(\psi_1^2+\psi_2^2)+\Omega(\Omega^2-h^2e^{-4u})(\chi_1^2+\chi^{22})]$$

$$-\frac{16\Pi e^{2u-p}}{h^2}[(\Omega^2-h^2e^{-4u})(\psi_1\chi_1+\psi_2\chi_2)]-(\Omega_1p_1+\Omega_2p_2) \tag{2.7}$$

$$u_{11}+u_{22}+\frac{1}{h}(u_1h_1+u_2h_2)+\frac{e^{4u}}{2h^2}(\Omega_1^2+\Omega_2^2)$$

$$= \frac{8\Pi e^{2u-p}}{2h^2}[(\psi_1^2+\psi_2^2)+(\Omega^2+h^2e^{-4u})(\chi_1^2+\chi_2^2)]$$

$$-\frac{8\Pi e^{2u-p}}{h^2}[\Omega(\psi_1\chi_1+\psi_2\chi_2)]-(p_1u_1+p_2u_2)$$

$$+\frac{e^p}{2(2\omega+3)}[p_1^2+p_2^2]\frac{d\omega}{d\Phi}, \tag{2.8}$$

$$h_{11}+h_{22}=-(p_1h_1+p_2h_2)+\frac{he^p}{(2\omega+3)}[p_1^2+p_2^2]\frac{d\omega}{d\Phi}, \tag{2.9}$$

$$p_{11}+p_{22}+p_1^2+p_2^2=-\frac{1}{h}(p_1h_1+p_2h_2)-\frac{e^p}{(2\omega+3)}[p_1^2+p_2^2]\frac{d\omega}{d\Phi}, \tag{2.10}$$

$$h\{2\Omega(u_1\chi_1+u_2\chi_2)-2(u_1\psi_1+u_2\psi_2)+(\Omega_1\chi_1+\Omega_2\chi_2)\}$$
$$+h\{\Omega(\chi_{11}+\chi_{22})-(\psi_{11}+\psi_{22})\}-\Omega(h_1\chi_1+h_2\chi_2)$$
$$+(h_1\psi_1+h_2\psi_2)=0, \tag{2.11}$$

$$he^{4u}\{(\Omega_1\psi_1+\Omega_2\psi_2)+\Omega(\psi_{11}+\psi_{22})+2\Omega(u_1\psi_1+u_2\psi_2)\}$$
$$-he^{4u}\{2\Omega(\Omega_1\chi_1+\Omega_2\chi_2)+4\Omega^2(u_1\chi_1+u_2\chi_2)\}$$
$$-\Omega(h_1\psi_1+h_2\psi_2)e^{4u}+2h^2(h_1\chi_1+h_2\chi_2)$$
$$-h(\Omega^2e^{4u}-h^2)(\chi_{11}+\chi_{22})$$
$$+(\Omega^2e^{4u}-h^2)\{(h_1\chi_1+h_2\chi_2)+2h(u_1\chi_1+u_2\chi_2)\}=0, \tag{2.12}$$

where $\Phi=e^p$ and $A_3=\psi$, $A_4=\chi$ and subscripts 1 and 2 denote partial differentiation with respect to x^1 and x^2, respectively.

3. Solutions from the axisymmetric stationary Einstein–Maxwell fields

Let us consider the Einstein–Maxwell field equations corresponding to the metric

$$ds^2 = e^{2v}(dt+\Omega d\varphi)^2 - e^{2k-2v}[(dx^1)^2+(dx^2)^2] - H^2 e^{-2v}\, d\varphi^2 , \tag{3.1}$$

where Ω and k are the same as those given in (2.1) and H and v are functions of x^1 and x^2 only. The set of equations A (of the Appendix) have one of the equations as

$$H_{11}+H_{22}=0 . \tag{3.2}$$

From (2.9) and (2.10) we have

$$(he^p)_{11}+(he^p)_{22}=0 . \tag{3.3}$$

The Equations (3.2) and (3.3) suggest as a possible relation

$$H=he^p . \tag{3.4}$$

Now if we use (3.4) and make the following substitution

$$v=u+\frac{1}{2}p \tag{3.5}$$

in the Einstein–Maxwell equations (A.1)–(A.7) corresponding to the metric (3.1) they reduce to

$$\begin{aligned} &2[u_2^2-u_1^2]+\frac{2k_1h_1}{h}-\frac{2k_2h_2}{h}+\frac{e^{4u}}{2h^2}[\Omega_1^2-\Omega_2^2] \\ &+\frac{1}{h}(h_{22}-h_{11})=\frac{8\Pi e^{2u-p}}{h^2}\{2\Omega(\psi_2\chi_2-\psi_1\chi_1)-(\psi_2^2-\psi_1^2) \\ &-(\Omega^2-h^2e^{-4u})(\chi_2^2-\chi_1^2)\}-\frac{3}{2}(p_2^2-p_1^2)-(p_{22}-p_{11}) \\ &-2(k_1-u_1)p_1+2(k_2-u_2)p_2+\frac{2}{h}(h_1p_1-h_2p_2) , \end{aligned} \tag{3.6}$$

$$\begin{aligned} &2u_1u_2-\frac{k_2h_1}{h}-\frac{k_1h_2}{h}-\frac{e^{4u}}{2h^2}\Omega_1\Omega_2+\frac{h_{12}}{h} \\ &=\frac{8\Pi e^{2u-p}}{h^2}[\Omega(\psi_1\chi_2+\psi_2\chi_1)-\psi_1\psi_2-(\Omega^2-h^2e^{-4u})\chi_1\chi_2] \\ &-\frac{3}{2}p_1p_2-p_{12}+(k_2-u_2)p_1+(k_1-u_1)p_2-\frac{1}{h}(h_1p_2+h_2p_1) , \end{aligned} \tag{3.7}$$

$$\Omega_{11}+\Omega_{22}-\frac{1}{h}(\Omega_1 h_1+\Omega_2 h_2)+4(u_1\Omega_1+u_2\Omega_2)$$
$$=\frac{8\Pi e^{2u-p}}{h^2}[\Omega(\psi_1^2+\psi_2^2)+\Omega(\Omega^2-h^2e^{-4u})(\chi_1^2+\chi_2^2)]$$
$$-\frac{16\Pi e^{2u-p}}{h^2}(\Omega^2-h^2e^{-4u})(\psi_1\chi_1+\psi_2\chi_2)-(\Omega_1 p_1+\Omega_2 p_2), \tag{3.8}$$

$$u_{11}+u_{22}+\frac{1}{h}(u_1h_1+u_2h_2)+\frac{e^{4u}}{2h^2}(\Omega_1^2+\Omega_2^2)$$
$$+\frac{1}{2}\left[p_{11}+p_{22}+p_1^2+p_2^2+\frac{1}{h}(h_1p_1+h_2p_2)\right]$$
$$=\frac{8\Pi e^{2u-p}}{2h^2}\{(\psi_1^2+\psi_2^2)+(\Omega^2+h^2e^{-4u})(\chi_1^2+\chi_2^2)\}$$
$$-\frac{8\Pi e^{2u-p}}{h^2}\{\Omega(\psi_1\chi_1+\psi_2\chi_2)\}-(p_1u_1+p_2u_2), \tag{3.9}$$

$$h_{11}+h_{22}+2(h_1p_1+h_2p_2)+h(p_{11}+p_{22}+p_1^2+p_2^2)=0, \tag{3.10}$$

$$h\{2\Omega(u_1\chi_1+u_2\chi_2)-2(u_1\psi_1+u_2\psi_2)+(\Omega_1\chi_1+\Omega_2\chi_2)\}$$
$$h\{\Omega(\chi_{11}+\chi_{22})-(\psi_{11}+\psi_{22})\}-\Omega(h_1\chi_1+h_2\chi_2)$$
$$+(h_1\psi_1+h_2\psi_2)=0, \tag{3.11}$$

$$he^{4u}\{(\Omega_1\psi_1+\Omega_2\psi_2)+\Omega(\psi_{11}+\psi_{22})+2\Omega(u_1\psi_1+u_2\psi_2)\}$$
$$-he^{4u}2\Omega(\Omega_1\chi_1+\Omega_2\chi_2)+4\Omega^2(u_1\chi_1+u_2\chi_2)\}$$
$$-\Omega(h_1\psi_1+h_2\psi_2)e^{4u}+2h^2(h_1\chi_1+h_2\chi_2)$$
$$-h(\Omega^2e^{4u}-h^2)(\chi_{11}+\chi_{22})$$
$$+(\Omega^2e^{4u}-h^2)\{(h_1\chi_1+h_2\chi_2)+2h(u_1\chi_1+u_2\chi_2)\}=0. \tag{3.12}$$

On comparing (3.6)–(3.9) with (2.5)–(2.8) we observe that they are equivalent if the following relations are satisfied:

$$\left(\omega-\frac{1}{2}\right)[p_2^2-p_1^2]=\frac{2}{h}(h_2p_2-h_1p_1), \tag{3.13}$$

$$\left(\omega-\frac{1}{2}\right)p_1p_2=\frac{1}{p}(h_1p_2+h_2p_1) \tag{3.14}$$

and

$$p_{11}+p_{22}+p_1^2+p_2^2=-\frac{1}{h}(h_1p_1+h_2p_2)-\frac{e^p}{(2\omega+3)}(p_1^2+p_2^2)\frac{d\omega}{d\Phi}. \tag{3.15}$$

The Eq. (3.10) together with (3.15) is equivalent to the Eqs (2.9) and (2.10). Hence the set of equations (3.6)–(3.12) along with (3.15) is equivalent to the set of equations (2.5)–(2.12) provided the relations (3.13) and (3.14) hold. Therefore the axisymmetric stationary solutions of Nordvedt–Maxwell equations can be obtained from the solutions of the Einstein–Maxwell equations when the relations (3.13) and (3.14) are satisfied.

We assume a functional relationship between p and $\log h=\theta$, then (3.13) and (3.14) reduce to

$$\frac{dp}{d\theta}=\frac{4}{(2\omega-1)}. \tag{3.16}$$

Now if ω is a known function of p, then p is known in terms of θ (i.e. $\log h$) and consequently p and h are known in terms of H. Hence we have established the result:

Given any Einstein–Maxwell axisymmetric stationary solution (u_E, Ω_E, k_E, H_E, A_3, A_4) one can generate a corresponding Nordvedt–Maxwell axisymmetric stationary solution (u_{ST}, Ω_{ST}, K_{ST}, H_{ST}, Φ, A_3, A_4), where

$$u_{ST}=u_E-\frac{1}{2}\log\Phi,\quad \Omega_{ST}=\Omega_E,\quad K_{ST}=K_E,\quad A_3=A_3,\quad A_4=A_4;\quad H_{ST}$$

and Φ are known in terms of H_E when $\omega(\Phi)$ is a known function of Φ.

Some particular cases

Case 1: If we choose ω in Barker's form [2], i.e. $\omega=\dfrac{4-3\Phi}{2\Phi-2}$, then from (3.16) we have

$$h=H(1-H^4)\qquad\text{and}\qquad \Phi=[1-H^4]^{-1}.$$

Hence the following theorem.

Theorem 1

If (Ω_E, K_E, u_E, h_E, A_3 and A_4) forms a stationary, axially symmetric solution to the Einstein–Maxwell field equations for the metric (2.1), then a corresponding axisymmetric stationary solution to the Barker–Maxwell field equations for the same metric is given by

$$(\Omega_B, K_B, u_B, h_B, \Phi, A_3, A_4),$$

where

$$\Omega_B=\Omega_E, \quad K_B=K_E, \quad u_B=u_E-\frac{1}{2}\log\Phi, \quad h_B=h_E(1-h_E^4),$$

$$\Phi=[1-H_E^4]^{-1}, \quad A_3=A_3, \quad A_4=A_4.$$

Case 2: If we choose ω in the form [5], [6]

$$2\omega+3=\frac{1}{\alpha\Phi}, \qquad \alpha=\text{constant},$$

then from (3.16) we have

$$h=H\log(M/H^{4\alpha}), \qquad M=\text{constant}$$

and

$$\frac{1}{\Phi}=\log\left(\frac{M}{H^{4\alpha}}\right).$$

Hence the following theorem.

Theorem 2

Given any Einstein–Maxwell axisymmetric stationary solution $(u_E, \Omega_E, K_E, H_E, A_3, A_4)$ one can obtain a corresponding Schwinger–Maxwell axisymmetric stationary solution

$$(u_S, \Omega_S, K_S, H_S, \Phi, A_3, A_4)$$

where

$$u_S=u_E-\frac{1}{2}\log\Phi, \quad \Omega_S=\Omega_E, \quad K_S=K_E, \quad A_3=A_3, \quad A_4=A_4,$$

$$H_S=\log\left(\frac{M}{H_E^{4\alpha}}\right) \quad \text{and} \quad \frac{1}{\Phi}=\log\left(\frac{M}{H_E^{4\alpha}}\right).$$

4. ST analogues of the Kerr–Newman solution

An application of these theorems is made to obtain the ST solution corresponding to the Kerr–Newman solution [12], [13]. The Kerr–Newman metric is given by

$$ds^2=-(r^2+a^2\cos^2\theta)\left[d\theta^2+\frac{dr^2}{(r^2+a^2-2mr+e^2)}\right]$$

$$-(r^2+a^2)\sin^2\theta\, d\varphi^2+dt^2$$

$$-\frac{(2mr-e^2)}{(r^2+a^2\cos^2\theta)}[dt+a\sin^2\theta\, d\varphi]^2\,. \tag{4.1}$$

The electromagnetic potentials are

$$A_3=-\frac{ear\sin^2\theta}{(r^2+a^2\cos^2\theta)}, \qquad A_4=\frac{er}{(r^2+a^2\cos^2\theta)}. \tag{4.2}$$

If we use a co-ordinate transformation similar to the one used by Misra and Pandey [14] for Kerr metric, the Kerr–Newman metric (4.1) can be written in the form (2.1) as given by

$$ds^2=-(L^2+a^2\cos^2\theta)[d\theta^2+dR^2]-(L^2+a^2)\sin^2\theta\, d\varphi^2$$

$$+dt^2-\frac{(2mL-e^2)}{(L^2+a^2\cos^2\theta)}(dt+a\sin^2\theta\, d\varphi)^2\,, \tag{4.3}$$

where

$$L=e^R+m+\frac{(m^2-a^2-e^2)}{4}e^{-R}$$

and coordinates r and R are related through

$$r=e^R+m+\frac{(m^2-a^2-e^2)}{4}e^{-R}. \tag{4.4}$$

The variable r in the expressions for A_3 and A_4 in (4.2) can be converted into R through (4.4).

Application of theorem 1 to the metric (4.3) leads to the Barker–Maxwell solution given by

$$ds^2=\frac{L^2+a^2\cos^2\theta-(2mL-e^2)}{(L^2+a^2\cos^2\theta)}[1-B^2\sin^4\theta]$$

$$\times\left[dt-\frac{(2mL-e^2)a\sin^2\theta}{L^2+a^2\cos^2\theta-(2mL-e^2)}d\varphi\right]^2$$

$$-(L^2+a^2\cos^2)[1-B^2\sin^4\theta]^{-1}(d\theta^2+dR^2)$$

$$-[1-B^{5/2}\sin^5\theta]^2[1-B^2\sin^4\theta]^{-1}\frac{L^2+a^2\cos^2\theta}{L^2+a^2\cos^2\theta-(2mL-e^2)}d\varphi^2 \tag{4.5}$$

with the scalar Φ given by

$$\Phi=(1-B^2\sin^4\theta]^{-1}, \tag{4.6}$$

where

$$B=L^2+a^2-(2mL-e^2)\,. \tag{4.7}$$

The electromagnetic 4-potentials A_3 and A_4 remain unchanged.

In view of theorem 2 the Schwinger–Maxwell solution corresponding to (4.3) is given by

$$ds^2 = \frac{L^2+a^2\cos^2\theta-(2mL-e^2)}{L^2+a^2\cos^2\theta} z\left[dt-\frac{(2mL-e^2)a\sin^2\theta}{L^2+a^2\cos^2\theta-(2mL-e^2)}d\varphi\right]^2$$

$$-\frac{L^2+a^2\cos^2\theta}{Z}[d\theta^2+dR^2]$$

$$-[\{L^2+a^2-(2mL-e^2)\}^{\frac{1}{2}}\sin\theta\, Z]^2\left(\frac{L^2+a^2\cos^2\theta-(2mL-e^2)}{L^2+a^2\cos^2\theta}\right)Zd\varphi^2\,, \quad (4.8)$$

$$\frac{1}{\Phi}=Z=\log\frac{M}{\{L^2+a^2-(2mL-e^2)\}^{2\alpha}\sin^{4\alpha}\theta}\,. \quad (4.9)$$

The electromagnetic 4-potentials A_3, A_4 remain unchanged.

5. Concluding remarks

The immediate utility of the results obtained in this paper is that starting from any stationary axially symmetric solution of Einstein–Maxwell equations one can generate solutions of the general ST theory coupled with electromagnetic field. Applying the method to the cases of Barker's and Schwinger's theories we have found the stationary, axially symmetric solutions corresponding to Kerr–Newman solution. The theorems could be easily applied to the charged Tomimatsu–Sato solution [15], Das and Banerjee [16] and Yamazaki [17] resulting in a class of solutions of the general ST theory coupled with electromagnetic field with parameters describing mass (m), electromagnetic charge (e), rotation (a) and deformation (δ).

Finally, we may add that it is also possible to develop a similar technique to generate the corresponding Einstein–Maxwell conformal field solutions. The problem is under our active consideration.

Appendix A

The Einstein–Maxwell equations for the metric (3.1) are

$$2(v_2^2-v_1^2)+\frac{2k_1H_1}{H}-\frac{2k_2H_2}{H}+\frac{e^{4\vartheta}}{2H^2}(\Omega_1^2-\Omega_2^2)+\frac{1}{H}(H_{22}-H_{11})$$

$$=\frac{8\Pi e^{2\vartheta}}{H}\{2\Omega(\psi_2\chi_2-\psi_1\chi_1)-(\psi_2^2-\psi_1^2)\}$$

$$-\frac{8\Pi e^{2\vartheta}}{H}\{(\Omega^2-h^2e^{-4\vartheta})(\chi_2^2-\chi_1^2)\}, \tag{A.1}$$

$$2v_1v_2-\frac{k_2H_1}{H}-\frac{k_1H_2}{H}-\frac{e^{4\vartheta}}{2H^2}\Omega_1\Omega_2+\frac{H_{12}}{H}$$
$$=\frac{8\Pi e^{2\vartheta}}{H^2}\{\Omega(\psi_1\chi_2+\psi_2\chi_1)-\psi_1\psi_2-(\Omega^2-H^2e^{-4\vartheta})\chi_1\chi_2\}, \tag{A.2}$$

$$\Omega_{11}+\Omega_{22}-\frac{1}{H}(\Omega_1H_1+\Omega_2H_2)+4(\Omega_1v_1+\Omega_2v_2)$$
$$=\frac{8\Pi e^{2v}}{H^2}\{\Omega(\psi_1^2+\psi_2^2)+(\Omega^2-H^2e^{-4v})\Omega(\chi_1^2+\chi_2^2)\}$$
$$-\frac{16\Pi e^{2v}}{H^2}\{(\Omega^2-H^2e^{-4v})(\psi_1\chi_1+\psi_2\chi_2)\}, \tag{A.3}$$

$$v_{11}+v_{22}+\frac{1}{H}(v_1H_1+v_2H_2)+\frac{e^{4v}}{2H^2}(\Omega_1^2+\Omega_2^2)$$
$$=\frac{8\Pi e^{2v}}{2H^2}\{\psi_1^2+\psi_2^2+(\Omega^2+H^2e^{-4v})(\chi_1^2+\chi_2^2)\}$$
$$-\frac{8\Pi e^{2v}}{H^2}\{\Omega(\psi_1\chi_1+\psi_2\chi_2)\}, \tag{A.4}$$

$$H_{11}+H_{22}=0, \tag{A.5}$$

$$H\{2\Omega(v_1\chi_1+v_2\chi_2)-2(v_1\psi_1+v_2\psi_2)+(\Omega_1\chi_1+\Omega_2\chi_2)\}$$
$$+H\{\Omega(\chi_{11}+\chi_{22})-(\psi_{11}+\psi_{22})\}-\Omega(H_1\chi_1+H_2\chi_2)$$
$$+(H_1\psi_1+H_2\psi_2)=0, \tag{A.6}$$

$$He^{4v}\{(\Omega_1\psi_1+\Omega_2\psi_2)+\Omega(\psi_{11}+\psi_{22})+2\Omega(v_1\psi_1+v_2\psi_2)\}$$
$$-He^{4v}(2\Omega(\Omega_1\chi_1+\Omega_2\chi_2)+4\Omega^2(v_1\chi_1+v_2\chi_2)\}$$
$$-\Omega(H_1\psi_1+H_2\psi_2)e^{4v}+2H^2(H_1\chi_1+H_2\chi_2)$$
$$-H(\Omega^2e^{4v}-H^2)(\chi_{11}+\chi_{22})$$
$$+(\Omega^2e^{4v}-H^2)\{(H_1\chi_1+H_2\chi_2)+2H(v_1\chi_1+v_2\chi_2)\}=0. \tag{A.7}$$

References

1. K. Nordvedt, Astrophysics J., *161*, 1059, 1970.
2. B. M. Barker, Astrophysics J., *219*, 5, 1978.
3. P. G. Bergmann, Int. J. Theor. Phys., *1*, 25, 1968.
4. R. V. Wagoner, Phys. Rev. D, *1*, 3209, 1970.
5. J. Schwinger, Particles, Sources and Fields, I, Addison–Wesley, Reading, Mass, 1970, p. 378.
6. A. M. Kimball and J. N. Yee, Phys. Rev. D, *10*, 420, 1974.
7. A. Banerjee and S. B. Duttachoudhury, J. Math. Phys., *21*, 2799, 1980.
8. N. Van den Burgh, Gen. Rel. Grav., *14*, 17, 1982.
9. T. Singh and Tarkeshwar Singh, Astrophys. Space Sci., *100*, 309, 1984.
10. T. Singh and L. N. Rai, Gen. Rel. Grav., *11*, 37, 1979.
11. C. H. Brans and R. H. Dicke, Phys. Rev., *124*, 925, 1961.
12. E. T. Newman, E. Couch, K. Chinapared, A. Exton, A. Prakash and R. Torrence, J. Math. Phys., *6*, 918, 1965.
13. F. J. Ernst., Phys. Rev., *168*, 1415, 1968.
14. R. M. Misra and D. B. Pandey, J. Math. Phys., *13*, 1538, 1972.
15. F. J. Ernst, Phys. Rev. D., *7*, 2520, 1973.
16. K. C. Das and S. Banerjee, Phys. Lett., *50A*, 409, 1975.
17. M. Yamazaki, J. Math. Phys., *19*, 1376, 1978.

Acta Physica Hungarica 56 (1—4), pp 67—71 (1984)

LuF MOLECULE: TRUE POTENTIAL ENERGY CURVE AND THE DISSOCIATION ENERGY

N. RAJAMANICKAM* and B. NARASIMHAMURTHY

Department of Physics, University of Mysore, Mysore 570-006, India

(Received in revised form 10 February 1983)

The true potential energy curve for the electronic ground state, $X^1\Sigma$, of the LuF molecule has been constructed by the Rydberg–Klein–Rees method. By curve fitting of the five-parameter Hulburt–Hirschfelder empirical potential function, the dissociation energy D_0^0 of LuF is found to be 402 ± 10 KJ mol^{-1}. The force constant of the electronic ground state of LuF molecule indicates that this value is of the correct order.

1. Introduction

During recent years, experimental potential energy curves have been constructed for many diatomic species which are of interest in various fields such as astrophysics, gas kinetics and aerodynamics. A detailed knowledge of potential energy curves will help in determining the Franck–Condon factors and the *r*-centroids which are required in testing the intensity theories, such as the variation of electronic transition moment with the internuclear separation, a knowledge of which is lacking for many diatomic molecules of astrophysical and general interest. A comparison with the experimental curve decides the empirical potential function which best fits the molecular electronic state. In particular the dissociation energy could be estimated reliably from the empirical function describing adequately the electronic ground state. Many methods are available to construct the true potential energy curves using the experimental data. The approach of Rydberg–Klein–Rees (RKR) as modified by Vanderslice et al [1] is the one largely employed.

For a molecular species to form and remain stable against dissociating influences in any environment, astronomical, chemical and so on, the temperature must be sufficiently low and other energetic interactions must be sufficiently mild that the probability of breaking chemical bond once formed is low. Since the dissociation energy is a prime factor in such phenomena, astrophysicists, chemists and spectroscopists are concerned with the determination of reliable values of dissociation energies for the diatomic molecules.

* On leave from VHNSN College, Virudhunagar 626-001, India

The curve fitting method has been found to yield reliable values for the dissociation energies of a large number of diatomic molecules [2–6]. The procedure consists in determining the D_e-parameterised empirical potential function which best fits the true potential energy curve for the electronic ground state of the molecule.

There has been no report on the true potential energy curve for the electronic ground state of the LuF molecule [7]. Experimental energy levels are known up to vibrational quantum number $v = 14$. Reliable true potential energy curve can therefore be constructed. It is proposed to adopt the RKR method in the present work.

Zmbov and Margrave [8] have arrived at the dissociation energy D_0^0 of LuF as 569 KJ mol^{-1} from mass-spectrometric studies. But this value is not confirmed [7]. Using the relation, $D_e = \omega_e^2/4\omega_e x_e$, the dissociation energy D_0^0 is reported as 437 KJ mol^{-1} [9]. The dissociation energies D_0^0 obtained with this method are often too high [10].

Many empirical potential functions are known for the diatomic molecules. Of these, functions given by Lippincott et al [11] in the modified form, by Hulburt–Hirschfelder [12] and by Szőke and Baitz [13] describe adequately the potential energies of many molecules. These functions are therefore examined in the present study to estimate the dissociation energy of the electronic ground state of LuF from the constructed true potential energy curve.

2. The true potential energy curve

For the known vibrational levels, the RKR method gives the turning points by

$$r_{\pm} = \left(\frac{f_v}{g_v} + f_v^2\right)^{1/2} \pm f_v . \tag{1}$$

Expressing the potential energy curve by a series of overlapping segments i, quadratic in $\left(v + \frac{1}{2}\right)$, Vanderslice et al [1] have simplified the RKR method. Further modifications by Singh and Jain [14], Murthy and Murthy [15] lead to

$$f_v = \left[\frac{8\pi^2 \mu_A c}{Nh}\right]^{-1/2} (\omega x)_i^{-1/2} z_v$$

and

$$g_v = \left[\frac{2\pi^2 \mu_A c}{Nh}\right]^{1/2} \Sigma \{2\alpha_i (\omega x)_i^{-1} [G(v)^{1/2} - G(v-1)^{1/2}] + [2B_i - \alpha_i \omega_i (\omega x)_i^{-1}] (z_v - z_{v-1})(\omega x)_i^{-1/2}\},$$

where

$$z_v = \ln \left[\frac{\omega_i - 2(\omega x)_i \left(v + \frac{1}{2}\right)}{\omega_i - 2\{(\omega x)_i G(v)\}^{1/2}}\right].$$

For a segment i of four vibrational levels the molecular constants ω_i, $(\omega x)_i$, B_i and α_i are determined from the experimental data of ω_e, $\omega_e x_e$, B_e, α_e by least squares fit of

$$\frac{G(v)}{\left(v+\frac{1}{2}\right)} = \omega_e - \omega_e x_e \left(v+\frac{1}{2}\right)$$

and

$$B_v = B_e - \alpha_e \left(v+\frac{1}{2}\right).$$

The constants so obtained are used over the middle two levels only. By a series of such overlapping segments the entire curve is constructed for the known v values. The experimental data [7] required for LuF in the present study are listed in Table I. In Table II, the computed values of the turning points are given for the molecular vibration in the electronic ground state of LuF.

Table I

Molecular constants for the electronic ground state $X^1\Sigma$ of LuF molecule

$\omega_e\,[m^{-1}]\times 10^4$	$\omega_e x_e\,[m^{-1}]\times 10^2$	$B_e\,[m^{-1}]\times 10^1$	$\alpha_e\,[m^{-1}]\times 10^{-1}$	$r_e\,[m]\times 10^{-10}$
6.1179	2.54	2.6764	1.56	1.9171

Table II

Energy values from the Hulburt–Hirschfelder function for the LuF molecule

v	$r_\pm \times [10^{-10}m]$	$G(v)$ [KJ mol^{-1}]	$U(r)$ in KJ mol^{-1}		
			$D_e = 395$ KJ mol^{-1}	$D_e = 405$ KJ mol^{-1}	$D_e = 415$ KJ mol^{-1}
0	1.9769	3.6515	3.6887	3.6887	3.6887
1	2.0243	10.9089	10.9675	10.9679	10.9683
2	2.0590	18.1056	18.1762	18.1776	18.1788
3	2.0885	25.2414	25.3199	25.3230	25.3260
4	2.1150	32.3166	32.3920	32.3961	32.4036
5	2.1395	39.3310	39.4006	39.4106	39.4201
6	2.1626	46.2846	46.3413	46.3569	46.3712
7	2.1847	53.1775	53.2178	53.2403	53.2611
8	2.2059	60.0096	60.0255	60.0566	60.0853
9	2.2264	66.7809	66.7684	66.8098	66.8480
10	2.2464	73.4915	73.4415	73.4950	73.5445
11	2.2658	80.1412	80.0324	80.0999	80.1625
12	2.2849	86.7303	86.5663	86.6498	86.7274
13	2.3037	93.2585	93.0222	93.1239	93.2184
14	2.3222	99.7259	99.4171	99.5391	99.6526

Table II. *(cont.)*

v	$r_{\pm} \times [10^{-10}\text{m}]$	$G(v)$ [KJ mol^{-1}]	$U(r)$ in KJ mol^{-1}		
			$D_e = 395$ KJ mol^{-1}	$D_e = 405$ KJ mol^{-1}	$D_e = 415$ KJ mol^{-1}
0	1.8633	3.6515	3.5062	3.5062	3.5062
1	1.8268	10.9089	10.8332	10.8329	10.8326
2	1.8031	18.1056	18.0068	18.0059	18.0050
3	1.7847	25.2414	25.1249	25.1228	25.1209
4	1.7693	32.3166	32.1854	32.1840	32.1805
5	1.7559	39.3310	39.1969	39.1908	39.1852
6	1.7441	46.2846	46.1504	46.1415	46.1333
7	1.7335	53.1775	53.0381	53.0257	53.0143
8	1.7238	60.0096	59.8780	59.8613	59.8463
9	1.7148	66.7809	66.6682	66.6468	66.6275
10	1.7065	73.4915	73.3920	73.3652	73.3409
11	1.6987	80.1412	80.0797	80.0467	80.0170
12	1.6915	86.7303	86.6944	86.6548	86.3149
13	1.6846	93.2585	93.2937	93.2467	93.2044
14	1.6781	99.7259	99.8139	99.7588	99.7093
Average percentage deviation			0.293	0.291	0.298

3. Dissociation energy

For the constructed true potential energy curve, the energies $U(r)$ are calculated with the empirical potential functions by varying the D_e value. An average percentage deviation is determined between the calculated $U(r)$ and the experimental $G(v)$ values. The dissociation energy from any function is that value of D_e which gives the least deviation. And the function leading to smallest deviation determines the dissociation energy of the molecule. The dissociation energy referred to $v=0$ level is given by $D_0^0 = D_e - G(0)$.

This procedure is applied to determine the adequacy of the empirical potential functions [11–13] to represent the electronic ground state of LuF. D_e is varied over a range of 290 to 580 KJ mol^{-1} in steps of 10 KJ mol^{-1}. It is found that the five-parameter Hulburt–Hirschfelder function fits the true curve best when $D_e =$ 405 KJ mol^{-1}. Relevant results of $U(r)$ are given in Table II. Combining the error of 0.29% with 2% error inherent to the Hulburt–Hirschfelder function [16] the dissociation energy is estimated to be $D_0^0 = 402 \pm 10$ KJ mol^{-1}.

4. Conclusions

Zmbov and Margrave [8] have reported the dissociation energy D_0^0 of LuF as 569 KJ mol^{-1} from the mass-spectrometric studies and the relation $D_e = \omega_e^2/4\omega_e x_e$ yields a lower value 437 KJ mol^{-1} [9]. Since the five-parameter Hulburt–Hirschfelder

function fits adequately the experimental data, the estimated value $D_0^0 = 402 \pm 10$ KJ mol^{-1} in the present study can be considered as satisfactory. The force constant for the electronic ground state of LuF also indicates that the dissociation energy obtained in the present study is of correct order.

Acknowledgements

The authors thank Prof B. Sanjeevaiah, Head of this Department, for encouragement. One of us (NR) thanks UGC (New Delhi) and the University of Mysore for the award of a FIP Fellowship. (BN) would like to thank the University of Mysore for a research grant.

References

1. J. T. Vanderslice, E. A. Mason, W. G. Maisch and E. R. Lippincott, J. Chem. Phys., *33*, 614, 1960.
2. J. Singh, K. P. R. Nair and D. K. Rai, J. Mol. Struct., *5*, 492, 1970.
3. M. L. P. Rao, D. V. K. Rao and P. T. Rao, Spectroscopy Letters, *8*, 745, 1975.
4. N. Sreedharamurthy, S. P. Bagare and B. Narasimhamurthy, JQSRT, *19*, 455, 1978.
5. N. Rajamanickam, U. D. Prahllad and B. Narasimhamurthy, Pramāna, *18*, 225, 1982.
6. N. Rajamanickam, U. D. Prahllad and B. Narasimhamurthy, Spectroscopy Letters, *15*, No. 7, 1982.
7. K. P. Huber and G. Herzberg, Molecular Spectra and Molecular Structure IV. Constants of Diatomic Molecules, Van Nostrand Reinhold, New York, 1979.
8. K. F. Zmbov and J. L. Margrave, Advances in Chemistry Series, No. 72, 267, 1968.
9. C. Effantin and G. Wannouset J. D'Incan, Can. J. Phys., *55*, 64, 1977.
10. A. Lagerqvist, U. Uhler and R. F. Barrow, Arkiv För Fysik, *28*, 281, 1954.
11. E. R. Lippincott, D. Steele and P. Caldwell, J. Chem. Phys., *35*, 123, 1961.
12. H. M. Hulburt and J. O. Hirschfelder, J. Chem. Phys., *9*, 61, 1941.
13. S. Szöke and E. Baitz, Can. J. Phys., *46*, 2563, 1968.
14. N. L. Singh and D. C. Jain, Proc. Phys. Soc., *79*, 274, 1962.
15. N. S. Murthy and B. N. Murthy, J. Phys. B: Atom. Molec. Phys., *3*, L15, 1970.
16. D. Steele, E. R. Lippincott and J. T. Vanderslice, Rev. Mod. Phys., *34*, 239, 1962.

Acta Physica Hungarica 56 (1—4), pp 73—85 (1984)

THREE-PARTICLE DECAYS OF HEAVY HIGGS BOSONS IN THE WEINBERG–SALAM MODEL

G. ZSIGMOND

Institute for Theoretical Physics, Roland Eötvös University
1088 Budapest, Hungary

(Received 3 March 1983)

We investigate the three-particle decays of heavy Higgs bosons in the Weinberg–Salam model with two Higgs doublets. The dominant decay mode is $H \to VH' \to f\bar{f}H'$, if the mixing angles in the Higgs sector are not very extreme. The decay width is a few percent of the decay $H \to VH'$, at $m_H = 100$–150 GeV it is about a few MeV. The fermion energy distribution can discriminate from the case of one Higgs doublet.

1. Introduction

In a previous paper [1] we have studied the decays of heavy Higgs bosons in the Weinberg–Salam model with two Higgs doublets and found that the decay $H_1 \to VH_2$ generally exceeds the known decay mode $H_1 \to V\bar{V}$ [2] as well as the decay into a fermion pair. The decays $H_1 \to H_2 H_3$ may be also large in some cases but these are not controllable easily because of the complicated couplings.

In this paper we go into the details of the above processes, investigating the three-particle decays of heavy Higgses. We consider the possible decay types, and give their widths, then we discuss their relevance. The concrete analyses are performed for the case of charged and pseudoscalar Higgses. It turns out that in general the main decay modes are $H_1 \to H_2 V \to H_2 f\bar{f}$.

In the Appendices we make general statements on the interference terms and give useful formulae for the evaluation of three-particle decays.

2. The possible decay types

We work in the standard electroweak model with two Higgs doublets [3], [4] because here there appear the typical features of the models with more than one doublet, but the Higgs sector is still rather simple. The five physical Higgs bosons are $H^{\pm}$, h^0, Φ^0, H^0, their masses and two mixing angles α and β, $0 < \beta < \pi/2$, $-\pi/2 < \alpha < -\pi/2 + \beta$, are free parameters. This is not too strong, so the phenomenology is relatively fixed.

From the trilinear interaction term of the model [4] we get the possible decays:

$$H^{\pm} \to W^{\pm} h^0,\ W^{\pm} \Phi^0,\ W^{\pm} H^0;$$

$$h^0 \to W^{\pm} H^{\mp},\ ZH^0;\ H^+ H^-,\ \Phi^0 \Phi^0,\ H^0 H^0;$$

$$\Phi^0 \to W^{\pm} H^{\mp},\ ZH^0;\ H^+ H^-,\ h^0 h^0,\ H^0 H^0;$$

$$H^0 \to W^{\pm} H^{\mp},\ Zh^0,\ Z\Phi^0.$$

If the virtual particle is the same as the decaying one there are also other possible decays, e.g. $H \to Hh \to f\bar{f}h$, here $H = H^0, H^{\pm}$; $h = h^0, \Phi^0$, but we shall see that these are not important. We investigate the three-particle decays where one of the secondary particles decays into a fermion pair.

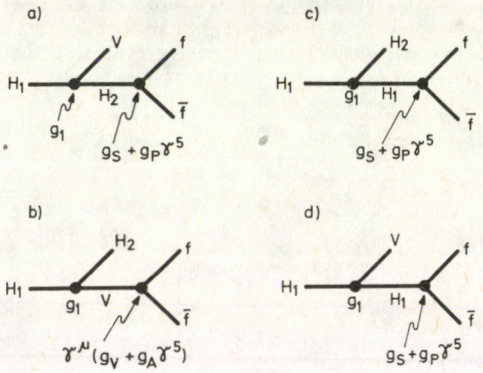

Fig. 1. The possible decay types of Higgs bosons in the model with two Higgs doublets

All of the above decays belong to one of the following four types (Fig. 1):

A) $H_1 \to VH_2 \to Vf\bar{f}$

B) $H_1 \to H_2 V \to H_2 f\bar{f}$

C) $H_1 \to H_2 H_1 \to H_2 f\bar{f}$

D) $H_1 \to VH_1 \to Vf\bar{f}$

In the next Section we evaluate these processes. The concrete model will appear only in the coupling constants.

3. Evaluation of the general decay modes

The double differential decay widths of the cases A–D) with the notations of Appendix 1 are:

$$\text{A:}\quad \frac{d^2\Gamma}{dx\,dy}=\frac{4|g_1|^2(|g_S|^2+|g_P|^2)}{(4\pi)^3}\frac{m_{H_1}^3}{m_V^2}\frac{(x_2-x)(x^2-x_1^2)}{(x-x_0)^2+\Delta_{H_2}^2},$$

$$\text{B:}\quad \frac{d^2\Gamma}{dx\,dy}=\frac{4|g_1|^2(|g_V|^2+|g_A|^2)}{(4\pi)^3}m_{H_1}\frac{x-x_2+2y(1-x-y)}{(x-x_0)+\Delta_V^2},$$

$$\text{C:}\quad \frac{d^2\Gamma}{dx\,dy}=\frac{16|g_1|^2(|g_S|^2+|g_P|^2)}{(4\pi)^3 m_{H_1}}\frac{x_2-x}{(\mu_H^2-2x)^2+\delta_{H_1}^2},$$

$$\text{D:}\quad \frac{d^2\Gamma}{dx\,dy}=\frac{4|g_1|^2(|g_S|^2+|g_P|^2)}{16\pi^3}\frac{m_{H_1}^3}{m_V^2}\frac{(x_2-x)(x^2-x_1^2)}{(\mu_V^2-2x)^2+\delta_{H_1}^2}.$$

It is important that in A) and B) there can be a resonance at $x=x_0$, while in C) and D) this is not possible, because $x\geq x_1=\mu$. Denote the couplings by G, $G^A=4|g_1|^2(|g_S|^2+|g_P|^2)$, etc. Integrating over the fermion energies gives

$$\text{A:}\quad \frac{d\Gamma}{dx}=\frac{G^A}{(4\pi)^3}\frac{m_{H_1}^3}{m_V^2}\frac{(x_2-x)(x^2-x_1^2)^{3/2}}{(x-x_0)^2+\Delta_{H_2}^2},$$

$$\text{B:}\quad \frac{d\Gamma}{dx}=\frac{G^B}{(4\pi)^3}m_{H_1}\frac{1}{3}\frac{(x^2-x_1^2)^{3/2}}{(x-x_0)^2+\Delta_V^2},$$

$$\text{C:}\quad \frac{d\Gamma}{dx}=\frac{G^C}{(4\pi)^3}\frac{1}{m_{H_1}}\frac{(x_2-x)(x^2-x_1^2)^{1/2}}{(2x-\mu_{H_2}^2)^2},$$

$$\text{D:}\quad \frac{d\Gamma}{dx}=\frac{G^D}{16\pi^3}\frac{m_{H_1}^3}{m_V^2}\frac{(x_2-x)(x^2-x_1^2)^{3/2}}{(2x-\mu_V^2)^2}.$$

Here we neglected δ_H^2 in the denominator, since $(2x-\mu^2)^2\geq[\mu(2-\mu)]^2\geq\mu^2\gg\delta^2$. In the cases A) and B) the Higgs energy distribution is a sharp resonance around x_0: it is a typical behaviour of these cases.

From here we get the total decay widths of the above processes. In A) and B) the main contribution to the integral comes from the resonance, we can neglect the tails. Also, if $x_0<x_1$, that is $m_{H_1}<m_V+m_{H_2}$, the decay width is very small. Finally,

$$\text{A:}\quad \Gamma=\frac{G^A}{(4\pi)^3}\frac{m_{H_1}^3}{m_V^2}\frac{\pi}{\Delta_{H_2}}\frac{m_{H_2}^2}{m_{H_1}^2}\frac{\Delta^{3/2}(1,(m_V/m_{H_1})^2,(m_{H_2}/m_{H_1})^2)}{16},$$

$$\text{B:}\quad \Gamma=\frac{G^B}{(4\pi)^3}m_{H_1}\cdot\frac{\pi}{12}\frac{1}{\mu_V\delta_V}\Delta^{3/2}(1,\mu_V^2,\mu_{H_2}^2),$$

$$\text{C:}\quad \Gamma = \frac{G^C}{(4\pi)^3}\frac{1}{m_{H_1}}\frac{1}{4}\left\{\frac{\mu}{2}\frac{5-\mu^2}{\sqrt{4-\mu^2}}\arccos\left(\mu\frac{3-\mu^2}{2}\right)+\frac{1-\mu^2}{2}\left(\ln\frac{1}{\mu}-2\right)\right\},$$

$$\text{D:}\quad \Gamma = \frac{G^D}{16\pi^2}\frac{m_{H_1}^3}{m_V^2}\frac{1}{4}\left\{\frac{1-\mu^2}{48}(1+64\mu^2-17\mu^4)+\right.$$

$$\left.+\frac{\mu^2}{2}(6-9\mu^2+\mu^4)\ln\mu-\frac{\mu^3}{8}(28-11\mu^2+\mu^4)\arccos\left(\mu\frac{3-\mu^2}{2}\right)\right\}.$$

We see that the presence of the resonance enhances the total width (the integral) strongly, so the decays A) and B) are more advantageous compared to C) and D). From A) and B), B) is preferred, since usually $m_f \propto g_{Hf} \ll g_{Vf}$ (see the details later).

We give here the fermion energy distribution of B):

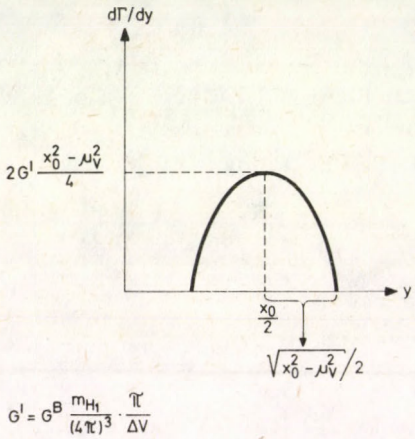

Fig. 2. The fermion energy distribution of the B graph in the resonance case

$$\text{B:}\quad \frac{d\Gamma}{dy} = \frac{G^B m_{H_1}}{(4\pi)^3}\left\{\left(\frac{1}{2}-y\right)\ln\frac{(\mu_V^2/2)^2+\Delta_V^2}{(\xi(y)-x_0)^2+\Delta_V^2}+[2y(1-y)-\right.$$

$$\left.-(\mu_V^2/2)]\Delta_V^{-1}\left[\operatorname{arctg}(\mu_V^2/2\Delta_V)-\operatorname{arctg}\frac{\xi(y)-x_0}{\Delta_V}\right]\right\}$$

with $\xi(y)=\dfrac{1+\mu_V^2-4y(1-y)}{2(1-2y)}$. In the resonance approximation

$$\frac{d\Gamma}{dy} \cong \frac{G^B m_{H_1}}{(4\pi)^3}\left\{y\left[1-\left(\frac{m_{H_2}}{m_{H_1}}\right)^2+\left(\frac{m_V}{m_{H_1}}\right)^2-2y\right]-\frac{1}{2}\left(\frac{m_V}{m_{H_1}}\right)^2\right\}\frac{\pi}{\Delta_V}$$

(Fig. 2).

In conclusion, we can say that the main decay mode is of the type B) (via a virtual vector boson).

4. Pseudoscalar and charged Higgs

Let us see the above statements in more detail, in the case of the pseudoscalar H^0. This particle has 8 decays in the model (Fig. 3). We can say:

1. A) and B) are negligible, if they contain no resonance.

2. The resonance condition both in A) and B) is:
$m_{H_1} > m_{H_2} + m_V$. Usually $g_{Hf} \ll g_{Vf}$, so that A is negligible beside B.

3. In C there is no resonance, and $g_{Hf} \ll g_{Vf}$, therefore $\Gamma(C) \ll \Gamma(B)$ for two reasons.

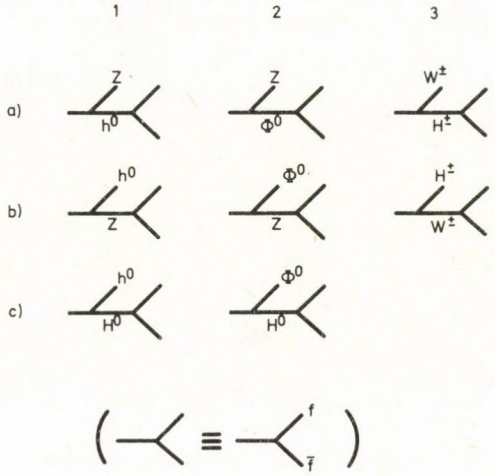

Fig. 3. The decay modes of the pseudoscalar H^0 in the model

2.* In the model with two doublets $g_{H_f} \propto \cos^{-1}\beta$ can hold (in the optimistic case), therefore, if $\beta \approx \pi/2$, the widths of processes A and C can grow.

For example, if the fermion couplings to the second doublet are absent (for $\beta > 45°$ it is an optimistic choice), g_{Hf} is the greatest coupling,

$$g_{hl} = \frac{g}{2}\frac{m_f}{m_W}\frac{\sin\alpha}{\cos\beta},$$

while

$$g_{Zl} = -\frac{g}{4\cos\Theta_W}[(4\sin^2\Theta_W - 1)I + \gamma^5]$$

and

$$g_{H^0h^0z} = \frac{g}{2\cos\Theta_W}\cos(\alpha-\beta).$$

From these

$$\frac{G^{A1}}{G^{B1}} \cong 4\frac{\sin^2\alpha}{\cos^2\beta}\left(\frac{m_f}{m_z}\right)^2 = 4\sin^2\alpha\left(\frac{m_f}{m_z\cos\beta}\right)^2.$$

For β we have an upper limit [5]

$$\operatorname{tg}\beta \lesssim 40$$

thus

$$\frac{G^{A1}}{G^{B1}} \lesssim 4\sin^2\alpha\left(\frac{m_f}{2,3\ \mathrm{GeV}}\right)^2.$$

If β is not exceptionally large, our conclusion remains valid, that is A is negligible beside B. With the optimistic choice of the $f-H$ couplings we also overestimated A.

3.* C can hardly be analyzed because of the complicated HHH couplings. For example, ([1], [4])

$$g_{H^0H^0h^0} = \frac{1}{2}\frac{g}{m_W}\left[m_{H^0}^2\cos^2(\beta-\alpha) + m_{h^0}^2\frac{\sin 2\alpha}{\sin 2\beta}(\sin\alpha\sin^3\beta + \right.$$

$$\left. + \cos\alpha\cos^3\beta) + m_{\Phi^0}^2\frac{\cos 2\alpha}{\sin 2\beta}(-\sin\alpha\cos^3\beta + \cos\alpha\sin^3\beta)\right]$$

the mass of the Φ^0 boson also appears. C1 can be relevant only if this coupling is able to compensate the smallness of g_{Hf} and the absence of a resonance.

If $\beta \approx \pi/2$,

$$g_{H^0H^0h^0} \cong \frac{1}{4}\frac{g}{m_W}\operatorname{tg}\beta(m_{h^0}^2\cos 2\alpha\sin\alpha - m_{\Phi^0}^2\sin 2\alpha\cos\alpha).$$

Let us choose $\alpha = -\pi/4$ to simplify our considerations. Then

$$g_{H^0H^0h^0} = \frac{g}{4\sqrt{2}}\operatorname{tg}\beta\frac{m_{\Phi^0}}{m_W}\cdot m_{\Phi^0}$$

and

$$G^{C1} = 2\left(\frac{g}{2\cos\Theta_W}\right)^4\operatorname{tg}^4\beta\left(\frac{m_{\Phi^0}}{m_Z}\right)^2\left(\frac{m_f}{m_Z}\right)^2\cdot m_{\Phi^0}^2$$

If the mass of Φ^0 is large, β is very near to its maximum value and the decay goes into heavy fermions, then C1 can be of the same order as B1.

Disregarding these not very likely cases, the decay of H^0 goes via the diagrams B.

These considerations hold for the charged $H^\pm$ decays, too.

After this analysis let us write the H^0 decay width from the B graphs as

$$\Gamma(H^0) = \Gamma(H^0\to h^0Z\to h^0f\bar{f}) + \Gamma(H^0\to\Phi^0Z\to\Phi^0f\bar{f}) +$$

$$+\Gamma(H^0\to H^\pm W^\mp\to H^\pm f_1\bar{f}_2)$$

(there are no relevant interference terms, see Appendix 2).

$$\Gamma(H^0) = \sum_{h=h^0,\Phi^0,H^\pm}\frac{m_{H^0}}{(4\pi)^3}G_hF_h,$$

here

$$F_h \cong \frac{\pi}{24} \Delta^{3/2}(1, \mu_V^2, \mu_H^2) \Delta_V^{-1},$$

$$V = \begin{cases} W & h = H^{\pm}, \\ Z & h = h^0, \Phi^0, \end{cases}$$

$$\mu_h = m_h/m_{H^0}, \quad \mu_V = m_V/m_{H^0}, \quad \Delta_V = m_V \Gamma_V / 2m_{H^0}^2,$$

$$G_{h^0} = G \cos^2(\alpha - \beta), \quad G_{\Phi^0} = G \sin^2(\alpha - \beta),$$

$$G = \left(\frac{g}{2 \cos \Theta_W}\right)^4 [(4 \sin^2 \Theta_W - 1)^2 + 1], \quad G_{H^{\pm}} = \frac{g^4}{2}.$$

Numerically see Table I (e.g. for $h = h^0$).

The width is determined mostly by m_{H^0}, m_h can give rise to threshold effects. In the region $m_{H^0} \approx 100$–150 GeV the width is of order MeV, then it grows rapidly with m_{H^0}.

Table I

The total decay width of $H^0 \to hf\bar{f}$

m_{H^0} [GeV]	120		150					200	
m_{h^0} [GeV]	10	20	10	20	30	40	50	10	50
$\frac{\Gamma(H^0 \to hf\bar{f})}{\cos^2(\alpha-\beta)}$ [MeV]	1.12	0.59	7.3	6.4	5.0	3.2	1.4	34	23
m_{H^0} [GeV]	200		350				500		
m_{h^0} [GeV]	90	10	50	90	150	200	10	120	350
$\frac{\Gamma(H^0 \to hf\bar{f})}{\cos^2(\alpha-\beta)}$ [MeV]	6.0	291	271	227	133	55	944	776	71

Comparing with the two-particle decay gives:

$$\frac{\Gamma(H^0 \to h^0 Z \to h^0 f \bar{f})}{\Gamma(H^0 \to Z h^0)} = \frac{\alpha}{48} \frac{[(4 \sin^2 \Theta_W - 1)^2 + 1]}{\sin^2 \Theta_W \cos^3 \Theta_W} \frac{m_W}{\Gamma_Z} = 2.56 \cdot 10^{-2}.$$

We also give some characteristics of the once differential decay widths. With

$$x_h = \frac{E_h}{m_{H^0}}, \quad x_{2h} = \frac{1 + \mu_h^2}{2}, \quad x_{0h} = \frac{1 + \mu_h^2 - \mu_V^2}{2}, \quad y = \frac{E_f}{m_{H^0}}$$

we see that

$$\frac{d\Gamma}{dx_h} = \frac{G_h m_{H^0}}{(4\pi)^3} \frac{1}{3} \frac{(x_h - \mu_h^2)^{3/2}}{(x_h - x_{0h})^2 + \Delta_V^2}$$

has a resonance behaviour around x_{0h}, its width is Δ_v, and at x_{0_h} its height is

$$\left.\frac{d\Gamma}{dx_h}\right|_{\max} = \frac{\varphi \cdot \alpha^2[(4\sin^2\Theta_W - 1)^2 + 1]}{384\pi \sin^4\Theta_W \cos^4\Theta_W} \frac{m_{H^0}^4}{m_Z^2 \Gamma_Z^2} \Delta^{3/2}(1, \mu_h^2, \mu_Z^2) \cdot m_H$$

that is not very large, at $m_{H^0} \approx 100(150)$ GeV it is about $O(10^{-4}) m_{H^0}$ ($O(10^{-3}) m_{H^0}$).

The fermion energy distribution is

$$\frac{d\Gamma}{dy} = \sum_h G_h \frac{m_{H^0}}{(4\pi)^3} \cdot f_h(y),$$

where

$$f_h(y) \cong \pi \cdot \Delta_V^{-1}[2y(1 - x_{0h} - y) - (\mu_V^2/2)]$$

that is, the superposition of three parabolas. It is a characteristic feature of the model with two doublets. (In the minimal model there are only graphs of C and D type, leading to very different energy distributions).

As far as $H^\pm$ decays are concerned.

$$\Gamma(H^\pm) = \Gamma(H^\pm \to h^0 W^\pm \to h^0 f_1 \bar{f}_2) + \Gamma(H^0 \to \Phi^0 W^\pm \to$$
$$\to \Phi^0 f_1 \bar{f}_2) + \Gamma(H^\pm \to H^0 W^\pm \to H^0 f_1 \bar{f}_2),$$

the formulae are similar to those of the H^0 decay. The h^0 and Φ^0 decays are going also likewise, the results hold qualitatively for these cases, too. The complementary decay widths (e.g. $H^0 \to H^\pm f_1 \bar{f}_2$ and $H^\pm \to H^0 f_1 \bar{f}_2$) are the same.

5. Conclusions

We investigated the three-particle decays of heavy Higgs bosons in the Weinberg–Salam model with two Higgs doublets. We considered the possible decay types, gave their widths and energy distributions. The main decay modes are

$$H_1 \to H_2 V \to H_2 f \bar{f}, \qquad H_{1,2} = H^0, \Phi^0, H^\pm, h^0$$

if the ratio of the two Higgs doublets' vacuum expectation value ($\operatorname{tg}\beta$) is not very extreme, e.g. for the pseudoscalar H^0

$$H^0 \to h^0 f \bar{f} + \Phi^0 f \bar{f} + H^\pm f_1 \bar{f}_2 .$$

In the region $m_{H^0} \approx 100$–150 GeV the total width of H^0 is about a few MeV, then rapidly grows with m_{H^0}, h^0 can give rise to threshold effects. This value is about 3% of the decay width $H_1 \to V H_2$. The energy distribution of H_2 is a resonance of width Γ_V, with a height of $O(10^{-3}) \cdot m_{H_1}$. The fermion energy distribution is a superposition of three

parabolas, this is characteristic for the model with two doublets, and from this some of the parameters of the model can be fixed. These results hold qualitatively also for the neutral and charged scalar Higgs particles. (We can expect to see the chain-like production of Higgs particles via these processes.)

Acknowledgement

The author thanks to Dr. G. Pócsik for valuable discussions.

References

1. G. Pócsik and G. Zsigmond, Phys. Lett. B, *112*, 157, 1982.
2. B. W. Lee, C. Quigg and H. B. Thacker, Phys. Rev. D, *16*, 1519, 1977.
3. H. E. Haber, G. L. Kane and T. Sterling, Nucl. Phys. B, *161*, 493, 1979.
4. H. Hüffel and G. Pócsik, Z. Phys. C, *8*, 13, 1981.
5. F. L. Abbott, P. Sikivie and M. B. Wise, Phys. Rev. D, *21*, 1393, 1980.

Appendix 1

General considerations on three-particle decays

Let us take the decay $1\to 2,\ 3\to 2, f_1\,\bar{f}_2$.
Introduce the notations

$$x=\frac{E_2}{m_1},\qquad y=\frac{E_{f1}}{m_1},\qquad y'=\frac{E_{f2}}{m_1},$$

$$\mu_2=\frac{m_2}{m_1},\qquad \mu_3=\frac{m_3}{m_1},\qquad \delta_3=\frac{\Gamma_3}{m_1},\quad \Delta_3=\frac{1}{2}\mu_3\delta_3,$$

$$x_1=\mu_2,\qquad x_2=\frac{1+\mu_2^2}{2},\qquad x_0=\frac{1}{2}(1+\mu_2^2-\mu_3^2).$$

Then

$$\frac{d^2\Gamma}{dx\,dy}=\frac{m_1}{(4\pi)^3}|M'|^2,$$

neglecting the fermion masses,

$$|M'|^2=\sum_{s_1 s_2}|M_{fi}(x,y,y'=1-x-y)|^2.$$

$$\frac{d\Gamma}{dx}=\int_{y_1} dy\,\frac{d^2\Gamma}{dx\,dy},\qquad y_2^1=\frac{1-x\mp\sqrt{x^2-\mu_2^2}}{2}.$$

In general

$$\frac{d\Gamma}{dx} \propto \frac{Q(x)}{(x-x_0)^2+\Delta^2} + \frac{R(x)\sqrt{x^2-x_1^2}}{(x-x_0)^2+\Delta^2},$$

Q and R are polynomials. Hence $d\Gamma/dx$ is a resonance around x_0, its width is Γ_3, and its maximal value is

$$\left.\frac{d\Gamma}{dx}\right|_{\max} \propto \frac{Q(x_0)}{\Delta^2} + \frac{R(x_0)\sqrt{x_0^2-x_1^2}}{\Delta^2},$$

$$\sqrt{x_0^2-x_1^2} = \frac{1}{2}\Delta^{1/2}(1, \mu_2^2, \mu_3^2),$$

$$\Delta(abc) = a^2+b^2+c^2-2(ab+bc+ca).$$

There are two cases:

a) If $m_1 > m_2+m_3$, $x_0 \in [x_1, x_2]$, $d\Gamma/dx$ is of resonance type.

b) If $m_1 < m_2+m_3$, $x_0 \notin [x_1, x_2]$, then $d\Gamma/dx$ is not resonance-like. (Fig. 4)

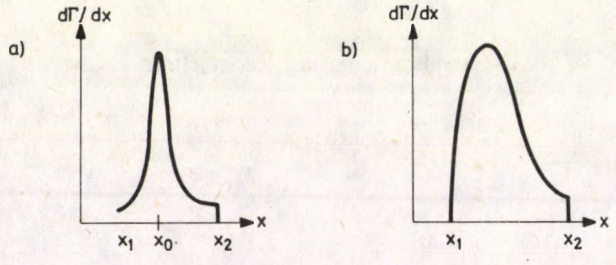

Fig. 4. Possible shapes of energy distributions $\frac{d\Gamma}{dx}$ vs x

Integrating over x we get Γ. In case *b)* usually $x-x_0 \gg \Delta$ therefore Δ^2 can be dropped out of the denominator. In case *a)* the dominant distribution comes from the resonance, integrating the tails can be neglected, and

$$\Gamma = \left.\frac{d\Gamma}{dx}\right|_{\max} \cdot \pi \cdot \Delta_3 .$$

Appendix 2

On the interference terms

Let us consider the interference of the two processes

$$M \to m, m_1 \to m f_1 \bar{f}_2$$

and

$$M \to m, m_2 \to m f_1 \bar{f}_2 .$$

(Fig. 5).

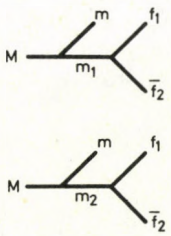

Fig. 5. Interfering graphs in three-particle decays

This appears in $|M'|^2$ in the combination

$$I = \frac{A_1}{k^2 - m_1^2 - i m_1 \Gamma_1} \frac{A_2^*}{k^2 - m_2^2 + i m_2 \Gamma_2} + \frac{A_1^*}{k^2 - m_1^2 + i m_1 \Gamma_1} \frac{A_2}{k^2 - m_2^2 - i m_2 \Gamma_2} =$$

$$= 2 \frac{\mathscr{R}[(x_{01} - x)(x_{02} - x) + \Delta_1 \Delta_2] + \mathscr{I}[(x_{01} - x)\Delta_2 - (x_{02} - x)\Delta_1]}{[(x_{01} - x)^2 + \Delta_1^2][(x_{02} - x)^2 + \Delta_2^2]}$$

with

$$\mathscr{R} = \mathrm{Re}\, A_1 \,\mathrm{Re}\, A_2 + \mathrm{Im}\, A_1 \,\mathrm{Im}\, A_2, \qquad \mathscr{I} = \mathrm{Re}\, A_1 \,\mathrm{Im}\, A_2 - \mathrm{Re}\, A_2 \,\mathrm{Im}\, A_1 ,$$

$$x_1 = \mu, \qquad 2x_{0i} = 1 + \mu^2 - \mu_i^2, \qquad x_2 = \frac{1}{2}(1 + \mu_2),$$

x_1 and x_2 border the integrating domain.

There exist four cases:

1) x_{01}, $x_{02} \notin [x_1, x_2]$, or $M < m_1 + m$, $M < m_2 + m$. Then $|x_{0i} - x| \gg \Delta_i$, neglecting Δ_i

$$I \cong 2 \frac{\mathscr{R}}{(x_{01} - x)(x_{02} - x)} .$$

2) Let us choose $m_2 > m_1$, $x_{02} \notin [x_1, x_2]$, $x_{0_1} \in [x_1, x_2]$, there is one resonance between x_1 and x_2, $|x_{02} - x| \gg \Delta_2$. $I_{\max}$ is at x_{0_1},

$$I_{\max} = 2\frac{\mathscr{R}\Delta_2 + \mathscr{I}(x_{01} - x_{02})}{\Delta_1 (x_{01} - x_{02})^2} \ll I_{\max}^{(\mathrm{diag})} \propto \Delta^{-2}$$

The interference term remains negligible beside the diagonal ones after integration, too.

3) $x_{0_1}, x_{0_2} \in [x_1, x_2]$, and $|x_{0_1} - x_{0_2}| \gg \Delta_i$. There are resonances, at x_{0_1} and at x_{0_2}, there

$$I_{\max(1)} \cong 2\frac{\mathscr{R}\Delta_2 + \mathscr{I}(x_{01} - x_{02})}{\Delta_1 (x_{02} - x_{01})^2}, \qquad I_{\max(2)} = I_{\max(1)}(\Delta_1 \leftrightarrow \Delta_2).$$

These two terms can be integrated separately, and it can be seen that both of them are negligible beside the diagonal terms.

4) $x_{0_1}, x_{0_2} \in [x_1, x_2]$, and $|x_{0_1} - x_{0_2}| \approx \Delta_i$. In this not likely case it is not easy to simplify the integral.

The conclusion is that the interference terms can be comparable with the diagonal terms only in the cases *1)* and *4)*. These considerations are of general nature.

Appendix 3

A useful integral

In calculating three-particle decays we often confront with the integral

$$I_n = \int \frac{x^n \sqrt{x^2 - a^2}}{(x - x_0)^2} dx$$

which cannot be found in tables. Using the decomposition

$$\frac{x^n(x^2 - a^2)}{(x - x_0)^2} = \sum_{i=0}^{n} c_{n,i} x^i + \frac{a_n x + b_n}{(x - x_0)^2},$$

where

$$c_{n,n} = 1; \quad c_{n,n-m} = (m+1)x_0^m - (m-1)x_0^{m-2}a^2, \qquad m = 1 \ldots n$$

$$a_n = (n+2)x_0^{n+1} - n x_0^{n-1} a^2,$$

$$b_n = -(n+1)x_0^{n+2} + (n-1)x_0^n a^2,$$

we can give it as

$$I_n = K_n + \sum_{m=1}^{n} c_{n,n-m} K_{n-m} + J_n.$$

Here

$$K_j = \int \frac{x^j dx}{\sqrt{x^2 - a^2}},$$

from tables

$$K_{2m} = \frac{\sqrt{x^2-a^2}}{2m}\left[x^{2m-1} + \sum_{k=1}^{m-1} \frac{(2m-1)!!(m-k-1)!}{(2m-2k-1)!!(m-1)!}\left(\frac{a^2}{2}\right)^k x^{2m-2k-1}\right] +$$

$$+ \left(\frac{a^2}{2}\right)^m \frac{(2m-1)!!}{m!} \operatorname{Arch}\frac{x}{a},$$

$$K_{2m+1} = \sum_{k=0}^{m} \binom{m}{k} \frac{a^{2m-2k}}{2k+1} (x^2-a^2)^{k+\frac{1}{2}},$$

and we can express also J_n:

$$J_n = -\frac{x_0^n}{x-x_0}\sqrt{x^2-a^2} + \frac{x_0^{n-1}[(n+1)x_0^2 - na^2]}{\sqrt{a^2-x_0^2}} \arccos\frac{a^2 - x_0 x}{a(x-x_0)}.$$

Acta Physica Hungarica 56 (1—4), pp 87—93 (1984)

COHESIVE ENERGY AND DEBYE TEMPERATURE OF SOME AROMATIC COMPOUNDS — AN INTERMOLECULAR POTENTIAL APPROACH

S. P. SRIVASTAVA

Indian Institute of Petroleum, Dehradun-248005, India

(Received 7 March 1983)

Cohesive energy and Debye temperature of some substituted, fused and non-fused aromatic compounds have been computed on the basis of Lennard–Jones (6–12), modified Buckingham and Morse intermolecular potential functions. The results have been compared with those determined from the experimental data and discussed. The cohesive energy of the present set of aromatic compounds, as a class, is found to be one order larger than that of normal alkanes and is comparable with cycloalkanes.

Introduction

In our earlier publications [1, 2] we have studied the lattice properties like cohesive energy, Grüneisen parameter, Debye temperature etc. of molecular crystals of globular hydrocarbons like adamantane, bicyclo (2.2.2) octane and methane on the basis of intermolecular potential function due to Lennard–Jones. Due to the apparent success of this approach, we now extend the work further to include the molecular organic crystals of benzoic acid, hexamethyl benzene, hexachloro benzene, hexabromo benzene (all substituted benzene compounds), bi-phenyl, benzophenone, benzil, *p*-terphenyl (all non-fused aromatic ring compounds) and naphthalene, perinaphthenone, anthracene, anthrone, anthraquinone, perylene, 9,10 bi-phenyl anthracene (all condensed aromatic ring compounds).

From a number of studies it has been inferred that the following three forms of the intermolecular potential functions, viz.

$$\psi = \left(\frac{N_A}{2}\right)[-AV^{-6n} + BV^{-12n}] \qquad \text{(Lennard–Jones)}, \qquad (1)$$

$$\psi = \left(\frac{N_A}{2}\right)[-AV^{-6n} + B\exp(-V^n/\rho)] \qquad \text{(modified Buckingham)} \qquad (2)$$

and

$$\psi = \left(\frac{N_A}{2}\right)[-A\exp(-V^n/\rho) + B\exp(-2V^n/\rho)] \qquad \text{(Morse)} \qquad (3)$$

Table I

Potential parameters of the Lennard–Jones, modified Buckingham and Morse functions for some substituted, non-condensed and condensed aromatic compounds

Compound	$\gamma_{expt.}$ (Eq. (4))	Potential parameters							
		Lennard–Jones		Modified Buckingham			Morse		
		$A \times 10^{62}$ [J · cm^6]	$B \times 10^{106}$ [J · cm^{12}]	$\rho \times 10^8$ [cm]	$A \times 10^{62}$ [J · cm^6]	$B \times 10^{12}$ [J]	$\rho \times 10^8$ [cm]	$A \times 10^{14}$ [J]	$B \times 10^{10}$ [J]
1. Benzoic acid	2.90	1.04	1.18	0.317	0.63	1.94	0.424	3.06	4.54
2. Hexamethyl benzene	2.78	5.82	18.63	0.389	3.77	2.60	0.554	2.25	2.23
3. Hexachloro benzene	2.61	4.42	10.61	0.263	1.66	8.81×10^2	0.460	9.40	22.98
4. Hexabromo benzene	3.87	7.73	25.59	0.252	2.55	80.56×10^2	0.481	12.97	35.07
5. Bi-phenyl	3.39	2.70	6.30	0.286	1.16	93.90	0.461	5.47	12.10
6. Benzophenone	3.59	8.02	31.44	0.287	3.05	8.18×10^2	0.499	10.47	23.90
7. Benzil	2.47	5.72	19.02	0.479	4.39	0.18	0.541	2.40	1.78
8. *p*-terphenyl	3.55	8.73	41.21	0.301	3.77	5.71×10^2	0.516	10.54	25.77
9. Naphthalene	3.07	2.34	4.26	0.316	1.25	9.33	0.457	3.62	9.33
10. Perinaphthenone	3.48	4.29	10.75	0.279	1.65	2.82×10^2	0.466	8.36	20.44
11. Anthracene	3.17	5.01	14.11	0.278	1.97	4.54×10^2	0.953	0.05	0.16×10^{-3}
12. Anthrone	3.18	5.30	14.74	0.323	2.62	29.17	0.481	7.54	13.65
13. Anthraquinone	3.66	6.58	19.59	0.267	2.41	16.05×10^2	0.476	11.25	27.49
14. Perylene	3.35	15.48	75.56	0.328	6.79	1.97×10^2	0.523	14.91	33.16
15. 9, 10 bi-phenyl anthracene	3.74	36.04	371.20	0.318	12.65	45.88×10^2	0.582	20.08	54.25

(where ψ is the potential energy per mole, V is the molar volume, $n=1/3$, N_A is Avogadro's number and A, B and ρ are the potential parameters) have been widely used in cases of gases and liquids [3] as well as in solids [1] for the calculations of molecular energy levels and lattice properties. In what follows in the present work, the cohesive energy (U_0) and the Debye temperature (θ) of these solids have been studied on the basis of the above forms of the intermolecular potential function and the results thus obtained have been discussed.

Theory

In order to study the lattice properties, a knowledge of the potential parameters, A, B and ρ, of the intermolecular potential functions for the individual solid is desirable. For the case of two-parametric Lennard–Jones function these can be easily computed by employing the static lattice conditions [1, 4], but for three-parametric modified Buckingham and Morse functions one more condition is necessary. Chang [5] has shown that under the quasi-harmonic approximation

$$\delta=\left[\left(\frac{d\beta_T}{dp}\right)-1\right]\simeq\left[\left(\frac{d\beta_s}{dp}\right)-1\right]=2\gamma \quad \text{or} \quad 2\gamma-2/3, \tag{4}$$

where δ is the Anderson–Grüneisen parameter, β_T and β_s are the isothermal and adiabatic bulk moduli and γ is the Grüneisen parameter. The two values of δ in terms of γ in Eq. (4) are due to two relationships — one due to Dugdale and MacDonald [6] and the other due to Slater [7] — between γ and the change of compressibility with volume, respectively.

The compression behaviour of the present set of aromatic crystals has been studied by Vaidya and Kennedy [8] and the bulk modulus, β, and its pressure-derivative have been determined using the Murnaghan equation and the modified Murnaghan equation. Using these data, the values of the potential parameters of the modified Buckingham and Morse functions for these solids have been computed and are reported in Table I. In this Table the values of γ computed using the relation $\delta=2\gamma$ are also listed.

Results

Using these potential parameters, the values of cohesive energy, U_0, have been computed [1, 9] and are given in Table II alongwith the melting point (m.p.) of the solids. In these values of U_0 are also added the zero-point energy, ϵ_0, of the crystal lattice which was calculated using the relation $\epsilon_0=\frac{9}{8}\frac{R\theta}{N_A}$[10] (where R is the gas constant). The θ-values as obtained by Plendl's equation (Table III, column 5) were used in these calculations and values of ϵ_0 thus obtained are listed in Table II, column 3.

Table II

Zero-point energy, ϵ_0 [kJ/mol], and the cohesive energy, U_0 [kJ/mol], of some substituted, non-condensed and condensed aromatic compounds

Compound	m.p. [°C]	ϵ_0	U_0 (calc.)				U_0 (exptl.)**	
			Lennard–Jones		Modified Buckingham	Morse		
1. Benzoic acid	122.4	1.13	69.50	(62.98)*	108.62	63.34	93.35	(70 – 114 °C)+
2. Hexamethyl benzene	167.0	1.17	138.29	(107.95)	225.10	131.75	82.22	–
3. Hexachloro benzene	230.0	0.96	147.07	–	154.93	116.82	97.32	(51 – 71 °C)
4. Hexabromo benzene	327.0	0.84	168.49	(150.25)	177.61	145.60	–	–
5. Bi-phenyl	70.5	1.00	88.37	(75.31)	108.11	75.48	77.40	(6 – 26 °C)
6. Benzophenone	48.0	1.13	155.35	(136.69)	173.96	109.45	96.99	(16 – 42 °C)
7. Benzil	95.0	1.00	130.79	(120.08)	219.28	130.12	100.16	(45 – 67 °C)
8. *p*-terphenyl	210.0	0.96	140.25	(126.61)	177.23	130.88	–	–
9. Naphthalene	80.6	1.17	97.95	(91.04)	139.95	86.86	71.84	(6 – 21 °C)
10. Perinaphthenone	156.5	1.08	129.79	–	144.68	104.18	–	–
11. Anthracene	216.2	1.13	139.20	(122.55)	154.77	131.71	103.26	(65 – 80 °C)
12. Anthrone	155.0	1.13	144.77	(138.59)	196.23	126.52	–	–
13. Anthraquinone	286.0	1.13	167.44	(146.69)	178.45	139.79	112.05	(224 – 286 °C)
14. Perylene	278.0	1.17	232.34	–	298.70	205.43	–	–
15. 9, 10 bi-phenyl anthracene	249.5	0.96		(248.53)	285.89	233.30	160.67	(208 – 229 °C)

* Values in parentheses are calculated using the modified Murnaghan equation [8] for the calculation of bulk modulus.

** Deduced from the data listed in ref. [13].

+ Temperature range to which U_0 belongs.

From the knowledge of the cohesive energy, the characteristic temperature, θ, can now be calculated on the basis of our earlier derived equation for θ [2]. Plendl [11] has connected the bulk modulus and the density of a solid with the characteristic temperature. A similar relation has also been earlier derived by Blackman [2, 12]. Using these equations the values of θ have been computed and are listed in Table III.

Table III

Debye temperature, θ(K), of some substituted, non-condensed and condensed aromatic compounds

Compound	Debye θ				
	Our Eq. (Eq. (3) ref. [2])			Plendl [11]	Blackman [12]
	Lennard–Jones	Modified Buckingham	Morse		
1. Benzoic acid	115	146	112	120	68
2. Hexamethyl benzene	119	153	126	123	70
3. Hexachloro benzene	98	101	88	103	56
4. Hexabromo benzene	85	86	80	89	52
5. Bi-phenyl	105	116	97	109	61
6. Benzophenone	116	124	107	120	68
7. Benzil	103	132	94	106	59
8. *p*-terphenyl	96	108	95	104	55
9. Naphthalene	124	149	118	127	73
10. Perinaphthenone	115	122	104	116	67
11. Anthracene	116	123	115	120	67
12. Anthrone	115	135	109	121	67
13. Anthraquinone	119	123	109	122	69
14. Perylene	116	132	109	123	69
15. 9, 10 bi-phenyl anthracene	99	101	92	101	58

Discussion

On a comparison of the values of U_0 (Table II) obtained on the basis of Lennard–Jones, Morse and the modified Buckingham intermolecular potential functions, some interesting trends have been noticed. These are increasing with the molecular weight and melting point of the solids and those obtained on the basis of Lennard–Jones inverse power law type potential function are larger for all the solids in comparison to those obtained using the double exponential function of Morse. The modified Buckingham function, which is of mixed type, yields values of U_0 which are larger than those obtained from both of these pure functions. However, the use of bulk modulus obtained from modified Murnaghan equation reported for some solids [8], in place of β values obtained from Murnaghan equation, yields somewhat lower values of U_0 (Table II, column 4, in parentheses).

In the last column of Table II are listed the experimental values of U_0 for some of the compounds alongwith the temperature range for which they are deduced. On a comparison with the theoretical values which are for absolute zero, the experimental values of U_0 are showing deviations the amount depending upon the temperature range. Thus, in case of 9, 10 bi-phenyl anthracene, as the experimental value of U_0 is belonging to very high temperature, the deviation from its theoretical value is also very large in this case as that of naphthalene and bi-phenyl. Nevertheless, both the pure functions, the Lennard–Jones and Morse, are giving satisfactory results.

From a critical analysis of U_0 values obtained on the basis of Lennard–Jones function (though the arguments that would follow are also valid for other sets of U_0 values as well) it may be seen that in a two six-membered rings compounds — whether directly united as in bi-phenyl or fused to form naphthalene — the cohesive energy does not change much. The difference being only about 9.5 kJ/mol, the fusion giving a more stable compound. Extending this argument to compounds like *p*-terphenyl and anthracene, we note that like their melting points, their cohesive energies are also nearly equal. It may thus be concluded that addition of one more ring to a two-ring compound increases U_0 by about 52 kJ/mol when non-fused (as in *p*-terphenyl) and when condensed to form anthracene, the increase in U_0 is about 42 kJ/mol. We may thus infer that the cohesive energy of benzene should be around 47 kJ/mol. The cohesive energy for higher ring compounds of this series can now be predicted and, for example, for linear quaterphenyl (m.p. 320 °C) and naphthacene (m.p. 357 °C) may be estimated to be around 165 and 180 kJ/mol, respectively.

In case of substituted benzenes, it can be seen that as the molecular weight of the substituent is increasing the value of U_0 is also increasing, in a somewhat linear manner. As such, by assuming the cohesive energy of benzene as 47 kJ/mol, the values of U_0 of toluene, xylene, etc can be estimated from the knowledge of U_0 of hexamethyl benzene. Following this procedure the values of U_0 for toluene, monochloro benzene and mono-bromo benzene have been estimated to be 62, 64 and 66 kJ/mol, respectively.

From Table II, it can be further noted that the addition of a C=O group at one of the positions 9 or 10 of anthracene, as in anthrone, increases the cohesive energy of anthracene by about 5kJ/mol, while a further addition of the C=O group at the other position, as in anthraquinone, increases U_0 further by about 20 kJ/mol. From these trends, U_0 values of still more complicated molecular solids could be analysed. In case of perylene it can be thus seen that its cohesive energy (Table II, column 4) is the sum of cohesive energies of anthracene and naphthalene whereas in the case of 9, 10 bi-phenyl anthracene, the value of U_0 is the sum of the cohesive energies of anthracene and *p*-terphenyl. These examples further lend credence to the additive nature of the cohesive energy.

The Debye θ values of these solids calculated on the basis of Lennard–Jones, modified Buckingham and Morse functions seem to be in good agreement with those obtained from Plendl's equation (Table III, column 5). The agreement for most of the

solids is particularly satisfactory for the Lennard–Jones function. Blackman's equation is yielding lower values of θ for all the solids.

It can also be seen from Table III that on a comparison of the values of Debye θ between substituted, directly connected and fused benzene rings compounds, the Debye θ, unlike the case of cohesive energy, does not vary much from simpler compounds like benzoic acid, hexamethyl benzene etc to complicated molecules like perylene, 9, 10 bi-phenyl anthracene etc. It seems that the complexity of the structure does not have any bearing on the characteristic temperature.

Conclusions

From this study it may thus be concluded that the cohesive energy of the aromatic compounds as a class is one order greater than for methane [1] — an alkane, and one order smaller in comparison to ionic solids [9]. These are comparable to those for adamantane and bicyclo (2.2.2) octane [1] — both cycloparaffins. It could then be of interest to investigate the cohesive energy of normal- and iso-paraffins and to study their comparison with the cyclo-paraffins and the present aromatic compounds. From the present investigation, it is indicated that for simpler members of the paraffinic and iso-paraffinic compounds, the cohesive energy should lie between 8 kJ/mol (for methane) to about 40 kJ/mol (for bicyclo octane).

Acknowledgement

My thanks are due to Dr. G. C. Joshi for his various comments and suggestions for the improvement of the manuscript.

References

1. S. P. Srivastava, I. D. Singh and P. L. Gupta, Acta Phys. Hung., *44*, 211, 1978.
2. S. P. Srivastava and I. D. Singh, J. Phys. Soc. Japan, *44*, 2005, 1978.
3. J. O. Hirschfelder, C. F. Curtiss and R. B. Bird, Molecular Theory of Gases and Liquids, Wiley, New York, 1967; I. M. Torrens, Interatomic Potentials, Academic Press, New York, 1972.
4. S. P. Srivastava and R. S. Saraswat, J. Phys. Chem. Solids, *36*, 351, 1975; R. C. Bowman Jr., J. Phys. Chem. Solids, *34*, 1754, 1973.
5. Y. A. Chang, J. Phys. Chem. Solids, *28*, 697, 1967.
6. J. S. Dugdale and D. K. C. MacDonald, Phys. Rev., *89*, 832, 1953.
7. J. C. Slater, Introduction to Chemical Physics, McGraw Hill, New York, 1939.
8. S. N. Vaidya and G. C. Kennedy, J. Chem. Phys., *55*, 987, 1971.
9. M. Born and K. Huang, Dynamical Theory of Crystal Lattices, Clarendon Press, Oxford, 1954.
10. J. A. Janik, K. Otnes, G. Solt and G. Koslay, Discussions Faraday Soc., *48*, 87, 1969.
11. J. N. Plendl, in 'Optical Properties of Solids', Pergamon Press, New York, 1969.
12. M. Blackman, Handbuch der Physik, VII/1, 325, 1955.
13. Handbook of Physics and Chemistry, 50th ed., Eited by R. C. Weast, Chemical Rubber Co., Ohio, 1969—70.

Acta Physica Hungarica 56 (1—4), pp 95—106 (1984)

EXTENSION OF THE ITERATIVE PROCEDURE OF HERMAN–TIPPING–SHORT

D. C. PATIL

Department of Physics, Karnatak University
Dharwad-58003 India

(Received 28 March 1983)

Herman et al have developed a simple iterative method to obtain vibrational wavefunctions for $^1\Sigma$ states of diatomic molecules. Tipping et al further extended their work to 5th iteration. We have, in the present work, improved upon the method by going up to 6th iteration.

To find out the applicability of the extended work, we have computed Franck–Condon factors, *r*-centroids for $D^1\Pi - X^1\Sigma$ of SnO assuming that the formulae developed hold for $^1\Pi$-states. Our results compare very well with the realistic R. K. R. results showing that the 6th iteration has yielded good results and our assumption of the applicability of the iterative procedure to $^1\Pi$-states is justified.

Introduction

The theoretical study of the intensities of diatomic molecular bands involves vibrational wavefunctions. These are to be obtained by solving the appropriate Schrödinger equation, with a proper potential function. The Schrödinger equation is solvable exactly for a very few potential functions although many have been proposed for diatomic molecules. One then normally resorts to approximation methods for solving the equation. Many approximation methods exist but not all of them are easy to handle. R.K.R. procedure is supposed to yield accurate results as it is based on experimentally determined parameters; but this procedure is rather cumbersome. In 1970 Herman et al [1] have proposed a simple approximation method, named 'Iteration Method' for solving the Schrödinger equation. They have evolved formulae in the 3rd iteration.

This iterative method was further extended to 5th iteration by Tipping et al [2] for $^1\Sigma$-state diatomic vibrational wavefunctions. Niay [3] also had extended the procedure to 5th iteration; however, his emphasis was entirely different.

We have actually processed Rydberg potential function [4] by this iterative method taking expressions for the third iteration [1] and calculated Franck–Condon Factors (FCF) and *r*-centroids for the $D^1\Pi$ to $X^1\Sigma$ transition of the SnO molecule. To improve the accuracy of the results, we extended the procedure to 6th iteration and then calculated FCFs and *r*-centroids for the same transition by processing Rydberg potential [4] by it. These results are compared with those calculated by the R.K.R. procedure [5].

To appreciate our extension-work, it is necessary to know some fundamentals of the iteration procedure before we present our formulae for the 6th iteration.

The Schrödinger equation to be solved is

$$\frac{d^2\psi_v(x)}{dx^2} + \frac{[E-V(x)]}{B_e}\psi_v(x)=0\,, \tag{1}$$

where

$$x=\frac{r-r_e}{r_e}\,.$$

This is solved by putting

$$\psi_v(x)=g_v(x)\psi_0(x)\,, \tag{2}$$

where

$$\psi_0(x)=e^{-\frac{1}{2}\int_0^x y(x')\,dx'}, \quad \text{[unnormalized wavefunction for } v=0 \text{ state]}$$

and hence $y(x)$ and $g_v(x)$ satisfy, respectively, the following differential equations

$$y^2(x)-2\frac{dy(x)}{dx}-\frac{4}{B_e}[V(x)-E_0]=0\,, \tag{3}$$

$$\frac{d^2g_v(x)}{dx^2} - y(x)\frac{dg_v(x)}{dx} + \frac{(E_v-E_0)}{B_e}g_v(x)=0\,. \tag{4}$$

Dunham [6] assumes that the potential function is expressible in a power-series as

$$\frac{V(x)}{B_e}=\gamma^{-2}x^2(1+a_1x+a_2x^2+\ldots+a_nx^n)\,, \tag{5}$$

where

$$\gamma=\frac{2B_e}{\omega_e}\,.$$

B_e and ω_e are the usual spectroscopic constants.

Equations (3) and (4) may be solved by the power series

$$y(x)=\sum_{i=0}^{\infty} b_i x\,, \tag{6}$$

$$g_v(x)=\sum_{i=0}^{\infty} C_{v_i}x^i \tag{7}$$

as follows. Under harmonic approximation, the solution is

$$\frac{V(x)}{hcB_e}=\gamma^{-2}x^2; \quad \frac{E_v}{B_e}=2\gamma^{-1}\left(v+\frac{1}{2}\right).$$

Then in the 1st iteration, one additional term is added to the harmonic potential

$$\frac{V(x)}{hcB_e} = \gamma^{-2}x^2(1+a_1x),$$

while terms higher than a_1 appearing in Dunham energies are neglected; at the same time, the series equations (6) and (7) are truncated according to

$$b_i = 0, \qquad i \geq 3,$$

$$C_{v_i} = 0, \qquad i \geq v+2$$

continuing this procedure, for the nth iteration we obtain the wave function for the Dunham potential equation (5) expressed in terms of the polynomial series truncated according to

$$b_i = 0, \qquad i \geq n+2,$$

$$C_{v_i} = 0, \qquad i \geq n+v+1.$$

Expressions for $y(x)$ and $g(x)$ developed by us in the 6th iteration are listed in Table I. Expression of $g_v(x)$ for $v>6$ are possible but rather more tedious.

These new formulae have been employed to calculate wavefunctions, FCFs and r-centroids for $D^1\Pi - X^1\Sigma$ state of SnO molecule; the results are given in Table II, along with the R.K.R. [5] results for comparison. As can be seen from the Table there is good agreement between the two sets of results.

To obtain the a's (the Dunham coefficients) in the case of a given analytical potential, this latter is expanded in a power series and the coefficients compared with those of Dunham expansion.

Table I

Unnormalized $g_v(x)$ and $y(x)$ functions for the pure vibration states of diatomic molecules in the 6th iteration

$$\Psi_v(x) = g_v(x)e^{\left(-\frac{1}{2}\int_0^x y(x')\,dx'\right)}$$

$$y(x) = \left[a_1 + \gamma\left(\frac{5}{4}a_1^3 - 3a_1a_2 + 2a_3\right) + \frac{1}{4}\gamma^2\left(\frac{681}{32}a_1^5 - \frac{2691}{32}a_1^3a_2 + \frac{125}{2}a_1a_2^2 - 46a_1a_4 - 42a_2a_3 + 24a_5\right)\right] + \left[\frac{2}{\gamma} + \frac{1}{2}\left(-\frac{7}{4}a_1^2 + 3a_2\right) + \frac{1}{4}\gamma\left(-\frac{305}{32}a_1^4 + \frac{123}{4}a_1^2a_2 - \frac{49}{2}a_1a_3 - \frac{21}{2}a_2^2 + 15a_4\right) + \gamma^2\left(-\frac{54\,895}{4096}a_1^6 + \frac{136\,767}{2048}a_1^4a_2 - \frac{11813}{256}a_1^3a_3 - \frac{31\,595}{512}a_1^2a_2^2 + \frac{973}{128}a_1^2a_4 + \frac{5139}{64}a_1a_2a_3 - \frac{309}{16}a_1a_5 + \frac{513}{64}a_2^3 - \frac{495}{32}a_2a_4 - \frac{215}{32}a_3^2 + \frac{15}{8}a_6\right)\right]x + \left[\frac{a_1}{\gamma} + \left(\frac{13}{16}a_1^3 - \frac{9}{4}a_1a_2 + 2a_3\right) + \frac{1}{4}\gamma\left(\frac{917}{64}a_1^5 - \frac{483}{8}a_1^3a_2 + \frac{199}{4}a_1^2a_3\right.\right.$$

Table I. *(cont.)*

$$\Psi_v(x)=g_v(x)e^{(-\frac{1}{2}\int_0^x y(x')dx')}$$

$$+\frac{193}{4}a_1a_2^2-\frac{77}{2}a_1a_4-36a_2a_3+24a_5\Big)\Big]x^2+\Big[\frac{1}{\gamma}\Big(-\frac{1}{2}a_1^2+a_2\Big)$$

$$+\frac{1}{2}\Big(-\frac{99}{64}a_1^4+\frac{47}{8}a_1^2a_2-\frac{11}{2}a_1a_3-\frac{11}{4}a_2^2+5a_4\Big)-\gamma\Big(\frac{169}{32}a_1^6-\frac{12957}{512}a_1^4a_2$$

$$+\frac{1209}{64}a_1^3a_3+\frac{439}{16}a_1^2a_2^2-\frac{293}{16}a_1^2a_4-42a_1a_2a_3+\frac{71}{8}a_1a_5-\frac{75}{16}a_2^3+\frac{75}{8}a_2a_4$$

$$+\frac{61}{16}a_3^2-\frac{5}{4}a_6\Big)\Big]x^3+\Big[\frac{1}{\gamma}\Big(\frac{1}{8}a_1^3-\frac{1}{2}a_1a_2+a_3\Big)+\frac{1}{4}\Big(\frac{191}{64}a_1^5-\frac{115}{8}a_1^3a_2$$

$$+\frac{55}{4}a_1^2a_3+\frac{55}{4}a_1a_2^2-13a_1a_4-13a_2a_3+12a_5\Big)\Big]x^4+\Big[\frac{1}{4\gamma}\Big(-\frac{5}{16}a_1^4+\frac{3}{2}a_1^2a_2$$

$$-2a_1a_3-a_2^2+4a_4\Big)+\Big(-\frac{953}{1024}a_1^6+\frac{565}{128}a_1^4a_2-\frac{95}{32}a_1^3a_3-\frac{291}{64}a_1^2a_2^2+\frac{23}{8}a_1^2a_4$$

$$+11a_1a_2a_3-\frac{7}{4}a_1a_5+\frac{15}{16}a_2^3-\frac{9}{4}a_2a_4-\frac{9}{4}a_3^2+\frac{1}{2}a_6\Big)\Big]x^5+\frac{1}{\gamma}\Big[\frac{7}{128}a_1^5$$

$$-\frac{5}{16}a_1^3a_2+\frac{3}{8}a_1^2a_3+\frac{3}{8}a_1a_2^2-\frac{1}{2}a_1a_4-\frac{1}{2}a_2a_3+a_5\Big]x^6+\frac{1}{\gamma}\Big[-\frac{21}{512}a_1^6+\frac{35}{128}a_1^4a_2$$

$$-\frac{5}{16}a_1^3a_3-\frac{15}{32}a_1^2a_2^2+\frac{3}{8}a_1^2a_4+\frac{3}{4}a_1a_2a_3-\frac{1}{2}a_1a_5+\frac{1}{2}a_2^3-\frac{1}{2}a_2a_4-\frac{1}{4}a_3^2+a_6\Big]x^7,$$

$$g_1=\Big[a_1\gamma+\gamma^2\Big(\frac{67}{16}a_2^3-\frac{27}{4}a_1a_2+3a_3\Big)+\gamma^3\Big(\frac{8973}{256}a_1^5-\frac{3507}{32}a_1^3a_2+\frac{1083}{16}a_1^2a_3$$

$$+\frac{937}{16}a_1a_2^2-\frac{269}{8}a_1a_4-30a_2a_3+12a_5\Big)\Big]+x+\Big[-\frac{1}{2}a_1+\frac{1}{2}\gamma\Big(-\frac{27}{8}a_1^3+\frac{15}{2}a_1a_2$$

$$-4a_3\Big)+\frac{1}{2}\gamma^2\Big(-\frac{1851}{64}a_1^5+\frac{429}{4}a_1^3a_2-\frac{587}{8}a_1^2a_3-\frac{289}{4}a_1a_2^2+\frac{89}{2}a_1a_4$$

$$+\frac{81}{2}a_2a_3-18a_5\Big)\Big]x^2+\Big[\frac{1}{4}\Big(\frac{5}{4}a_1^2-a_2\Big)+\frac{1}{4}\gamma\Big(\frac{561}{64}a_1^4-\frac{185}{8}a_1^2a_2$$

$$+\frac{89}{6}a_1a_3+\frac{17}{4}a_2^2-5a_4\Big)+\frac{1}{4}\gamma^2\Big(\frac{17479}{2048}a_1^6-\frac{50435}{128}a_1^4a_2+\frac{13173}{48}a_1^3a_3$$

$$+\frac{90403}{256}a_1^2a_2^2-\frac{2637}{16}a_1^2a_4-\frac{1275}{4}a_1a_2a_3+\frac{963}{8}a_1a_5-\frac{57}{2}a_2^3+45a_2a_4$$

$$+\frac{597}{16}a_3^2-\frac{125}{4}a_6\Big)\Big]x^3+\Big[\frac{1}{2}\Big(-\frac{7}{16}a_1^3+\frac{3}{4}a_1a_2-\frac{1}{3}a_3\Big)+\frac{1}{2}\gamma\Big(-\frac{1223}{256}a_1^5$$

$$+\frac{519}{32}a_1^3a_2-\frac{21}{2}a_1^2a_3-\frac{151}{16}a_1a_2^2+\frac{11}{2}a_1a_4+5a_2a_3-2a_5\Big)\Big]x^4$$

$$+\Big[\frac{1}{8}\Big(\frac{21}{16}a_1^4-\frac{7}{2}a_1^2a_2+\frac{13}{6}a_1a_3+a_2^2-a_4\Big)+\frac{1}{8}\gamma\Big(\frac{40829}{1024}a_1^6-\frac{21665}{256}a_1^4a_2$$

$$+\frac{2819}{48}a_1^3a_3+\frac{10315}{128}a_1^2a_2^2-\frac{2649}{80}a_1^2a_4-\frac{2987}{40}a_1a_2a_3+\frac{167}{10}a_1a_5$$

Table I. *(cont.)*

$$\Psi_v(x) = g_v(x) e^{\left(-\frac{1}{2}\int_0^x y(x')dx'\right)}$$

$$-9a_2^3+15a_2a_4+\frac{29}{3}a_3^2-4a_6\Big)\Big]x^5+\frac{1}{2}\Big[-\frac{33}{128}a_1^5+\frac{15}{16}a_1^3a_2-\frac{2}{3}a_1^2a_3$$
$$-\frac{5}{8}a_1a_2^2+\frac{17}{40}a_1a_4+\frac{23}{60}a_2a_3-\frac{1}{5}a_5\Big]x^6+\frac{1}{4}\Big[\frac{427}{1024}a_1^6-\frac{495}{256}a_1^4a_2$$
$$+\frac{967}{579}a_1^3a_3+\frac{135}{64}a_1^2a_2^2-\frac{173}{160}a_1^2a_4-\frac{477}{240}a_1a_2a_3+\frac{7}{10}a_1a_5-\frac{5}{16}a_2^3$$
$$+\frac{5}{8}a_2a_4+\frac{11}{30}a_3^2-\frac{1}{3}a_6\Big]x^7,$$

$$g_2=\Big[-\frac{1}{2}\gamma+\frac{1}{8}\gamma^2\Big(-\frac{13}{4}a_1^2+9a_2\Big)+\frac{1}{8}\gamma^3\Big(-\frac{1731}{128}a_1^4+\frac{2415}{16}a_1^2a_2-\frac{191}{2}a_1a_3$$
$$-\frac{459}{8}a_2^2+45a_4\Big)+\frac{1}{4}\gamma^4\Big(\frac{1\,460\,395}{2048}a_1^6+\frac{1\,566\,501}{1024}a_1^2a_4-\frac{178\,645}{128}a_1^3a_3$$
$$-\frac{393\,419}{128}a_1^2a_2^2+\frac{76\,435}{64}a_1^2a_4+\frac{62\,373}{32}a_1a_2a_3-\frac{3135}{8}a_1a_5+\frac{22\,797}{32}a_2^3$$
$$-\frac{11\,835}{16}a_2a_4-\frac{3885}{16}a_3^2+\frac{525}{4}a_6\Big)\Big]+\Big[4a_1\gamma+\gamma^2\Big(\frac{151}{4}a_1^3-45a_1a_2$$
$$+18a_3+\frac{1}{2}\gamma^3\Big(\frac{18\,429}{16}a_1^5-2916a_1^3a_2+\frac{3221}{2}a_1^2a_3+1187a_1a_2^2$$
$$-623a_1a_4-552a_2a_3+192a_5\Big)\Big]x+x^2+\Big[-a_1+\gamma\Big(-\frac{21}{4}a_1^3+9a_1a_2$$
$$-\frac{16}{3}a_3\Big)+\frac{1}{2}\Big(-\frac{8523}{64}a_1^5+\frac{3267}{8}a_1^3a_2-\frac{1651}{6}a_1^2a_3-\frac{907}{4}a_1a_2^2$$
$$+145a_1a_4+132a_2a_3-60a_5\Big)\Big]x^3+\Big[\frac{1}{2}\Big(\frac{7}{4}a_1^2-a_2\Big)+\frac{1}{4}\gamma\Big(\frac{4549}{128}a_1^4$$
$$-\frac{1253}{16}a_1^2a_2+\frac{557}{12}a_1a_3+\frac{85}{8}a_2^2-\frac{25}{2}a_4\Big)+\frac{1}{4}\gamma^2\Big(\frac{8\,354\,847}{2045}a_1^6$$
$$-\frac{485\,927}{256}a_1^4a_2+\frac{319\,777}{96}a_1^3a_3+\frac{195\,993}{128}a_1^2a_2^2-\frac{1369}{2}a_1^2a_4$$
$$-\frac{9705}{8}a_1a_2a_3+\frac{2419}{8}a_1a_5-\frac{2919}{32}a_2^3+\frac{1245}{8}a_2a_4+\frac{2301}{16}a_3^2-\frac{165}{4}a_6\Big)\Big]x^4$$
$$+\Big[\Big(-\frac{3}{4}a_1^3+a_1a_2-\frac{1}{3}a_3\Big)+\frac{1}{2}\gamma\Big(-\frac{2901}{128}a_1^5+\frac{1053}{16}a_1^3a_2-\frac{155}{4}a_1^2a_3$$
$$-\frac{245}{8}a_1a_2^2+\frac{157}{10}a_1a_4+\frac{76}{5}a_2a_3-\frac{24}{5}a_5\Big)\Big]x^5+\Big[\frac{1}{8}\Big(\frac{165}{32}a_1^4-\frac{45}{4}a_1^2a_2$$
$$+\frac{17}{3}a_1a_3+\frac{5}{2}a_2^2-2a_4\Big)+\frac{1}{8}\gamma\Big(\frac{1673}{16}a_1^6-\frac{49\,493}{128}a_1^4a_2+\frac{12\,559}{16}a_1^3a_3$$
$$+\frac{2533}{8}a_1^2a_2^2-\frac{4541}{40}a_1^2a_4-\frac{14\,791}{60}a_1a_2a_3+\frac{471}{10}a_1a_5-\frac{55}{2}a_2^3+43a_2a_4$$

Table I. *(cont.)*

$$\Psi_v(x) = g_v(x) e^{(-\frac{1}{2}\int_0^x \gamma(x')dx')}$$

$$+\frac{1141}{36}a_3^2-\frac{31}{3}a_6\Big)\Big]x^6+\Big[-\frac{143}{256}a_1^5+\frac{55}{32}a_1^3a_2-\frac{25}{24}a_1^2a_3-\frac{15}{16}a_1a_2^2$$

$$+\frac{11}{26}a_1a_4+\frac{7}{15}a_2a_3-\frac{1}{5}a_5\Big]x^7+\frac{1}{4}\Big[-\frac{1001}{512}a_1^6+\frac{1001}{128}a_1^4a_2-\frac{253}{48}a_1^3a_3$$

$$-\frac{231}{32}a_1^2a_2^2+\frac{133}{40}a_1^2a_4+\frac{347}{60}a_1a_2a_3-\frac{9}{5}a_1a_5+\frac{7}{8}a_2^3-\frac{3}{2}a_2a_4-\frac{13}{18}a_3^2+\frac{2}{3}a_6\Big]x^8,$$

$$g_3=\Big[-\frac{7}{2}a_1\gamma^2+\frac{1}{2}\gamma^3\Big(-\frac{4893}{32}a_1^3+\frac{1041}{8}a_1a_2-41a_3\Big)+\frac{1}{2}\gamma^4\Big(-\frac{4\,276\,013}{1024}a_1^5$$

$$+\frac{26\,495\,613}{256}a_1^3a_2-\frac{124\,273}{32}a_1^2a_3-\frac{157\,037}{64}a_1a_2^2+\frac{4451}{4}a_1a_4+\frac{7917}{8}a_2a_3$$

$$-276a_5\Big)\Big]+\Big[-\frac{3}{2}\gamma+\frac{9}{16}\gamma^2\Big(-\frac{23}{4}a_1^2+11a_2\Big)+\frac{3}{16}\gamma^3\Big(-\frac{5201}{128}a_1^4+\frac{15\,669}{16}a_1^2a_2$$

$$-\frac{1119}{2}a_1a_3-\frac{2601}{8}a_2^2+225a_4\Big)+\frac{1}{64}\gamma^4\Big(\frac{50\,564\,555}{1024}a_1^6+\frac{28\,420\,011}{128}a_1^4a_2$$

$$-\frac{250\,029}{32}a_1^3a_3-\frac{6\,520\,077}{16}a_1^2a_2^2+\frac{2\,281\,917}{16}a_1^2a_4+\frac{2\,455\,011}{8}a_1a_2a_3$$

$$-\frac{135\,441}{2}a_1a_5+\frac{803\,061}{16}a_2^3-\frac{64\,425}{4}a_2a_4-\frac{160\,635}{4}a_3^2+20\,115a_6\Big)\Big]x$$

$$+\Big[\frac{39}{4}a_1\gamma+\frac{3}{2}\gamma^2\Big(\frac{7997}{64}a_1^3-\frac{1689}{16}a_1a_2+40a_3\Big)+\frac{3}{2}\gamma^2\Big(\frac{6\,785\,537}{2048}a_1^5$$

$$-\frac{1\,628\,133}{256}a_1^3a_2+\frac{103\,273}{32}a_1^2a_3+\frac{245\,209}{128}a_1a_2^2-\frac{15\,317}{16}a_1a_4$$

$$-\frac{3429}{4}a_2a_3+273a_5\Big)\Big]x^2+x^3+\Big[-\frac{3}{2}a_1+\frac{3}{4}\gamma\Big(-\frac{77}{4}a_1^3+19a_1a_2$$

$$-13a_3\Big)+\frac{3}{2}\gamma^2\Big(-\frac{415}{2}a_1^5+\frac{12\,829}{32}a_1^3a_2-\frac{17\,125}{64}a_1^2a_3-\frac{1121}{8}a_1a_2^2$$

$$+\frac{815}{8}a_1a_4+\frac{1453}{16}a_2a_3-45a_5\Big)\Big]x^4+\Big[\frac{3}{4}\Big(\frac{9}{4}a_1^2-a_2\Big)+\frac{3}{8}\gamma\Big(75a_1^4$$

$$-\frac{477}{4}a_1^2a_2+\frac{259}{4}a_1a_3+13a_2^2-\frac{29}{2}a_4\Big)+\frac{1}{4}\gamma^2\Big(\frac{2\,829\,237}{1024}a_1^6-\frac{19\,582\,657}{2048}a_1^4a_2$$

$$+\frac{1\,089\,561}{256}a_1^3a_3+\frac{611\,349}{128}a_1^2a_2^2-\frac{4\,443\,513}{640}a_1^2a_4-\frac{2\,106\,957}{640}a_1a_2a_3$$

$$+\frac{20\,823}{40}a_1a_5-\frac{34\,857}{128}a_2^3+\frac{26\,019}{64}a_2a_4+\frac{1407}{4}a_3^2-\frac{195}{2}a_6\Big)\Big]x^5$$

$$+\frac{1}{2}\Big(-\frac{55}{16}a_1^3+\frac{15}{4}a_1a_2-a_3\Big)+\frac{3}{2}\gamma\Big(-\frac{3397}{128}a_1^5+\frac{1959}{32}a_1^3a_3-\frac{1035}{32}a_1^2a_3$$

$$-\frac{89}{4}a_1a_2^2+\frac{809}{80}a_1a_4+\frac{54}{5}a_2a_3-\frac{27}{10}a_5\Big)\Big]x^6+\Big[\frac{3}{8}\Big(\frac{143}{32}a_1^4-\frac{33}{4}a_1^2a_2$$

Table I. *(cont.)*

$$\Psi_v(x) = g_v(x) e^{\left(-\frac{1}{2}\int_0^x \gamma(x')dx'\right)}$$

$$+\frac{7}{2}a_1a_3+\frac{3}{2}a_2^2-a_4\Big)+\frac{1}{8}\gamma\Big(\frac{418\,065}{1024}a_1^6-\frac{672\,481}{512}a_1^4a_2+\frac{5439}{8}a_1^3a_3$$

$$+\frac{13\,689}{16}a_1^2a_2^2-\frac{19\,887}{16}a_1^2a_4-\frac{96\,129}{160}a_1a_2a_3+\frac{891}{10}a_1a_5-\frac{2091}{32}a_2^3$$

$$+\frac{1455}{16}a_2a_4+\frac{141}{2}a_3^2-18a_6\Big)\Big]x^7+\frac{3}{2}\Big[-\frac{273}{256}a_1^5+\frac{91}{32}a_1^3a_2-\frac{3}{2}a_1^2a_3$$

$$-\frac{21}{16}a_1a_2^2+\frac{27}{40}a_1a_4+\frac{11}{40}a_2a_3-\frac{1}{5}a_5\Big]x^8+\frac{1}{12}\Big[\frac{20\,589}{1024}a_1^6-\frac{4095}{64}a_1^4a_2$$

$$+\frac{2467}{64}a_1^3a_3+\frac{819}{16}a_1^2a_2^2-\frac{2931}{160}a_1^2a_4-\frac{2853}{80}a_1a_2a_3+\frac{99}{10}a_1a_5-\frac{21}{5}a_2^3$$

$$+\frac{63}{8}a_2a_4+\frac{15}{4}a_3^2-3a_6\Big]x^9,$$

$$g_4=\Big[\frac{3}{4}\gamma^2+\frac{1}{8}\gamma^3\Big(\frac{173}{4}a_1^2-63a_2\Big)+\frac{1}{8}\gamma^4\Big(\frac{40\,403}{256}a_1^4-\frac{95\,343}{32}a_1^2a_2+\frac{11\,621}{8}a_1a_3$$

$$+\frac{15\,291}{16}a_2^2-\frac{2115}{4}a_4\Big)+\frac{1}{2048}\Big(-\frac{5\,253\,050\,455}{64}a_1^6-\frac{2\,000\,577\,005}{8}a_1^4a_2$$

$$+\frac{2\,702\,306\,771}{48}a_1^3a_3+\frac{4\,993\,552\,461}{32}a_1^2a_2^2-\frac{316\,593\,423}{8}a_1^2a_4$$

$$-\frac{416\,252\,787}{4}a_1a_2a_3+\frac{29\,958\,439}{4}a_1a_5-\frac{157\,183\,275}{8}a_2^3+\frac{35\,592\,705}{2}a_2a_4$$

$$+\frac{12\,012\,615}{4}a_3^2-471\,861a_6\Big)\Big]+\Big[-20a_1\gamma^2+3\gamma^3\Big(-\frac{547}{2}a_1^3+172a_1a_2$$

$$-50a_3\Big)+\gamma^4\Big(-\frac{2\,445\,197}{64}a_1^5+\frac{93\,291}{2}a_1^3a_2-\frac{831\,239}{48}a_1^2a_3-\frac{51\,571}{4}a_1a_2^2$$

$$+5617a_1a_4+849a_2a_3-1248a_5\Big)\Big]x+\Big[-3\gamma+\frac{1}{4}\gamma^2\Big(-\frac{281}{4}a_1^2+81a_2\Big)$$

$$+\frac{1}{4}\gamma^3\Big(-\frac{53\,493}{64}a_1^4+\frac{33\,867}{8}a_1^2a_2-\frac{8221}{4}a_1a_3-\frac{4545}{4}a_2^2+\frac{1395}{2}a_4\Big)$$

$$+\frac{1}{4}\gamma^4\Big(\frac{5\,813\,067\,473}{32\,768}a_1^6+\frac{3\,597\,369\,567}{8192}a_1^4a_2-\frac{292\,322\,621}{3072}a_1^3a_3$$

$$-\frac{544\,217\,931}{2048}a_1^2a_2^2+\frac{35\,555\,553}{512}a_1^2a_4+\frac{45\,190\,089}{256}a_1a_2a_3$$

$$-\frac{3\,402\,815}{128}a_1a_5+\frac{16\,592\,829}{512}a_2^3-\frac{3\,620\,205}{128}a_2a_4-\frac{1\,119\,045}{256}a_3^2$$

$$+\frac{42\,831}{64}a_6\Big)\Big]x^2+\Big[19a_1\gamma+\gamma^2\Big(\frac{11\,061}{16}a_1^3-\frac{1645}{4}a_1a_2+148a_3\Big)$$

$$+\frac{1}{2}\gamma^3\Big(\frac{8\,044\,187}{128}a_1^5-\frac{1\,394\,729}{16}a_1^3a_2+\frac{492\,913}{8}a_1^2a_3-\frac{38\,079}{4}a_1a_4$$

Table I. *(cont.)*

$$\Psi_v(x) = g_v(x) e^{\left(-\frac{1}{2}\int_0^x y(x')dx'\right)}$$

$$+\frac{154\,359}{8}a_1a_2^2-225a_2a_3+2484a_5\Big)\Big]x^3+x^4+\Big[-2a_1+3\gamma\Big(-\frac{25}{2}a_1^3$$

$$+6a_1a_2-5a_3\Big)+\frac{1}{2}\gamma^2\Big(-\frac{47\,045}{16}a_1^5+\frac{6401}{2}a_1^3a_2-\frac{33\,789}{8}a_1^2a_3-525a_1a_2^2$$

$$+\frac{2592}{5}a_1a_4-\frac{1803}{5}a_2a_3-\frac{1248}{5}a_5\Big)\Big]x^5+\Big[\Big(\frac{11}{4}a_1^2-a_2\Big)+\frac{1}{4}\gamma\Big(\frac{1297}{4}a_1^4$$

$$-343a_1^2a_2+\frac{502}{3}a_1a_3+32a_2^2-32a_4\Big)+\frac{1}{4}\gamma^2\Big(\frac{47\,139\,027}{4096}a_1^6-\frac{12\,010\,443}{1024}a_1^4a_2$$

$$+\frac{5\,179\,499}{384}a_1^3a_3+\frac{1\,014\,001}{256}a_1^2a_2^2-\frac{656\,091}{320}a_1^2a_4-\frac{3\,606\,619}{160}a_1a_2a_3$$

$$+\frac{3949}{5}a_1a_5+\frac{14\,511}{64}a_2^3-\frac{9063}{16}a_2a_4+\frac{11\,869}{3}a_3^2+174a_6\Big)\Big]x^6$$

$$+\Big[\Big(-\frac{13}{4}a_1^3+3a_1a_2-\frac{2}{3}a_3\Big)+\gamma\Big(-\frac{3983}{32}a_1^5+\frac{435}{2}a_1^3a_2-\frac{299}{2}a_1^2a_3$$

$$-\frac{121}{2}a_1a_2^2+\frac{121}{5}a_1a_4+\frac{146}{5}a_2a_3-\frac{29}{5}a_5\Big)\Big]x^7+\Big[\frac{1}{8}\Big(\frac{455}{16}a_1^4-\frac{91}{2}a_1^2a_2$$

$$+\frac{50}{3}a_1a_3+7a_2^2-4a_4\Big)+\frac{1}{4}\gamma\Big(\frac{42\,275}{64}a_1^6-\frac{847\,295}{512}a_1^4a_2+\frac{7913}{8}a_1^3a_3$$

$$+\frac{58\,435}{64}a_1^2a_2^2-\frac{10\,461}{40}a_1^2a_4-\frac{32\,887}{16}a_1a_2a_3+\frac{187}{10}a_1a_5-\frac{1755}{32}a_2^3$$

$$+\frac{357}{8}a_2a_4+\frac{609}{2}a_3^2-13a_6\Big)\Big]x^8+\Big[-\frac{119}{16}a_1^5+\frac{35}{4}a_1^3a_2-\frac{49}{12}a_1^2a_3$$

$$-\frac{7}{2}a_1a_2^2+\frac{8}{9}a_1a_4+\frac{19}{15}a_2a_3-\frac{2}{5}a_5\Big]x^9+\frac{1}{12}\Big[\frac{2907}{64}a_1^6-\frac{2295}{16}a_1^4a_2$$

$$+\frac{155}{2}a_1^3a_3+\frac{219}{2}a_1^2a_2^2-\frac{192}{5}a_1^2a_4-\frac{312}{5}a_1a_2a_3+\frac{81}{10}a_1a_5-9a_2^3$$

$$+12a_2a_4+\frac{17}{3}a_3^2-4a_6\Big]x^{10},$$

$$g_5=\Big[\frac{55}{4}a_1\gamma^3+\frac{1}{4}\gamma^4\Big(\frac{33\,563}{8}a_1^3-\frac{4203}{2}a_1a_2+493a_3\Big)+\frac{1}{4}\gamma^5\Big(\frac{380\,962\,101}{248}a_1^5$$

$$-\frac{41\,794\,505}{128}a_1^3a_2+\frac{14\,337\,961}{192}a_1^2a_3+\frac{2\,011\,387}{32}a_1a_2^2-\frac{1\,476\,189}{64}a_1a_4$$

$$-\frac{126\,459}{4}a_2a_3+79a_5\Big)\Big]+\Big[\frac{15}{4}\gamma^2+\frac{5}{16}\gamma^3\Big(\frac{773}{4}a_1^2-189a_2\Big)$$

$$+\frac{5}{32}\gamma^4\Big(\frac{1\,944\,325}{256}a_1^4-\frac{119\,013}{4}a_1^2a_2+\frac{96\,557}{8}a_1a_3+7857a_2^2-\frac{15\,255}{4}a_4\Big)$$

$$+\frac{1}{64}\gamma^5\Big(\frac{12\,894\,222\,855}{8192}a_1^6-\frac{33\,328\,033\,385}{2048}a_1^4a_2+\frac{4\,427\,525\,651}{256}a_1^3a_3$$

Table I. *(cont.)*

$$\Psi_v(x) = g_v(x) e^{\left(-\frac{1}{2}\int_0^x \gamma(x')dx'\right)}$$

$$+\frac{4039414575}{256}a_1^2a_2^2-\frac{501240515}{128}a_1^2a_4-\frac{86062455}{8}a_1a_2a_3+\frac{18485155}{4}a_1a_5$$

$$-1851415a_2^3+\frac{14881725}{8}a_2a_4+\frac{6842775}{8}a_3^2-\frac{802575}{2}a_6\Bigg)\Bigg]x$$

$$+\Bigg[-\frac{535}{8}a_1\gamma^2+\frac{5}{2}\gamma^3\left(-\frac{123519}{64}a_1^3+\frac{14607}{16}a_1a_2-245a_3\right)+\frac{5}{2}\gamma^4\Bigg(-\frac{320944143}{2048}a_1^5$$

$$+\frac{35991215}{256}a_1^3a_2-\frac{27292565}{768}a_1^2a_3-\frac{3251955}{128}a_1a_2^2+\frac{1200525}{128}a_1a_4$$

$$+\frac{117333}{8}a_2a_3-35a_5\Bigg)\Bigg]x^2+\Bigg[-5\gamma+\frac{15}{16}\gamma^2\left(\frac{29}{4}a_1^2+55a_2\right)+\frac{5}{32}\gamma^3\Bigg(-\frac{242915}{16}a_1^4$$

$$+\frac{29213}{1}a_1^2a_2-\frac{23537}{2}a_1a_3-6291a_2^2+3575a_4\Bigg)+\frac{5}{64}\gamma^4\Bigg(-\frac{169667077}{128}a_1^6$$

$$+\frac{509359945}{128}a_1^4a_2-\frac{373851779}{192}a_1^3a_3-\frac{45591195}{16}a_1^2a_2^2+\frac{27798823}{32}a_1^2a_4$$

$$+\frac{33983433}{16}a_1a_2a_3-\frac{616047}{2}a_1a_5+\frac{2264229}{8}a_2^3-\frac{2439135}{8}a_2a_4$$

$$-\frac{608085}{4}a_3^2+71325a_6\Bigg)\Bigg]x^3+\Bigg[\frac{65}{2}a_1\gamma+\frac{5}{8}\gamma^2\left(\frac{53643}{16}a_1^3-\frac{5735}{4}a_1a_2\right.$$

$$\left.+487a_3\right)+\frac{5}{8}\gamma^3\Bigg(\frac{17237679}{64}a_1^5-\frac{6901323}{32}a_1^3a_2+\frac{847131}{16}a_1^2a_3$$

$$+\frac{69069}{2}a_1a_2^2-\frac{59181}{4}a_1a_4-\frac{103445}{4}a_2a_3+61a_5\Bigg)\Bigg]x^4+x^5$$

$$+\Bigg[-\frac{5}{2}a_1+\frac{5}{2}\gamma\left(-\frac{283}{8}a_1^3+\frac{15}{2}a_1a_2-\frac{25}{3}a_3\right)+\frac{5}{8}\gamma^2\Bigg(-\frac{685947}{64}a_1^5+\frac{38615}{8}a_1^3a_2$$

$$-\frac{61969}{48}a_1^2a_3-\frac{867}{4}a_1a_2^2+\frac{1157}{2}a_1a_4+\frac{4171}{4}a_2a_3-327a_5\Bigg)\Bigg]x^6$$

$$+\Bigg[\frac{1}{4}\left(\frac{65}{4}a_1^2-5a_2\right)+\frac{5}{4}\gamma\left(\frac{339}{2}a_1^4-\frac{239}{2}a_1^2a_2+\frac{613}{12}a_1a_3+10a_2^2-\frac{17}{2}a_4\right)$$

$$+\frac{5}{8}\gamma^2\Bigg(\frac{8185091}{2048}a_1^6-\frac{9001337}{512}a_1^4a_2+\frac{620057}{96}a_1^3a_3+\frac{1015369}{128}a_1^2a_2^2$$

$$-\frac{81311}{32}a_1^2a_4-4101a_1a_2a_3+\frac{1281}{2}a_1a_5-\frac{10689}{32}a_2^3+441a_2a_4$$

$$+\frac{4627}{12}a_3^2-121a_6\Bigg)\Bigg]x^7+\Bigg[\frac{5}{6}\left(-\frac{105}{16}a_1^3+\frac{21}{4}a_1a_2-a_3\right)+\frac{5}{2}\gamma\Bigg(-141a_1^5$$

$$+\frac{1407}{8}a_1^3a_2-\frac{1183}{16}a_1^2a_3-\frac{79}{2}a_1a_2^2+\frac{109}{8}a_1a_4+19a_2a_3-3a_5\Bigg)\Bigg]x^8+\Bigg[\frac{1}{8}\Bigg(\frac{425}{8}a_1^4$$

$$-75a_1^2a_2+\frac{145}{6}a_1a_3+10a_2^2-5a_4\Bigg)+\frac{5}{8}\gamma\Bigg(\frac{5098331}{2048}a_1^6-\frac{394147}{256}a_1^4a_2$$

Table I. *(cont.)*

$$\Psi_v(x) = g_v(x) e^{\left(-\frac{1}{2}\int_0^x y(x')dx'\right)}$$

$$+\frac{200\,077}{288}a_1^3a_3+\frac{21\,887}{32}a_1^2a_2^2-\frac{12\,259}{64}a_1^2a_4-\frac{3151}{8}a_1a_2a_3+\frac{75}{2}a_1a_5$$
$$-\frac{307}{8}a_2^3+47a_2a_4+\frac{383}{9}a_3^2-\frac{20}{3}a_6\Big)\Big]x^9+\Big[-\frac{969}{128}a_1^5+\frac{225}{16}a_1^3a_2$$
$$-\frac{20}{3}a_1^2a_3-\frac{45}{8}a_1a_2^2+\frac{37}{16}a_1a_4+\frac{43}{24}a_2a_3-\frac{1}{2}a_5\Big]x^{10}+\frac{5}{4}\Big[\frac{847}{128}a_1^6$$
$$-\frac{4525}{256}a_1^4a_2+\frac{599}{64}a_1^3a_3+\frac{765}{64}a_1^2a_2^2-\frac{71}{16}a_1^2a_4-\frac{317}{48}a_1a_2a_3+\frac{3}{2}a_1a_5$$
$$-\frac{15}{16}a_2^3+\frac{9}{8}a_2a_4+\frac{19}{36}a_3^2-\frac{1}{3}a_6\Big]x^{11},$$

$$g_6=\Big[-\frac{15}{8}\gamma^3+\frac{1}{32}\gamma^4(-16\,795a_1^2+675a_2)\Big]+\Big[\frac{1}{128}\gamma^5\Big(\frac{13\,777\,893}{64}a_1^4-\frac{225\,249}{8}a_1^2a_2$$
$$-\frac{479\,273}{2}a_1a_3-\frac{65\,685}{4}a_2^2+34\,125a_4\Big)\Big]+\Big[\frac{1}{768}\gamma^6\Big(\frac{6\,189\,896\,435}{16}a_1^6$$
$$-\frac{2\,197\,915\,855}{4}a_1^4a_2+\frac{439\,304\,187}{1}a_1^3a_3-\frac{6\,697\,058\,937}{160}a_1^2a_2^2+\frac{89\,139\,665}{32}a_1^2a_4$$
$$+\frac{887\,497\,917}{40}a_1a_2a_3+\frac{30\,883\,671}{2}a_1a_5+\frac{30\,199\,185}{16}a_2^3-\frac{20\,342\,289}{8}a_2a_4$$
$$-\frac{20\,470\,575}{4}a_3^2+\frac{2\,532\,375}{1}a_6\Big)\Big]+\Big[105a_1\gamma^3+\gamma^4\frac{3}{4}\Big(\frac{70\,383}{8}a_1^3-\frac{6933}{2}a_1a_2$$
$$+743a_3\Big)+\frac{1}{10}\gamma^5\Big(\frac{8\,726\,079\,033}{512}a_1^5-\frac{6\,873\,222\,055}{256}a_1^3a_2+\frac{113\,638\,545}{16}a_1^2a_3$$
$$+\frac{73\,523\,769}{32}a_1a_2^2-\frac{26\,204\,675}{16}a_1a_4-\frac{7701}{4}a_2a_3-37\,440a_5\Big)\Big]x+\Big[-\frac{45}{4}\gamma^2$$
$$+\frac{1}{8}\gamma^3\Big(\frac{200\,175}{8}a_1^2-540a_2\Big)+\frac{1}{8}\gamma^4\Big(-\frac{104\,542\,257}{512}a_1^4+\frac{10\,027\,431}{64}a_1^2a_2$$
$$+\frac{1\,230\,087}{16}a_2a_3-\frac{169\,965}{32}a_2^2-\frac{60\,075}{8}a_4\Big)+\frac{1}{8}\gamma^5\Big(-\frac{5\,210\,329\,735}{256}a_1^6$$
$$+\frac{8\,396\,131\,625}{256}a_1^4a_2-\frac{8\,001\,322\,377}{256}a_1^3a_3+\frac{149\,825\,367}{256}a_1^2a_2^2+\frac{675\,286\,035}{512}a_1^2a_4$$
$$+\frac{177\,293\,229}{640}a_1a_2a_3-\frac{40\,146\,363}{32}a_1a_5+\frac{12\,106\,935}{256}a_2^3-\frac{14\,657\,811}{128}a_2a_4$$
$$+\frac{12\,265\,299}{64}a_3^2-\frac{1\,518\,075}{16}a_6\Big)\Big]x^2+\Big[-\frac{685}{4}a_1\gamma^2+\frac{5}{2}\gamma^3\Big(-\frac{131\,229}{16}a_1^3$$
$$+\frac{11\,991}{4}a_1a_2-740a_3\Big)+\frac{1}{6}\gamma^4\Big(-\frac{2\,156\,574\,295}{128}a_1^5+\frac{3\,378\,795\,505}{128}a_1^3a_2$$
$$-\frac{436\,710\,465}{64}a_1^2a_3-\frac{285\,455\,013}{128}a_1a_2^2+\frac{199\,676\,993}{128}a_1a_4+\frac{15\,333}{4}a_2a_3$$

Table I. *(cont.)*

$$\Psi_v(x) = g_v(x) e^{\left(-\frac{1}{2}\int_0^x \gamma(x')dx'\right)}$$

$$+37\,575a_5\Big)\Big]x^3+\Big[\frac{15}{2}\gamma+\frac{1}{4}\gamma^2\Big(-\frac{70\,125}{8}a_1^2+405a_2\Big)+\frac{1}{4}\gamma^3\Big(\frac{8\,086\,155}{64}a_1^4$$

$$-\frac{3\,063\,615}{32}a_1^2a_2-\frac{72\,945}{2}a_1a_3+\frac{7245}{8}a_2^2+\frac{20\,475}{4}a_4\Big)+\frac{1}{4}\gamma^4\Big(\frac{2\,692\,474\,295}{512}a_1^6$$

$$-\frac{1\,367\,332\,255}{128}a_1^4a_2+\frac{3\,003\,261\,755}{256}a_1^3a_3-\frac{34\,764\,663}{128}a_1^2a_2^2-\frac{353\,017\,953}{512}a_1^2a_4$$

$$+\frac{12\,915\,357}{64}a_1a_2a_3+\frac{4\,549\,905}{16}a_1a_5+\frac{815\,715}{32}a_2^3-\frac{80\,713}{128}a_2a_4-\frac{4\,236\,579}{32}a_3^2$$

$$+\frac{506\,475}{8}a_6\Big)\Big]x^4+\Big[51a_1\gamma+\frac{3}{2}\gamma^2\Big(\frac{14\,647}{4}a_1^3-1162a_1a_2+\frac{739}{2}a_3\Big)$$

$$+\frac{1}{2}\gamma^3\Big(\frac{384\,082\,383}{256}a_1^5-\frac{39\,167\,289}{16}a_1^3a_2+\frac{5\,105\,145}{8}a_1^2a_3+\frac{1\,374\,993}{8}a_1a_2^2$$

$$-143\,565a_1a_4+\frac{42\,405}{4}a_2a_3-3762a_5\Big)\Big]x^5+x^6+\Big[-3a_1+3\gamma\Big(-\frac{251}{4}a_1^3+5a_1a_2$$

$$-9a_3\Big)+\frac{1}{4}\gamma^2\Big(-\frac{9\,101\,193}{64}a_1^5+\frac{3\,501\,003}{16}a_1^3a_2-\frac{204\,819}{4}a_1^2a_3-\frac{110\,007}{8}a_1a_2^2$$

$$+\frac{27\,453}{2}a_1a_4-\frac{1356}{1}a_2a_3+351a_5\Big)\Big]x^7+\Big[\frac{1}{2}\Big(\frac{45}{4}a_1^2-3a_2\Big)+\frac{1}{8}\gamma\Big(\frac{256\,017}{64}a_1^4$$

$$-\frac{15\,737}{8}a_1^2a_2+\frac{1551}{2}a_1a_3+\frac{609}{4}a_2^2-105a_4\Big)+\frac{1}{8}\gamma^2\Big(\frac{5\,018\,699}{1024}a_1^6-\frac{1\,991\,991}{2}a_1^4a_2$$

$$+\frac{4\,256\,423}{16}a_1^3a_3+\frac{47\,087}{8}a_1^2a_2^2-\frac{1\,231\,377}{16}a_1^2a_4-\frac{6813}{1}a_1a_2a_3-\frac{1221}{4}a_1a_5$$

$$-\frac{55\,053}{8}a_2^3+495a_2a_4+\frac{56\,607}{4}a_3^2+\frac{345}{2}a_6\Big)\Big]x^8+\Big[\Big(-\frac{17}{2}a_1^3+6a_1a_2-a_3\Big)$$

$$+\gamma\Big(-\frac{97\,365}{96}a_1^5+\frac{54\,639}{48}a_1^3a_2-\frac{8979}{24}a_1^2a_3-\frac{10\,431}{48}a_1a_2^2+\frac{1143}{12}a_1a_4+\frac{189}{6}a_2a_3$$

$$+2a_5\Big)\Big]x^9+\Big[\frac{1}{8}\Big(\frac{2907}{32}a_1^4-\frac{459}{4}a_1^2a_2+33a_1a_3+\frac{27}{2}a_2^2-6a_4\Big)$$

$$+\frac{1}{8}\gamma\Big(\frac{7\,628\,583}{640}a_1^6-\frac{2\,578\,935}{128}a_1^4a_2+\frac{37\,524}{5}a_1^3a_3+\frac{561\,087}{80}a_1^2a_2^2-\frac{77\,193}{40}a_1^2a_4$$

$$-\frac{4821}{2}a_1a_2a_3+\frac{99}{2}a_1a_5-\frac{1539}{4}a_2^3+375a_2a_4+\frac{1287}{4}a_3^2+93a_6\Big)\Big]x^{10}$$

$$+\frac{1}{10}\Big[-\frac{17\,913}{128}a_1^5+\frac{4245}{16}a_1^3a_2-99a_1^2a_3-84a_1a_2^2+\frac{57}{2}a_2a_4\Big)\Big]x^{11}$$

$$+\frac{1}{4}\Big[\frac{167\,937}{2560}a_1^6-\frac{21\,569}{128}a_1^4a_2+\frac{6109}{80}a_1^3a_3+\frac{15\,653}{160}a_1^2a_2^2-\frac{1213}{40}a_1^2a_4$$

$$-\frac{161}{4}a_1a_2a_3+8a_1a_5-\frac{55}{8}a_2^3+\frac{15}{2}a_2a_4+\frac{7}{2}a_3^2-2a_6\Big]x^{12}.$$

Table II

SnO ($D^1\Pi - X^1\Sigma$)

Band	FC factors		r-centroids	
	R.K.R.	VI iteration	R.K.R. [nm]	VI iteration [nm]
(0, 0)	0.125	0.132	0.1889	0.1858
(0, 1)	0.275	0.265	0.1909	0.1937
(0, 2)	0.275	0.273	0.1957	0.1955
(0, 3)	0.187	0.188	0.1989	0.1987
(0, 4)	0.087	0.096	0.2022	0.2018
(0, 5)	0.246	0.259	0.1865	0.1863
(1, 1)	0.158	0.141	0.1902	0.1906
(1, 2)	0.0014	0.0015	0.1878	0.1919
(1, 3)	0.099	0.088	0.1966	0.1961
(1, 4)	0.202	0.192	0.1992	0.1993
(2, 0)	0.254	0.258	0.1843	0.1845
(2, 2)	0.128	0.121	0.1908	0.1906
(2, 3)	0.094	0.098	0.1942	0.1941

Acknowledgement

The author is grateful to Dr. V. M. Korwar for his invaluable help and guidance during this work.

References

1. R. M. Herman, R. H. Tipping and S. Short, J. Chem. Phys., *53*, 595, 1970.
2. R. H. Tipping and J. F. Ogilvie, Mol. Structure, *35*, 1, 1976.
3. P. Niay, Faculté des Sciences et Techniques de Lille, France, 1978, (private communication).
4. R. Rydberg, Z. Phys., *73*, 376, 1931; *80*, 514, 1933.
5. D. C. Patil and V. M. Korwar, Acta Phys. Hung., 44, 371, 1978.
6. J. L. Dunham, Phys. Rev., *41*, 713, 1932.

Acta Physica Hungarica 56 (1—4), pp 107—110 (1984)

DECAY OF CATHODOLUMINESCENCE FROM SiO_2 LAYERS*

A. FREY

Central Institute for Electron Physics
Academy of Sciences of the GDR
*1086 Berlin, GDR***

(Received 5 May 1983)

Cathodoluminescence steady state and decay measurements on SiO_2 glass and gate oxides were carried out.

The recorded spectra show luminescence bands at 1.9 eV, 2.7 eV and 4.3 eV. The bands at these energetic positions decay in very different time ranges.

The time dependence is not described by an exponential function with a single time constant.

The results are discussed on the basis of intrinsic defects in SiO_2.

Cathodoluminescence (CL) is one technique to investigate the nature of irradiation defects in gate oxides and can be applied to both thin film and bulk samples.

It is well known that irradiation of SiO_2 material with KeV electrons produces radiation induced defects which can reheal spontaneously or result in permanent damage [1]. Besides this luminescence radiation is produced.

In the UV/VIS range pure SiO_2 emits three characteristic CL bands at 4.2 eV, 2.7 eV and 1.9 eV shown in Fig. 1. For comparison the spectra are taken from dry thermal oxide (full line) and Suprasil (dashed line). The experimental details are described elsewhere [2].

At room temperature the three CL bands decay in very different time ranges [2]:

CL band	time range
4.2 eV	<250 ns
2.7 eV	≈ 4 ms
1.9 eV	≈ 5 μs

* This paper was presented at the School on Defect Complexes in Semiconductor Structures, Mátrafüred, Hungary, 1982.

** 1086 Berlin, Hausvogteiplatz 5—7

Within the limits of 5% the results agree for dry thermal oxide and Suprasil. From these findings it is concluded that luminescence emitted from radiation induced defects in thermal grown dry oxides and Suprasil glass can be compared.

The time dependence of the 2.7 eV CL following a 10 μs excitation pulse is given in Fig. 2. The decay consists of an initial fast part and bends over in a slower exponential function dependence with a time constant $\tau = 4.6$ ms, hence the duration of an excitation pulse is very much smaller than τ.

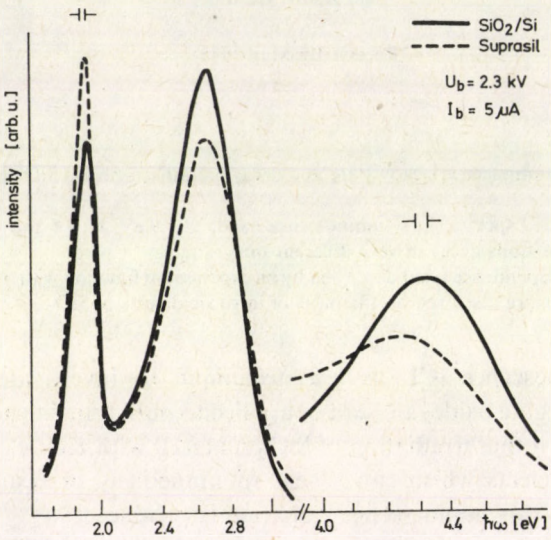

Fig. 1. Steady state cathodoluminescence of a SiO_2 layer (oxide thickness $d_{ox} = 168$ nm) and Suprasil. The energetic resolution is indicated by parallel bars. Note the different energy scales

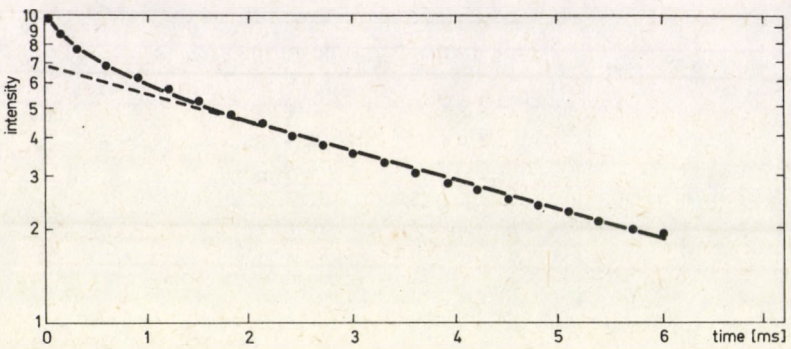

Fig. 2. Semilogarithmic plot of the 2.7 eV CL decay for a thermal grown oxide ($d_{ox} = 168$ nm). τ (dashed line) $= 4.6$ ms. Primary electron energy: 2.3 KeV

The assumption of a three level energetic system for a single metastable recombination level gives the time dependence $A\exp(-t/\tau_1)-B\exp(-t/\tau_2)$. This function does not fit the measured decay.

Now it is assumed that additional fast relaxing energetic systems exist which may interact with the 2.7 eV luminescence centres via multipolar forces and transfer energy directly. The theory for this energy transfer was developed by Förster [3] and by Dexter [4] for multipolar coupling.

Consider a configuration of 2.7 eV and a second kind of recombination centres (called energy donors and energy acceptors for brevity) distributed randomly throughout the material. The distance between acceptors should be very much greater than the distance between donors. In the case of weak dipole—dipole coupling and for direct transitions from donors to acceptors, the time dependence of luminescence is given by [5]

$$I(t)=I(0)\exp\{-t/\tau-b\cdot(t/\tau)^{1/2}\}, \qquad b=7.41\cdot N_a R_0^3. \tag{1}$$

N_a is the concentration of energy acceptors. R_0 represents the separation at which the probability for energy transfer between a donor—acceptor pair is equal to the intrinsic decay probability τ^{-1} of the donors without interaction effects.

Luminescence of this time dependence does not exhibit a simple exponential decay. At earlier times $t/\tau \ll 1$ the emission intensity is given by

$$I(t)\approx I_0\{1-b\cdot(t/\tau)^{1/2}\}. \tag{2}$$

As shown in Fig. 3 Eq. (2) makes a good fit of the fast initial decay of the 2.7 eV band supporting the proposed model. Candidates for energy acceptors are 1.9 eV luminescence centres because (i) the 1.9 eV band decays faster in three orders of magnitude than the 2.7 eV band; hence the 1.9 eV emission centres are well suited to serve as fast relaxing energy sinks for the 2.7 eV emission centres and (ii) in irradiated

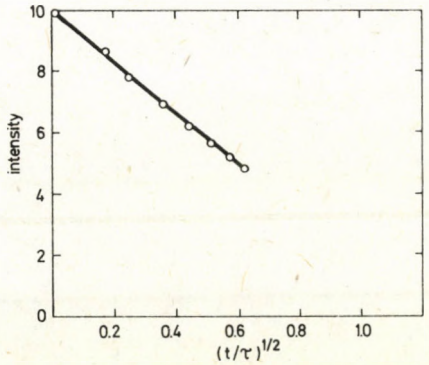

Fig. 3. Initial part of the 2.7 eV CL decay plotted over $(t/\tau)^{1/2}$, $t/\tau<0.4$

quartz glass the 1.9 eV emission can be excited with photons in the 2.5 eV region [6] which overlaps the relatively broad 2.7 eV band. Further support is provided by the fact that irradiated quartz glass excited in the 4...5 eV range at 77 K shows a broad emission at 2.9 eV and an emission at 1.9 eV [1].

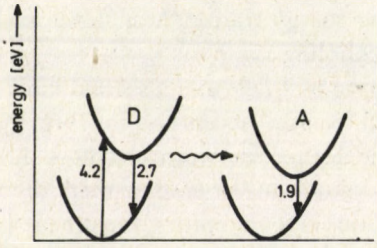

Fig. 4. Illustration of the proposed model in terms of configuration coordinate diagrams

Fig. 4 shows the proposed model of energy dissipation in terms of conventional configuration coordinate diagrams. The energy donors and energy acceptors are designated by *D* and *A*, respectively.

The model considered here does not take into account any migration of energy over many interatomic distances, but in principle this effect should be possible.

References

1. G. H. Sigel, Jr., J. Non-Cryst. Solids, *13*, 372, 1973/74.
2. A. Frey, Physik der Halbleiteroberfläche, *12*, 223, 1981.
3. T. Förster, Ann. Physik, *2*, 55, 1948; Naturforsch., *4a*, 321, 1949.
4. D. L. Dexter, J. Chem. Phys., *21*, 836, 1953.
5. M. Inokuti and F. Hirayama, J. Chem. Phys., *43*, 1978, 1965.
6. G. H. Sigel, Jr. and M. J. Marrone, J. Non-Cryst. Solids, *45*, 235, 1981.

Acta Physica Hungarica 56 (1—4), pp 111—118 (1984)

INVESTIGATIONS ON Al/Si INTERFACE*

P. GLASER and D. SAWICKA

Enterprise for Microelectronics, 1325 Budapest, Hungary

(Received 5 May 1983)

Aluminium and aluminium alloys are widely used as interconnecting materials in silicon integrated circuits. The processing technique includes vacuum deposition and—after patterning—heat treatment of the metal film. The heat treatment of aluminium metallization is accompanied by the dissolution of the underlying silicon into the metal and the consequent penetration of aluminium into the silicon. The dissolution process is highly nonuniform on the contact surface creating crystallographic etch pits, which can cause excessive leakage or even shorting of the $p-n$ junction. Furthermore, silicon precipitation in the contact windows that occurred on cooling down can cause increased contact resistance.

We intend to present surface analytical investigations and electrical measurements on the Al/Si interface in case of pure and silicon-alloyed aluminium metallization. The results show the effect of various postmetallization heat treatments on the Al/Si contact.

1. Introduction

One of the most important problems of the N-channel MOS device processing is that of the ohmic contacts connected with the defect structure of the Al/Si interface. This interface can be characterized—among others—by the contact resistance. We intend to report on the effect of metallization and sintering processes on the contact resistance.

2. Contact problems associated with aluminium metallization

Aluminium is the material most frequently used for ohmic contact in MOS integrated circuits. The processing technique includes vacuum deposition and—after patterning—the heat treatment of the metal film. The heat treatment is accompanied by the dissolution of the underlying silicon into the metal and subsequent penetration of aluminium into the silicon [1]. The Al—Si interdiffusion results in the so-called etch pits (Figs 1, 2), also in case of polycrystalline silicon underlayer (Fig. 3).

The etch pits are large but shallow on (111) oriented silicon wafers, however, they are deep in the (100) wafers. The etch pits may cause excessive leakage or even shorting of the $p-n$ junction.

* This paper was presented at the School on Defect Complexes in Semiconductor Structures, Mátrafüred, Hungary, 1982.

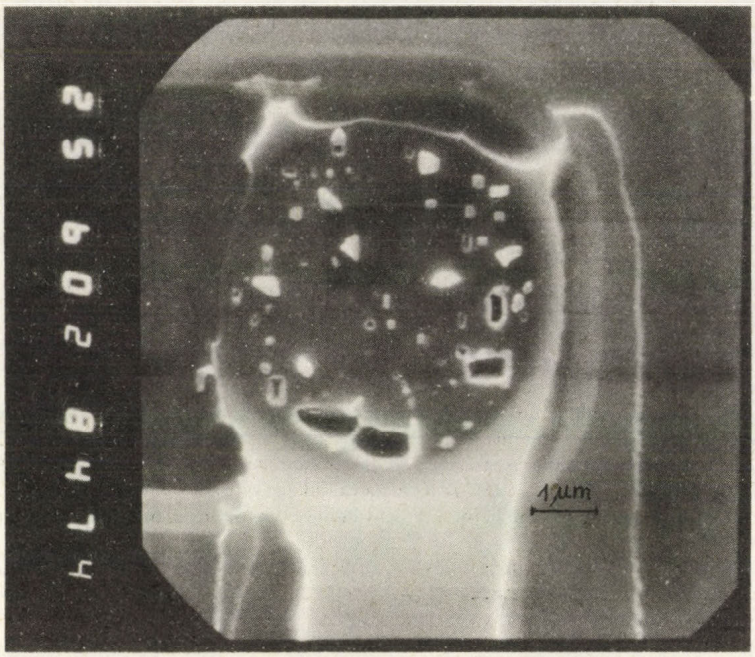

Fig. 1. Contact window on phosphorus diffused (100) monocrystalline silicon area after removal of the pure Al metallization

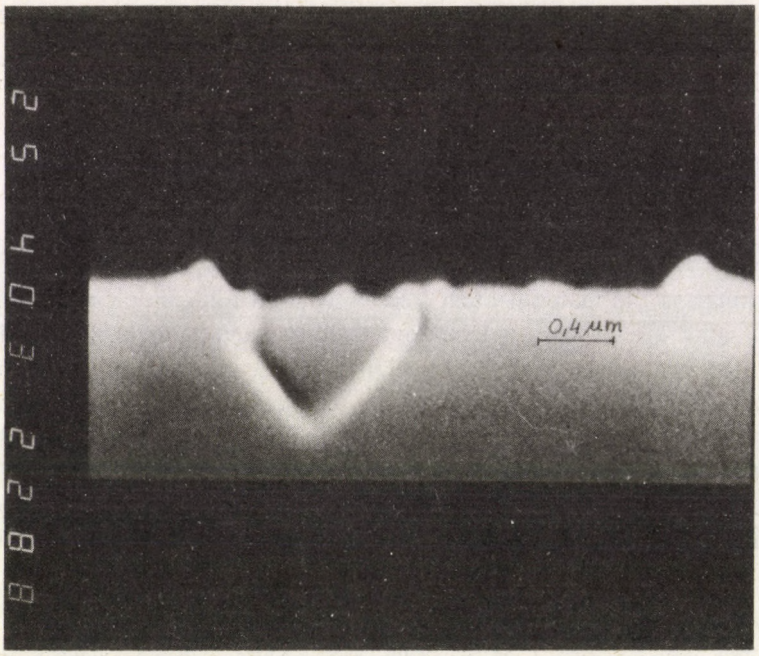

Fig. 2. Cross-section of an etch pit in Fig. 1

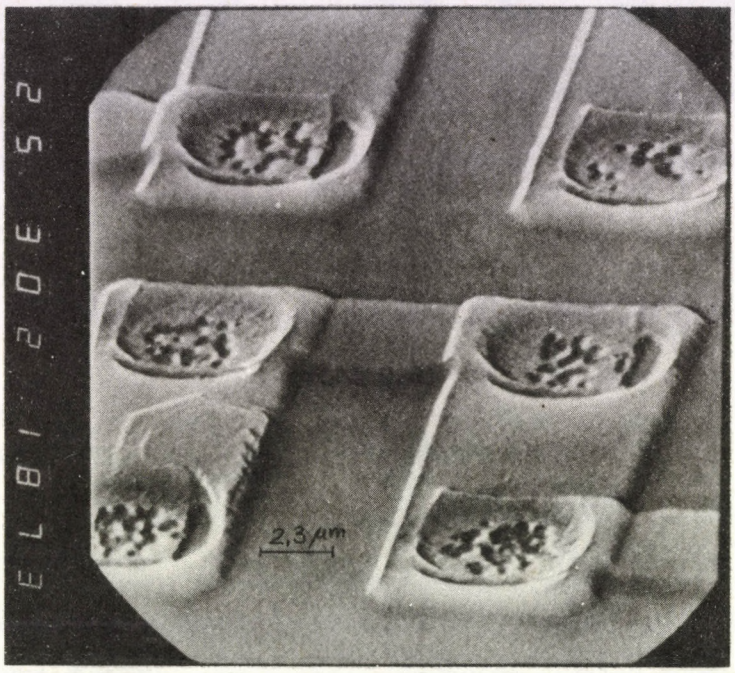

Fig. 3. Contact windows on polycrystalline silicon stripes after removal of the pure Al metallization

Furthermore, on cooling down an epitaxially regrown silicon layer saturated with aluminium develops in the contact windows. This *p*-type layer can modify the ohmic character of the contact and it increases the contact resistance.

These problems can be eliminated by using Si-alloyed Al metallization. The minimum Si-concentration of the film to prevent interdiffusion is about 0,9%, i.e. the solid solubility of silicon in aluminium at the sintering temperature [2]. The Si-concentration is limited by the film resistivity: over about 1,6% Si the film resistivity increases sharply [3], probably because of precipitates.

3. Preparation possibilities of AlSi films

(i) *Simultaneous evaporation of the pure materials from two electron beam evaporation sources.*

The film composition can be easily controlled by the evaporation rates over a wide range, and the method itself is compatible with the MOS technique.

(ii) *Sputtering of an AlSi alloy target*
The modern Penning sputtering sources (their well-known names are "Magnetron" or "S-gun") provide a sufficient rate. The film composition is determined by the target composition.

(iii) *In-situ saturation of the aluminium film with silicon by the annealing of a poly-Si/Al sandwich layer*
This method implies more problems than the others, therefore it is not widely used.

(iv) *Flash evaporation of AlSi alloy*
It is not suitable for MOS devices because of contaminations.

In our work we applied the first and the second metallization methods.

4. Experimental

The test vehicles were prepared with a Si-gate N-channel MOS process on 5–7 ohmcm (100) *p*-type silicon wafers. The thickness of the poly-Si layer was 600 nm, the concentration of phosphorus doping was 5×10^{20} cm^{-3}. The thickness of the PSG isolation layer was 1.10 μm with about 7% phosphorus.The area of contact windows was 5×5 μm^2. Metallization was carried out at about 100 °C wafer temperature. The film parameters are given in Table I.

Table I

Metal film parameters

Method	Film	Thickness [μm]	R_s [mohm/□]	Spec. resistivity [μohm/cm]
EB evaporation	Al	1.30	21.4	2.78
	AlSi	1.42	22.5	3.19
Penning* sputtering	Al	1.20	35.6	4.27
	AlSi	0.94	86.0	8.08

* Deposition of the sputtered films was performed in the Central Research Institute for Physics of the Hungarian Academy of Sciences.

The specific resistivity of the different films is quite different: the method of sputtering results in an increased resistivity, and so does the alloying.

The passivation glass made by CVD at 400 °C was 1.20 μm thick. The various sintering processes were carried out in a $N_2 + H_2$ (about 20%) atmosphere at 450–500 °C for 20–60–120 min, respectively.

5. Results and discussion

The contact resistances were calculated from four-point probe measurements [4].

5.1. Contact resistance of Al and AlSi to monocrystalline silicon ($R_s^{diff} = 25 - 30$ ohm/□) (Fig. 4)

The contact resistance (R_c) of AlSi metallization is always higher than that of the pure Al before sintering. It is due to the higher film resistivity.

R_c drops after 20 min heat treatment in every case. Pure Al still gives lower resistance, however, the difference between pure and Si-alloyed Al is decreased. This period of resistance changes can be explained by a chemical reaction: Al reduces the native SiO_2 which is always present on the surface of silicon.

The reduction is followed by dissolution of the underlying Si in the Al film, then by Al-diffusion into the silicon wafer. Thus, the etch pits are developed.

The critical step is the dissolution which can be eliminated by presaturation of Al with Si from an outer source. Its effect is shown in Fig. 5: after removal of the AlSi metallization there are no etch pits present in the contact window.

After longer heat treatment we measured higher contact resistances for pure Al, but the AlSi metallization hardly changed. The difference was much remarkable at 500 °C sintering. The reason of this phenomenon may be the formation of the *p*-type (Al-doped) epitaxial silicon layer mentioned above.

These processes are complicated by the simultaneous recrystallization of the metal films.

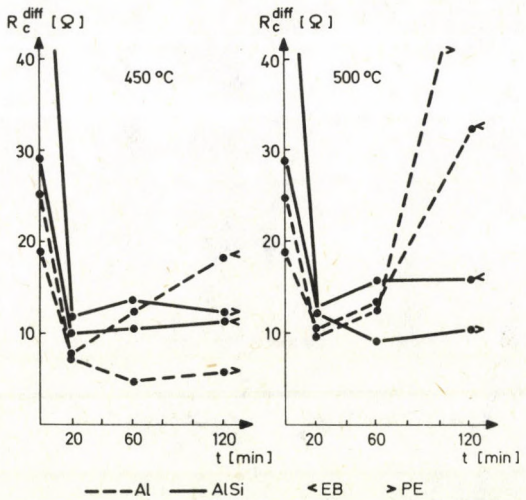

Fig. 4. Contact resistance (R_c^{diff}) of Al and AlSi metallization to monocrystalline silicon as function of the sintering time

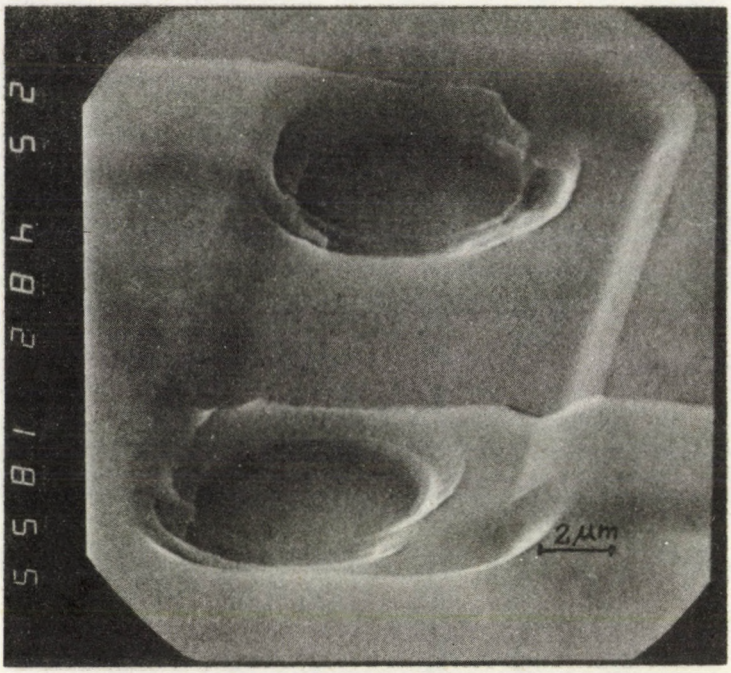

Fig. 5. Contact window after removal of the AlSi metallization from diffused area

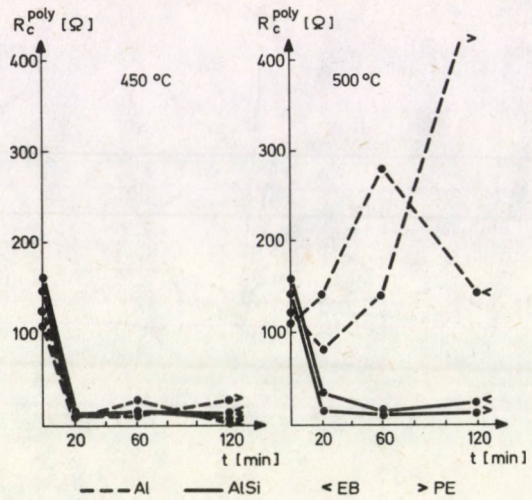

Fig. 6. Contact resistance of Al and AlSi metallization to polycrystalline silicon (R_c^{poly}) as function of the sintering time

5.2. Contact resistance of Al and AlSi to polycrystalline silicon ($R_S^{poly} = 70 - 80$ ohm/□) (*Fig. 6*)

The curves are similar to the former ones, thus the processes taking place may be similar as well. Fig. 7 shows the etch pit free contact window on poly-Si after removal of the AlSi metallization.

The initial structure of the poly-Si layer and its recrystallization has an important role, but opinions differ concerning the details [5].

The difference in contact resistance of evaporated and sputtered pure Al might be explained by the different crystal structure of these films.

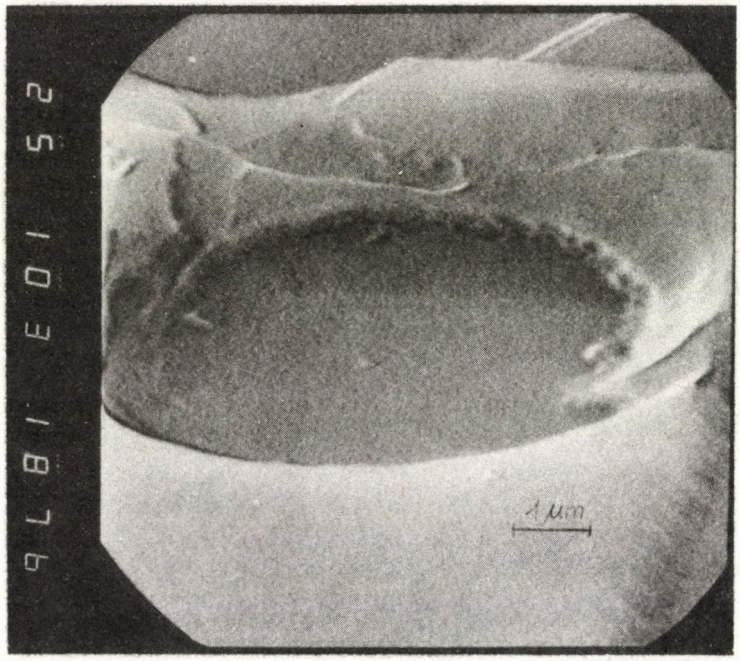

Fig. 7. Contact window after removal of the AlSi metallization from poly-Si

6. Conclusions

We can state that

(i) AlSi metallization eliminates the formation of etch pits;
(ii) AlSi metallization tolerates long heat treatment even at elevated temperatures;
(iii) in most cases there is no significant difference between EB evaporation and Penning sputtering (from the point of view of the contact resistance).

We wish to express our acknowledgement to our Colleagues for their help both in the experimental work and in the discussion.

References

1. Thin Films—Interdiffusion and Reactions (ed. J. M. Poate et al), John Wiley and Sons, Inc., New York, 1978.
2. M. Hansen, Constitution of Binary Alloys, McGraw-Hill Book Company, New York, 1958.
3. P. Glaser and D. Sawicka, Proc. 3rd Microelectronics Conference of the Socialist Countries, p. 51, Siófok (Hungary), 5–7th May, 1982.
4. H. M. Naguib and L. H. Hobbs, J. Electrochem. Soc., *124*, 537, 1977.
5. R. S. Nowicki and A. J. Learn, Thin Solid Films, *67*, 385, 1980.

Acta Physica Hungarica 56 (1—4), pp 119—130 (1984)

DISLOCATIONS IN SEMICONDUCTOR MATERIALS AND DEVICES*

T. FIGIELSKI

Institute of Physics, Polish Academy of Sciences
02-668 Warsaw, Poland

(Received 5 May 1983)

The possible influence of dislocations on device operation is discussed. The first part deals with the properties of dislocations themselves (development, electronic structure), then the effects of the recombination and trapping are described. In the last part dislocations in concrete devices (silicon and optoelectronic devices) are examined.

The problem of dislocations in semiconductor materials and devices is as old as semiconductor electronics itself. Dislocations were very early recognized as important faults of the active materials used for device fabrication. Consequently, dislocations in those materials began to be intensively studied and this fact, in turn, became extremely stimulating in the development of the physics of dislocation itself.

The present paper demonstrates in what ways dislocations may affect the device operation. The first part of this paper deals with the properties of dislocations themselves. It is perhaps surprising that after many years of intensive studies we are not able to answer definitely such fundamental question as: what is the electronic structure of dislocation in a given material? It is a consequence of the fact that the problem of dislocations in semiconductor crystals turned out to be much more complicated than anybody suspected in the early fifties.

1. Dislocations in tetrahedrally coordinated semiconductors

Dislocation is characterized by its Burgers vector that is invariant for a whole dislocation line and is conserved during the dislocation motion. For a curvilinear dislocation the angle α between the dislocation line (axis) and its Burgers vector is varying and, in consequence, the character of dislocation may change from a screw one ($\alpha = 0°$) to the edge one ($\alpha = 90°$). Under the shear stress a dislocation is able to move conservatively by gliding on its glide plane, i.e., on the plane containing both the dislocation line and its Burgers vector. The dislocation can leave its original glide plane

* This paper was presented al the School on Defect Complexes in Semiconductor Structures Mátrafüred, Hungary, 1982.

by nonconservative motion, or climb, in which interstitials or vacancies are being absorbed or emitted at the dislocation core. The segment of dislocation that leads out a dislocation line from one glide plane to another is called a jog. Thus jogs are the sites on the dislocation line where point defects are easily accepted or emitted during the climb motion.

In diamond- and sphalerite-type structures the privileged glide occurs on the $\{111\}$ crystallographic planes. As those structures are composed of two sublattices, of the f.c.c. type, displaced by the vector $\langle 111\rangle/4$ (in lattice constant units), the glide may occur either between closely spaced or between widely spaced atomic $\{111\}$ planes (Fig. 1). Although in the first case the number of covalent bonds which have to be broken to allow for shearing parallel to the $\{111\}$ plane is three times greater than in the second case, the first one is actually realized in nature. Dislocations in that case are called to belong to the glide set. The glide set dislocation lowers its elastic energy by splitting into two Shockley partial dislocations, and it is connected with the creation of a stacking fault ribbon between them. Two main types of dislocations, occurring in the structures under consideration, dissociate as follows: screw dislocation splits into two 30° partials, and 60° dislocation into a 30° and edge partial [1] (Fig. 2).

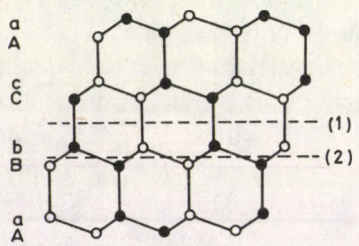

Fig. 1. Projection of diamond (sphalerite) type structure on the $\{110\}$ plane. Black balls correspond to atom positions shifted by $\langle 110\rangle/4$ with respect to white ones. Two possible shearing planes are shown by dotted lines: (1) shuffle set, (2) glide set

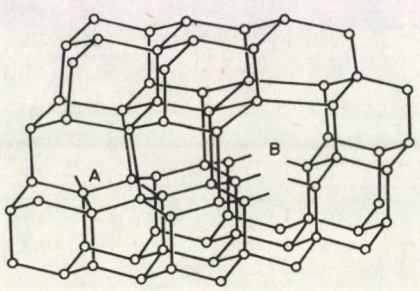

Fig. 2. Split glide-set 60°-dislocation. (1) 30°-partial, (B) 90°-partial

2. Electronic structure of dislocations

Semiconductor people wish to know, first of all, what electron states are created by various types of dislocations present in a crystal. For a long time the dangling bonds, which were expected to exist in the core of edge-component dislocation, were assumed to be responsible for dislocation-induced energy levels lying inside the band gap and, consequently, for the electrical activity of dislocations. This assumption had to be altered in view of recent investigations. The dominant types of dislocations occurring in the crystals under consideration are 30° and edge partials. These kinds of partials nominally contain the dangling bonds in their cores. The cores, however, can be easily reconstructed in a way that no dangling bonds remain there. Actually, only a small fraction of all topologically possible dangling bonds in plastically deformed silicon is detected by the EPR [2].

In a series of recent works, done by Marklund and Jones [3, 4, 5], the electron energies of split glide-set dislocations in Si and GaAs were calculated by tight binding calculation. The one-electron energies of partial dislocations were represented by the eigenvalue spectrum of a large periodic cluster of atoms treated in the LCAO

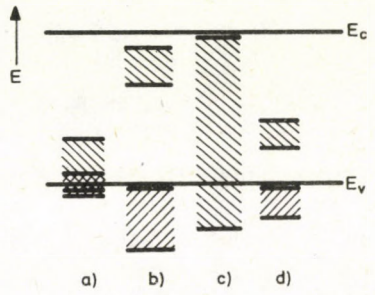

Fig. 3. Energy bands connected with partial dislocations in diamond (sphalerite) structure (a) not reconstructed 90°-partial, (b) partially reconstructed 90°-partial, (c) not reconstructed 30°-partial, (d) partially reconstructed 30°-partial [3]

approximation. Electron states, localized in the heavily distorted core region of the dislocation, are produced even in the case when, after reconstruction, no dangling bonds exist there. These states form narrow one-dimensional energy bands with a k-vector parallel to the dislocation axis; the position and width of these bands depend critically on the core atom configuration (Fig. 3). The core reconstruction is found to be energetically favourable and it usually leads to an occupied band separated from an empty one; at least one of them enters the energy gap of the semiconductor. The results obtained so far show that a selfconsistent calculation, in which both electronic and atomic configurations are simultaneously taken into account, is needed to obtain more realistic data. Moreover, such calculation has to get beyond the one-electron approximation so as in narrow energy bands correlation effects between electrons become important.

Unfortunately, experiments also do not allow for unambiguous localization of dislocation-induced states in the energy scale. One can find in literature a great variety of divergent results concerning these states. The large discrepancy in the results obtained by different authors and different methods can be attributed mainly to the fact that dislocations are always accompanied by interfering point defects. Point defects are created in a considerable amount during the plastic deformation when preparing the samples; the number of stable defects is the higher, the lower is the temperature of deformation. Nevertheless, it follows from the photoconductivity [6] and DLTS [7] measurements performed on plastically deformed silicon that the Fermi level is locally pinned at some dominant trap levels lying at ~ 0.6 eV below the conduction band edge. In the opinion of the present author this value is indicative of the localization of dislocation-induced states in Si. The situation in GaAs is much less clear than that in Si. Two pinning energies were found by photoconductivity in plastically deformed GaAs [8] but those just coincide with the energy levels recently attributed to the arsenic antisite defect [9].

3. Recombination and trapping

Dislocation-induced states offer intermediate steps for electron transitions in the process of electron–hole recombination. Moreover, the energy dissipated in the recombination act may be supposed to be easily accepted by the dislocation line giving rise to its excitation of the electronic or elastic type. In fact, the most drastic effect of dislocations has been observed on the recombination of excess charge carriers. Reciprocal proportionality between the lifetime of minority carriers and dislocation density has been observed in various semiconductors for a dislocation density exceeding a certain value [10]. Since this property is a drawback in the operation of semiconductor devices, like bipolar transistors, it attracted the attention of physicists, especially in the early stage of semiconductor electronics development. Today, the interest in recombination properties of dislocations resurges in connection with LED's and laser devices in which dislocations seem to be killers of luminescence and laser action. Despite of many works devoted to the problems mentioned above, the present understanding of recombination processes at dislocations is still unsatisfactory.

According to various works there is no unique relation between the minority carrier lifetime and dislocation density for different samples of a given semiconductor, and it has to be attributed to a variable impurity (defect) decoration of dislocation. Both the EBIC contrast [11] and the DLTS spectrum [7, 12] in dislocated silicon seem to confirm the above conclusion.

As in the case under consideration the distribution of recombination sinks is strongly inhomogeneous, the question arises if the recombination of minority carriers is a process controlled by the sinking of carriers at dislocation lines (capture-limited case) or by the diffusion of carriers to the lines (diffusion-limited case). In the latter case the direct proportionality between the recombination probability, $1/\tau$, and dislocation

density, N, fails. For the idealized case of homogeneous distribution of parallel dislocation lines the relationship between τ and N may be expressed in the following approximate form [14]:

$$\tau = [-\ln(\pi r_0^2 N) - 6/5]/4\pi ND\,, \tag{1}$$

which assumes that the dislocation exhibits a capture distance r_0 and that the minority carrier concentration is zero within this distance. D is here the carrier diffusion coefficient. There is some evidence that capture-limited recombination occurs in Ge and Si while diffusion-limited one in GaAs and GaP (Fig. 4).

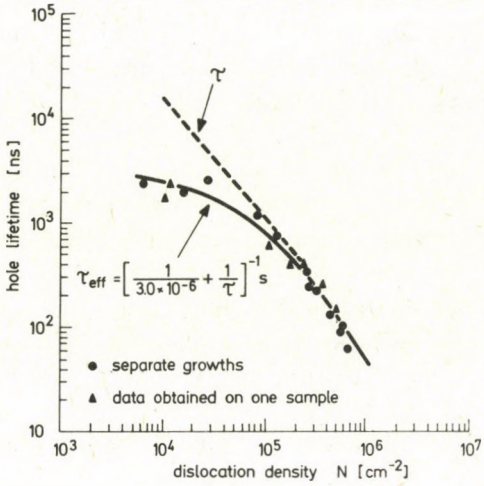

Fig. 4. The dependence of transient lifetime (300 K) on dislocation density in GaP. The data are fitted using the diffusion-limited theory (Eq. (1)), with a residual lifetime of 3.0 μs

At a sufficiently low temperature a trap behaviour of dislocation is distinctly revealed in a sense that the lifetime of majority carriers becomes extremely long due to the repulsive action of an electrostatic potential of dislocation. This potential is built up due to the electric charge of majority carriers accepted by the dislocation when reaching the equilibrium with matrix [14]. The equilibrium charge of dislocation, counted per one available site, is only a small fraction of unity because an increase in the electrostatic energy of interacting charges limits the population of dislocation states. Under conditions of excess carrier generation this charge is reduced by the opposite one of minority carriers trapped at the line. Consequently, the capture probability for majority carriers is not a constant value but depends on the number of minority carriers already trapped at the dislocation.

The mechanism mentioned above is the reason for a strong nonlinearity of the recombination process in the trapping regime. The recombination process can be quantitatively described by the barrier model of recombination at dislocations [6].

One of the consequences of this model is a specific run of transient photoconductivity. For instance, the decay of photoconductivity from a steady state, expressed in terms of the concentration of minority carriers trapped at the dislocations, Δm, is described by the formula, valid for times $t<\tau$

$$\Delta m = N(-kT\eta_0/e^2\Phi_0)\ln[(t+t_0)/\tau], \tag{2}$$

where t_0 is a parameter determined by the steady state condition, and τ has the meaning of the lifetime of majority carriers ($1/\tau$ is a thermally activated parameter with an activation energy equal to the difference between the conduction band edge and local Fermi energy in the dislocation core region). The η_0 is the line density of electric charge and Φ_0 the potential of dislocation, both under thermal equilibrium conditions. According to (2), for $\tau>t>t_0$ the decay occurs logarithmically as a function of time (Fig. 5). For longer times, $t>\tau$, the decay is exponential and characterized by the lifetime τ.

The onset of the trapping regime shifts to higher temperature as dislocation density increases, and in wide-gap semiconductors with moderate dislocation density it can enter the room temperature range. Then, at a low excitation level, the difference between the minority- and majority-carrier lifetimes may be significant even under conditions of device operation or material diagnosing.

The importance of dislocations in the luminescence efficiency of GaAs and GaP materials and devices was recognized quite early. Dislocations crossing the surface are seen as dark spots in these materials when observed in the scanning electron microscope in the cathodoluminescence mode. Moreover, the precise 1 : 1 correspondence between dark spots and dislocations is often reported by various investigators [15]. These results strongly point to dislocations as the main sinks for nonradiative recombination. Only recently a new point of view on the role of

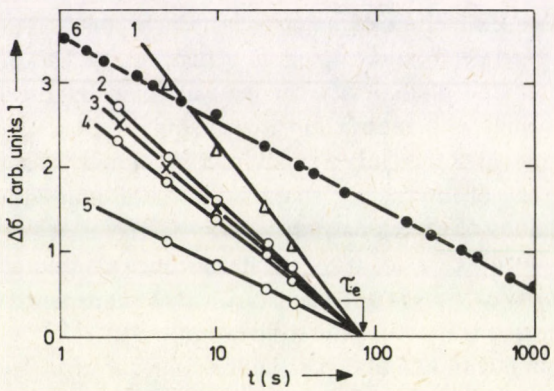

Fig. 5. Decay of photoconductivity $\Delta\sigma$ in plastically deformed Si samples with various electron concentrations and dislocation densities (1–5) at 195 K [6], and in GaAs (6) at 273 K [8]

dislocations in this phenomenon appeared in literature [9]. It is connected with recent EPR identification of antisite defects in GaP and GaAs. These antisite defects, As_{Ga}, have the character of deep double donors, and act probably as the main electron traps in those materials [16]. On the other hand, these defects are found to be closely related to dislocations in crystals and are likely produced by moving dislocations (Fig. 6). The suggestion is that these antisite defects associated with dislocations are directly responsible for the nonradiative recombination and not the dislocations themselves.

4. Dislocations in silicon devices

In practice, only a weak correlation between dislocations and bad device characteristics is observed since good quality silicon crystals with low dislocation densities have been obtained and applied to device production [17]. Surprisingly, it has been found that materials with zero dislocation density were generally not better for device operation than those with dislocation densities of the order of $10^3\,cm^{-2}$. However, as it was quite early recognized, the "dislocation-free" crystals may, in fact, contain a great number of small dislocation prismatic loops (called also swirl defects) formed through clustering of excess interstitials when cooling the crystal. The clustering occurs heterogeneously at some nuclei in which carbon atoms are involved. Dislocations present previously in the crystal may act as sinks for excess point defects and thus prevent their supersaturation.

During the device fabrication the initial dislocation density in the as-grown crystal is changed by process-dependent effects. An example of process-induced dislocations which may affect silicon device yield are dislocations created in bipolar integrated circuits with isolated transistor elements [18]. During the fabrication of those circuits a selective oxidation process is applied, using silicon nitride as a mask to protect the device area against oxidation. One of the severe disadvantages of this procedure is the stress field created in the wafer at the oxide–nitride edges (Fig. 7). Dislocations which are formed to release the stresses may extend into the active transistor area and cause emitter–collector shorts. Evidence was supplied by special experiments that enhanced the diffusion of emitter dopant along the dislocation lines, i.e., the so-called pipe diffusion, constitutes the main cause for emitter–collector leakage.

One of the most frequently observed effects in junction devices is the correlation between dislocations which thread a $p-n$ junction and the softening of the reverse characteristics. Microscopically, it is connected with the appearance of microplasma breakdown sites where the multiplication of charge carriers begins. It is now well established that soft breakdown sites do in fact occur in metal precipitates occurring at some dislocations, and not at the dislocations themselves [19, 20]. Electric field concentration at the site is the primary cause of this phenomenon.

It has to be added that stacking faults (SF) may succesfully compete with dislocations as sinks for metal impurities. The SF's are usually formed during epitaxy

and oxidation processes and reduce considerably the yield of bipolar and MOS integrated circuits. Stacking faults are found to reduce the storage time of MOS capacitors: this time decreases with increasing decoration of Frank partial dislocations bounding the SF. In dynamic MOS memories the information, stored as charge in MOS capacitors, is gradually reduced due to different leakage processes and it must be refreshed before vanishing. The failures which occur in the refresh cycles are due mainly to the enhanced minority carrier generation in the space charge region of the MOS capacitor and they are very often correlated with the presence of SF [18].

5. Dislocations in optoelectronic devices

In heterostructure light-emitting devices the so-called misfit dislocations appear. The misfit dislocations occur in the interface between two different materials, in order to accommodate a part of the lattice misfit [17]. The simplest case is when an epitaxial layer is grown on the crystalline substrate of a different material. Then, if the layer

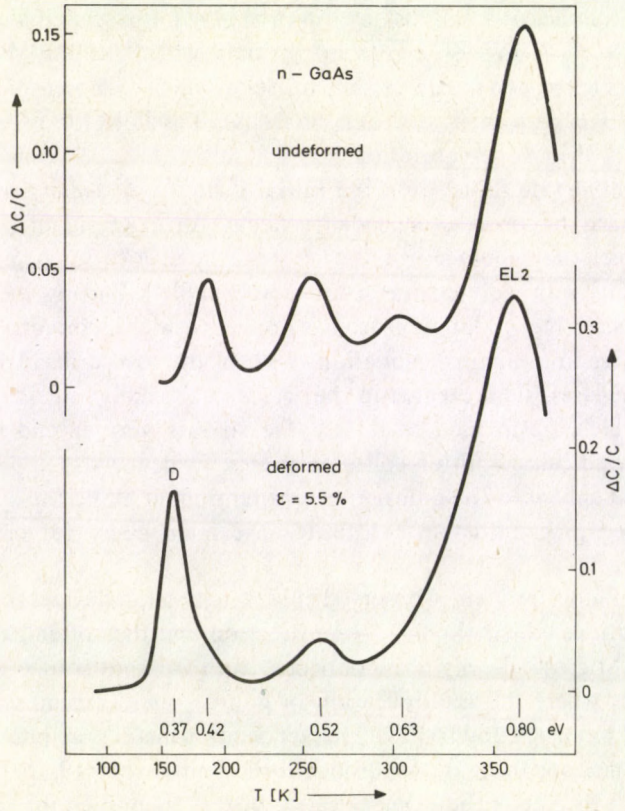

Fig. 6. DLTS spectra of undeformed GaAs samples and GaAs samples plastically deformed by compression. Increase in concentration of the main electron trap with activation energy 0.8 eV in seen after deformation [16]

thickness exceeds a critical value, it is energetically favourable to create the misfit dislocations. The misfit dislocation may be generated from a dislocation replicated from the substrate and threading the interface plane or from a small halfloop nucleated at the layer surface and next expanding to the interface (Fig. 8). Another source of dislocations and stacking faults in the interface may be inclusions (like graphite particles) incorporated into the layer during the LPE growth. The misfit dislocations in

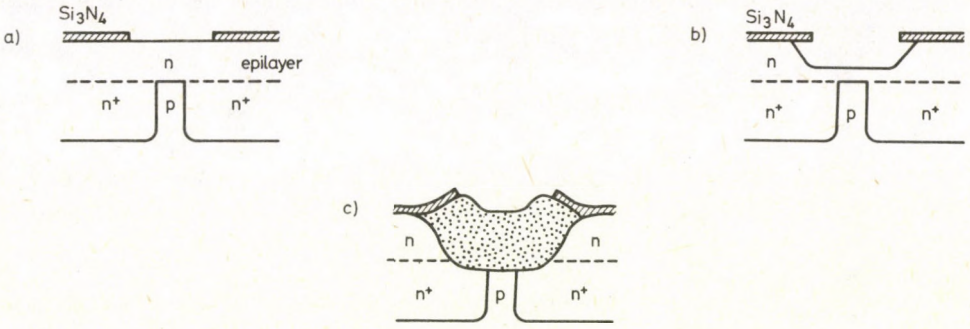

Fig. 7. Fragment of integrated $n-p-n$ transistor in OXIS technology in various stages of oxide isolation process. (a) deposition, structuring and etching of nitride film, (b) etching of silicon well, (c) oxidation resulting in the creation of stresses at the oxide-nitride edges [18]

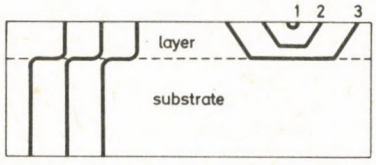

Fig. 8. Generation of misfit dislocations in the interface between LPE layer and substrate: (left) by replication of substrate dislocations and (right) by expanding of a halfloop occurring on the layer surface

an interface plane produce there localized electron states. In a heterojunction those states, when charged, change the potential profile of the junction. The misfit dislocations are also the centres of additional recombination and trapping of charge carriers. They reduce the injection coefficient of a $p-n$ heterojunction and the luminescence efficiency of light emitting devices.

A very important feature of light emitting devices, from the point of view of their utility to optoelectronic applications, is their reliability. Degradation processes, occurring in the devices during their operation, give rise to a decrease in the efficiency of LED's and limits the lifetime of lasers. Among different degradation mechanisms the

dislocation-related ones are dominant in a short-term gradual degradation of GaAlAs-GaAs DH lasers. Generally, this kind of failure consists in gradual elongation of an initial dislocation present in the device, occurring under high injection conditions. The total dislocation length in the active layer of the device is at last so drastically increased that the enhancement of the nonradiative recombination rate kills laser action.

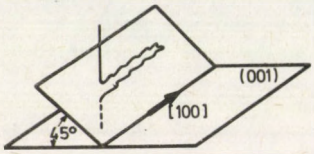

Fig. 9. Configuration of dislocation dipole growing in degraded area of GaAlAs-GaAs DH laser

One of the dislocation-related mechanisms, which leads to a failure of the device in a time period shorter than 1h, has been identified as due to the dislocation glide [21, 22]. A small initial dislocation half-loop originating from a microscratch on the external device surface glides under high injection conditions down to the interface between the active layer and the adjacent one, becoming there a misfit dislocation; the process is similar to that shown in Fig. 8. The glide velocity of dislocation occurring in this process is by several orders of magnitude higher than the usual thermal velocity of glide observed at the temperature of device operation. This enormous speed gives evidence for a new physical phenomenon: the excitation-enhanced glide motion of dislocation.

Another major mode of rapid degradation occurring in GaAlAs-GaAs DH lasers is the dislocation-related process which leads to the appearance of the so-called dark line defects (DLD) [23]. DLD's—nonemitting areas within the active layer of laser device—are gradually enlarged during the device operation. Microscopically, they are composed of networks of giant dislocation dipoles originating at an initial dislocation, usually that threading the active layer, and next expanding under high injection conditions [24]. The dislocation lines forming the dipoles are highly convoluted which points out climb as the main mechanism of dislocation motion in this process. The mean dipole plane is usually inclined at 45° to the junction (001) plane and is normal to the Burgers vector of dislocation (Fig. 9). The TEM contrast indicates an interstitial character of the dipoles. It means that interstitials of both atomic species migrate towards the growing dipole front during the degradation process and build a ribbon of extra lattice atoms there. It has been proved that the dipoles develop as a result of the high injection of charge carriers and not of the thermal heating of the device.

The dark line defect problem—one of the most striking in crystal defect physics—raises numerous questions: What is the origin of point defect supersaturation

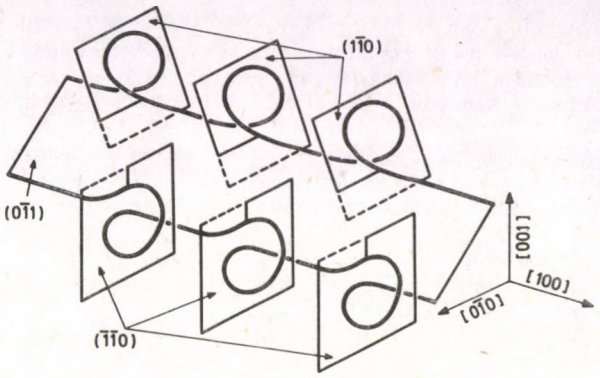

Fig. 10. Postulated geometry of dislocation dipole which assures its continuous growth through pipe diffusion of lattice atoms along dislocation line [27]

necessary to account for the observed amount of climb? What is the driving force for the climb of dislocations? What is the reason for a very high speed and highly directional growth of the dipoles? Although more or less reasonable hypotheses do exist regarding particular questions [25, 26], the whole problem has not been satisfactorily solved till now. The most commonly accepted opinion is that the formation of dipoles is due to the recombination-enhanced migration of interstitials to dislocation lines that causes their climb motion. Only one species of interstitial atoms, present initially in the crystal in a concentration of about $5 \times 10^{18}\,\mathrm{cm}^{-3}$, may be sufficient for this process so as the other ones can be produced by the climb process itself [26].

In an alternative model proposed by the present author [27] no supersaturation of interstitials is needed at all and the dipoles are assumed to develop by the pipe diffusion of lattice atoms along the dislocation lines. Some areas of definite atomic planes are emptied and other ones are filled in by lattice atoms in that process which tends to release the tangent stresses between the active layer and the adjacent ones (Fig. 10). Independently of the detailed mechanism of dipole development, one practical solution of the DLD problem is to prepare a laser material which is free of dislocations and other macrodefects in order to avoid the seeds for dislocation growth.

References

1. H. Alexander, J. Physique Colloq., *40*, C6–1, 1979.
2. E. Weber and H. Alexander, J. Physique Colloq., *40*, C6–101, 1979.
3. S. Marklund, Phys. Stat. Sol. (b), *92*, 83, 1979.
4. S. Marklund, Phys. Stat. Sol. (b), *100*, 77, 1980.
5. R. Jones, Microscopy of Semiconductor Materials, 1981. Proc. 2nd Oxford Conference, Bristol, 1981, p. 45.

6. T. Figielski, Solid State Electron., *21*, 1403, 1978.
7. W. Szkiełko, O. Breitenstein and R. Pickenhein, Crystal Res. and Technology, *16*, 197, 1981.
8. H. Nakata and J. Ninomiya, J. Phys. Soc. Jap., *47*, 1912, 1979.
9. E. R. Weber, H. Ennen, U. Kaufmann, J. Windscheif, J. Schneider and T. Wosiński, J. Appl. Phys. *53*, 6140, 1982.
10. A. T. Vink, C. J. Werkhoven and C. V. Opdorp, Topical Conf. on Characterization Techniques for Semiconductor Materials and Science, Spring Meeting, Seattle, 1978.
11. J. Heydenreich, H. Blumtritt, R. Gleichmann and H. Johansen, Crystal Res. and Technology, *16*, 133, 1981.
12. J. R. Patel and L. C. Kimerling, Crystal Res. and Technology, *16*, 187, 1981.
13. D. R. Wight, I. D. Blenkinsop and W. Harding, Phys. Rev., *23*, 5495, 1981.
14. W. T. Read, Phil. Mag., *45*, 775, 1954.
15. G. R. Booker, A. Ourmazd and D. B. Darby, J. Physique Colloq. *40*, C6–19, 1979.
16. T. Wosiński A. Morawski and T. Figielski, Appl. Phys., *A30*, 223, 1983.
17. D. B. Holt, J. Physique Colloq., *40*, C6–189, 1979.
18. B. O. Kolbesen and H. Strunk, Inst. Phys. Conf. Ser. No 57, 21, 1981.
19. A. G. Cullis and L. E. Katz, Phil. Mag., *30*, 1419, 1974.
20. C. J. Varker and K. V. Ravi, J. Appl. Phys., *45*, 272, 1974.
21. B. Monemar and G. R. Woolhouse, Inst. Phys. Conf. Ser. No 33a, 400 1976.
22. B. Monemar, R. M. Potemski, M. B. Small, J. A. van Vechten and G. R. Woolhouse, Phys. Rev. Lett., *41*, 260, 1978.
23. D. H. Newman and S. Richie, IEEE J. Quantum Electron., *QE9*, 300, 1973.
24. P. W. Hutchinson, P. S. Dobson, S. O'Hara and D. H. Newman, Appl. Phys. Lett., *26*, 250, 1975.
25. S. O'Hara, P. Hutchinson and P. S. Dobson, Solid State Commun., *30*, 368, 1977.
26. P. M. Petroff and L. C. Kimerling, Appl. Phys. Lett., *29*, 461, 1976.
27. T. Figielski, Czech. J. Phys., *B30*, 318, 1980.

Acta Physica Hungarica 56 (1—4), pp 131—137 (1984)

EFFECTIVE MASSES AND PHONON DISPERSION IN bcc METALS

K. C. GUPTA* and R. P. S. RATHORE

Department of Physics, R. B. S. College, Agra-282002 India

(Received 10 May 1983)

A shell model incorporating a consistent equilibrium condition is developed to derive the effective masses of the electrons in complex bcc metals. The validity of the model is tested by predicting the phonon dispersion in α-iron.

1. Introduction

Fielek [1], while discussing the inclusion of equilibrium condition into the Krebs [2] scheme, has considered the contributions of the ground state and pseudopotential energies of the electrons. The former part involves the correlation energy which despite of extensive investigations [3–6] needs a final complete expression. The latter part makes use of the weak local pseudopotential, which is treated as a perturbation on the system of interacting electrons. The treatment requiring tedious computational efforts, is subjected to some questions [7]. The locality of the pseudopotential, particularly with complex metals appears to be doubtful. The exclusive effectiveness of the energies associated with the electrons seems to be inconsistent with the structure of the metals. It may be noted that because of the drawbacks Fielek could not incorporate the proposed equilibrium condition [1] in his latter studies [8, 9].

The present communication derives an equilibrium condition in terms of the interaction energies coupling the cores and the electrons. The bindings among the former are assumed to be central pairwise and those for the latter are derived from their potential and the kinetic energies. The kinetic part incorporates the effective mass of the electrons which seems to be an important entity. (i) The effective mass undertakes the effect of lattice periodicity, which in turn governs the behaviour of the electrons against the uniform background of the positive charges. The effective mass apparently governs the plasma-frequency. (ii) The interband couplings invariably depend on the effective mass of the electrons. (iii) The form of pseudopotential in reciprocal space shows an obvious correlation with the effective mass. The latest refinement of the theory demands inclusion [10] of the effective mass correction into the energy and the wave number dependence of the diagonal matrix elements of the pseudopotential.

* Department of Physics, C. L. Jain College, Firozabad (Agra) 283203

(iv) The non-locality of the pseudopotential has explicit dependence on the effective mass. The correction factor, applied to the band structure energy depends on the effective mass, which determines the magnitude of band gap. For small values of momentum transfers, a more careful study [11] is needed. (v) Effective valence which is so important with the transition metals, is also determined by the effective mass. (vi) Finally, the screening effects and the dielectric constants show the specific dependence on the effective mass.

The present study includes the potential energy of the electrons in a manner which is consistent with the scheme incorporating the volume forces. The careful analysis of the literature reveals that the various expressions [12–15, 2] for the volume interactions have been developed for the lattice dynamical study of the metals but none of them imply the adequate role of these forces towards the stability of the lattices.

The volume forces employed by Fielek [8, 9, 16] contain various philosophical inconsistencies [17]. We have therefore used the Bhatia [18] expression, which has been modified for the proper convergence without the use of usual g^2 factor. The new expression renders the proper slope and the desired continuity at the zone boundary.

The model reported here is essentially a screened shell model, which accounts for the core–shell interactions in terms of harmonic forces. The shell–shell couplings are assumed to be angular [19]. The core–core bindings follow the said central pairwise forces and the volume forces, for the systems of core–conduction electrons and shell–conduction electrons follow the said modified Bhatia scheme. The model is employed to evaluate the effective masses in representative 3d, 4d and 5d metals, i.e. α-Fe, Cr, Mo, W and Ta. The phonon dispersion in the representative transition metal i.e. α-iron is also presented.

2. Dynamical matrices

Under the harmonic approximation, the phonon frequencies (ν) may be expressed as the solution of the following secular equation:

$$|D_{\alpha\beta}(\mathbf{q}) - 4\pi^2\nu^2 mI| = 0\,, \tag{1}$$

where m is the mass of the core and I is the 3×3 unit matrix and the dynamical matrix

$$D(\mathbf{q}) = R(\mathbf{q}) - S^{-1}(\mathbf{q})K\,, \tag{2}$$

where the elements of the dynamical matrix $R(\mathbf{q})$ are derived by the knowledge of the interaction of cores with its neighbouring environment, i.e.

$$R_{\alpha\beta}(\mathbf{q}) = \frac{8}{3}(\beta_1 - \alpha_1) S_\alpha S_\beta C_\gamma + BG_{\alpha\beta}(\mathbf{q})(1-P)\,,$$

$$R_{\alpha\alpha}(\mathbf{q}) = \frac{8}{3}(\beta_1 + 2\alpha_1)(1 - C_\alpha C_\beta C_\gamma) + BG_{\alpha\alpha}(\mathbf{q})(1-P) + K\,, \tag{3}$$

where $C_\alpha = \cos(1/2\, aq_\alpha)$, $S_\alpha = \mathrm{Sin}(1/2\, aq_\alpha)$, a is the lattice constant and q_α is the αth component of the phonon wave vector $\mathbf{q}$. α_1 and β_1 are the first and the second derivatives of the central pairwise potential coupling the neighbouring cores. B is the parameter of the volume interactions, which are expressed by $G(\mathbf{q})$. Following Fielek, the value of P, which determines the strength of the volume interactions is fixed at 0.2. K is the harmonic force parameter representing the coupling of the cores with the shells.

The details of the elemental equation for the dynamical matrix $S(\mathbf{q})$ depend on the nature of the interactions operating amongst the shell and its surrounding entities

$$S_{\alpha\beta}(\mathbf{q}) = K - 8\gamma_1 S_\alpha S_\beta C_\gamma + BG_{\alpha\beta}(\mathbf{q})P\,,$$

$$S_{\alpha\alpha}(\mathbf{q}) = 16\gamma_1(1 - C_\alpha C_\beta C_\gamma) - 2\gamma_1(4C_{\alpha_1} - C_{\beta_1} - C_{\gamma_1} - 2) + BG_{\alpha\alpha}(\mathbf{q})P\,, \tag{4}$$

where γ_1 is the CGW [19] type angular force constant for the noncentral couplings among the nearby shells,

$$C_{\alpha_1} = \cos(aq_\alpha), \text{ etc.}$$

The modified form of the Bhatia [18] expression for $G(\mathbf{q})$ may be written as

$$G_{\alpha\beta}(\mathbf{q}) = \frac{2S_\alpha S_\beta}{1 + 4/a^2 K_c^2 (S_\alpha^2 + S_\beta^2 + S_\gamma^2)}\,,$$

$$G_{\alpha\alpha}(\mathbf{q}) = \frac{2S\alpha^2}{1 + 4/a^2 K_c^2 (S_\alpha^2 + S_\beta^2 + S_\gamma^2)}\,, \tag{5}$$

where K_c is the screening parameter, which has been evaluated in the Bohm–Pine [20] limit.

3. Equilibrium condition

The total energy of the lattice comprises the core (Ec) and the electron (Ee) energy, i.e.

$$E = Ec + Ee\,. \tag{6}$$

For the equilibrium of the lattice $\dfrac{\partial E}{\partial \Omega}$ should vanish obviously, and

$$\frac{\partial E_c}{\partial \Omega} = \frac{2}{a}\alpha_1\,. \tag{7}$$

The energy of the electron may be expressed as the algebraic sum of the potential (Up) and the kinetic (uk) energy, i.e.

$$Ee = Uk - Up\,. \tag{8}$$

The kinetic part may be written as

$$Uk = \frac{\hbar^2 K_F^2}{2m^*}; \tag{9}$$

where $K_F = \left(\frac{3\pi^2 Z^*}{\Omega}\right)$ is the radius of the Fermi sphere. Ω is the atomic volume and m^* is the effective mass of the electron. Z^* is the effective valence.

Within the framework of the Bhatia scheme, the potential part may be written as

$$Up = \frac{B\Omega^{2/3}}{2^{1/3}\left(1 + \frac{16\pi^2}{a^2 K_c^2}\right)}. \tag{10}$$

The equilibrium condition may now assume the form

$$\alpha_1 = \frac{a}{2}\frac{\partial}{\partial\Omega}(U_k - U_p). \tag{11}$$

4. Evaluation of the parameters

The model comprises the six model parameters (α_1, β_1, γ_1, KB and m^*). One of them is yielded by the equilibrium constraint (11). Three of them are evaluated by the three elastic relations and the remaining two are calculated making use of the two zone boundary frequencies, i.e. $\nu_L(100)$ and $\nu_{T_1}(110)$ for α-iron and $\nu_L(100)$ and $\nu_L(110)$ for the other metals. Input data for these evaluations are shown in Table I [21–25].

Table I

Input data for the five bcc transition metals

Input data	α-iron	Ta	W	Cr	Mo
a [A. U.]	2.866	3.3	3.16	3.68	3.14
C_{11} [10^{11}N/m^2]	2.331	2.609	5.3255	3.398	4.4077
C_{12} [10^{11}N/m^2]	1.355	1.574	2.0495	0.586	1.7243
C_{44} [10^{11}N/m^2]	1.1783	0.818	1.6373	0.990	1.2165
m [10^{-27} Kg]	92.7060	300.3770	305.191	86.3134	159.2604
$\nu_L(100)$ [T. Hz·]	8.52	5.03	5.5	7.7	5.52
$\nu_L(110)$ [T. Hz·]	9.19	4.35	6.8	9.4	8.14
$\nu_{T_1}(110)$ [T. Hz·]	4.55	2.63	4.1	5.8	4.56
$\nu_{T_2}(110)$ [T. Hz·]	6.49	4.35	4.2	7.8	5.73
Source of input data	[21]	[22]	[23]	[24]	[25]

5. The effective masses of the electrons

The present study is the first to employ the model to calculate the effective mass of the electrons in the five transition metals, which are given in Table II. It may be mentioned that so far the tedious model potential calculations [26–28] have revealed the values of the effective mass of the electrons in simple metals only.

Table II

Computed effective masses of electrons (m^*/m) for five bcc transition metals

	α-iron	Ta	W	Cr	Mo
(m^*/m) where m^* = effective mass of electron, m = rest mass of electron	−0.772 64	−0.648 76	−0.235 29	−0.131 71	−0.312 50

6. Phonon dispersion

The computed model parameters needed for the exposition of the phonon dispersion in α-iron are listed in Table III, Fig. 1 depicts the dispersion relations for α-iron along the principle symmetry directions. The experimental data (○ △ ▲) [29] are also plotted alongside the curves for comparison purposes.

Table III

Computed model parameters for α-iron [10^1 N/m]

α_1	β_1	γ_1	K	B	m^*/m
−1.0101	−3.2425	0.069 30	4.6456	3.9898	−0.772 64

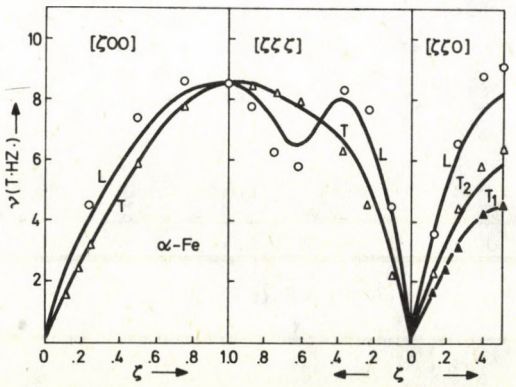

Fig. 1. Phonon dispersion curves for α-iron along three major symmetry directions. Solid lines represent the theoretical curves of the present study. (○ △ ▲) represent experimental points due to [29]

7. Discussion

Five metals, namely α-iron, chromium, molybdenum, tungsten and tantalum, which cover almost all the anomalous behaviours shown in the phonon dispersion of bcc transition metals are analysed. The corresponding metallic electronic structure outside the core of closed shells may be expressed as $3d^64S^2$ (α-Fe), $3d^54S$(Cr), $4d^55S'$(MO), $5d^46S^2$(W) and $5d^36S^2$(Ta). We find from the comparison of our theoretical curves with the experimental ones that in α-Fe the results are in fairly good agreement in all the directions.

The experimental curves available for Cr, Mo, W and Ta [30, 25, 31, 22] indicate that they have quite different shapes along the $[\zeta\zeta\zeta]$ direction between $\zeta = 0.5$ to $\zeta = 1.0$. The usual hump present in the *L*-branch disappears in these metals except for Ta. Our theoretical curves obtained for these metals (not reported here) successfully predict this change of behaviour. They also show fair agreement in $[\zeta\zeta 0]$ and $[\zeta 00]$ directions. The striking anomaly observed along the $[\zeta 00]$ direction of Ta is the crossing of *L* and *T* branches, which is exhibited successfully by our model. However, the model fails to reproduce reasonably the *T*-branches in $[\zeta\zeta\zeta]$ direction at higher wave vectors which may be attributed to the crudity of the scheme used for expressing volume forces.

8. Conclusions

The efficiency of the model should be seen in the light of the fact that the single model like the present one predicts dispersion curves in metals bearing striking anomalies of different nature. The model making use of consistent equilibrium condition has one extra advantage in that it provides, of course with many understandable limitations, a tool for determining the effective masses of the electrons in bcc transition metals, which are perhaps not known to date. The resulting effective masses are small negative values, contrary to the expected high positive values [32] for the metals considered here.

References

1. B. L. Fielek, J. Phys., *F-8*, 577, 1978.
2. K. Krebs, Phys. Rev., *138*, A, 148, 1965.
3. K. S. Singwi, A. Jolander, M. P. Tosi and R. H. Land, Phys. Rev., *B1*, 1044, 1970.
4. F. Toigo and T. O. Woodruff, Phys. Rev., *B4*, 371, 1971.
5. P. Vashishta and K. S. Singwi, Phys. Rev. *B6*, 875, 1972.
6. S. S. Mandal, B. R. Rao and D. N. Tripathi, Phys. Rev., *B18*, 2524, 1978.
7. M. M. Shukla, J. Phys., *F-8*, L-289, 1978.
8. B. L. Fielek, J. Phys., *F*-10, 1665, 1980.
9. B. L. Fielek, J. Phys., *F-11*, 2381, 1980.
10. D. Weaire, J. Phys., *C-11*, 210, 1968.
11. R. W. Shaw, J. Phys., *C-2*, 2350, 1969.

12. P. K. Sharma and S. K. Joshi, J. Chem. Phys., *39*, 2633, 1963.
13. J. de Launay, J. Chem. Phys., *21*, 1975, 1953.
14. V. Ramamurthy and K. NeelKandan, Ind. J. Pure and Appld. Phys., *15*, 312, 1977.
15. L. Cheaveau, Phys. Rev., *169*, 496, 1968.
16. B. L. Fielek, J. Phys., *F-5*, 17, (1975.
17. R. N. Khanna and R. P. S. Rathore, Phys. Stat. Sol., (b) *107*, 267, 1981; Acta Phys. Polonica, *A60*, 333, 1981; Acta Crystall., A. *37*, 332, 1981.
18. A. B. Bhatia, Phys. Rev., *97*, 363, 1955.
19. B. C. Clark, D. C. Gazis and R. F. Wallis, Phys. Rev., *134*, A1486, 1964.
20. D. Bohm and D. Pines, Phys. Rev., *92*, 609, 1953.
21. J. A. Rayne and B. S. Chandrashekhar, Phys. Rev., *122*, 1714, 1964.
22. A. D. W. Woods, Phys. Rev., *136*, 781, 1964.
23. A.O.E. Animalu and V. Heine, Phil. Mag., *12*, 1965.
24. A. Sumner and J. B. Smith, J. Appl. Phys., *34*, 2691, 1963.
25. B. M. Powell, P. Martee and A. D. W. Woods, Canad. Journ. of Phys., *55*, 160, 1977.
26. D. Weaire, Proc. Phys. Soc., *92*, 956, 1967.
27. R. W. Shaw, Jr and W. A. Harrison, Phys. Rev., *163*, 604, 1967.
28. R. W. Shaw, Jr., Phys. Rev., *174*, 769, 1968.
29. B. N. Brockhouse, N. E. Abou-Hetal and E. D. Hallne, Solid. State Commun., *5*, 211, 1967.
30. R. W. Shaw and L. D. Muhlestein, Phys. Rev., *B4*, 969, 1971.
31. A. Larose and B. N. Brockhouse, Canad. Journ. of Phys., *54*, 1819, 1976.
32. C. Kittel, Introduction to Solid State Phys., John Wiley and Sons, New York, 1966, p. 295.

Acta Physica Hungarica 56 (1—4), pp 139—145 (1984)

NON-UNIFORM PROPAGATION OF WEAK DISCONTINUITIES IN RADIATION MAGNETOGASDYNAMICS

RAMA SHANKAR, MOHAN PRASAD and S. S. PRABHU

Department of Mathematics, Indian Institute of Technology, Hauz Khas Delhi-110016, India

(Received 10 May 1983)

Singular surface theory is applied to study the non-uniform propagation of weak discontinuities in radiation magnetogas dynamics. The fundamental differential equations governing the growth and decay of these discontinuities are formulated and these equations are solved completely. The criteria for decay or 'blowup' of these discontinuities are obtained. It turns out that the weak discontinuity grows into a shock and the effect of radiation is to delay the shock formation while the electrical conductivity causes the rapid onset of shock wave.

1. Introduction

Recently Rama Shankar and Jain [1] while discussing the uniform propagation of weak discontinuities in radiation magnetogas dynamics have derived the fundamental differential equations governing the growth and decay of weak discontinuities and solved for various wave fronts. They showed that the effect of electrical and radiative heat transfer is to cause damping in the formation of the shocks. But if the medium ahead is moving then it can be shown [2] that the wave propagation is anisotropic. In order to study anisotropic wave propagation Lighthill [3] has developed an elegant method. Numerous applications of this method followed. Ludwig [4] and Duff [5] further generalized and developed this technique.

Elcrat [6] studied the non-uniform propagation of weak discontinuities in an unsteady flow of a perfect gas. In order to integrate the growth equations Elcrat transformed them into an equation along the bicharacteristic curve in the characteristic manifold. When this is done an ordinary differential equation is obtained, which when solved gives an explicit criterion for the decay or 'blowup' of sonic discontinuities.

In the present paper following the aforementioned analysis we have derived and discussed the fundamental differential equations in radiation magnetogas dynamics and their solutions. The criterion for the decay or 'blowup' of sonic discontinuities has also been given.

2. Equations of propagation

The set of non-linear differential equations governing the three-dimensional unsteady flow in radiation magnetogas dynamics are [1]

$$\frac{\partial \rho}{\partial t} + u_i \rho_{,i} + \rho u_{i,i} = 0, \tag{1}$$

$$\rho \frac{\partial u_i}{\partial t} + \rho u_j u_{i,j} + p_{,i} + \mu H_k H_{k,i} - \mu H_k H_{i,k} = 0, \tag{2}$$

$$\frac{\partial H_i}{\partial t} + u_k H_{i,k} - H_k u_{i,k} + H_i u_{k,k} - (\sigma\mu)^{-1} H_{i,kk} = 0, \tag{3}$$

$$\rho T\left(\frac{\partial S}{\partial t} + u_i S_{,i}\right) = -q^R_{j,j} + \frac{J^2}{\sigma}, \tag{4}$$

$$J^2 = J_i J_i; \qquad J_i = e_{ijk} H_{k,j}, \tag{5}$$

$$p = \rho R T, \qquad S = S(\rho, p), \tag{6}$$

where H_i denote the components of magnetic field, J the electric current density, σ the electrical conductivity, q^R_j radiation heat flux vector, t the time, p the pressure, ρ the density, T the temperature, u_i the components of flow velocity, S the entropy and μ the magnetic permeability constant.

We have used the tensor notation. A comma followed by a latin index denotes the partial differentiation with respect to a space variable.

We consider a moving singular surface $S(t)$ across which the magnetic field and temperature and their first derivatives are continuous, but may have possible discontinuities in the second derivatives. All other flow quantities are continuous but have possible discontinuities in their first derivatives.

Suppose that $S(t)$ is $\psi(x_i, t) = 0$. We denote by n_i the components of the unit normal vector $\dfrac{\psi_{,i}}{|\operatorname{grad}\psi|}$ and let $G = -\dfrac{\partial\psi/\partial t}{|\operatorname{grad}\psi|}$ be the normal speed of advance of $S(t)$. The surface $S(t)$ is imagined to have two sides denoted by (1) and (2) with n directed into (2). The relative speed of advance of $S(t)$ through fluid is $U = G - u_i n_i$. We use a square bracket to denote the difference in the value of quantity behind and ahead of the surface $S(t)$. Possible discontinuities may be written in the form (Thomas [7])

$$[u_{i,j}] = \lambda n_i n_j, \qquad \left[\frac{\partial u_i}{\partial t}\right] = -G\lambda_i,$$

$$[\rho_{,i}] = \zeta n_i, \qquad \left[\frac{\partial \rho}{\partial t}\right] = -G\zeta,$$

$$[p_{,i}] = \xi n_i, \qquad \left[\frac{\partial p}{\partial t}\right] = -G\xi.$$

Making use of first order compatibility conditions in (1)–(3) we get

$$\rho\lambda = U\zeta\,, \tag{7}$$

$$-\rho U\lambda + \xi = 0\,, \tag{8}$$

$$\bar{\eta}_i = \sigma U\lambda(H_i - H_n n_i)\,, \tag{9}$$

where

$$\bar{\eta}_i = [H_{i,kk}]\,.$$

From (7) and (8) we obtain

$$\xi = \rho U\lambda = U^2\zeta\,.$$

Further taking jump in the first derivative of $p = \rho RT$ yields

$$\xi = c^2\zeta\,.$$

From the above equations we write

$$U^2 = c^2\,,$$

which indicates that the propagation speed of weak discontinuities in a non-uniform medium is just the isothermal speed of sound.

Differentiating (1) and (2) w.r.t. x_j and applying the jump conditions of Thomas [7], we have

$$U\frac{\delta\zeta}{\delta t} - (U^2\bar{\zeta} - \rho U\bar{\lambda}_i n_i) + 2U\lambda\left[\left(\frac{\partial\rho}{\partial n}\right)_2 - \rho\Omega\right]$$

$$-2U\zeta\lambda + 2U\zeta(u_{i,j}n_i n_j)_2 + Ug^{\alpha\beta}u_i\,\zeta_{,\alpha}x_{i,\beta} = 0 \tag{10}$$

and

$$\rho\frac{\delta\lambda}{\delta t} + (\bar{\xi} - \rho U\bar{\lambda}_i n_i) - U\lambda\left(\frac{\partial\rho}{\partial n}\right)_2 + \left(\frac{\partial u_i}{\partial t} + u_k u_{i,k}\right)_2\zeta n_i + U\zeta\left(\frac{\partial u_i}{\partial n}\right)_2 n_i$$

$$+ U\zeta(u_{k,j}n_k n_j)_2 + \rho g^{\alpha\beta}\lambda_{,\alpha}\,x_{k,\beta}u_k + \mu(H_k\bar{\eta}_k - H_n\bar{\eta}_i n_i) = 0\,. \tag{11}$$

Now addition of (10) and (11) gives

$$U\frac{d\zeta}{dt} + \rho\frac{d\lambda}{dt} + (\bar{\xi} - U^2\bar{\zeta}) + U\lambda\left(\frac{\partial\rho}{\partial n}\right)_2 - 2\rho U\,\lambda\Omega - 2U^2\zeta^2 + 3U\zeta(u_{i,j}n_i n_j)_2$$

$$+\left(\frac{\partial u_i}{\partial t} + u_k u_{i,k}\right)_2 n_i\zeta + U\zeta\left(\frac{\partial u_i}{\partial n}\right)_2 n_i + \mu(H_k\bar{\eta}_k - H_n\bar{\eta}_i n_i) = 0\,. \tag{12}$$

Here $\dfrac{\delta}{\delta t}$ denotes differentiation along an orthogonal trajectory of the surface $S(t)$, Ω is the mean curvature of $S(t)$ defined by $2\Omega = g^{\alpha\beta}b_{\alpha\beta}$, while $g^{\alpha\beta}$ and $b_{\alpha\beta}$ are the first and second fundamental forms of $S(t)$. While writing Eq. (12) we made use of the following transformation

$$\frac{d\zeta}{dt}=\frac{\delta\zeta}{\delta t}+g^{\alpha\beta}\zeta_{,\alpha}u_i x_{i,\beta},$$

$$\frac{d\lambda}{dt}=\frac{\delta\lambda}{\delta t}+g^{\alpha\beta}\lambda_{,\alpha}u_i x_{i,\beta},$$

$$\frac{d\xi}{dt}=\frac{\delta\xi}{\delta t}+g^{\alpha\beta}\xi_{,\alpha}u_i x_{i,\beta}.$$

Differentiation of $p=p(\rho, S)$ and application of jump conditions yields

$$\bar{\xi}=\frac{\partial^2 p}{\partial\rho^2}\left[2\left(\frac{\partial\rho}{\partial n}\right)_2\zeta-\zeta^2\right]+\frac{\partial^2 p}{\partial S\,\partial\rho}(S_{,i})_2\zeta n_i+U^2\bar{\zeta}+\frac{\partial p}{\partial S}[S_{,ij}]n_i n_j. \tag{13}$$

Differentiating (4) w.r.t. t, we get after taking jumps across $S(t)$ and using $T=T(\rho, S)$ and $q^R_{j,j}=4\alpha_p a_R T^4$ (Vincenti and Kruger [8])

$$[S_{,ij}]n_i n_j=\frac{\zeta}{\rho TU}\left[\left(\rho\left(\frac{\partial T}{\partial\rho}\right)_\Pi+T\right)\left(\frac{\partial S}{\partial t}+u_i S_{,i}\right)_2\right.$$
$$+TU\left(\frac{\partial S}{\partial n}\right)_2-16\alpha_p a_R T^3\left(\frac{\partial T}{\partial\rho}\right)_2$$
$$\left.-2\mu\frac{U}{\rho}(J_i)_2 e_{ijk}n_j(H_k-H_n n_i)\zeta\right]. \tag{14}$$

Substituting (14) in (13) we get

$$\bar{\xi}-U^2\bar{\zeta}=\frac{\partial^2 p}{\partial\rho^2}\left[2\left(\frac{\partial\rho}{\partial n}\right)_2\zeta-\zeta^2\right]$$
$$+\frac{\partial^2 p}{\partial S\,\partial\rho}(S_{,i})_2\zeta n_i+\frac{\partial p}{\partial S}\frac{\zeta}{\rho TU}\left[\left(\rho\left(\frac{\partial T}{\partial\rho}\right)_2+T\right)\right.$$
$$\left.+\left(\frac{\partial S}{\partial t}+u_i S_{,i}\right)_2+TU\left(\frac{\partial S}{\partial n}\right)_2-16\alpha_p a_R T^3\left(\frac{\partial T}{\partial\rho}\right)_2\right.$$
$$\left.-2\mu\frac{U}{\rho}(J_i)_2 e_{ijk}n_j(H_k-H_n n_i)\right]. \tag{15}$$

Further use of (15) into (12) leads to

$$U\frac{d\zeta}{dt}+\rho\frac{d\lambda}{dt}+\frac{\partial^2 p}{\partial\rho^2}\left[2\left(\frac{\partial\rho}{\partial n}\right)_2\zeta-\zeta^2\right]+\frac{\partial^2 p}{\partial S\,\partial\rho}\left(\frac{\partial S}{\partial n}\right)_2\zeta$$
$$+\frac{\zeta}{\rho TU}\left(\frac{\partial p}{\partial S}\right)\left[\left(\rho\left(\frac{\partial T}{\partial\rho}\right)_2+T\right)\left(\frac{\partial S}{\partial t}+u_i S_{,i}\right)_2+TU\left(\frac{\partial S}{\partial n}\right)_2\right.$$
$$\left.-16\alpha_p a_R T^3\left(\frac{\partial T}{\partial\rho}\right)_2-2\mu\frac{U}{\rho}(J_i)_2 e_{ijk}n_j(H_k-H_n n_k)\right]$$

$$+U\lambda\left(\frac{\partial\rho}{\partial n}\right)_2-2\rho U\lambda\,\Omega-2\frac{U^2\zeta^2}{\rho}+3U\zeta(u_{i,j}n_in_j)_2$$
$$+\left(\frac{\partial u_i}{\partial t}+u_ku_{i,k}\right)_2 n_i\zeta+U\zeta\left(\frac{\partial u_i}{\partial n}\right)_2 n_i$$
$$+\mu(H_i-H_nn_i)\bar{\eta}_i=0\,. \tag{16}$$

Now using the relation $\rho\lambda=U\zeta$ we write (16) as follows:

$$2U\frac{d\zeta}{dt}+\zeta\left[\left(\frac{dU}{dt}-\frac{U}{\rho}\frac{d\rho}{dt}\right)+2\frac{\partial^2p}{\partial\rho^2}\left(\frac{\partial\rho}{\partial n}\right)_2\right.$$
$$+\frac{\partial^2p}{\partial S\,\partial p}\left(\frac{\partial S}{\partial n}\right)_2+\frac{1}{\rho TU}\left(\frac{\partial p}{\partial S}\right)\left\{\left(\rho\left(\frac{\partial T}{\partial\rho}\right)_2+T\right)\right.$$
$$\times\left(\frac{\partial S}{\partial t}+u_iS_{,i}\right)_2+TU\left(\frac{\partial S}{\partial n}\right)_2-16\alpha_pa_RT^3\left(\frac{\partial T}{\partial\rho}\right)_2$$
$$\left.-2\mu\frac{U}{\rho}(J_i)_2e_{ijk}n_j(H_k-H_nn_k)\right\}+\frac{U^2}{\rho}\left(\frac{\partial\rho}{\partial n}\right)_2$$
$$-2U^2\Omega+3U(u_{i,j}n_in_j)_2+\left(\frac{\partial u_i}{\partial t}+u_ku_{i,k}\right)_2 n_i$$
$$\left.+U\left(\frac{\partial u_i}{\partial n}\right)_2 n_i+\sigma\frac{\mu^2}{\rho}U(H_i^2-H_n^2)\right]-\zeta^2\left(\frac{\partial^2p}{\partial\rho^2}+2\frac{U^2}{\rho}\right)=0$$

or

$$\frac{d\zeta}{dt}+\zeta\left[\frac{1}{2U}\frac{dU}{dt}-\frac{1}{2\rho}\frac{d\rho}{dt}+\frac{1}{2U}\left\{2\frac{\partial^2p}{\partial\rho^2}\left(\frac{\partial\rho}{\partial n}\right)_2\right.\right.$$
$$+\frac{\partial^2p}{\partial S\,\partial\rho}\left(\frac{\partial S}{\partial n}\right)_2+\frac{1}{\rho TU}\left(\frac{\partial p}{\partial S}\right)\left[\left(\rho\left(\frac{\partial T}{\partial\rho}\right)_2+T\right)\right.$$
$$\times\left(\frac{\partial S}{\partial t}+u_iS_{,i}\right)_2+TU\left(\frac{\partial S}{\partial n}\right)_2-16\alpha_pa_RT^3\left(\frac{\partial T}{\partial\rho}\right)_2$$
$$\left.-2\mu\frac{U}{\rho}(J_i)_2e_{ijk}n_j(H_k-H_nn_k)\right]+\frac{U^2}{\rho}\left(\frac{\partial\rho}{\partial n}\right)_2-2U^2\Omega$$
$$+3U(u_{i,j}n_in_j)_2+\left(\frac{\partial u_i}{\partial t}+u_ku_{i,k}\right)_2 n_i+U\left(\frac{\partial u_i}{\partial n}\right)_2 n_i$$
$$\left.\left.+\sigma\frac{\mu^2}{\rho}U(H_i^2-H_n^2)\right)\right\}\left.\right]-\zeta^2\left(\frac{U}{\rho}+\frac{1}{2U}\frac{\partial^2p}{P\rho^2}\right)=0\,. \tag{17}$$

Eq. (17) can be expressed as

$$\frac{d\zeta}{dt}+\zeta\left\{\frac{1}{2}\frac{d}{dt}\left(\log\frac{U}{\rho}\right)+\frac{Q}{2U}\right\}-\zeta^2\left(\frac{U}{\rho}+\frac{1}{2U}\frac{\partial^2 p}{\partial\rho^2}\right)=0, \tag{18}$$

where

$$\begin{aligned}Q=&2\frac{\partial^2 p}{\partial\rho^2}\left(\frac{\partial\rho}{\partial n}\right)_2+\frac{\partial^2 p}{\partial S\,\partial\rho}\left(\frac{\partial S}{\partial n}\right)_2\\&+\frac{1}{\rho TU}\frac{\partial p}{\partial S}\left\{\left(\rho\left(\frac{\partial T}{P\rho}\right)_2+T\right)\left(\frac{\partial S}{\partial t}+u_i S_{,i}\right)_2\right.\\&+TU\left(\frac{\partial S}{\partial n}\right)_2-16\alpha_p a_R T^3\left(\frac{\partial T}{\partial\rho}\right)_2\\&\left.-2\mu\frac{U}{\rho}(J_i)_2 e_{ijk}n_j(H_k-H_n n_k)\right\}\\&+\frac{U^2}{\rho}\left(\frac{\partial\rho}{\partial n}\right)_2-2U^2\Omega+3U(u_{i,j}n_i n_j)_2\\&+\left(\frac{\partial u_i}{\partial t}+u_k u_{i,k}\right)_2 n_i+U\left(\frac{\partial u_i}{\partial n}\right)_2 n_i+\sigma\frac{\mu^2}{\rho}U(H_i^2-H_n^2).\end{aligned}$$

Eq. (18) is the basic differential equation for the growth and decay of weak discontinuities associated with the wave surface $S(t)$ existing in R.M.G.D.* As a necessary check to our calculations we deduce from the preceding equations the differential equation for growth and decay of weak discontinuities in uniform propagation in magnetogasdynamics and these agree with the one derived in [1].

Integrating (18) with $S(t)=S_0$, $\zeta=\zeta_0$, $\lambda=\lambda_0$, $\xi=\xi_0$, $U=U_0$ and $\rho=\rho_0$ at $t=0$ we get

$$\zeta=\frac{\zeta_0\left(\frac{U}{U_0}\right)^{-1/2}\left(\frac{\rho}{\rho_0}\right)^{1/2}\exp(-\varphi t))}{1-\left(\frac{U_0}{\rho_0}\right)^{1/2}\zeta_0 I(t)}, \tag{19}$$

where

$$I(t)=\int_0^t\left(\frac{U}{\rho}+\frac{1}{2U}\frac{\partial^2 p}{\partial\rho^2}\right)\left(\frac{U}{\rho}\right)^{-1/2}\exp(-\varphi(\tau))d\tau$$

and

$$\varphi(t)=\int_0^t\frac{Q}{2U}dt.$$

* Radiation Magnetogas Dynamics

3. Discussion of the solution

If the functions $\varphi(t)$ and $I(t)$ are continuous for $0 \leq t < T^*$ and have finite limits $\varphi(T^*)$ and $I(T)$ as $t \to T^*$ and if sgn $\zeta_0 = -$sgn $I(t)$ then the right hand side of (19) will not only remain continuous throughout $0 \leq t < T^*$ but will approach a finite limit as $t \to T^*$. Also if sgn $\zeta_0 =$ sgn $I(t)$, the right hand side of (19) will remain finite throughout $0 \leq t < T^*$ provided that $|\zeta_0| < \zeta_c$ where ζ_c is a positive critical value of the initial discontinuity given by

$$\zeta_0 = \left[\left(\frac{U_0}{\rho_0} \right)^{1/2} |I(t)| \right]^{-1}.$$

If sgn $\zeta_0 =$ sgn $I(t)$ and $|\zeta_0| > \zeta_c$ it follows from (19) that there will exist a time $t^* < T^*$ given by $I(t^*) = \left[\left(\frac{U_0}{\rho_0} \right)^{1/2} \zeta_0 \right]^{-1}$ such that $|\zeta_c| \to \infty$ as $t \to t^*$. This is the criterion for the discontinuity to blow up at a finite time T^*, i.e. actually for the appearance of a shock wave at T^*. Finally if $|\zeta_0| = \zeta_c$ and sgn $\zeta_0 =$ sgn $I(t)$, then ζ is continuous for t in $[0, T^*]$ but approaches infinity as $t \to T^*$.

Thus the role of radiation and electrical conduction is to resist the formation of shocks and delay the onset of shock wave. The effect of radiation is to delay the shock formation but the electrical conductivity causes the onset of shock wave rapidly.

References

1. Rama Shankar and S. K. Jain, Acta Phys. Hung., *50*, 297, 1981.
2. L. D. Landau and E. M. Lifshitz, Fluid Mechanics, Pergamon Press, London 1959.
3. M. J. Lighthill, Philosophical Trans. of Roy. Soc. London, *252A*, 397, 1960.
4. D. A. Ludwig, A.E.C. Rept., NYO-9351, 1961.
5. G. F. D. Duff, Comm. of Pure and Applied Mathematics, *17*, 189, 1964.
6. A. R. Elcrat, Int. Journ. of Engg. Sci., *15*, 29, 1977.
7. T. Y. Thomas, Journ. Math. Mech., *6*, 455, 1957.
8. W. C. Vincenti and C. H. Kruger, Introduction to Physical Gas Dynamics, John Wiley and Sons, N. Y. 1965.

Acta Physica Hungarica 56 (1—4), pp 147—158 (1984)

HOLLOW ANODE-CATHODE He–Kr ION LASER

M. JÁNOSSY, K. RÓZSA, L. CSILLAG

Central Research Institute for Physics
H-1525 Budapest, Hungary

and

LE TRONG MUU

University of Hanoi, Vietnam

(Received 17 May 1983)

Laser operation parameters were investigated in a 469 nm He–Kr hollow anode–cathode laser. In this type of discharge tube voltage could be changed by varying the number of internal anode rods. Increasing tube voltage resulted in higher output power and lower threshold current. Optimum He and Kr partial pressure values were found to depend on discharge current. A maximum output power of 75 mW and a gain of 16%/m was obtained.

1. Introduction

The hollow cathode discharge has been found useful in research for developing low or medium output power gas lasers operating in the green, blue and ultraviolet region of the spectrum. The main advantage of the hollow cathode discharge is that the density of high energy electrons is larger than in the positive column discharge region. Since most of the blue–green laser transitions belong to the spectrum of singly ionized atoms, this explains the need of high energy electrons to excite these lasers. The use of hollow cathode discharge excitation resulted in achieving cw laser operation in He–Kr, He–Ar and He–Ne–Xe noble gas mixture active materials [1–3], which oscillate at transitions of the Kr, Ar and Xe ion, respectively, and could be operated earlier only pulsed in positive column tubes. The strongest transition of these lasers has been found to be the 469 nm line of the He–Kr system.

The high energy component of electrons in the hollow cathode discharge is related to tube voltage, so any increase in the latter should produce more high energy electrons and thus laser output is expected to increase. The problem is that in a given diameter the tube voltage can be usually increased only by decreasing gas pressure, but this decreases the possible number of atoms to be excited for the laser, so this way to increase tube voltage may be unfavourable for laser operation. A modified hollow cathode discharge tube was developed to increase tube voltage independently of changing gas pressure [4]. This is achieved bv placing a series of anode rods inside the

cathode in the way shown in Fig. 1. This configuration is named hollow anode–cathode (HAC) tube. The bright part of the discharge is formed in the centre of the tube, the discharge operates properly if the distance D between the cathode and the nearest anode is too small to produce all the ions necessary for self sustained discharge. At a given tube diameter, pressure and discharge current, this type of discharge tube operates at a higher voltage than a conventional hollow cathode. Since the increased

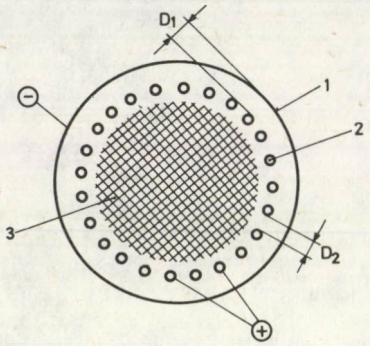

Fig. 1. Scheme of hollow anode–cathode discharge. 1 — cathode, 2 — anodes, 3 — bright part of the discharge

Table I

Laser transitions in He-Kr gas mixture

KrII wavelength [nm]	Intensity
651.0	medium
512.6	weak
469.4	strong
458.3	medium
438.7	medium
431.8	strong

tube voltage indicates a larger number of high energy electrons in the discharge the population of high energy states will be increased. It is noted that other methods for increasing tube voltage have been developed, these are an internal rotatable anode structure [5], the use of a coil cathode [6], and the division of the cathode surface into small independent parts [7]. A high voltage discharge occurs also if the working surface of the anodes and the hollow cathode are on the same cylinder jacket [8]

An increase of intensity of some neutral and ionic spectral lines was observed in HAC discharges, the increase of ionic line intensities being quite significant [4]. Laser oscillation was obtained in noble gas mixture HAC discharge tubes and in the He–Kr and He–Ar lasers a decrease of threshold current and increase of output power was observed [3]. From these measurements for the effect of higher voltage only

preliminary conclusions could be made, since the geometry of the hollow cathode lasers used for comparison was not equivalent to the HAC laser. For this reason a series of experiments were performed to investigate within more exact conditions the dependence of laser output on tube voltage, the latter being changed by using within the same cathode structure a different number of internal anode rods. As noble gas mixture active medium, the He–Kr system was used. Table I shows laser transitions of the He–Kr system, the investigations were performed at the 469 nm transition. Measurements of output power at 469 nm as a function of He and Kr partial gas pressure and discharge current were performed in HAC discharge tubes with one, three, and six internal anode rods. Some experiments were performed with twelve internal anode rods but technical difficulties due to the very high voltage (~ 1500 V) prevented detailed measurements in this tube. The results of measurements show a quite complicated behaviour of the dependence of laser output on all these parameters.

2. Experimental arrangement

The scheme of the laser tube used in our experiments is shown in Fig. 2. The inner diameter of the hollow cathode was 8.5 mm, the tube was built of four cathode sections with metal rings between them. These served to hold the different number of anode

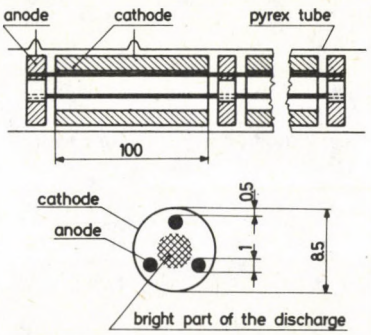

Fig. 2. Scheme of hollow anode–cathode laser tube

rods. Insulation between the anode-holders and the cathode were steatit rings. The distance between anode rods and the cathode surface was 0.5 mm. The whole hollow anode–cathode structure was contained inside a pyrex glass tube. The discharge was excited by half wave rectified alternating current, where the repetition rate was reduced to 12.5 Hz. High reflectivity mirrors were used in the measurements to be able to perform the investigations in a possible broadest range of discharge paremeters. In most cases the radius of mirrors was 3 m and 1.15 m, respectively, the latter had a transmission of 0.1%, which was used for detecting laser intensity. For optimum laser output measurements a higher transmission mirror was used. The output power was measured by a Spectra Physics 404 type power meter.

3. Results of measurements

The voltage–current characteristics of the discharge tubes were investigated in detail, some results of measurements are shown in Fig. 3. It can be seen from the Figure in accordance with earlier experiments, that tube voltage increases with increasing internal anode rod number. High voltages exceeding 1000 V were observed in the case of twelve internal anode rods at 2 A discharge current in the 16–20 mbar He pressure range.

Figure 4 shows dependence of tube voltage on He pressure. It can be seen from the Figure that in the case of six anode rods the shape of the curve changes, a significant increase of voltage occurs at pressures below 20 mbar.

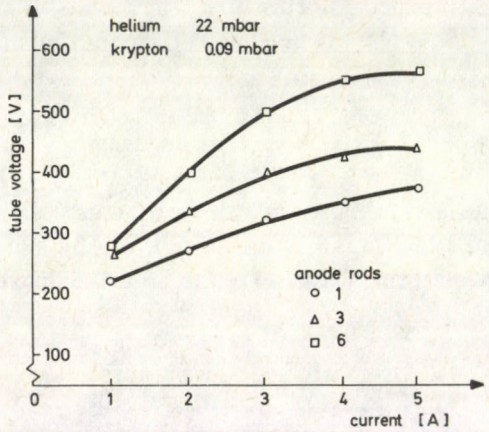

Fig. 3. Voltage–current characteristics in hollow anode–cathode tubes with a different number of internal anode rods

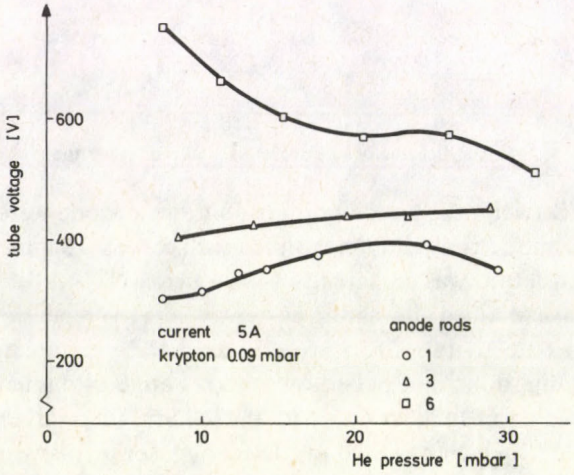

Fig. 4. Dependence of tube voltage on He pressure in hollow anode–cathode tubes with a different number of internal anode rods

Measurements were performed on the laser output power as a function of different discharge parameters in tubes having various anode rod numbers. The main results are summarized in Table II. It can be seen from the Table that laser threshold current decreases and output power increases with the increasing number of anode rods. Laser efficiency that is output power/input electrical power shows an optimum in the case of the three rod system. In the following some data measured in this tube are given.

Table II

Hollow anode–cathode He–Kr ion laser
$\lambda = 469.4$ nm; $P_{He} = 23$ mbar; $P_{Kr} = 9 \times 10^{-2}$ mbar

Number of anode rods	Tube voltage[a] [V]	Threshold current [A]	Output power[a,b] [mW]	Efficiency $\times 10^{-5}$
1	390	3.3	12	0.45
3	450	2.3	35	1.1
6	590	2.2	38	0.92

[a] At 7A discharge current;
[b] Using output mirror with 1% transmission

Figure 5 shows laser threshold current as a function of He pressure at different Kr partial pressure values. It can be seen that minimum threshold current occurs in the 10–15 mbar He pressure range. It is noted that in the case of six anode rods minimum threshold current was 0.9 A, while using twelve anode rods it decreased to 0.7 A.

Figure 6 shows tube voltage as a function of He pressure. Comparing Fig. 6 to Fig. 5 it seems that minimum voltage at a given current occurs in the same range as where minimum threshold current is observed. The accuracy of the data is not enough, however, to conclude whether these two minima coincide exactly or not.

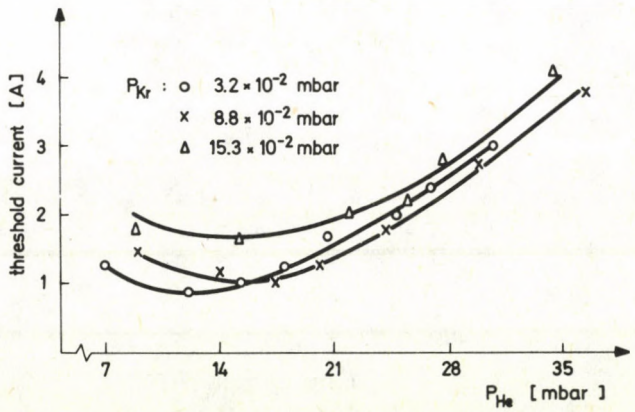

Fig. 5. Laser threshold current as a function of He pressure (3 anode rods)

The dependence of laser output power on He pressure is shown in Fig. 7. At 5 A discharge current the optimum He pressure is 24–28 mbar slightly depending on the value of Kr partial pressure. The measurements performed at different currents have shown that optimum He and Kr partial pressure depend on the value of discharge

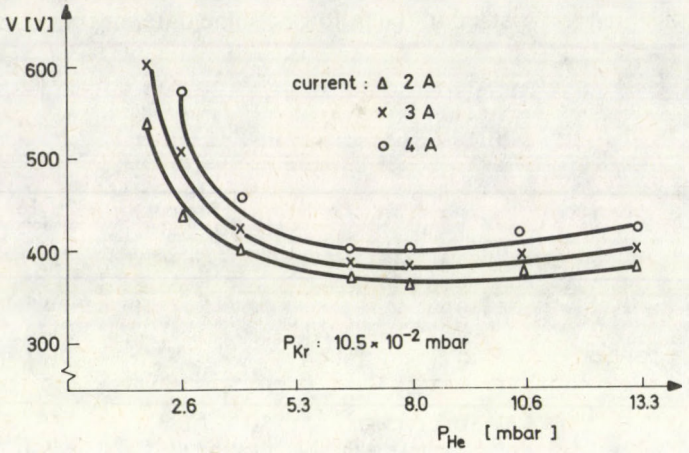

Fig. 6. Tube voltage as a function of He pressure (3 anode rods)

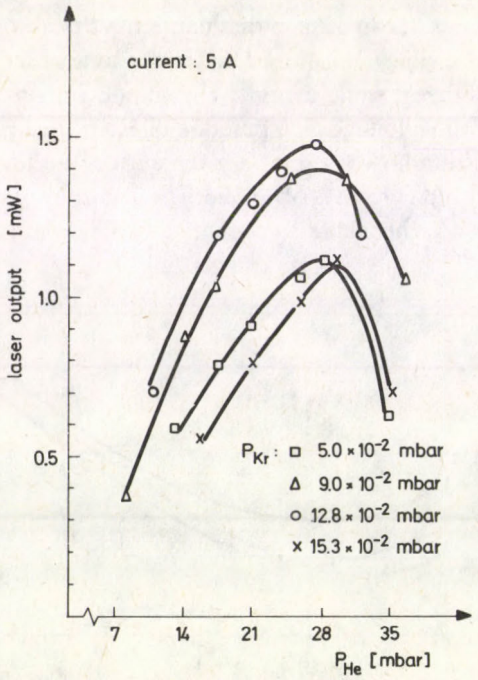

Fig. 7. Dependence of laser output power on He pressure (3 anode rods)

Table III

Hollow anode–cathode He–Kr ion laser
$\lambda = 469.4$ nm, 3 anode rods

Discharge current [A]	3	5	7	9
Tube voltage [V]	405	435	465	510
Optimum Kr partial pressure [10^{-2} mbar]	8.5	11	12.5	18.5
Optimum He partial pressure [mbar]	23	24.5	31.5	41
Output power[a] [mW]	0.9	1.8	2.1	2.7

[a] Using high reflectivity output mirror with 0.1% transmission

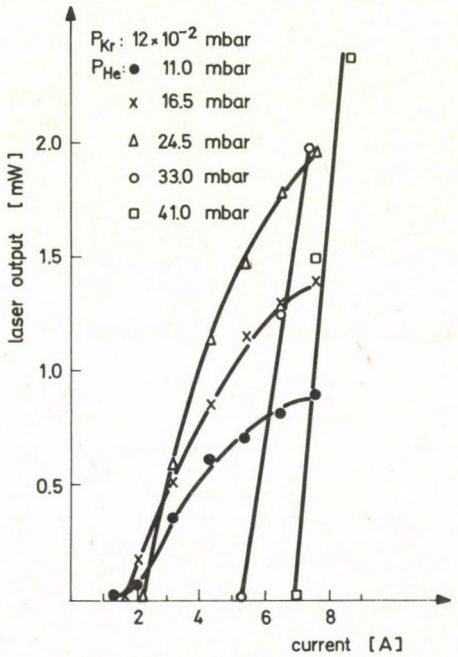

Fig. 8. Dependence of laser power on discharge current (3 anode rods)

current. The results obtained are summarized in Table III, where output power obtained with high reflectivity mirrors is also given. It can be seen from the data that with increasing discharge current tube voltage, optimum He and Kr partial pressure increases and maximum output power is obtained, when all these values are at the possible maximum. This result is shown in a different way in Fig. 8, where laser power is plotted as a function of discharge current at different He pressure parameters. At low He pressure the threshold current is low and laser power saturates with increasing

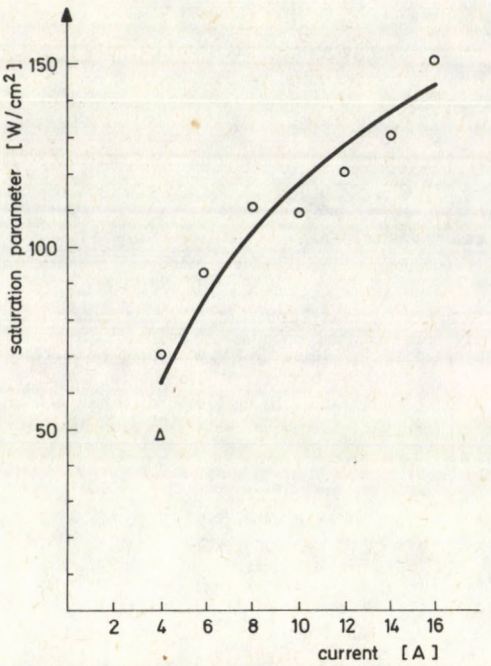

Fig. 9. Saturation parameter as a function of discharge current (6 anode rods)

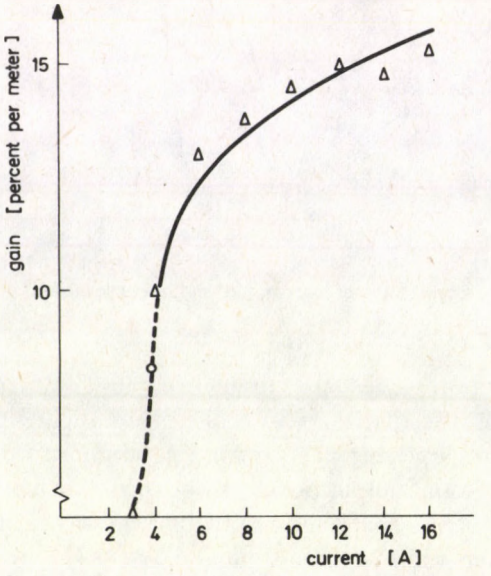

Fig. 10. Gain as a function of discharge current (6 anode rods)

discharge current. At high pressures the situation is different, however, threshold current is high and laser power increases very rapidly with increasing discharge current and no saturation occurs in the current range investigated. In this case at a He pressure 41 mbar and Kr pressure 0.18 mbar using an output mirror of 2.3% transmission at 10 A discharge current 66 mW output power was measured. In accordance with data given in Table II in the six rod system 75 mW power output was obtained. Using quasi-cw excitation with 100 μs halfwidth 20 A current pulses a peak output power of 450 mW was measured, in this case tube voltage in the six rod system was 1 kV and the He pressure was 26 mbar.

Measurements were performed in the six rod system on the gain and saturation parameter of the 469 nm laser transition as a function of discharge current. These data were obtained from measuring output power as a function of loss produced by rotating a quartz window inside the laser resonator [9]. In this measurement a big advantage of the He–Kr laser system was that due to the large pressure broadening, the 469 nm transition has a homogeneous linewidth and oscillates only in a single axial mode. For measurement of the saturation parameter TEM_{00} mode operation was produced by inserting a diaphragm in the resonator. Excitation of the laser tube was quasi-cw with 100 μs halfwidth current pulses. The results of measurements are shown in Fig. 9 and Fig. 10. It can be seen from Fig. 9 that the saturation parameter increases with increasing discharge current and reaches a value of 150 W/cm^2 at 16 A peak current. Fig. 10 shows gain as a function of current, a value of 16%/m is measured at 16 A. Gain increases slower than linear with increasing discharge current, while the increase of output power is linear. Considering that output power is qualitatively proportional to the product of gain and saturation parameter since the latter increases also slower than linear the product of them gives approximately a linear dependence.

4. Discussion

The measurements performed in similar configuration hollow anode–cathode tubes with a different number of internal anodes show a gradual increase of voltage with increasing rod number and at the same time a significant change occurs in laser parameters. The increasing voltage is related to an increasing density of high energy electrons and this results in the observed change in laser data.

Considering the excitation mechanism of the 469 nm laser transition the following can be said. The upper laser state is excited by second kind collisions between He 2^3S metastables and ground state Kr ions. The electron excitation cross-section of the He 2^3S metastables is maximum near threshold energy and drops with increasing energy, so although the higher density of high energy electrons increases somewhat the metastable density, this effect is not too large. The main effect of the high energy electrons in the HAC discharge is the increased production of Kr ions by electron impact. The cross-section of this ionization process has a broad peak at 80 eV and

significant ionization can occur at high energies, too [10]. It was shown in [11] that the role of Penning ionization in producing Kr ions by collisions with He metastables is comparable to electron impact only in positive column discharges with Maxwellian electron energy distribution, but here up to now no cw laser oscillation has been observed at 469 nm. Thus the observed decrease of threshold current and increase of laser power by increasing voltage in the He–Kr HAC discharge may be attributed to increased production of Kr ions by electron impact.

It was observed in the tube with medium increased voltage (3 rods) that minimum laser threshold current falls in the pressure range where the hollow cathode effect occurs, that is at a constant discharge current a minimum is found in tube voltage as a function of He pressure. It is not clear whether this observation is a consequence of any basic phenomenon or not. We note that the maximum stability of hollow cathode discharges against glow to arc transitions was observed also to fall in this pressure region.

The increase of threshold current with increasing He pressure can be explained by change in the radial distribution of the light intensity produced by the discharge; the changes in atomic excitation process rates are less significant in producing this variation of threshold current. It was observed that at high He pressures and at low currents the central part of hollow cathode discharges is dark, the negative glow has a ring form and a certain discharge current is needed to make this region bright, to get the negative glow to fill the whole tube cross-section. It is clear that laser oscillation can only occur in this latter condition and by increasing He pressure high currents are needed to fulfil the condition of the negative glow filling the whole discharge tube cross-section, thus the laser threshold current has to be higher, too. Optimizing tube diameter and pressure together are important to reach low current operation.

An interesting feature is that if the discharge current is considerably higher than threshold values then the optimum He pressure significantly differs from the value where threshold current is minimum. In the low pressure region laser power saturates with increasing discharge current and at high pressures this is not observed. The reason of saturation could be increased ionization of He from the 2^3S metastable state and increased production of double ionized Kr from the single ionized state, both processes occurring by electron impact. The rates of these processes are high in the low pressure region due to the large density of high energy electrons. At higher pressures due to the smaller density of energetic electrons the rates of the mentioned loss processes for He 2^3S metastables and Kr ions decreases and saturation of laser power does not appear in the current region investigated. It is possible that in the saturation of laser power the effect of sputtered cathode material plays also a role, the amount of metal vapour due to sputtering is smaller at high pressures.

Considering optimum discharge parameters for laser operation it can be concluded that in the range investigated up to 1 kV voltage laser power can be increased. Regarding practical aspects maximum efficiency occurs at only a medium increase of tube voltage, however. In a given system then the optimum gas fill values are

determined by the discharge current of the tube. Optimum He and Kr partial pressure values increase with discharge current, which is believed to be connected to the condition for the negative glow to fill the whole tube cross-section. At higher discharge currents the bright discharge in the central region of the tube can be reached at higher He and Kr pressure values. This results in more He 2^3S metastables and Kr ions, which leads to a higher degree of population inversion and more laser output power.

The change of the saturation parameter with current can be attributed to the change of the spontaneous linewidth due to increased temperature or some other broadening mechanism. Further measurements are necessary to clarify details of this problem.

5. Summary

Laser output power as a function of discharge parameters was investigated in hollow anode–cathode tubes with a different number of internal anodes. It was found that the three anode rod system resulting in a medium increase of tube voltage gives output power increase with best efficiency. Optimum gas filling data were found to depend on discharge current. High laser output power can be reached in high current–high pressure hollow anode–cathode tubes. Although the blue 469 nm laser transition is perspective in building hollow anode–cathode lasers for practical uses, significant efforts are still required to construct lasers for this aim, since special tube technology is needed, which is not yet developed. The features observed of the hollow anode–cathode He-Kr laser refer only to the noble gas mixture systems. Some experiments indicate that other noble gas–metal vapour lasers having a different excitation mechanism behave differently in increased tube voltage hollow cathode discharges [12–14].

Acknowledgements

The work was supported by the State Office for Technical Development. Thanks are due to Mr. J. Tóth, Mr. A. Majorosi, Mr. Gy. Császár and Miss J. Forgács for their valuable work in constructing the laser tubes and for help in the measurements. The contribution of Mr. T. Adamowicz (Warsaw Technical University) to this series of investigations is also acknowledged.

References

1. M. Jánossy, L. Csillag, K. Rózsa and T. Salamon, Physics Letters, *45A*, 379, 1974.
2. M. Jánossy, L. Csillag and K. Rózsa, Physics Letters, *63A*, 84, 1977.
3. K. Rózsa, M. Jánossy, J. Bergou and L. Csillag, Optics Communications, *23*, 15, 1977.
4. K. Rózsa, Reports of the Central Research Institute for Physics, KFKI-1975-63.
5. T. Iijima, Japanese Journal of Applied Physics, *20*, L470, 1981.
6. M. Grozeva and N. V. Sabotinov, Optics Communications, *41*, 57, 1982.
7. K. Rózsa, J. Bergou, M. Jánossy and J. K. Mizeraczyk, Reports of the Central Research Institute for Physics, KFKI-1979-15.
8. K. Takasu, T. Goto and S. Hattori, Physica, *113C*, 271, 1982.
9. B. S. Patel, Sh. Charan, A. Mallik and P. Swarup, Journal of Physics D, Applied Physics, *7*, L40-44, 1974.
10. F. Egger and T. D. Märk, Proceedings of the Symposium on Atomic and Surface Physics, Tirol, 1978, p. 51.
11. M. Jánossy and P. Tuovinen, Acta Phys. Hung., *46*, 167, 1979.
12. K. Rózsa, M. Jánossy, L. Csillag and J. Bergou, Physics Letters, *63A*, 231, 1977.
13. K. Rózsa, M. Jánossy, L. Csillag and J. Bergou, Optics Communications, *23*, 162, 1977.
14. J. Mizeraczyk, J. Konieczka, J. Wasilewski and K. Rózsa, Proceedings of International Conference "Lasers 80", New Orleans, 1980, p. 177.

Acta Physica Hungarica 56 (1—4), pp 159—170 (1984)

CRYSTALLIZATION PROCESS OF NATURAL IRON ORES IN QATAR

H. A. SALLAM*, N. A. EISSA* and H. A. SALEH

Mössbauer Laboratory, Physics Department, Faculty of Science
University of Qatar, Doha, Qatar

(Received 20 May 1983)

A very surprising anisotropy in the magnetic hyperfine interaction was observed in the Mössbauer effect spectra of some iron ore deposits in Qatar (Arabian Gulf). This was attributed to the presence of the stable as well as the metastable states of the oxyhydroxide (α-FeOOH) in the ore (glassy, mesocrystalline and holocrystalline).

The ordering temperatures for the magnetic and superparamagnetic particles were defined. The decomposition of the metastable forms of the oxyhydroxide to metastable forms of the oxide (α-Fe_2O_3), which is a new observation in the natural phenomena, was investigated. The increase in the crystallinity of the oxide during growth was followed up.

The physical and geochemical conditions of formation of the different iron ore deposits, as well as their relative geological ages, were evaluated.

Introduction

The usefulness of the Mössbauer effect technique in the study of mineralogical systems has been demonstrated in a large number of literatures through the past two decades. In view of the great importance of iron in the earth's crust and the widespread occurrence of this element in rock-forming minerals, we are interested in applying this technique for studying local iron ores. The ME technique has been successfully used in the study of Egyptian iron ore deposits which included goethite, heamatite, pyrite and chalcopyrite (Eissa et al [1, 2]). These studies provided important information about the chemical and physical properties of the different forms of iron in each deposit and the influence of the geochemical conditions of formation on these properties.

The present work deals with the use of the ME technique in the study of the recently discovered iron ores in the State of Qatar (Arabian Gulf), in order to reveal some information about the fine properties of these ores.

* Permanent address: Mössbauer Laboratory, Physics Department, Faculty of Science, Al-Azhar University, Cairo Egypt.

Experimental details

The iron-ore samples used in the present study were collected from Haloul (Haloul-1 and Haloul-2) and Sauda Nathil localities. They were provided by the Geology Department of Qatar University and the Qatari Industrical Development Technical Centre. The ME measurements and X-ray diffraction analysis have been carried out on a set of representative samples taken from each of the three deposits.

The ME measurements were performed at different temperatures ranging between the liquid nitrogen temperature to 67 °C. In addition, the samples were annealed for two hours at different temperatures up to 1100 °C and were then measured at room temperature. The ME absorbers were prepared from the finely powdered material so that the natural iron abundance in the absorber was $\sim 15\ \mathrm{mg\ cm^{-2}}$. The channel for zero Doppler velocity between source (30 mC ^{57}Co in palladium matrix) and the absorber was specified using a laser system. The curves were fitted using a computer programme.

Results

The X-ray diffraction results revealed that the Haloul-1 deposit is entirely composed of heamatite (α-Fe_2O_3), while Haloul-2 is composed of goethite (α-FeOOH). On the other hand, the X-ray results of the Sauda Nathil deposit revealed only the three strongest lines characteristic of goethite (Fig. 1).

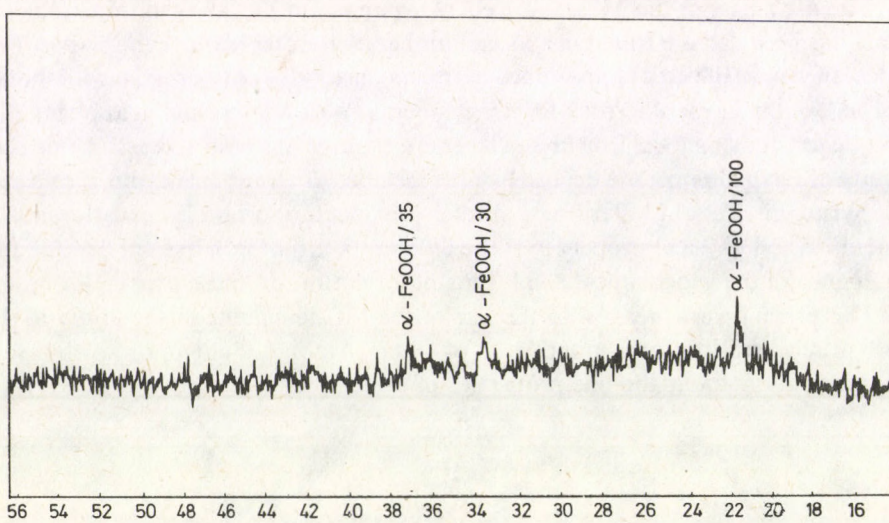

Fig. 1. X-ray diffraction pattern of a representative sample of Sauda-Nathil ore. Only the three strongest lines, characterizing goethite, have appeared

Table I

ME parameters of representative samples from the different iron ore deposits

Temperature	Haloul-1				Haloul-2				Sauda-Nathil			
	H [kOe]	*Q.S.* [mm/s]	*I.S.* [mm/s]		*H* [kOe]	*Q.S.* [mm/s]	*I.S.* [mm/s]	Fe%	*H* [kOe]	*Q.S.* [mm/s]	*I.S.* [mm/s]	Fe%
L.N.	533	0.684	0.309		519	0.720	0.244		527	–	–	
				A				38	512	0.760	0.215	27
					512	0.720	0.244		507.5			
					474	0.684	0.282		463	–	–	
				B	462	0.760	0.282	62	455	0.494	0.114	73
					450	0.760	0.244		425	–	–	
					419.5	0.836	0.244		404	–	–	
R.T.	517.5	0.413	0.384		507	0.416	0.232		515	0.416	0.258	
				A	407	0.416	0.284		507	0.416	0.284	
					484	0.416	0.258		495	0.468	0.232	
					460	0.416	0.258		484	0.468	0.258	
					373	0.416	0.284		458	0.468	0.206	
					361	0.416	0.284		353	0.416	0.284	
				B	|				340	0.468	0.271
					251	–	–		319	0.468	0.284	
									|			
									193	–	–	

Error in velocity scale $= \pm 0.052$
Error in fields $= \pm 1.6$

Error in Fe percentage $= \pm 2$
I.S. with respect to Pd matrix

The room temperature ME results of Haloul-1 samples showed a simple six-lines pattern with parameters characteristic of a well-crystallized, bulk heamatite (Fig. 2 and Table I). On the other hand, the spectra of Haloul-2 and Sauda Nathil samples showed complicated magnetic patterns with many relaxed and superimposed lines (Fig. 3). The analysis of the spectra obtained revealed the presence of two different groups of magnetic patterns and a central paramagnetic doublet of small intensity. For Haloul-2

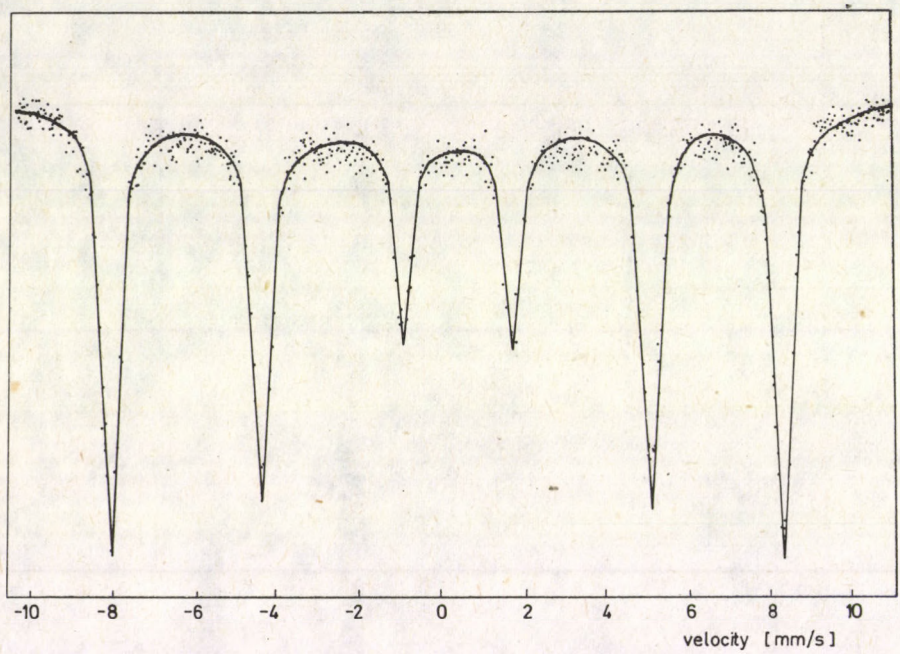

Fig. 2. Room temperature ME spectrum of Haloul-1 ore

samples, the first group of patterns (A) could be resolved into four different magnetic patterns, having fields ranging from 507 kOe to 460 kOe. All the patterns have nearly the same quadrupole splitting and very close values of isomer shifts (Table I). The second group (B) showed a broader distribution of the fields to much reduced values. Only two patterns of group (B) could be resolved. They have field values of 373 and 361 kOe and their quadrupole splitting and isomer shift are similar to those of group (A). The value of the smallest field in group (B) could be estimated from the separation between the innermost two lines surrounding the paramagnetic doublet by applying the ratios 0.16 : 0.58 : 1.00 for the separation between the three doublets of the field (van der Woode [3]). The spectra of Sauda Nathil samples showed the same two groups of magnetic patterns (A & B), but with a larger number of distributed fields and more reduced values for the fields of group (B).

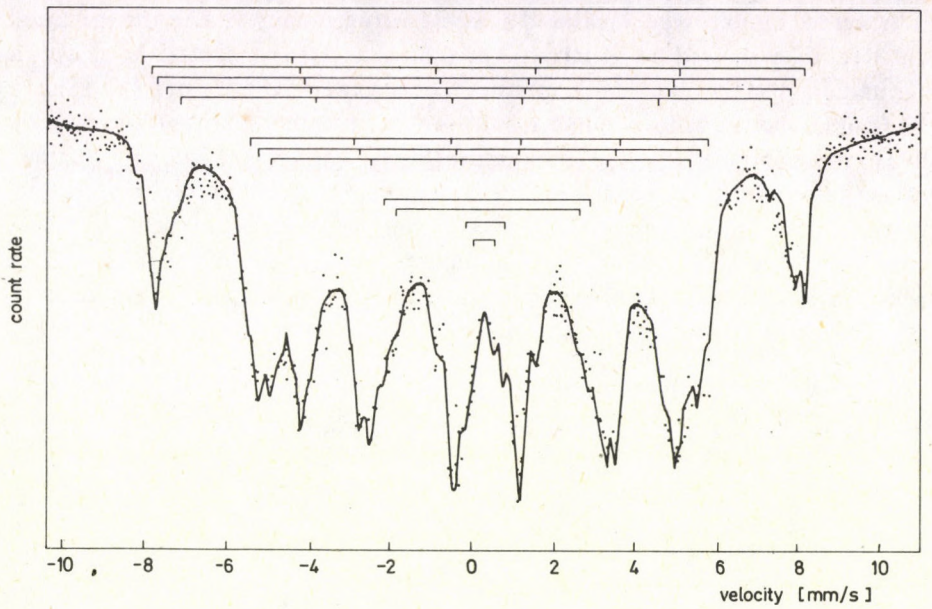

Fig. 3. Room temperature ME spectrum of a representative sample of Sauda-Nathil ore. Two different groups of many superimposed magnetic patterns could be observed

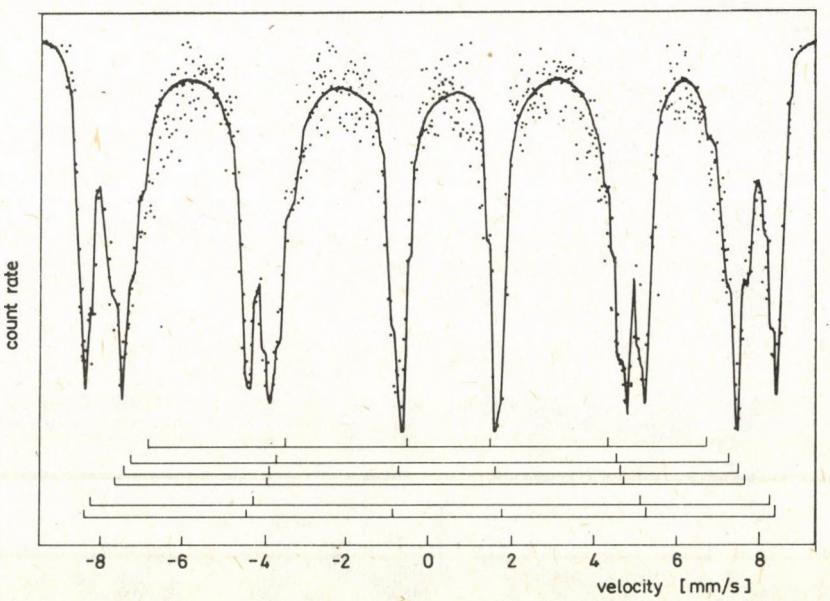

Fig. 4. ME spectrum of Haloul-2 ore at liquid nitrogen temperature. Recovery of the magnetic properties of the superparamagnetic grains is obvious

When the samples were measured at liquid nitrogen temperature, the spectra of Haloul-1 samples showed some increase in the value of the magnetic field, with a change in the sign of the quadrupole splitting. The spectra of both Haloul-2 and Sauda Nathil samples showed a more compact and less relaxed pattern for the groups (A & B), relative to those obtained at room temperature (Fig. 4). The fields of group (A) attained very close values which are slightly higher than those obtained at room temperature. The values of the fields of group (B) showed a more remarkable increase (463–404); however they were still smaller than the values characteristic of goethite at such temperatures (Hrynkiwicz et al [4] and Szytuca et al [5]. Although the parameters of

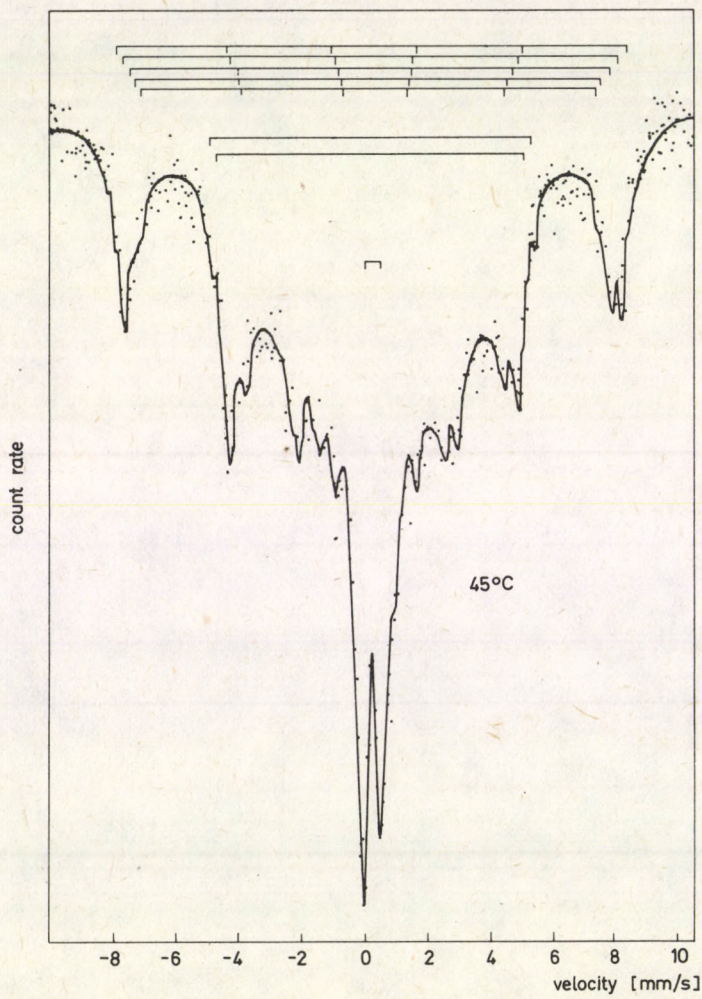

Fig. 5. ME spectrum of a Sauda-Nathil sample at 45 °C. An increase in the intensity of the central paramagnetic doublet, due to the disordering of some of the goethite components, is seen clearly

group (A), at both room and liquid nitrogen temperatures, are in the order of those characterizing heamatite, the Morin transition (Kunding et al [6]) was not observed for Haloul-2 or Sauda Nathil samples.

When Haloul-2 and Sauda Nathil samples were measured at temperatures slightly higher than room temperature, the intensity of the central doublet began to

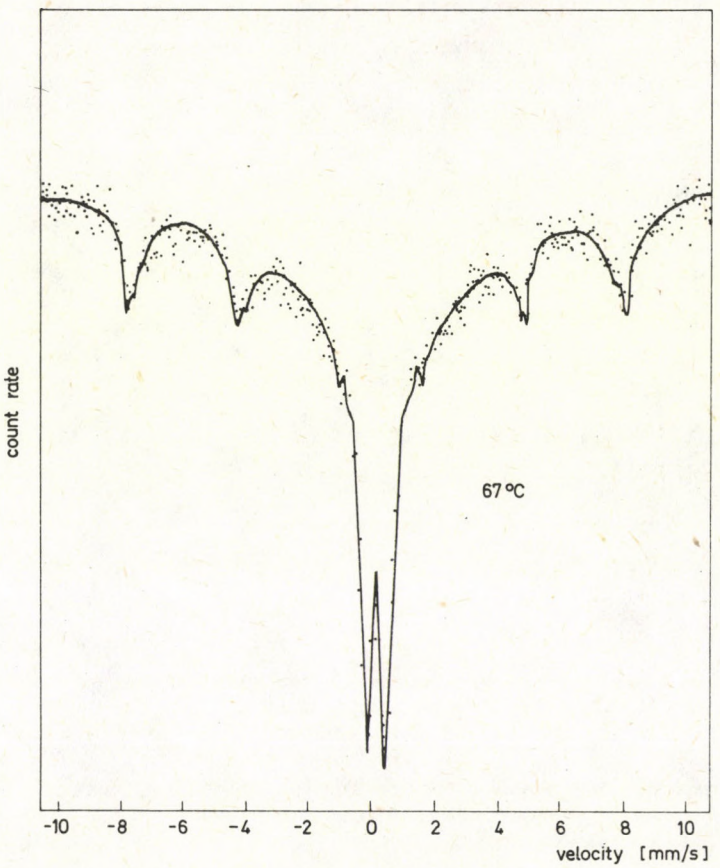

Fig. 6. ME spectrum of Sauda-Nathil ore at 67 °C. All goethite present has been transformed to its paramagnetic state

increase with a corresponding collapse in the different magnetic components of group (B) (Fig. 5). Further heating resulted in a continuous disordering of the different components of group (B) at different temperatures. Disordering of all the components was completed at 67 °C (Fig. 6).

The spectra of the pre-annealed Haloul-2 and Sauda-Nathil samples showed the disappearance of the group (B) lines and an accompanying increase in the number and

intensity of group (A) lines (Fig. 7). These changes, which are due to the decomposition of goethite to heamatite, began at ~223 °C. This temperature is much lower than that at which the bulk, well-crystallized goethite starts to decompose to heamatite, 350–390 °C. (Mackenzie [7]).

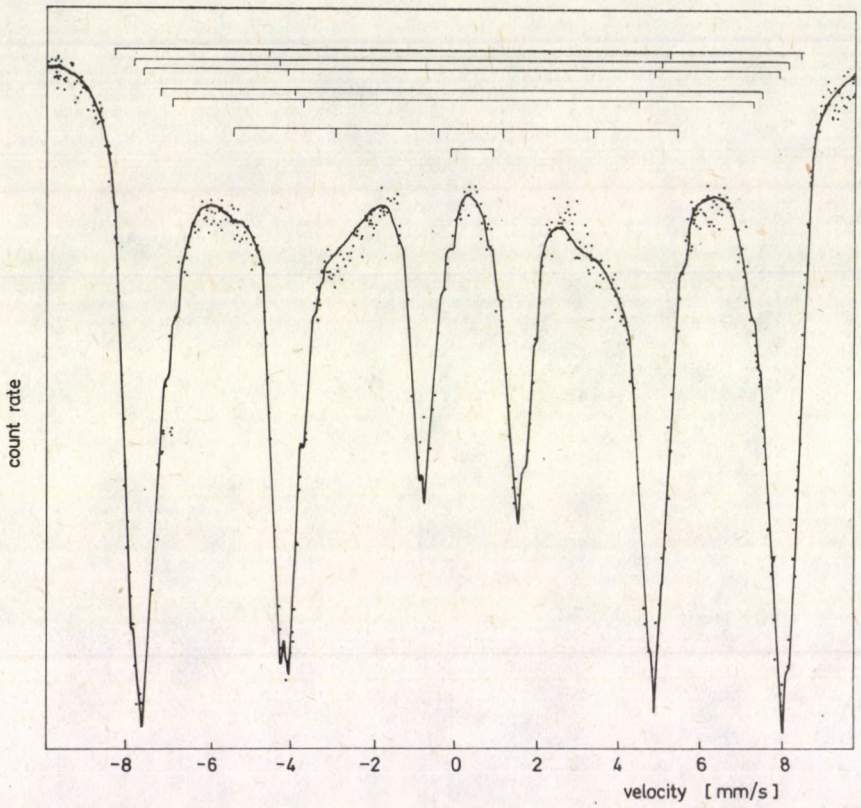

Fig. 7. Room temperature ME spectrum of a Haloul-2 sample preannealed at 225 °C for 2 hours. Most of goethite has been decomposed to heamatite

The increase in the annealing temperatures resulted in an increase in the compactness of the group (A) composite patterns. This was due to a systematic increase in the values of the smaller fields to join the larger ones (Figs 8 and 9). After annealing the samples at 800 °C, a single magnetic pattern, having the parameters characteristic of the well-crystallized heamatite, was obtained.

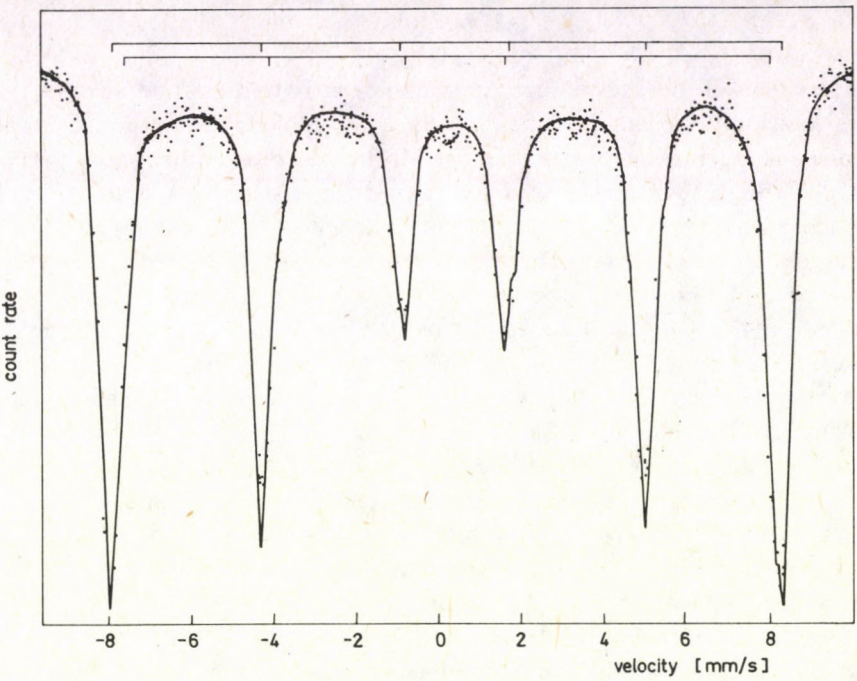

Fig. 8. Room temperature ME spectrum of a Haloul-2 sample preannealed at 700 °C for 2 hours. All heamatite components joined up the two ones of largest fields

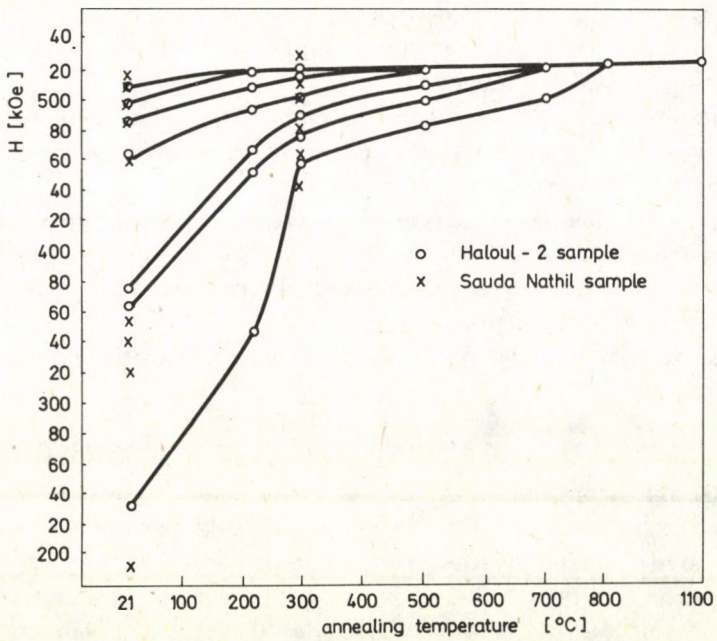

Fig. 9. The relation between the annealing temperature and the magnetic components present in the ores of Haloul-2 and Sauda-Nathil deposits. The fields for the goethite grains, having sizes near to the critical one, could not be resolved before annealing.
The decomposition of metastable forms of goethite to metastable forms of heamatite and the growth of the different metastable forms of heamatite to the final stable form could be observed

Discussion

The values of the fields of Haloul-1 samples, at both room and liquid nitrogen temperatures, and the change of the sign of the quadrupole splitting when the samples were cooled to a temperature less than the Morin transition temperature (~ 260 K), indicate that this deposit contains ordered haematite. At Morin temperature, the spins change their direction and the oxide transforms from antiferromagnetic at low temperatures to a weak ferrimagnetic above the so-called Morin temperature (Greenwood and Gibb, [8]). The presence of a well crystallized heamatite is in agreement with the X-ray results obtained for the same deposit. On the other hand, the results of the X-ray diffraction and the ME of Haloul-2 and Sauda Nathil samples, showed some remarkable discrepancies and revealed many questionable characteristics which can be summarized as follows:

(i) The X-ray data showed the presence of goethite as the sole iron mineral, while the ME results revealed the presence of both goethite and heamatite.
(ii) The ME results showed that goethite is considerably abundant; however, it is represented in the X-ray diffraction patterns, expecially for Sauda Nathil samples, by very few lines.
(iii) The magnetic behaviour of the minerals is anisotropic.
(iv) Goethite is composed of many components. These components acquired their magnetic ordering over a wide range of temperatures which are much lower than the normal temperature (~ 120 °C, van der Woode and Dekker [3]).
(v) The different components of goethite decomposed to heamatite at unusually low temperature. Moreover, the resulting heamatite has abnormal properties.
(vi) Heamatite lacks Morin transition.
(vii) Heamatite is represented by different components, having different field values. Upon annealing the fields with the smaller values showed a systematic increase and joined the larger ones.

The above peculiar magnetic properties of the investigated iron minerals can be explained by the assumptions:

(i) The minerals possess a wide range of particle sizes and/or
(ii) The minerals have a wide range of crystallinities.

The particle size is known to affect the electron spin relaxation time, according to the equation:

$$\tau = \tau_0 \exp(KV/kT),$$

where K is the anisotropy constant, V the particle volume, T the absolute temperature and k the Boltzmann constant. In the investigated deposits, particles with sizes close to the critical size ($d_{cr} \sim 17.0$ nm (170 Å)) for goethite at room temperature, Suzdalev [9]) will have electron spin relaxation time in the order of the nuclear Larmor precession time; hence they produce the broadened and relaxed lines. The paramagnetic doublet resulted from the particles, having sizes less than the critical size (Eissa et al [10]). On

the other hand, particles with sizes larger than the critical size are responsible for the normal magnetic patterns.

The deviation in the magnetic properties of synthetic goethite was interpreted by Oosterhout [11] to be due to defect structure which leads to a partial breakdown of the antiferromagnetic structure of the crystallites. Van der Woode and Dekker [3] emphasized the possibility of the presence of the same varieties in naturally occurring goethite. In α-FeOOH with a defect structure, the chains of antiferromagnetically coupled ferric ions along the X-axis are interrupted. If the clusters in these chains are small enough, the reversal frequency of the sublattice magnetization may become of the same order of magnitude as Larmor precession frequency. This effect, which is already observed in the Mössbauer spectra of superparamagnetic particles, leads to broadening of the absorption peaks, a decrease of the effective magnetic field and finally to a complete destruction of the hyperfine structure below the Neel temperature of a well-crystallized material. According to the studies of Oosterhout [11] and Van der Woode [3] it can be strongly suggested that the observed properties of the investigated iron deposits are the result of the presence of particles having different states of crystallinities (glass, crystallites, microlites and holocrystalline crystals). These represent the whole range of metastable to stable states (Tyrrell, [12]).

In the present work, it is thought that the crystallinity factor contributed much more than the particle size factor in affecting the iron-minerals' behaviour. However, this does not imply that the particle-size factor did not play a considerable role. An important criterion for the effect of crystallinity factor is the sudden decomposition of goethite to heamatite at abnormally low temperature. Moreover, the pattern of the resulting heamatite indicated the presence of a wide range of crystallites and stabilities which, upon heating, gradually changed into the stable well-crystallized form.

The heamatite lacking Morin transition, which is reported in Haloul-2 and Sauda-Nathil samples, most probably originated under a rapid rate of formation. Riederer [13] emphasized that slow oxidation under mildly oxidizing conditions and at a fairly low temperature is favourable to the growth of heamatite crystallites that are large enough to yield a ME pattern typical for antiferromagnetic heamatite.

Conclusions

The results obtained in the present work reveal that the iron ore deposits in Qatar are either composed entirely of heamatite or a mixture of heamatite and goethite. Heamatite, which occurs as a sole constituent in some deposits, acquires a high degree of crystallinity and large particle size and, hence, normal magnetic properties. On the other hand, heamatite which accompanies goethite, possesses a wide range of crystallinity and particle size resembling in this aspect goethite; both showing many peculiar characteristics.

The mode of occurrence of the different iron deposits indicates that they were originally composed of goethite and heamatite deposited under normal sedimentary conditions. However, some of these deposits were taken on and invariably subjected to sudden heating and cooling conditions of complicated nature (mostly by the effect of younger basalt flows which are known to exist in the area studied). These conditions resulted in the change of the iron minerals to their amorphous and highly disordered states. As time elapsed, goethite crystallites and microlites of abnormal nature started to develop (Tyrrell, [12]). A considerable part of these metastable forms was transformed into a corresponding abnormal heamatite before achieving their normal crystalline states.

Taking into consideration the degree of crystallinity and the relative abundances of goethite and heamatite in the investigated deposits, and realizing the effect of the time factor on these aspects, it can be predicted that the Haloul-2 deposit is older than the Sauda-Nathil one; both are younger than the Haloul-1 deposit.

The present work clearly shows the usefulness and effectiveness of the Mössbauer effect technique in solving many problems concerning natural ores.

Acknowledgements

The authors are grateful to Professor Dr. M. A. Gneith, Geology Department, Boston University, Mass. (U.S.A.). and Dr. M. M. Abu-Zeid, Geology Department, Faculty of Science, University of Qatar, for interesting discussions.

References

1. N. A. Eissa, H. A. Sallam, S. S. Gomaa, S. A. Saleh and Z. Miligy, J. Phys. D.: Appl. Phys., 7, 2121, 1974.
2. N. A. Eissa, H. A. Sallam, M. M. El-Ocker, E. A. Mahmoud and S. A. Saleh, J. de Phys., *37*, no. 12, C6-793, 1976.
3. F. van der Woode and A. J. Dekker, Phys. Stat. Sol., *13*, 181, 1966.
4. Az. Hrynkiewicz, D. S. Kulgawczuk and K. Tomala, Phys. Lett., 1793, 1965.
5. A. Sztuca et al.: Inst. Nucl. Phys. Cracow, Rep. no. 486/PS, 1966.
6. W. Kunding, H. Bemmel, G. Constabaris and R. H. Lindquist, Phys. Rev., *142*, 327, 1966.
7. R. C. Mackenzie, Min. Soc. London, 1957.
8. N. N. Greenwood and T. C. Gibb, Mössbauer Spectroscopy, Chapman and Hall Ltd., London, 1971.
9. I. P. Suzdalev, Proc. Conf. App. Mössbauer Effect, Tihany, 193, 1969.
10. N. A. Eissa, H. A. Sallam and B. A. Ashi, J. de Phys., *40*, no. 3, C2-499, 1979.
11. G. W. Oosterhout, Proc. Int. Conf. of Magnetism, Nottingham, 529, 1964.
12. G. W. Tyrrell, The Principles of Petrology, Methuen and Co. Ltd., London, 1941.
13. J. Riederer, U. Wagner and F. E. Wagner, Radiochem. and Radioanal. Letters, 1981.

Acta Physica Hungarica 56 (1—4), pp 171—175 (1984)

LUMINESCENCE CENTRE RESPONSIBLE FOR ULTRAVIOLET EMISSION IN KCl:Sr CRYSTALS

N. L. KEKAN and N. A. PATIL

Department of Physics, Faculty of Science, M. S. University of Baroda Baroda 390 002, India

(Received 26 May 1983)

The luminescence spectra of potassium chloride phosphors doped with strontium have been studied in microcrystalline powder specimens as-received and thermally treated with varying amounts of strontium content, with the help of Aminco Bowmann spectrophotofluorometer. From the detailed examination of the excitation and emission spectra of these specimens, it is concluded that the emission at 320 nm is presumed to consist of dipoles being situated in the strained region of a dislocation at a distance where only elastic interaction is of significance.

Introduction

A small amount of strontium introduced into an alkali halide produces a luminescent material of considerable fundamental interest. Much experimental and theoretical work has therefore been reported on the luminescence of thallium-doped alkali halide phosphors and a little on divalent impurities (Ca, Ba, Sr and Pb etc.) doped in alkali halide phosphors. According to the Seitz, Williams and Joshi et al [1–5] theory, thallium or strontium ions replacing a cation in the host lattice act as a luminescence centre. This model could satisfactorily explain many of the features arising in lightly as well as heavily doped phosphors. At higher strontium concentration ($\approx 10^{-4}$ m.f. and above) one has, however, to deal with a more complex problem. The present work arises out of an attempt to understand the luminescent behaviour of the KCl:Sr phosphor in more detail. The experiments involved the study of the excitation and emission spectra of variously pre-treated KCl:Sr phosphors differing in Sr concentration. All the measurements were made at room temperature.

Experimental details

The samples used in the present study were microcrystalline in nature, prepared by the usual method of crystallization from aqueous solution, and contained varying amounts of Sr (from 10^{-4} to 10^{-1} mole fraction). A large number of as-received and pre-treated KCl:Sr specimens were examined for their excitation and emission spectra.

The excitation and emission spectra of these specimens were determined after UV — irradiation at room temperature. The instrument used in the present study was an Aminco–Bowmann spectrophotofluorometer supplied by the American Instrument Co., Inc.

Results and discussion

The present work concerns the investigation of the nature of the centre responsible for luminescence in as-received and heat pre-treated doped potassium chloride. One specimen batch was taken as-received prepared from aqueous solution. Another specimen batch was quenched rapidly to room temperature in a platinum crucible after annealing at 500 °C for 5 h (quenched in air). In yet another pretreatment, KCl:Sr specimens prepared from aqueous solution with different Sr contents were annealed in evacuated and sealed tubes, and slowly cooled to room temperature (0.8 °C/min) after annealing at 500 °C for 5 h. In all cases the excitation and emission measurements were carried out with powder specimens on a Aminco–Bowmann spectrophotofluorometer. The area of the sample exposed to the exciting radiation, the geometry of the experimental arrangments, etc., remain unaltered throughout the course of the experiments. The luminescence output was recorded on Honeywell stripchart recorder. In Figs 1 and 2 Curves 1 and 2 represent the emission spectra of the phosphor with 10^{-2} and 10^{-1} m.f. respectively. In Fig. 3 Curves 1, 2, 3 and 4 represent the emission spectra of the phosphor with 10^{-4} to 10^{-1} m.f. respectively. It is obvious from these Figures that the emission spectra consist of a single dominant band at

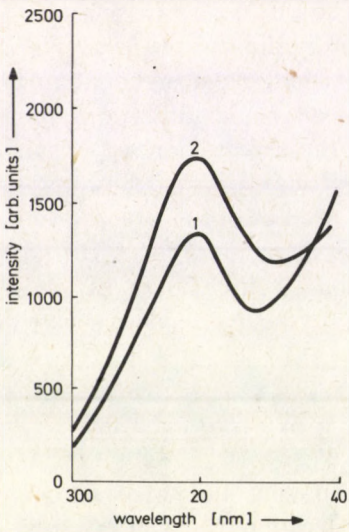

Fig. 1. Emission spectra of KCl:Sr powder phosphor (Curves 1 and 2 as-received from solution with Sr concentration 10^{-2} and 10^{-1} m.f., respectively)

320 nm for 272 to 278 nm excitation. It is worth noting that the emission band is favoured if the heat treatment is carried out in air and in an evacuated sealed tube (compare Fig. 1 with Figs 2 and 3). It was observed that the increase in Sr concentration reduces the emission preferably in the ultraviolet region (compare Curve 2 in Figs 1 and 2, and Curve 4 in Fig. 3).

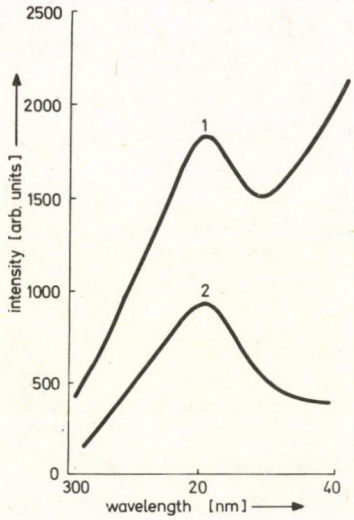

Fig. 2. Emission spectra of KCl:Sr powder phosphor (Curves 1 and 2 annealed in air at 500 °C for 5 h and quenched rapidly to room temperature with Sr concentration 10^{-2} and 10^{-1} m.f. respectively)

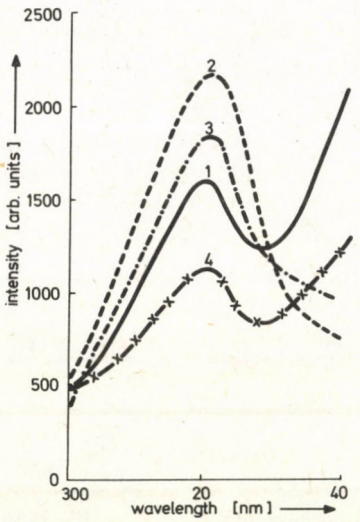

Fig. 3. Emission spectra of KCl:Sr powder phosphor (Curves 1, 2, 3 and 4 annealed in an evacuated and sealed tube at 500 °C for 5 h and slowly cooled at room temperature 0.8 °C/min with Sr concentration 10^{-4} to 10^{-1} m.f. respectively)

The emission spectra for the specimen annealed and quenched from higher temperature, the 320 nm band appears quite prominent. This is due to the fact that a thermal treatment would provide uniform distribution of isolated Sr^{++} ions in the bulk of the specimens. One may therefore conclude that at higher concentration two or more Sr^{++} ions occupy nearest-neighbour positions and thereby cause quenching of the specimen in the ultraviolet region.

From the emission spectra of the annealed and slowly cooled specimen it is inferred that the solubility of Sr in KCl is quite high. Hence at higher Sr concentrations most of the strontium is retained in solid solution by the host lattice even after the specimen is subjected to slow cooling treatment. The emission spectra of annealed and slowly cooled specimens also show a dominant band in the ultraviolet. Slow cooling should bring about aggregation of Sr^{++} ions in the lattice. Hence one would expect in this case Sr^{++} ions in dispersed state in the lattice. This naturally results in exhibiting prominent ultraviolet emission. At higher Sr concentrations the aggregation of Sr^{++} ions will be significant which leads to the destruction of isolated Sr^{++} ions and hence the suppression of ultraviolet emission.

When divalent metal impurity ions are incorporated into an alkali halide lattice, they go in substitutionally for alkali ions [6, 7]. Because of the requirement of charge neutrality, the divalent cation addition is accompanied by the introduction of an equal number of positive ion vacancies. At low temperatures, a large number of divalent ion-positive ion vacancy pairs (dipoles) are formed since their formation lowers the energy of the crystal [8]. Since impurity — vacancy dipoles in alkali halides produce asymmetric strain in the matrix, it has been suggested by Pratt et al [9] that dipole interaction with dislocation mainly accounts for the hardening of the alkali halide crystals. There is now general agreement that below about 500 °C dislocations in alkali halide are negatively charged with a surrounding cloud of positive charges, namely negative ion vacancies. At lower temperatures, divalent impurity ions are significantly associated with their charge compensating cation vacancies and hence instead of free Sr^{++} ion, single dipole or aggregates of dipoles [10, 11] together with the negative ion vacancies will be involved in the cloud formation around dislocations. Dipoles being electrically neutral relative to the KCl matrix, their presence will not affect the sign of the charge cloud surrounding the dislocation and that born by the dislocation itself. Hence it is concluded that the luminescence centre responsible in the region at 320 nm is presumed to consist of dipoles, situated in the strain region of a dislocation at a distance where only elastic interaction is of significance.

Acknowledgement

The authors are highly thankful to Dr. S. K. Shah, Head, Physics Department, for his encouragement.

References

1. F. Seitz, J. Chem. Phys., *6*, 150, 1938.
2. F. E. Williams, J. Chem. Phys., *19*, 457, 1951.
3. R. V. Joshi and L. H. H. Prasad, J. Lum., *15*, 105, 1977.
4. R. V. Joshi and J. K. Wessly, Acta Cryst., *A33*, 344, 1977.
5. R. V. Joshi and J. G. Nene, Indian J. Pure and Appl. Phys., *19*, 1033, 1981.
6. F. Seitz, Rev. Mod. Phys., *26*, 7, 1954.
7. A. B. Lidiard, Handb. Phys. Ed. S. Flügge, Springer Verlag, Berlin, *20*, 246, 1957.
8. A. B. Lidiard, J. Appl. Phys. (Suppl.), *33*, 414, 1962.
9. P. L. Pratt, R. P. Horrison and C. W. A. Newey, Discuss, Faraday Soc., *38*, 211, 1964.
10. J. S. Cook and J. S. Dryden, Aust. J. Phys., *13*, 260, 1960.
11. J. S. Cook and J. S. Dryden, Proc. Phys. Soc., *80*, 479, 1962.

Acta Physica Hungarica 56(1—4), pp 177—184 (1984)

EFFECT OF INVERSE EUTECTOID TRANSFORMATION AND GRAIN SIZE ON THE CREEP BEHAVIOUR OF MILD STEEL

M. R. NAGY, M. M. EL-SAYED and A. A. MOHAMED*

Physics Department, Faculty of Education
Ain Shams University, Cairo, Egypt

(Received in revised form 30 May 1983)

Creep curves were obtained under a constant applied stress, $\sigma = 7$ Kg/mm^2, for mild steel samples with various grain sizes between 660 °C and 750 °C. (The eutectoid temperature (723 °C) falls into this temperature range).

Slightly below the eutectoid temperature, at 710 °C, the creep rate showed a maximum which increased with increasing grain size. This effect was attributed to spherodization, coarsening and dissolution of iron carbide.

In this region the activation energy of steady state creep may be attributed to decomposition of pearlite.

Introduction

In proeutectoid mild steel various processes take place upon heating, i.e. [1–3]:

(i) spherodization, coarsening and dissolution of the carbide phase below the eutectoid temperature, and

(ii) nucleation and growth of the austenite phase and dissolution of the carbide phase above the eutectoid temperature.

These phase transformations proceeding in the proeutectoid structure might be designated as inverse eutectoid transformations.

Several creep mechanisms have been proposed to account for the plasticity associated with the above mentioned transformations:

1. Recovery creep enhanced by the abundance of lattice defects connected with the transformation of ferrite and carbide into austenite [1,4–6];
2. Dislocation creep governed by the interaction and annihilation of dislocation pile-ups at austenite/ferrite, ferrite/carbide [7, 8] interfaces or connected with the segregation of carbon atoms at grain boundaries [9];
3. One of the creep mechanisms during eutectoid transformation of mild steel is diffusional creep. It is associated with the vacancy-carbon migration [10, 11].

* Physics Department, Faculty of Science, Ain Shams University, Cairo, Egypt.

Grain size is known to influence the creep characteristics (especially the strength [12, 13]) of the material which undergoes no transformations. (Refining the grain size in mild steel increases its strength [14, 15].) The aim of the present work is to examine the effect of the grain size and the inverse eutectoid transformation on the atomic mechanisms controlling the creep behaviour of mild steel.

Experimental technique

Mild steel (0.15% C) was obtained from Delta Steel Company, Cairo, Egypt. Its chemical analysis is given in the following Table:

Composition of the tested mild steel in wt %

C	Mn	Si	P	S	Fe
0.15	0.4	0.1	0.05	0.05	balance

The as-received specimens were in the form of wires of gauge length 40 mm and of diameter 0.8 mm with an initial grain diameter of 5 μm. They were preannealed in vacuo at 800 °C for various annealing times (30, 60 and 90 min) followed by slow cooling with an average cooling rate of 2 °C/min, the achieved grain diameters were 10, 15 and 20 μm, respectively. Slow cooling is required to allow the austenite to decompose into ferrite grains and granular pearlite islands. The purpose of this heat treatment is to obtain high ductility and to relieve internal stresses.

Optical microscopy was carried out after etching in 1 pct. Nital. The metallographic micrographs of preannealed samples indicated the formation of primary ferrite grains (see Fig. 1a).

A simple creep lever machine was used for creep tests under a constant stress ($\sigma = 7$ Kg/mm^2) at various temperatures ranging from 660 to 750 °C, increasing in steps of 10 °C to include the eutectoid temperature (723 °C). The creep run was repeated several times on a number of samples until reliable and reproducible results were obtained.

Structural investigation by means of light microscopy and X-ray diffraction were carried out before and after the creep test. To this end the deformed samples were slowly cooled in the vicinity of the eutectoid point.

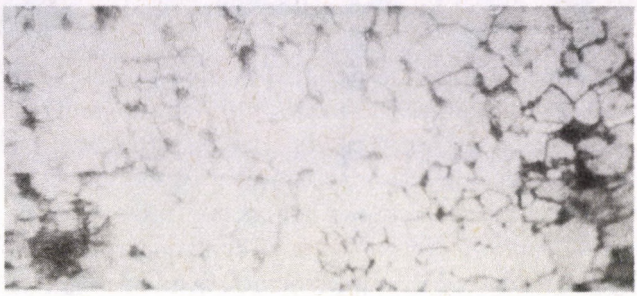

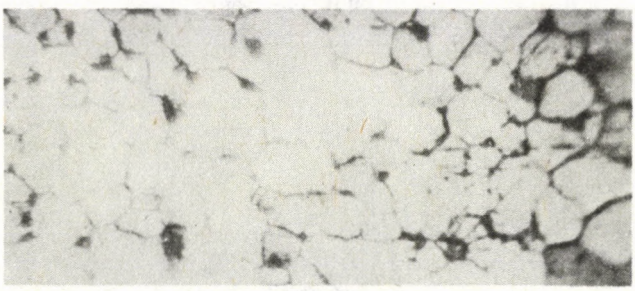

Fig. 1a. Metallographic micrographs on mild steel preannealed at 800 °C for 30, 45, 60 min and cooled at a cooling rate of 2 °C/min (Magnification × 450)

Experimental results

The creep deformation ($\epsilon\%$) was recorded as a function of the creep time (t) for each temperature. The creep curves for samples with various grain sizes are shown in Fig. (1b). The sequence of the creep curves with respect to the temperature was anomalous in the transformation region, i.e. between 700 and 750 °C. This anomaly, in terms of the stationary creep rate, is shown in Fig. 2a. (This rate was determined from the slopes of the linear parts of the creep curves.) The stationary creep rate was affected also by the initial grain size (Fig. 2b): at temperatures below the eutectoid point, the stationary creep rate increased with increasing initial diameter, while at temperatures above this point the rate decreased with increasing *initial* grain diameter.

The energy activating the steady-state creep was found to be independent of the grain size, but it was dependent on the range of the testing temperature (Fig. 3).

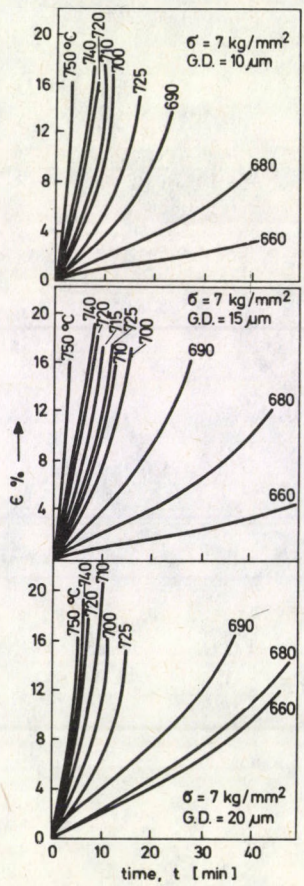

Fig. 1b. Creep curves for mild steels with various grain diameters crept under a constant applied stress of 7 kg/mm² in the temperature range of 660 and 750 °C

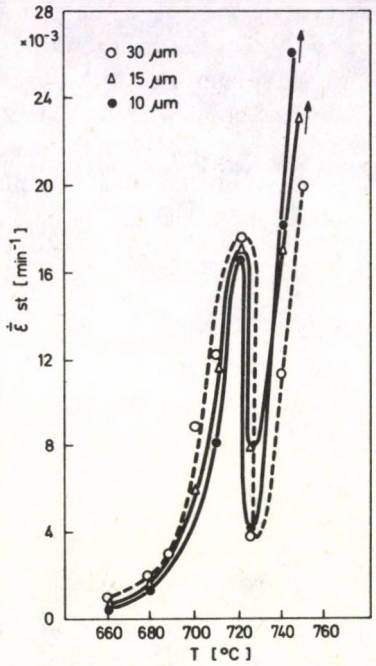

Fig. 2a. Temperature dependence of steady state strain rate for annealed mild steel with various grain diameters

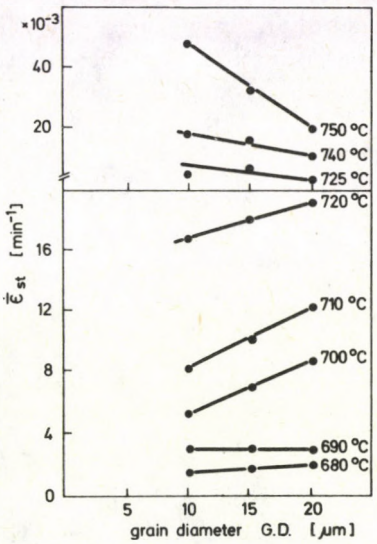

Fig. 2b. Relation between steady state strain rate ($\dot{\varepsilon}_{st}$) and grain diameter (G. D.) at various testing temperatures

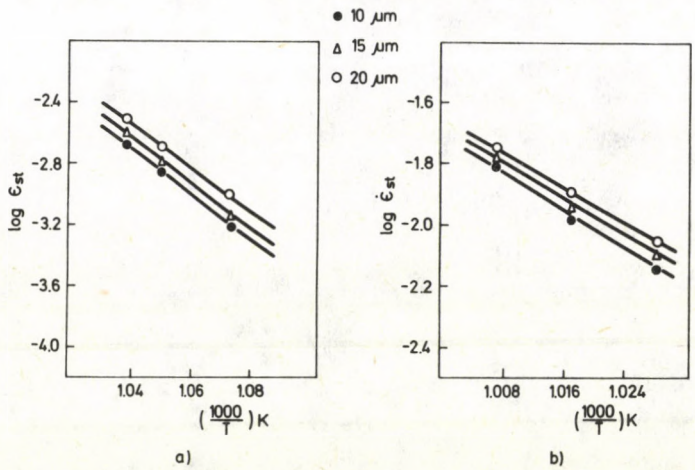

Fig. 3. Relation between creep temperature and logarithmic strain rate for mild steel samples with various grain diameters a) $Q = 256 \pm 4$ kJ/mole, $T = 660 - 690$ °C b) $Q = 260 \pm 4$ kJ/mole, $T = 700 - 720$ °C

Fig. 4 shows the lattice parameter, a, the X-ray line width, ΔL, and the grain diameter, $G.\ D.$, of the deformed material as a function of the creep temperature. The lattice parameter and the line width has a minimum on the samples which crept with the highest anomalous strain rate. On the other hand, the post-creep grain diameter increases with increasing creep rate as long as the grain size is not determined by the phase transformation taking place upon cooling. (The iron carbide phase cannot be observed here via X-ray diffraction, due to its small volume fraction.)

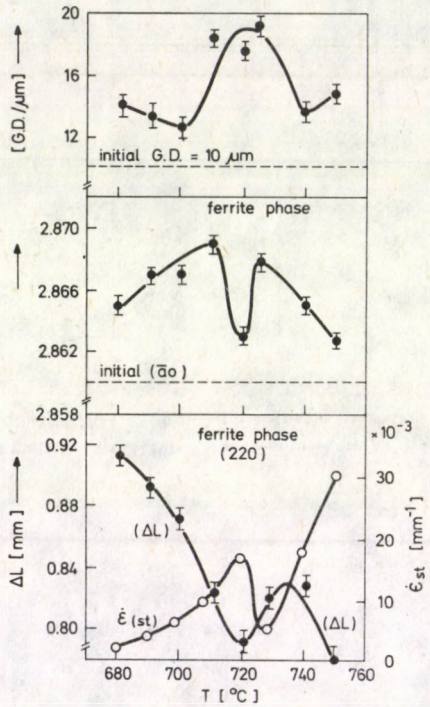

Fig. 4. Grain diameter (G. D.), lattice parameter (a) and line width (ΔL) after creep fracture at various creep temperatures

Discussion

The stationary creep rate shows an anomalous temperature dependence in the temperature region of the inverse eutectoid transformation, i.e. between 690 and 750 °C. This behaviour may be attributed to the effects of the phase transformation on the microstructure, when we bear in mind that the kinetics of the transformation depends also on the initial grain size of the material [1–3].

At temperatures below the eutectoid point, i.e. between 690 and 720 °C, the stationary creep rate increased both with the *initial* (Fig. 2b) and with the *actual* grain size (Fig. 4). This is in accordance with the expectation, since with increasing grain size the materials become softer. Further on, the spherodization, coarsening and dissolution of the carbide phase increases both the free path of the dislocation motion and the rate of recrystallisation in the ferrite matrix. Since both effects soften the material, the explanation of the strain rate increase via the transformation is at hand.

At temperatures above the eutectoid point, i.e. between 725 and 750 °C, the stationary strain rate is inversely proportional to the initial grain size. This effect may be ascribed to the influence of the initial grain size on the austenitization [1–3]. The behaviour at a certain initial grain size can be explained as follows:

At the very beginning of the creep, the material consists of ferrite, carbide and austenite. Slightly above the eutectoid temperature the rate of austenitization is relatively slow, hence the austenite grains are small and have a relatively high solute content, since the carbide is already dissolved. Slightly above the eutectoid temperature this solid solution strengthening should bring about relatively low creep rates (Fig. 2a). As the austenite grains grow, a second softening is expected, in agreement with the observations (Fig. 2a).

The activation energy of creep below the eutectoid temperature was about 256 ± 1 kJ/mole which is in good agreement with the activation energy for the decomposition of pearlite [16]. This supports the conclusion that the anomalous creep behaviour in the vicinity of the eutectoid temperature was mainly due to dissolution, spherodization and coarsening of carbide in pearlite. The driving force of these processes is the approach to the actual equilibrium.

The X-ray data of Fig. 4 prove that the internal stresses relax both during creep and in the course of phase transformation upon cooling. The first conclusion is based on the line width decrease below the eutectoid point and the second suggestion is supported by the line width decrease at creep temperatures, where the investigated structure was due to a common eutectoid phase transformation taking place during the cooling of the crept samples.

References

1. N. C. Law and D. V. Edmonds, Met. Trans. A, *11A*, 33, 1980.
2. M. Nemoto, Met. Trans. A. Vol. 8 A, 431, 1977.
3. S. Kinoshita and R. Ueda, Trans. Iron. Steel. Inst., Japan, *14*, 411, 1974.
4. R. G. Davies, Met. Trans. A, *9A*, 41, 1978.
5. P. W. Clinard and O. D. Sherby, Trans. Met. Soc. AIME, 233, 1475, 1965.
6. S. Matsuda and Y. Okamura, Trans. Iron Steel Inst. J. p. n, *14*, 363, 444, 1974.
7. R. W. K. Honeycombe, Met. Trans. A, Vol. *17A*, 915, 1976.
8. L. F. Porter and R. C. Rosenthal, Acta. Met., *7*, 504, 1959.
9. M. G. Lozinsky and I. S. Simeonova, Acta. Met., *7*, 709, 1959; *9*, 689, 1961.
10. R. I. Entin, Austenite transformation, Moscow, Metallurgia, 1960.
11. D. Oelschlangel and V. Weiss, Trans A. S. M., 58, 143, 1966.
12. A. Querales and J. G. Byrne, Met. Trans. A, *11A*, 255, 1980.
13. L. L. Kogan, L. M. Kleyner and R. I. Entin., Fiz. metal Metalloved., *41*, No 1, 118, 1976.
14. R. A. Grange, Met. Trans., *2*, 65, 1971.
15. R. L. Miller, Met. Trans., *3*, 905, 1972.
16. C. R. Brooks and E. E. Stansbury, J. Iron and Steel Inst., *5*, 514, 1965.

Acta Physica Hungarica 56 (1—4), pp 185—188 (1984)

COMMENTS ON THE PAPER "SOME REMARKS ON THE ORIGIN OF X-RAY DIFFRACTION PHENOMENA"

L. ZSOLDOS

Research Institute for Technical Physics of the Hungarian Academy of Sciences
1325 Budapest, Hungary

(Received in revised form 6 June 1983)

A proposed model of scattering of X-rays on atoms is criticized and it is shown that a Rayleigh–Mie scattering, based on the shadow effect of the photoelectric absorption and the Compton scattering only, cannot explain the coherent scattering of X-rays.

Two papers have been published recently in this journal [1, 2], criticising the usual treatment of X-ray scattering on atoms and pointing out some apparent contradictions in the theory. Herewith we would like to show that the contradictions presented by the author are not existing at all and the proposed new way of treatment—the perturbation of the wawe field by "opaque" electrons—cannot explain the process of scattering. All questions touched upon in [1] and [2] will not be discussed here, however. We shall restrict ourselves to the important points only.

1. "Thomson scattering"

The correct treatment is based on quantum mechanics. This does not give simply an "interpretation of the Thomson scattering" but offers a unified, complete description of the scattering. The theory requires the solution of the Schrödinger equation in the presence of the electromagnetic field. The main difficulty of the quantitative treatment is to find the appropriate solutions of the Schrödinger equation [3], but we can make important statements without knowing the exact form of the wave-functions.

i. We know that the perturbing electromagnetic field results in charge oscillations (and this is *not* a "dubious philosophy") which can be described as oscillating current density. On this basis one can define the dielectric and magnetic susceptibilities (polarizabilities) of the atoms for X-ray frequencies and these can be expressed by the set of the stationary (unperturbed) eigenfunctions of the Schrödinger equation by expanding the perturbed wave function as a linear combination of these orthonormal eigenfunctions [4, 5].

ii. The existence of the "coherent" and "incoherent" scattering *is* an inherent property of the scattering of X-rays on bounded electrons (and not of the electron itself) and the well known relation

$$I_{\text{tot}} = I_{\text{coh}} + I_{\text{inc}} = I_e \left| \sum_{j=1}^{Z} f_j \right|^2 + I_e \left(Z - \sum_{j=1}^{Z} |f_j|^2 - \sum_{\substack{j=1 \\ j \neq k}}^{Z} \sum_{k=1}^{Z} |f_{jk}|^2 \right) \neq Z I_e \qquad (1)$$

is *not* the definition of the incoherent part of the scattered intensity (as stated in [1] following Eq. (4a)), but the result of the orthonormality of eigenfunctions. (For the notations see [1].)

iii. For atoms with single electron Eq. (1) reduces to

$$I_{\text{coh}} = I_e |f|^2, \quad I_{\text{inc}} = I_e (1 - |f|^2), \quad I_{\text{tot}} = I_e, \qquad (2)$$

but this does not mean that "*each electron contributes* (to the total intensity) *by one electron unit*" (I_e). This is obvius if we consider the integrated scattered intensity from two samples, having the same structure but consisting of different atoms (e.g. Si and Ge). At least for *thin* crystals the integrated intensity is propotional to Z^2 instead of Z, because the intensity redistribution, as a result of the coherent scattering, takes place not only within the scattered waves but within the whole wave field.

iv. It must be also emphasized that the assumption of "continuous tunable oscillators" is not necessary. It is a simple forced oscillation taking place, far from the absorption edge (the resonant frequency), and therefore it is trivial that any frequency can be "reproduced" by the scattering whereas the atom remains in the original but perturbed state.

2. Agreement with physical optics

It is claimed in [2] that "coherent scattering" should be explained on the basis of the existing laws of the physical optics, the Huygens–Fresnel and the Babinet principles.

i. The application of the Huygens–Fresnel principle for slits and obstacles being much smaller than the wavelength is questionable [6], and even the most rigorous formulation, the Helmoltz–Kirchhoff integral theorem contains *no* information on the mechanism of the scattering. The theorem is simply the consequence of the wave equation and *must* agree with any consequences of the Maxwell equations, too.

ii. Similarly, there is no contradiction between the existing treatment of scattering and the Babinet principle, which is a very useful theorem, but again gives no information about the origin of the scattering.

3. The application of the Rayleigh–Mie scattering

The application of the Mie theory of scattering, without further supplementary assumptions, considering the effect of charge oscillations, cannot explain the scattering of X-rays on atoms.

1. The Mie theory also presumes implicitly some charge oscillations near the surface, through the boundary conditions, implied in the values of the conductivity and the dielectric constant.
2. For very small particles (Rayleigh scattering) the Mie theory gives a scattered intensity proportional to λ^{-4}, whereas for X-rays I_{coh} is practically independent of λ. (The monotonous decrease with $\sin \vartheta/\lambda$ is the result of the electronic structure of the atoms.)
3. Coherent X-ray scattering is often regarded as a special case of Rayleigh scattering [7, 8], but also in these cases the treatment starts always with the consideration of the charge oscillations in the atoms. Otherwise we have to define appropriate boundary conditions and the definition of the boundary itself would result in several serious difficulties.
4. The Mie scattering is not necessarily connected with the opacity of the objects. The absorption often plays a secondary role in modifying the wave field.

4. The "shadow effect"

A simple shadow effect of the photoelectric and Compton effects cannot explain the Z and wavelength dependence of the atomic form factors.

i. At the absorption edges the "opacity of the electrons" suffers drastic changes (jumps) and there are no similar changes in the real parts of the form factors. This occurs in the imaginary part of the dispersion correction (f'') only.

ii. It would be rather difficult to explain with the model that the real part of the form factor (scattering) is usually much greater than the imaginary one (absorption).

iii. The assumption that "*if the opacity of such* (excitable) *electrons exceeds very much the average value, the effect* (increased scattering) *must change the sign*..." is false and has nothing to do with the Babinet principle.

References

1. F. Hajdu, Acta Phys. Hung., *52*, 59, 1982.
2. F. Hajdu, Acta Phys. Hung., *52*, 77, 1982.
3. L. E. Azároff (Editor), X-ray Diffraction, Ch. 1, McGraw-Hill, New York, 1974.
4. R. W. James, The Optical Principles of X-ray Diffraction (The Crystalline State, Vol. 2), G. Bell and Sons, London, 1984.
5. J. Boumann, Theoretical Principles of Structural Research by X-rays (In Handb. d. Physik XXXII, Ed. by S. Flügge), Spinger, Berlin, 1957.
6. M. Born and E. Wolf, Principles of Optics, Ch. XIII, Pergamon Press, Oxford, 1970.
7. Encyclopedic Dictionary of Physics, Ed. by J. Thewlis, Pergamon Press, Oxford, 1962.
8. B. K. Argawal, X-ray Spectroscopy, Springer, Berlin, 1979.

Acta Physica Hungarica 56 (1—4), pp 189—197 (1984)

EIN MAGNETOHYDRODYNAMISCHES DYNAMO-MODELL

J. SZABÓ

Technische Universität für die Schwerindustrie, Lehrstuhl für Physik
Miskolc, Ungarn

(Eingegangen 16 Juni 1983)

Es wird gezeigt, dass das anfängliche magnetische Feld durch spezielle magnetohydrodynamische Strömungen verstärkt werden kann. Vorausgesetzt wird, dass die hydrodynamische Viscosität des Plasmas vernachlässigbar klein, die elektrische Leitfähigkeit aber endlich ist. Es werden zwei zweidimensionale Dynamo-Modelle ausführlicher untersucht. In dem ersten Modell bewegt sich ein halb-unendlich ausgedehntes Plasma, in dem zweiten eine Plasmaschicht in einem, anfänglich homogenen magnetischen Feld. Es ergibt sich, dass das magnetische Feld in beiden Fällen durch die Strömung des Plasmas verstärkt wird.

1.

Es wird heutzutage allgemein angenommen, dass das Problem der Sonnenflecken mit Hilfe der Magnetohydrodynamik zu lösen, dass das starke Magnetfeld in den Sonnenflecken mit einem magnetohydrodynamischen Dynamo-Modell zu erklären sind. Obwohl das — ziemlich zusammengesetzte — Problem der Sonnenaktivität noch nicht endgültig, oder befriedigend gelöst ist, sind diesbezüglich interessante Ideen veröffentlicht worden. In erster Linie sind vielleicht die Arbeiten von Gurevich und Lebedinsky [1], Cowling [2], Parker [3], Schlüter und Temesváry [4], Babcock [5] und Steenbeck [6] zu erwähnen. Von allen diesen Verfassern wird angenommen, dass die Sonne ein allgemeines (ewtl. bipolaris) Magnetfeld besitzt und dass das starke Magnetfeld der Sonnenflecken ein sekundäres Feld sei, das durch Strömung von gut leitenden Plasmamassen in dem primären, allgemeinen Magnetfeld induziert wird.

Man hat auch schon versucht, das Magnetfeld der Sterne mittels ähnlichen magnetohydrodynamischen Dynamo-Modellen theoretisch zu erklären [7].

Es sei noch erwähnt, dass man im Laboratorium sehr intensive elektrische Ströme und sehr starke magnetische Felder so induzieren konnte, dass man Plasmabündel quer zu dem primären, äusseren Magnetfeld eingeschossen hat [8].

Wegen der Kompliziertheit des Gleichungssystems der Magnetohydrodynamik gibt es wenige instationäre magnetohydrodynamische Randwertprobleme, welche man exakt lösen könnte. Auch deshalb wird es vielleicht lehrreich sein ein exakt lösbares, zweidimensionales magnetohydrodynamisches Dynamo-Modell ausführli-

cher zu untersuchen. (Das entsprechende stationäre Problem wurde bereits im Jahre 1937 von Hartmann theoretisch [9] und noch im selben Jahr von Hartmann und Lazarus [10] experimentell untersucht.)

2.

Wir wollen zuerst das folgende, vereinfachte Modell untersuchen. Das homogene, inkompressible und unendlich ausgedehnte Plasma befindet sich zum Zeitpunkt $t=0$ im homogenen, äusseren Magnetfeld H_0. Die z-Achse des Cartesischen Koordinatensystems wählen wir in der Richtung von H_0. Die Geschwindigkeitsverteilung für $t=0$ sei $v_x=v_0 I(z)$, wo $I(z)=1$ für $z<0$ und $I(z)=0$, für $z>0$. Wir untersuchen das in der Richtung x induzierte magnetische Feld, die Geschwindigkeit v_x und das in Richtung y induzierte elektrische Feld E_y für $t>0$.

Die Anfangsbedingungen lauten:

$$\left.\begin{array}{lll} v_x=v_0 I(z), & v_y=0, & v_z=0 \\ H_x=0, & H_y=0, & H_z=H_0 \\ p=p\,, & & \end{array}\right\} \quad \text{für } t=0\,. \tag{1}$$

Die hydrodynamische Viscosität der Flüssigkeit wird vernachlässigt, die elektrische Leitfähigheit ist aber endlich. In diesem Fall sind die Grundgleichungen der Magnetohydrodynamik:

$$\rho\frac{\partial \mathbf{v}}{\partial t}+\rho(\mathbf{v}\nabla)\mathbf{v}=-\nabla p-\frac{1}{4\pi}(\nabla\times\mathbf{H})\,, \tag{2}$$

$$\nabla\mathbf{v}=0\,, \tag{3}$$

$$\frac{\partial \mathbf{H}}{\partial t}=\nabla\times(\mathbf{v}\times\mathbf{H})+\frac{c^2}{4\pi\sigma}\Delta\mathbf{H}\,, \tag{4}$$

$$\nabla\times\mathbf{E}=-\frac{1}{c}\frac{\partial \mathbf{H}}{\partial t}\,, \tag{5}$$

$$\nabla\mathbf{H}=0\,, \tag{6}$$

wo die gewöhnlichen Bezeichnungen gebraucht wurden. Aus der Symmetrie des Problems folgt, dass die hier vorkommenden Grössen nur von der Koordinate z und von der Zeit t abhängen. So bekommen wir aus (2)–(6):

$$\rho\frac{\partial v_x}{\partial t}+\rho v_z\frac{\partial v_x}{\partial z}=\frac{H_z}{4\pi}\frac{\partial H_x}{\partial z}\,, \tag{7}$$

$$\rho\frac{\partial v_z}{\partial t}=-\frac{\partial}{\partial z}\left(p+\frac{H_x^2}{8\pi}\right), \tag{8}$$

$$\frac{\partial H_x}{\partial t} = H_z \frac{\partial v_x}{\partial z} + \frac{c^2}{4\pi\sigma} \frac{\partial^2 H_x}{\partial z^2}, \tag{9}$$

$$\frac{\partial H_z}{\partial t} = \frac{c^2}{4\pi\sigma} \frac{\partial^2 H_z}{\partial z^2}, \tag{10}$$

$$\frac{\partial E_y}{\partial z} = \frac{1}{c} \frac{\partial H_x}{\partial t}. \tag{11}$$

Hier haben wir schon in Betracht gezogen, dass nach (3) bzw. (6) die Grössen v_z und H_z von der Koordinate z unabhängig sind. Aus den Anfangsbedingungen und aus den Gleichungen (8) und (10) folgt:

$$v_z \equiv 0; \qquad H_z \equiv H_0. \tag{12}$$

Es ist zweckmässig, dimensionslose Veränderlichen einzuführen:

$$u = \frac{v_x}{v_0}, \qquad h = \frac{H_x}{H_0}; \qquad \xi = \frac{z}{\frac{c^2}{4\pi\sigma v_0}}, \qquad \tau = \frac{t}{\frac{c^2}{4\pi\sigma v_0^2}},$$

$$P = \frac{p}{\frac{H_0^2}{8\pi}}, \qquad E = \frac{E_y}{\frac{v_0 H_0}{c}}, \qquad \lambda^2 = \frac{H_0^2}{4\pi\rho v_0^2}. \tag{13}$$

Mit diesen Veränderlichen lassen sich die Gleichungen (7), (8), (9), (11) folgendermassen schreiben:

$$\frac{\partial u}{\partial \tau} = \lambda^2 \frac{\partial h}{\partial \xi}, \tag{14}$$

$$\frac{\partial}{\partial \xi}(P + h^2) = 0, \tag{15}$$

$$\frac{\partial h}{\partial \tau} = \frac{\partial u}{\partial \xi} + \frac{\partial^2 h}{\partial \xi^2}, \tag{16}$$

$$\frac{\partial E}{\partial \xi} = \frac{\partial h}{\partial \tau}. \tag{17}$$

Die Anfangsbedingungen haben jetzt folgende Form:

$$h = 0, \qquad u = I(\xi), \qquad \frac{\partial u}{\partial \xi} = -\delta(\xi), \qquad \text{für} \quad \tau = 0.$$

Die Lösung der Gleichungen (14)–(17) suchen wir mittels Laplacesche-Transformation hinsichtlich τ. Die Laplacesche-transformierte einer Funktion $\varphi(\xi, \tau)$ bezeichnen wir, wie folgt:

$$\bar{\varphi}(\xi, s) = \int_0^\infty \varphi(\xi, \tau) e^{-s\tau} d\tau. \tag{18}$$

Nach der Laplaceschen-Transformation bekommen wir aus (14) und (16):

$$s\bar{u} - I(\xi) = \lambda^2 \frac{\partial \bar{h}}{\partial \xi}, \tag{19}$$

$$s\bar{h} = \frac{\partial \bar{u}}{\partial \xi} + \frac{\partial^2 \bar{h}}{\partial \xi^2}. \tag{20}$$

Eliminiert man die Grösse $\bar{u}$ aus diesen beiden Gleichungen und berücksichtigt man, dass $\frac{\partial I}{\partial \xi} = -\delta(\xi)$ ist, so erhält man:

$$\frac{\partial^2 \bar{h}}{\partial \xi^2} - \frac{s^2}{s+\lambda^2}\bar{h} - \frac{\delta(\xi)}{s+\lambda^2} = 0. \tag{21}$$

Jetzt nehmen wir die Fourier-transformierte der Funktion $\bar{h}$ nach ξ, die wir folgendermassen bezeichnen:

$$h(k, s) = \int_{-\infty}^{\infty} \bar{h}(\xi, s) e^{-ik\xi} d\xi, \tag{22}$$

und die Invers-transformierte:

$$\bar{h}(\xi, s) = \frac{1}{2\pi} \int_{-\infty}^{\infty} e^{ik\xi} h(k, s)\, dk. \tag{23}$$

Für die Funktion $h(k, s)$ erhalten wir aus (21):

$$h(k, s) = -\frac{1}{s+\lambda^2} \frac{1}{k^2 + \frac{s^2}{s+\lambda^2}}. \tag{24}$$

Die Invers-transformierte von $h(k, s)$ hinsichtlich der Fourierschen Transformation ist leicht zu finden:

$$\bar{h}(\xi, s) = \frac{-e^{-\frac{s|\xi|}{\sqrt{s+\lambda^2}}}}{2s\sqrt{s+\lambda^e}}. \tag{25}$$

Bei Umkehr der Laplaceschen Transformation ergibt sich:

$$h(\xi, \tau) = -\frac{1}{2\lambda} + |\xi| e^{-\lambda^2 \tau} + \frac{1}{2\pi} \int_{\lambda^2}^{\infty} \frac{e^{-R\tau} \cos \frac{R\xi}{\sqrt{R-\lambda^2}}}{R\sqrt{R-\lambda^2}}\, dR. \tag{26}$$

Es ergibt sich auf ähnliche Weise für die (dimensionslosen) Grössen u und E:

$$u(\xi,\tau)=\frac{1}{2}\mp e^{-\lambda^2\tau}+\frac{\lambda^2}{2\pi}\int_{\lambda^2}^{\infty}\frac{e^{-R\tau}\sin\dfrac{R\xi}{\sqrt{R-\lambda^2}}}{R(R-\lambda^2)}\,dR\,, \tag{27}$$

$$E(\xi,\tau)=\frac{1}{2}\mp\frac{\lambda^2\xi^2}{2}e^{-\lambda^2\tau}-\frac{1}{2\pi}\int_{\lambda^2}^{\infty}\frac{e^{-R\tau}\sin\dfrac{R\xi}{\sqrt{R-\lambda^2}}}{R}\,dR\,, \tag{28}$$

wo das obere Vorzeichen für $\xi>0$, das untere für $\xi<0$ gilt.

Es wurden also ein zusätzliches Magnetfeld in der Richtung der Strömung, und ein elektrisches Feld senkrecht zu der Strömungsrichtung und zu dem anfänglichen Magnetfeld induziert. Für $\tau\to\infty$, d. h. für $t\to\infty$ verschwinden die beiden letzten Glieder in (26)–(28). In diesem Grenzfall wird das induzierte Magnetfeld $H_x=\sqrt{\pi\rho}\cdot v_0$, und das induzierte elektrische Feld $E_y=\dfrac{v_0H_0}{2c}$ homogen; das ganze unendlich ausgedehnte Plasma bewegt sich mit der Geschwindigkeit $v_x=\dfrac{v_0}{2}$; die für $t=0$ sich bewegende Plasmamasse wurde also auf die Hälfte der anfänglichen Geschwindigkeit gebremst, die anfänglich ruhende Plasmamasse wurde aber in Bewegung gesetzt; die relative Geschwindigkeit der Plasmamassen in den beiden Halbräumen $z>0$ bzw. $z<0$ klingt mit der Relaxationszeit $t_r=\rho c^2/\sigma H_0^2$ ab.

Betrachten wir noch den speziellen Fall, wo die Strömungsgeschwindigkeit v_0 in dem Gebiet $z<0$ mittels irgendeiner äusseren Kraft für alle $t<0$ aufrecht erhalten wird, und wo das Medium in dem Gebiet $z>0$ für alle $t>0$ festgehalten wird.

Da es jetzt für alle $t>0$ gilt, dass $v_x=v_0I(z)$ ist, so bekommen wir aus der Gleichung (16):

$$\frac{\partial h}{\partial\tau}-\frac{\partial^2h}{\partial\xi^2}=-\delta(\xi)\,. \tag{29}$$

Die für $\tau=0$ und $\xi=\infty$ verschwindende Lösung der Gleichung (29) ist:

$$h(\xi,\tau)=-\sqrt{\frac{\tau}{\pi}}e^{-\frac{\xi^2}{4\tau}}+\frac{|\xi|}{2\sqrt{\tau}}\operatorname{erf}\left(\frac{|\xi|}{2\sqrt{\tau}}\right), \tag{30}$$

wo

$$\operatorname{erf}(\alpha)=\frac{2}{\sqrt{\pi}}\int_0^{\alpha}e^{-v^2}dv$$

die Fehlerfunktion ist.

Für $\frac{|\xi|}{\sqrt{\tau}} \ll 1$ erhalten wir die asymptotische Formel: $h(\xi, \tau) \approx \sqrt{\frac{\tau}{\pi}}$, d. h:

$$H_x(t) \approx H_0 \sqrt{\frac{4\tilde{\pi}\sigma v_0^2 t}{c^2}}, \qquad \text{für} \quad t \gg \frac{\frac{z^2}{c^2}}{4\pi\sigma v_0}.$$

Durch Plasmaströmung im äusseren magnetischen Feld kann sich also ein starkes Magnetfeld induzieren. Nebenbei erwähnen wir, dass für die Konvektionszone der Sonne: $\sigma/c^2 \approx 10^{-8}$ CGSE, $v_0 \approx 10^4$ cms^{-1}: für $t = 10^4$ s ergibt sich $H_x \approx 2.10^3$ Oe.

3.

Wir untersuchen jetzt das folgende, weniger idealisierte Dynamo-Modell. Eine Plasma-Schicht von endlicher Dicke $2a$ bewegt sich in Richtung der x-Achse senkrecht zu dem anfänglichen, homogenen magnetischen Feld $H_z \equiv H_0$. Die sich bewegende Plasmaschicht ist in einem unendlich ausgedehnten Plasma von gleichem Charakter eingebettet. Wir nehmen noch an, dass eine nur von z und t abhängige Kraft in Richtung x auf die Plasmaschicht wirkt. Den Charakter dieser Kraft werden wir später näher angeben.

Die Grundgleichungen sind auch in diesem Fall die Gleichungen (2) bis (6) mit dem Unterschied, dass die hydrodynamische Bewegungsgleichung die äussere Kraftdichte $F(z, t)$ enthält. Die Anfangsbedingungen lauten jedoch:

$$\begin{aligned} &v_x = v_0[I_+(z+a) + I_-(z-a)], \\ &H_x = 0, \qquad H_y = 0, \qquad H_z = H_0, \qquad \text{für} \quad t = 0, \\ &p = p_0, \end{aligned} \tag{31}$$

wo

$$I_+(\xi) = \begin{cases} 1, & \text{für} \quad \xi > 0 \\ 0, & \text{für} \quad \xi < 0 \end{cases}$$

$$I_-(\xi) = \begin{cases} -1, & \text{für} \quad \xi > 0 \\ 0, & \text{für} \quad \xi < 0 \end{cases} \tag{32}$$

Aus der Symmetrie und der Voraussetzung, dass die äussere Kraft nicht von den Koordinaten x und y abhängt, folgt, dass die zu bestimmenden Grössen nur von z und t abhängen. Es sind nun die Grössen v_x, H_x und E_y für $t > 0$ zu bestimmen. Nach Einführung der obigen dimensionslosen Veränderlichen bekommen wir für die unbekannten Grössen, wie früher:

$$\frac{\partial u}{\partial \tau} = \lambda^2 \frac{\partial h}{\partial \xi} + \Phi(\tau, \xi), \tag{33}$$

$$\frac{\partial h}{\partial \tau} = \frac{\partial u}{\partial \xi} + \frac{\partial^2 h}{\partial \xi^2}, \tag{34}$$

$$\frac{\partial E}{\partial \xi} = \frac{\partial H}{\partial \tau}, \tag{35}$$

wo

$$\Phi(\tau, \xi) = \frac{F \cdot c^2}{4\pi\sigma \rho v_0^3} \tag{36}$$

die dimensionslose "Kraftdichte" ist. Die Anfangsbedingungen lauten jetzt in den neuen Veränderlichen:

$$\left.\begin{aligned} u &= I_+(\xi+\alpha) + I_-(\xi-\alpha) \\ \frac{\partial u}{\partial \xi} &= \delta(\xi+\alpha)\delta(\xi-\alpha) \\ h &= 0, \end{aligned}\right\} \quad \text{für} \quad \tau = 0, \tag{37}$$

wo

$$\alpha = \frac{a}{\frac{c^2}{4\pi\sigma v_0}}. \tag{38}$$

Für die Kraftdichte $\Phi(\xi, \tau)$ nehmen wir nun an, dass sie nur in dem Intervall $|\xi| < \alpha$ wirkt und dass sie die Form hat:

$$\Phi(\xi, \tau) = \Phi(\tau)\,[I_+(\xi+\alpha) + I_-(\xi-\alpha)]\,. \tag{39}$$

Es wird weiter vorausgesetzt, dass die Funktion sich langsam mit τ ändert, dass wir also schreiben können:

$$\Phi(\tau) = \Phi(0) + \tau\Phi'(0)\,. \tag{40}$$

Die Gleichungen (33) und (34) lösen wir wieder mit Hilfe der Laplaceschen und der Fourierschen Transformation. Nach der Laplaceschen Transformation und nach Elimination von $\bar{u}$ erhalten wir für die Laplaceschen Transformierte $\bar{h}(\xi, s)$ von $h(\xi, \tau)$ die folgende Gleichung:

$$\left(1 + \frac{\lambda^2}{s}\right)\frac{\partial^2 \bar{h}}{\partial \xi^2} - s\bar{h} + \frac{1}{s}[\delta(\xi+\alpha) - \delta(\xi-\alpha)] + \left[\frac{\Phi(0)}{s^2} + \frac{\Phi'(0)}{s^3}\right][\delta(\xi+\alpha) - \delta(\xi-\alpha)]$$

$$= 0\,. \tag{41}$$

Nach der Fourierschen Transformation ergibt sich dann:

$$h(k,s)=\frac{1+\dfrac{\Phi(0)}{s}+\dfrac{\Phi'(0)}{s^2}}{s+\lambda^2}\cdot\frac{e^{-ik\alpha}-e^{-ik\alpha}}{k^2+\kappa^2}, \tag{42}$$

wo

$$\kappa^2=\frac{s^2}{s+\lambda^2}. \tag{43}$$

Die Fouriersche Transformation kann man ziemlich leicht umkehren; es ergibt sich:

$$\bar{h}(\xi,s)=\frac{1+\dfrac{\Phi(0)}{s}+\dfrac{\Phi'(0)}{s^2}}{s+\lambda^2}\cdot\frac{e^{\kappa(\xi+\alpha)}-e^{\kappa(\xi-\alpha)}}{2\kappa}, \qquad \text{für} \quad |\xi|\leq\alpha,$$

$$\bar{h}(\xi,s)=\frac{1+\dfrac{\Phi(0)}{s}+\dfrac{\Phi'(0)}{s^2}}{s+\lambda^2}\cdot\frac{e^{\mp\kappa\alpha}-e^{-\kappa\alpha}}{2\kappa}\cdot e^{-\kappa|\xi|}, \qquad \text{für} \quad \begin{matrix}\xi\geq\alpha\\ \xi\leq-\alpha\end{matrix}. \tag{44}$$

Nach der Umkehrung der Laplaceschen Transformation bekommen wir endlich:

$$h(\xi,\tau)=\mp\frac{\alpha}{\lambda^2}\Phi(0)\mp\Phi'(0)\left[\tau-\frac{|\xi|}{\lambda}-\frac{1}{\lambda^2}\right]\mp 2\alpha e^{-\lambda^2\tau}\mathrm{v}1-\frac{\Phi(0)}{\lambda^2}+\frac{\Phi'(0)}{\lambda^4}\Bigg)+$$

$$+\frac{1}{\pi}\int_{\lambda^2}^{\infty}\left(\frac{1}{R}-\frac{\Phi(0)}{R^2}+\frac{\Phi'(0)}{R^3}\right)e^{-R\tau}\sin\frac{R\alpha}{\sqrt{R-\lambda^2}}\sin\frac{R\xi}{\sqrt{R-\lambda^2}}\,dR,$$

$$\text{für} \quad |\xi|\leq\alpha, \tag{45}$$

$$h(\xi,\tau)=-\frac{\xi}{\lambda^2}\Phi(0)-\frac{\xi}{\lambda^2}\Phi'(0)\left(\tau-\frac{\alpha}{\lambda}-\frac{1}{\lambda^2}\right)-2\xi e^{-\lambda^2\tau}\left(1-\frac{\Phi(0)}{\lambda^2}+\frac{\Phi'(0)}{\lambda^4}\right)+$$

$$+\frac{1}{\pi}\int_{\lambda^2}^{\infty}\left(\frac{1}{R}-\frac{\Phi(0)}{R^2}+\frac{\Phi'(0)}{R^3}\right)e^{-R\tau}\sin\frac{R\alpha}{\sqrt{R-\lambda^2}}\sin\frac{R\xi}{\sqrt{R-\lambda^2}}\,dR,$$

$$\text{für} \quad |\xi|\geq\alpha. \tag{46}$$

Aus den Formeln (45) und (46) ist zu ersehen, dass für $\Phi(0)=0$, $\Phi'(0)=0$ und $\tau\to\infty$ kein induziertes Magnetfeld existiert. [Dasselbe gilt auch für die Geschwindigkeit $u(\infty)$]. Das will aber nicht bedeuten, dass es ohne äussere Kraft keinen Dynamo-Effekt gibt, sondern dass im Fall $\Phi(\tau)=0$ der Dynamo-Effekt, den das Integralglied enthélt, mit der Zeit abklingt. Die Relaxationszeit der Abnahme des induzierten Magnetfeldes ist auch jetzt $t=\rho c^2/\sigma H_0^2$.

Betrachten wir noch den speziellen Fall, wo die äussere Kraft Φ von der Zeit unabhängig ist, d. h. wo $\Phi'(0)=0$ ist. Wir bekommen leicht aus (45) und (46) für den Grenzfall $\tau \gg \frac{1}{\lambda^2}$:

$$h=\frac{\alpha\Phi(0)}{\lambda^2}, \quad \text{für} \quad \xi<-\alpha; \qquad h=-\frac{\alpha\Phi(0)}{\lambda^2}, \quad \text{für} \quad \xi>\alpha;$$

$$h=-\frac{\xi\Phi(0)}{\lambda^2}, \quad \text{für} \quad |\xi|<\alpha. \tag{47}$$

Das induzierte Magnetfeld ist also mit der äusseren Kraftdichte proportional.

Der Verfasser dankt Herrn Prof. Dr. N. G. van Kampen für wertvolle Diskussionen.

Literatur

1. L. E. Gurevich, A. I. Lebedinsky, C. R. Acad. Sci. USSR, *49*, 92, 1945.
2. T. G. Cowling, Mon. Not. R. A. S., *106*, 446, 1946.
3. E. N. Parker, Astrophys. J., *121*, 491, 1955.
4. A. Schlüter, S. Temesváry, Electromagnetic Phenomena in Cosm. Phys., Camb. Univ. Press, S. 263, 1958.
5. H. D. Babcock, Astrophys. J., *130*, 364, 1959.
6. M. Steenbeck, Beitr. Plasmaphys., *3*, 153, 1961.
7. H. W. Babcock, Stellar Atmospheres, Univ. Chicago Press, 1960, p. 282.
8. R. J. Rosa, Phys. Fluids, *4*, 182, 1961.
9. J. Hartmann, Kgl. Danske Vidensk. Selskab, Math.-Fys. Med. Vol. 15. No. 6. Copenhagen, 1937.
10. J. Hartmann, F. Lazarus, ibid. Vol. 14. No. 7. Copenhagen, 1937.
11. N. G. van Kampen, B. U. Felderhof, Theoretical Methods in Plasma Physics, North-Holland Publ. Co., Amsterdam, 1967, S. 49.

Acta Physica Hungarica 56 (1—4), pp 199—207 (1984)

EFFECTS OF NUCLEAR STRUCTURE AND TRIPLET-SINGLET INTERACTION IN THE 1s2s $^3S_1$ HYPERFINE MULTIPLET OF Li^+*

J. KOWALSKI, R. NEUMANN, S. NOEHTE, H. SUHR and G. ZU PUTLITZ

Physics Institute of Heidelberg University, D-6900 Heidelberg, FRG

R. HERMAN

Davey Laboratory, The Pennsylvania State University, University Park Pennsylvania 16802 USA

(Received 23 June 1983)

From combined laser-microwave spectroscopy of the $1s2s^3S_1$ hyperfine structure (hfs) splittings in helium-like $^{6,7}Li^+$ ions, the magnetic dipole hfs interaction constant A and a small displacement δ of the $F=I$ substate, caused by 1s2s $^3S_1$–1s2s $^1S_0$ hyperfine mixing, have been obtained. Analysis of A yields nuclear structure effects in the hfs splittings of the isotopes $^{6,7}Li^+$. The result of a calculation of $^{6,7}\delta$ with accurate integral-transform 2 $^1S_0$ and 2 $^3S_1$ wave functions is presented.

1. Introduction

Methods of perturbation theory are of key importance for a quantitative understanding of the interactions between singlet and triplet states in atomic and molecular spectra. I. Kovács dealt with singlet–triplet perturbations in diatomic molecules [1–6]. In atomic spectra, the problem of singlet–triplet mixing has been discussed e.g. by Breit and Wills [7]. Regarding the hyperfine structure (hfs), Schwartz [8] and Lurio, Mandel and Novick [9] developed the principal formulae for the practical evaluation of the perturbations from the measured hfs spectra.

The present article briefly describes the measurement of hyperfine splitting frequencies in the Li^+ ion spectrum and provides a theoretical analysis of the experimental results, including aspects of singlet–triplet hyperfine mixing.

The spectrum of singly ionised lithium is helium-like and thus of fundamental interest for modern atomic structure theory. Its characteristics like e.g. fine structure, hyperfine structure, isotope shift, Lamb shift and lifetimes can be calculated accurately with advanced perturbation methods. Many theoretical as well as experimental studies concerned the lowest excited states, the metastable 1s2s $^3S_1$ term ($\tau \approx 50$ s) and the short-lived 1s2p ^3P multiplet ($\tau \approx 43$ ns). A part of the Li^+ spectrum for the stable

* Dedicated to Prof. Dr. István Kovács on his 70th birthday

isotopes $^6Li^+$ and $^7Li^+$ with $2\,^3S_1$ and $2\,^3P$ is shown in Fig. 1. Since the two isotopes have a nuclear spin, $I=1$ for ^6Li and $I=3/2$ for ^7Li, hfs splittings arise in both states. As indicated by the frequency scale on the right side of Fig. 1 the size of the hfs splittings is between 1 and 20 GHz. The 1s2s $^3S_1$ hfs splittings were measured with a combined laser-microwave technique [10, 11]. Somewhat modified, this experimental scheme

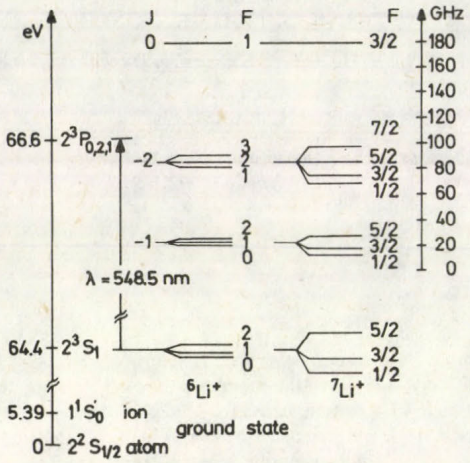

Fig. 1. Energy level scheme of the 1s2s $^3S_1$ and 1s2p ^3P multiplets of $^{6,7}Li^+$

had been applied for the first time to molecules and ions by Rosner, Gaily and Holt [12, 13] and to atoms by Ertmer and Hofer [14]. The theoretical treatment of the experimental splitting frequencies concerns two different aspects:

a. The $2\,^3S_1$ hyperfine structure arises exclusively from magnetic dipole Fermi contact interaction between electron spins and nuclear spin. Ignoring the influence of nuclear structure on the hfs splittings, the constant A can be calculated, using precise fundamental constants and relativistic and quantumelectrodynamic corrections, available in the literature. Thus a comparison between the measured and calculated A factors provides a small nuclear structure effect in the hfs. It arises from the fact that the nucleus, rather than being a point-like particle, exhibits a finite distribution of its charge and magnetism.

b. The precise laser-microwave measurement revealed a small energy displacement δ in the splitting pattern of the $2\,^3S_1$ hfs multiplet of $^7Li^+$. The hfs operator selectively mediates a triplet–singlet interaction between the ($2\,^3S_1$, $F=I$) substate and the unsplit ($2\,^1S_0$, $F=I$) state, causing a mutual repulsion of the two levels while the two $^3S_1$ substates with quantum numbers $F=I\pm1$ remain unperturbed. The shift δ can be therefore extracted without theoretical assumptions from the experimental data as a deviation from the Landé interval rule. A calculation of δ with accurate integral transform $2\,^1S_0$ and $2\,^3S_1$ wave functions is presented. Electron exchange and correlation effects which differ for parallel ($^3S_1$) and antiparallel ($^1S_0$) spins, are treated

in detail, in order to obtain very good agreement between measured and theoretical values for this tiny perturbation. Hyperfine induced triplet–singlet mixing has been reported for various atoms, e.g., for ^{3}He [15, 16, 17, 18], ^{87}Sr [19, 20] and Ba [21]. But, only in He is the mixing as simple in origin as in Li^+, while the other atoms experience additional core effects. However, since ^{3}He has a nuclear spin $I=1/2$, the $2\,^3S_1$ state splits into two hyperfine substates, and the displacement δ could not be extracted directly from the measurement [22].

2. Experimental setup and measurement

The experimental arrangement is shown in Fig. 2. Lithium atoms are evaporated from a stainless steel oven and ionized by concentric electron impact when leaving the oven aperture. A small fraction of the ions (about 10^{-3}) is excited to the $2\,^3S_1$ state. After acceleration to a kinetic energy of 200–400eV, an electrostatic lens system focuses the ions to a narrow and well collimated beam. The beam of a continuous-wave single-mode dye laser crosses the ion beam at right angles and selectively excites ions from a certain $2\,^3S_1$ hfs substate to a suitable $2\,^3P$ hfs sublevel through a resonance transition at wavelength $\lambda=548.5$ nm. Since the $2\,^3P$ decays back to the $2\,^3S_1$ via all allowed channels, obeying the selection rule $F-F'=0, \pm 1$, F and F' being the hyperfine quantum numbers of ^3P and ^3S states, respectively, depletion of the initial $2\,^3S_1$ hfs substate by optical pumping occurs.

The Li^+ beam then passes a waveguide where microwave transitions between adjacent F substates restore the original statistical level population. This is detected via

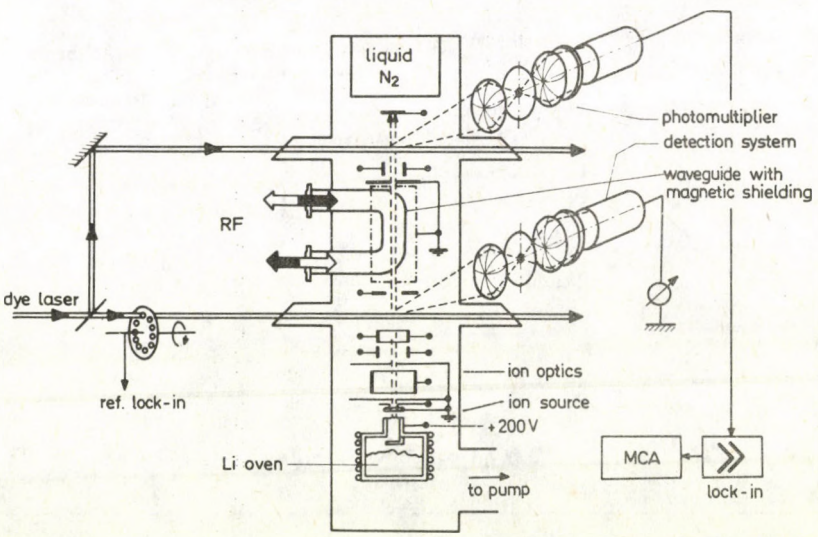

Fig. 2. Experimental arrangement of laser-microwave spectrometer and ion-beam apparatus

an increase of resonance fluorescence light intensity in a second laser-beam ion-beam crossing zone. The microwave field in the waveguide is reflected back on itself at one end, so that one wave travels with the ion motion and the other wave in the opposite direction. Hence, as a function of frequency two Doppler shifted microwave signals appear. The lower laser beam is amplitude modulated with a frequency of typically 2 kHz. The fluorescence signal in the second beam crossing region is monitored with lock-in technique at this frequency and stored in a multichannel analyzer. A microcomputer varies the microwave generator frequency in steps and synchronously switches the channel number. For each of the four frequencies, about 3 and 6 GHz in $^6Li^+$ and 12 and 20 GHz in $^7Li^+$, a different waveguide setup had to be prepared. In Fig. 3 the microwave system with X and K band versions used for 12 GHz and 20 GHz is drawn. Fig. 4 shows the two Doppler shifted signals for the $2\,^3S_1$ ($F=3/2-F=5/2$) transition of $^7Li^+$.

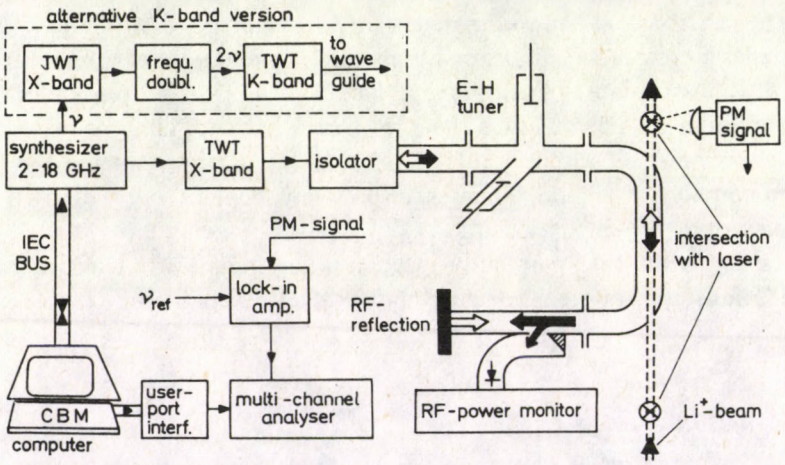

Fig. 3. Microwave system

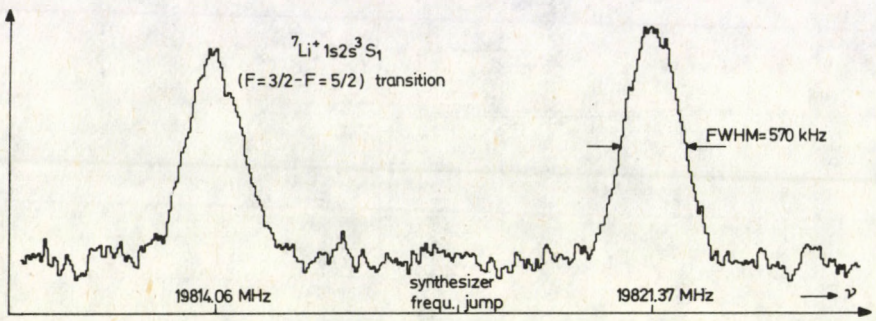

Fig. 4. Doppler shifted microwave signals of $2\,^3S_1$ ($F=3/2-F=5/2$) transition in $^7Li^+$

3. Discussion of the experimental results*

a. Magnetic hyperfine interaction constant

A more detailed sketch of the $2\,^3S_1$ hyperfine multiplet of $^7Li^+$ is given in Fig. 5. The measurement of both splittings yielded the magnetic hyperfine interaction constant A. In the case of the $2\,^3S_1$ state A arises exclusively from Fermi contact interaction between electron spins and nuclear spin and can be expressed by the following formula [25]:

$$A(2\,^3S_1)_{exp} = 36\alpha^2\,(g_I/\mu_N)\,(m_e/m_p)\,R_\infty\,cM^*\,[1+\Delta_{rel}\,(1s)+\Delta_{qed}\,(1s)+\Delta_{M,rel}+$$
$$+\varepsilon(1+\Delta_{rel}\,(2s)+\Delta_{qed}\,(2s)+\Delta_{M,rel})]\,(1+\Delta_{nuc})\,.$$

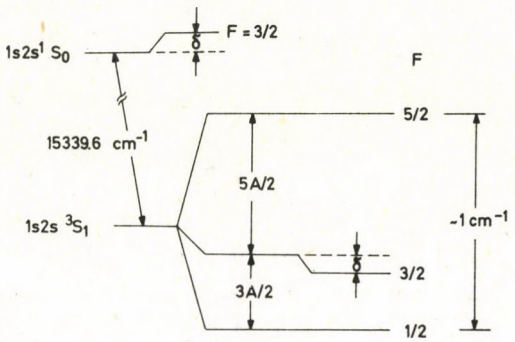

Fig. 5. Diagram of the $2\,^3S_1$ hyperfine multiplet and $2\,^1S_0$ state of $^7Li^+$, including the $F=I=3/2$ displacement (enlarged). The constant A can be extracted from the unperturbed ($F=5/2-F=1/2$) splitting

$M^*=(1+m_e/M)^{-3}$ corrects for the reduced mass of the nucleus. The terms in brackets represent relativistic (Δ_{rel}; $\Delta_{M,rel}$) and quantum-electrodynamic (Δ_{qed}) corrections as well as corrections for the presence of the 2s electron (ε) and for effects of nuclear structure on hyperfine splitting ($\Delta_{nuc}=\Delta$). If all numbers equal for both isotopes are comprised in a factor C, the ratio

$$\frac{^7A_{exp}}{^6A_{exp}} = \frac{C\,^7g_I\,^7M^*\,(1+^7\Delta)}{C\,^6g_I\,^6M^*\,(1+^6\Delta)}$$

can be transformed to

$$\frac{^7A_{exp}\,^6g_I\,^6M^*}{^6A_{exp}\,^7g_I\,^7M^*} = \frac{1+^7\Delta}{1+^6\Delta} \approx 1+^7\Delta-^6\Delta = 1-^{6,7}\Delta\,.$$

* Some of the results, including the values A_{calc}, Δ_{nuc} and $\rho^2\cdot\delta'_{theor}$ have been briefly reported in [23]. More recently theoretical values for δ have been also presented by other authors [24].

The expression $^{6,7}\Delta = {}^{6}\Delta - {}^{7}\Delta$ is called hyperfine structure anomaly. Evaluation of $A_{exp} = A_{cal}(1+\Delta)$ for each isotope with the most precise data available in the literature for the constants and corrections leads to explicit values for $^{6}\Delta$ and $^{7}\Delta$. This means that a decomposition of the hyperfine anomaly $^{6,7}\Delta$ into the contributions of the single isotopes has been achieved. Taking $^{7,8}\Delta$ from [26] allows us also to calculate $^{8}\Delta$. The measured splitting frequencies and extracted constants A_{exp}, together with the calculated values A_{cal} and the nuclear structure effects Δ are compiled in Tables I and II. Nuclear structure effects in hyperfine structure of single isotopes have been obtained before only for hydrogen, deuterium, tritium and ^{3}He and were treated theoretically. A review of these investigations can be found in [27].

Table I

Measured $2\,^{3}S_1$ hfs splittings in MHz (Errors are 3σ)

$^{6}Li^{+}$	$F=0-F=1$ splitting	3001.780 (50)
	$F=1-F=2$ splitting	6003.600 (50)
$^{7}Li^{+}$	$F=1/2-F=3/2$ splitting	11890.018 (40)
	$F=3/2-F=5/2$ splitting	19817.673 (40)

Table II

Experimental and calculated hfs interaction constants (in MHz) of the $2\,^{3}S_1$ multiplet and nuclear structure effects. Experimental errors are 3σ. The errors of A_{cal} and Δ are based on the assumption that the relativistic and radiative corrections are uncertain within $1 \cdot 10^{-5}$ each.

$A(^{6}Li^{+})_{exp}$	3001.793(17)	$\Delta(^{6}Li)\ 10^{6} = -276(30)$
$A(^{6}Li^{+})_{cal}$	3002.6(1)	$\Delta(^{7}Li)\ 10^{6} = -383(30)$
$A(^{6}Li^{+})_{exp}$	7926.923(14)	$\Delta(^{8}Li)\ 10^{6} = -307(36)$
$A(^{6}Li^{+})_{cal}$	7929.95(24)	

b. Hyperfine induced $2\,^{3}S_1 - 2\,^{1}S_0$ interaction

Comparison of the two $^{3}S_1$ hfs splitting frequencies of $^{7}Li^{+}$ showed that the Landé interval rule does not hold strictly, indicating that a small perturbation of the $2\,^{3}S_1$ wave function must exist. A small lowering δ of the inner hfs substate is inserted in Fig. 5, enlarged by a factor of about 10^{4} with respect to the total splitting. The hyperfine quantum number F of this substate is equal to the nuclear spin quantum number I. The $2\,^{1}S_0$ state which has no hyperfine splitting and is represented by the quantum number $F=I$ is also drawn in the picture. The hfs operator selectively induces a triplet–singlet mixing between the $(2\,^{3}S_1, F=I)$ sublevel and the $2\,^{1}S_0$ state [28]. This causes a mutual

repulsion of the two levels and results in a small depression δ of the ($2\,^3S_1$, $F=I$) substate, since the $2\,^3S_1$ lies below the $2\,^1S_0$.

The hfs theory for *ls* configurations of two-electron atoms as developed by Breit and Wills [7], Schwartz [8] and Lurio, Mandel and Novick [9] serves as a basis for the calculation of δ. Evaluation of the magnetic dipole matrix elements of an *ls* configuration as given in [9] provides the following energy submatrices:

$^6Li^+$	$^1S_0$, $F=1$	$^3S_1$, $F=1$
$^1S_0$, $F=1$	0	$\frac{\sqrt{2}}{2}a_s$
$^3S_1$, $F=1$	$\frac{\sqrt{2}}{2}a_s$	$-\frac{a_s}{2}-W$

$^7Li^+$	$^1S_0$, $F=3/2$	$^3S_1$, $F=3/2$
$^1S_0$, $F=3/2$	0	$\frac{\sqrt{15}}{4}a_s$
$^3S_1$, $F=3/2$	$\frac{\sqrt{15}}{4}a_s$	$-\frac{a_s}{2}-W$

Diagonalisation of the matrices provides the expressions

$$^6\delta'_{\text{theor}} = \frac{\frac{1}{2}a_s^2(^6Li^+)}{\frac{1}{2}a_s(^6Li^+)+W} = 39.188(3)\,\text{kHz},$$

$$^7\delta'_{\text{theor}} = \frac{15}{16}\cdot\frac{a_s^2(^7Li^+)}{\frac{1}{2}a_s(^7Li^+)+W} = 512.39(3)\text{kHz}.$$

In the above formula the magnetic hfs interaction constant a_s is related to the constant A by $a_s=2A$ as defined in [29], while $W=15339.62(20)\,\text{cm}^{-1}$ [30] is the $2\,^3S_1-2\,^1S_0$ energy splitting. The diagonal and nondiagonal matrix elements in [9] contain identical spatial wave functions expressed by the same a_s. This is not completely correct because the exchange interaction between the two electrons differs for parallel and antiparallel electron spins. Since a_s used for the evaluation of δ'_{theor} was taken from the $2\,^3S_1$ hfs measurement, δ'_{theor} includes the square of the diagonal spatial matrix element

$$\langle 2\,^3S_1(r_1,r_2)\,|\,\delta^3(r_1)+\delta^3(r_2)\,|\,2\,^1S_0(r_1,r_2)\rangle = d$$

rather than of the nondiagonal element

$$\langle 2\,^3S_1(r_1,r_2)\,|\,\delta^3(r_1)-\delta^3(r_2)\,|\,2\,^1S_0(r_1,r_2)\rangle = n.$$

Multiplying δ'_{theor} with the factor $\rho^2=\left(\frac{n}{d}\right)^2$ corrects for this imperfection. The calculation of $\rho^2=0.725457(1)$ was performed [31] with accurate integral-transform

wave functions from [32]. The experimental results for δ together with the calculated values δ'_{theor} and $\delta'_{\text{theor}} \cdot \rho^2$ are given in Table III. The error of δ'_{theor} is dominated by the uncertainty of W, neglecting isotope shift and hyperfine splitting leading to an error of 1–2 cm^{-1}. The accuracy of ρ^2 is limited to a few parts in 10^5 since the wave functions in [32] have been developed for infinite mass Li nucleus.

Table III

Experimental and calculated values (in kHz) for the displacement δ of the $2\,^3S_1$ hfs substate with $F = I$. Experimental errors are 3σ. For errors in δ'_{theor} and ρ^2 see text.

	δ_{exp}	δ'_{theor}	$\rho^2 \cdot \delta'_{\text{theor}}$
$^6Li^+$	13(37)	39.188(3)	28.429(3)
$^7Li^+$	366(29)	512.39(3)	371.72(4)

4. Conclusion

The combined method of laser optical pumping and microwave transitions has been used to determine the splitting frequencies of the metastable $2\,^3S_1$ hyperfine multiplet of $^{6,7}Li^+$. The resulting magnetic hyperfine interaction constants A are compared with calculated values using the most precise fundamental constants and relativistic and quantum-electrodynamic corrections available in the literature. A nuclear structure effect Δ in the interaction constant A is extracted for $^6Li^+$ and $^7Li^+$, thus yielding a decomposition of the hyperfine anomaly into the contributions of the single isotopes.

A small deviation δ of the $2\,^3S_1$ hfs splitting frequencies from the Landé interval rule was found for $^7Li^+$. This displacement of the $(2\,^3S_1, F = I)$ substate is caused by $2\,^3S_1 - 2\,^1S_0$ hyperfine mixing. It could also be calculated with accurate wave functions, taking into account that the spatial parts of the $2\,^3S_1$ and $2\,^1S_0$ wave functions are not identical, since the electron exchange interaction differs for parallel and antiparallel electron spins. Very good agreement between measured and calculated values is obtained.

Acknowledgements

The Li^+ experiment was sponsored by the Deutsche Forschungsgemeinschaft. R. H. thanks the Alexander von Humboldt-Foundation for an Award in the Special Program for U. S. Senior Scientists, and to the University of Heidelberg for its hospitality. The authors take the pleasure in thanking V. H. Smith, Jr., for supplying the Li^+ wave functions. K. S. Meyer is thanked for her help with the numerical computations.

References

1. A. Budó, I. Kovács, Z. Physik, *109*, 393, 1938.
2. A. Budó, I. Kovács, Z. Physik, *111*, 633, 1939.
3. A. Budó, I. Kovács, Acta Phys. Hung., *1*, 84, 1950.
4. I. Kovács, A. Lagerqvist, Ark. Fys. *2*, 411, 1950.
5. I. Kovács, Can. J. Phys., *36*, 309, 1958.
6. I. Kovács, Acta Phys. Hung., *40*, 131, 1976.
7. G. Breit, L. A. Wills, Phys. Rev., *44*, 470, 1933.
8. C. Schwartz, Phys. Rev., *97*, 380, 1955.
9. A. Lurio, M. Mandel, R. Novick, Phys. Rev., *126*, 1758, 1962.
10. U. Kötz, J. Kowalski, R. Neumann, S. Noehte, H. Suhr, K. Winkler, G. zu Putlitz, Z. Physik, A*300*, 25, 1981.
11. R. Neumann, J. Kowalski, F. Mayer, S. Noehte, R. Schwarzwald, H. Suhr, K. Winkler, G. zu Putlitz, in Laser Spectroscopy V, Springer-Verlag, Berlin, Heidelberg, New York, 1981, p. 130.
12. S. D. Rosner, R. H. Holt, T. D. Gaily, Phys. Rev. Lett., *35*, 785, 1975.
13. S. D. Rosner, R. H. Holt, T. D. Gaily, Phys. Rev. Lett., *40*, 851, 1978.
14. W. Ertmer, B. Hofer, Z. Physik A, *276*, 9, 1976.
15. N. Bessis, H. Lefebvre-Brion, C. M. Moser, Phys. Rev., *135*, A957, 1964.
16. P. F. Liao, R. R. Freeman, R. Panock, L. M. Humphrey, Opt. Commun., *34*, 195, 1980.
17. R. L. Brooks, V. F. Streif, H. G. Berry, Nucl. Instr. Meth., *202*, 113, 1983.
18. L. A. Bloomfield, H. Gerhardt, T. W. Hänsch, Phys. Rev. A, *26*, 3716, 1982.
19. R. Beigang, E. Matthias, A. Timmermann, Phys. Rev. Lett., *47*, 326, 1981.
20. H. Rinneberg, Z. Physik, A, *302*, 363, 1981.
21. H. Rinneberg, J. Neukammer, Phys. Rev. Lett., *49*, 124, 1982.
22. S. D. Rosner, F. M. Pipkin, Phys. Rev., A*1*, 571, 1970.
23. R. Herman, J. Kowalski, H. Suhr, G. zu Putlitz, Book of Abstracts, Eighth International Conference on Atomic Physics, Göteborg, August 2–6, 1982, p. A 67.
24. M. Ya. Amusia, M. Ju. Kuchiev, V. L. Yakhontov, J. Phys. B: At. Mol. Phys., *16*, L129, 1983.
25. H. A. Bethe, E. E. Salpeter, Quantum Mechanics of One- and Two-Electron Atoms, Springer-Verlag, Berlin, Göttingen, New York, 1957.
26. A. Winnacker, D. Dubbers, F. Fujara, K. Dörr, H. Ackermann, H. Grupp, P. Heitjans, A. Körblein, H.-J. Stöckmann, Phys. Lett., *67A*, 423, 1978.
27. D. A. Greenberg, H. M. Foley, Phys. Rev., *120*, 1684, 1960.
28. M. M. Sternheim, Phys. Rev. Lett., *15*, 545, 1965.
29. H. Kopfermann, Kernmomente, Akademische Verlagsgesellschaft, Frankfurt a. M., 1956.
30. S. Bashkin, J. O. Stoner, Jr., Atomic Energy Levels and Grotrian Diagrams, Vol. I, North-Holland, Amsterdam, Oxford, American Elsevier, New York, 1975.
31. J. Kowalski, R. Neumann, S. Noehte, H. Suhr, G. zu Putlitz, R. Herman, Z. Physik A. *313*, 147, 1983.
32. A. J. Thakkar, V. H. Smith, Jr., Phys. Rev., A*15*, 16, 1977.

Acta Physica Hungarica 56 (1—4), pp 209—215 (1984)

DENSITY OF GAP STATES IN AMORPHOUS SEMICONDUCTORS BY THE FIELD EFFECT

J. GAZSÓ

Central Research Institute for Physics
1525 Budapest, Hungary

(Received in revised form 28 June 1983)

Amorphous semiconductors contain broad distributions of localised states in their mobility gaps. The paper presents an analysis of how the density of these states may be deduced from the field effect. In response to the application of a transversal field F_x a space charge distribution results. The gross features of the corresponding distorted band structure are reflected in the longitudinal conductance G_z. The main task is to convert this implicit information into explicit formulae which enable the direct estimate of the density of the localised states from the measured G_z versus F_x functions. This is accomplished by studying a somewhat simplified model which approximates the density of states by piecewise constant parts.

Wide gap amorphous semiconductors contain broad distributions of localised states in their mobility gaps, i.e. between E_v and E_c in Fig. 1. For any practical description, there is a need for a reliable estimate on the density function $g(E)$. The field-effect method, first applied to amorphous semiconductors by Spear and Le Comber [2], is regarded widely as one appropriate to the task.

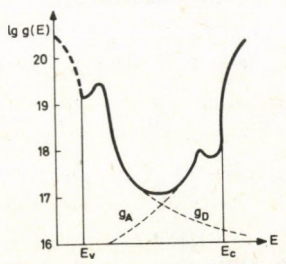

Fig. 1. Density of states distribution for a-Si prepared by the glow discharge method (from [1])

From the experimental point of view, the method looks deceptively simple. In a thin film ($d \sim 1\mu m$) of amorphous semiconductor (a-SC), the longitudinal conductance G_z is measured whenever the new steady state has settled down in response to the deliberate alterations in the transverse electric field F_x. The resulting distortion in the

energy profile can be characterized by the band bending $U(x)$ (Fig. 2). Owing to the wide gap, the contribution of the mobile charge carriers to the space charge $\rho[U(x)]$ will usually be negligible compared to the localised charges.

In contrast to the space charge forming ability, only the carriers with energy outside the mobility gap will contribute noticeably to the conductivity σ, at least at not too low temperatures $T(kT > 10$ meV). Since the equilibrium concentration of the

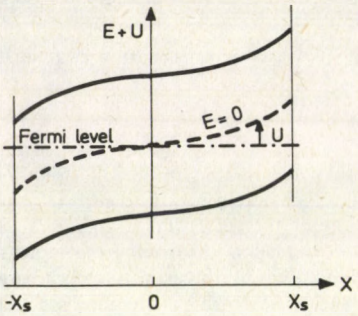

Fig. 2. Band bending by the field effect

mobile carriers varies as $\exp(U/kT)$, the changes in $U(x)$ induced by F_x may be felt strongly even in the conductivity integral $G_z \sim \int \sigma[U(x)] \cdot dx$. Furthermore, since the behaviour of $U(x)$ depends also on the energetic distribution of the charged localised states, the information implicit in G_z may be sufficient for deducing a $g(E)$ function. However, the matter of interpretation has never been settled with certainty [3–4]. Thus, for example, [3] suggests a procedure which claims validity for arbitrary density of states functions. It leaves, however, the real task to the persons who try to interpret their data: the $g(E)$ function must be adjusted until self-consistency is obtained. On the other hand, [4] admits that its procedure assumes relatively thick films ($d > 1\mu$m) and a quadratic function for the logarithm of $g(E)$. Nevertheless, the relevant parameters still have to be found by adjustment. Being aware of the aforementioned difficulties, we wish to circumvent these problems by restricting ourselves to the study of deliberately simplified distributions of the localised states. If such a starting point is once accepted, however, our treatment will proceed without further simplifying assumptions, and we will provide explicit formulae for the calculation of the few parameters characterizing our approximate model.

The review article [1], from which also Fig. 2 is taken, summarizes the notions prevailing among experimenters concerning the nature of the band gap states. It is thus suggested that the broad minimum of $g(E)$ around the midgap arises from overlapping tails of two distributions of defect centres which differ by their charge state. The dotted curves in Fig. 1 show a likely division of $g(E)$ into its two components, which is also consistent with the observed Fermi level position. Distribution g_A, extending from the E_c side into the gap contains acceptor-like states which are neutral when empty, so that

below the Fermi level E_F they will carry a negative charge. Curve g_D contains states from the opposite side of the gap which are neutral when occupied and therefore provide positively charged donor-like states above E_F. The charge states described are identical to those envisaged in the Cohen–Fritzsche–Ovshinsky model [5] but the important difference is that here we are dealing with the overlap of defect distributions, whereas the original CFO model considered the tail state overlap in alloy glasses.

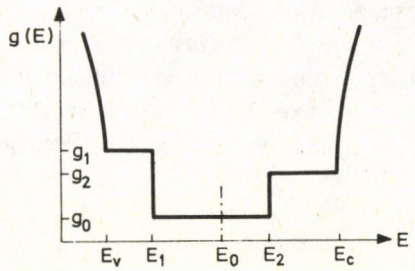

Fig. 3. The simplified density of states model

Let us now turn to our model of the gap states (Fig. 3). As it is apparent from the comparison with Fig. 1, our model retains the gross overall shape of the gap distribution, while replacing the smooth transition regions by abrupt jumps in $g(E)$. In our opinion, however, this approach may be justified on the ground that the more detailed studies all agree on the point that the resolving power of the field effect cannot be better than a few kT anyway. The values of E_1, E_0, E_2 and g_1, g_0, g_2 are as yet free parameters.

We have in mind a double-gated arrangement such that the dielectric displacement is the same at both sides $|x_s| = d/2$ of the semiconductor:

$$\varepsilon_0 \varepsilon_i F = \varepsilon_0 \varepsilon_{sc} \cdot U_s'/q^*, \tag{1}$$

where U_s' is the potential energy gradient within the semiconductor at $|x_s|$, $\varepsilon_0 = 8.8542 \cdot 10^{-14}$ As/Vcm, $q^* = 1$ eV/V, while the elementary charge will be distinguished by $q = 1.6 \cdot 10^{-19}$ As. Typical values are $\varepsilon_i = 4$ for the insulator and $\varepsilon_{sc} = 20$ for the amorphous semiconductor ($d = 1$ μm).

If we assume that the role of the possible surface states is negligible, then charge neutrality must hold everywhere in the a-SC in the unperturbed state, which is also the sensible reference zero for band bending:

$$\rho_0 = \rho(U = 0) = 0. \tag{2}$$

In this state of neutrality (flat band condition), E_0 is the position of the Fermi level in the reference system relative to the band structure. Mathematically, E_0 is the root of the following equation:

$$\int_{E_v}^{E_c} g_D(E) \cdot [1 - f(E)] dE = \int_{E_v}^{E_c} g_A(E) \cdot f(E) \cdot dE, \tag{3}$$

where E_0 is contained in the Fermi–Dirac occupation function:

$$f(E) = \left[1+\exp\frac{E-E_0}{kT}\right]^{-1}. \tag{4}$$

Since the g_A, g_D states too far away from E_0 are inactive, numerical-graphical estimates will convince that E_0 must lie somewhere close to the middle of the gap, where $g_A(E_0)$ and $g_D(E_0)$ are of the same order of magnitude.

In the modulated case, thanks to the insulators, no net current j_x may flow in the steady state. Thus the concept of the Fermi level is still meaningful, and it is horizontal. On the other hand, the level E_0, fixed to the band energy system, is displaced by just $U(x)$. Where $U(x)\neq 0$, $\rho(U)$ is given by the charge imbalance between empty donors and occupied acceptors:

$$\rho(U)=q\cdot\int_{E_1}^{E_2} g_D(E)\cdot[1-f(E+U)]\cdot dE - q\cdot\int_{E_1}^{E_2} g_A(E)\cdot f(E+U)\cdot dE, \tag{5}$$

By making use of (2) and (3), however, (5) may be rewritten:

$$\rho(U)=\rho(U)-\rho_0=-qg_0\cdot\int_{E_1}^{E_2} f(E+U)-f(E)\cdot dE\approx g_0\cdot q\cdot U(x). \tag{6}$$

(6) is valid for $E_0-E_2<U<E_0-E_1$. As it can be shown by some elaboration, similar relations hold:

$$\rho(U)\approx g_1\cdot q\cdot U \qquad \text{for} \qquad E_0-E_1<U<E_0-E_v, \tag{7}$$

$$\rho(U)\approx g_2\cdot q\cdot U \qquad \text{for} \qquad E_0-E_c<U<E_0-R_2. \tag{8}$$

Thus the individual g_A, g_D functions are important only in setting E_0; otherwise the field effect senses only their sum $g(E)=g_A(E)+g_D(E)$.

By (6)–(8), the Poisson equation takes the form:

$$\frac{d^2U}{dx^2}=\frac{U}{L^2}, \tag{9}$$

where L denotes the respective Debye length:

$$L=\sqrt{\frac{\varepsilon_0\cdot\varepsilon_{sc}}{q\cdot q^*\cdot g}}. \tag{10}$$

At moderate fields the modulation is limited so that (6) is valid through the whole cross section. Then the solution is of the form:

$$U(x)=\frac{U_s'\cdot L_0}{\cosh(x_s/L_0)}\cdot\sinh(x/L_0). \tag{11}$$

We plotted both L and $L\cdot\tanh(x_s/L)$ in Fig. 4. Also, on the right hand scale are indicated the values of U_s induced by an external field $F=10^5$ V/cm across the insulators, which by (1) corresponds to $U_s'=2\cdot 10^4$ eV/cm. One can judge from this that working with practical fields, sizeable modulations (a few kT, at least) can be expected only below $g_0\lesssim 10^{18}$ cm^{-3} eV^{-1}. We dealt with the case of higher g_0 densities in two

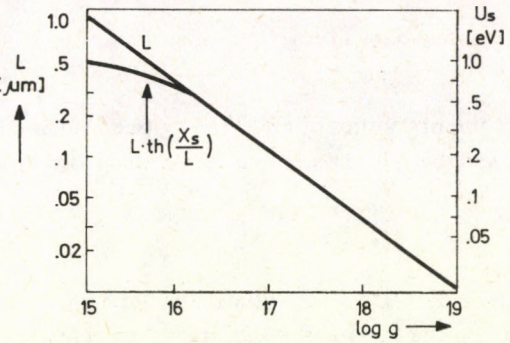

Fig. 4. Debye length L versus density of localised states g. The plot of $L\cdot\tanh(x_s/L)$ if read off the right hand scale, gives also the values of U_s induced by an external field $F=10^5$ V/cm across the insulators with $\varepsilon_i=4$

recent publications [6–7]. Here we mention for completeness that in that case a minimum has to be found in the empirical $(dG/dF)\cdot(1/F^2)$ versus F function. By this,

$$g_0=\frac{\varepsilon_0\varepsilon_i}{qkT}\sqrt{\frac{\varepsilon_i q^*\cdot 0.6564\cdot\sigma_0}{\varepsilon_{sc}\cdot kT\cdot\min\left(\frac{1}{F^2}\frac{dG}{dF}\right)}}. \tag{12}$$

Once an average g_0 is obtained, then the corresponding sweep in energy U_s can be calculated via (10) and (11).

Let us now turn to the case when g_0 is low enough to allow modulations U large enough so that the shoulders E_1 or E_2, if present, may be reached. (For a practical estimate, let $g_0=10^{17}$ cm^{-3} eV^{-1}, $E_2-E_0=E_0-E_1=0.4$ eV. Then the right hand scale of Fig. 4 would immediately give $|U_s|=0.21$ eV for $F=10^5$ V/cm. To achieve $|U_s|=0.4$ eV, $F=1.9\cdot 10^5$ V/cm suffices, which is well within the feasibility of practical fields.) It was proved in [6] that in this range $\log G$ varies against F with a slope proportional to L (Fig. 5). A heuristic explanation may sound like the following. Whenever U_s is several kT large, then let x_1 denote the place where $U(x_1)=u_1\cdot kT$, $u_1=0.37251$. (The particular choice for u_1 will be justified below on the ground that it is a root of the exponential integral: $Ei(u_1)=0$, see [8].) Then the variation in G takes part mostly in the much better conducting skin-region beyond x_1, where $u(x)=U(x)/(kT)$ is nearly exponential:

$$u(x)\approx u_1\exp\left(\frac{x-x_1}{L}\right), \tag{13}$$

$$\sigma(x) \approx \sigma_1 \exp[u(x) - u_1], \tag{14}$$

$$G \approx G_{\text{outer}} \approx \sigma_1 \cdot \int_{x_1}^{x_s} \exp[u(x) - u_1] dx \approx \frac{\sigma_1 L}{\exp u_1} \cdot \int_{u_1}^{u_s} \frac{\exp u}{u} du, \tag{15}$$

$$\log G \approx \text{const} + u_s + 1/u_s - \log u_s, \tag{16}$$

$$\frac{d \log G}{du_s'} \approx L\left(1 - \frac{1}{u_s} - \frac{1}{u_s^2}\right), \tag{17}$$

where we made use of the properties of $Ei(u_s)$ in (15) (see [8]) and of (13). Since $1/u_s \ll 1$ and L is by (10) connected to g, the explicit formula for the latter:

$$g \approx \frac{\varepsilon_0 \varepsilon_{sc}}{q q^* L^2} \approx \frac{\varepsilon_0 q^*}{\varepsilon_{sc} q} \left(\frac{kT}{\varepsilon_i} \frac{d \log G}{dF}\right)^{-2}. \tag{18}$$

Owing to the logarithmic derivative, the value of the flat band conductance G_0 does not enter into (18). However, the flat band condition is the reference zero for the energy sweep U_s.

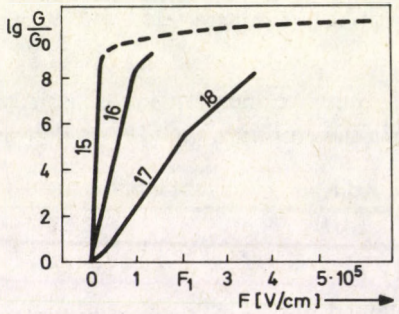

Fig. 5. Plots of $\log G/G_0$ versus inducing field F. The parameters are the orders of magnitude of g

In Fig. 5, we give some characteristic examples ($T = 295$ K). For completeness, the plots for $g = 10^{15}$ and 10^{16} cm^{-3} eV^{-1}, respectively, are also given, assuming that the whole mobility gap would be filled uniformly by these unusually low g_0 densities, which are seldom encountered in practice. The uppermost dashed line represents the takeover in controlling the space charge by the mobile carriers in the delocalised bands [6].

By contrast, the lowest broken line demonstrates that at field F_1 the shoulder E_2 has been reached. (For $E_2 - E_0 = 0.4$ eV this happens at about $F_1 \approx 2 \cdot 10^5$ V/cm, as it was already mentioned.) Should this broken line be obtained experimentally, with unknown densities and location of the jump in density, the procedure is straightforward. From the logarithmic slope below F_1, $g_0 \approx 10^{17}$ cm^{-3} eV^{-1} can be deduced via (18). Then, with the help of (10) and (11), $U_1 = E_2 - E_0$ can be calculated. The procedure is entirely similar above F_1. Obviously, the method may be generalized also for the case when $g(E)$ is approximated by piecewise constant parts, provided each constant part extends at least several kT in energy (> 0.1 eV).

References

1. P. G. LeComber and W. E. Spear, Ch9 in: Amorphous Semiconductors, ed. M. H. Brodsky, Springer, Berlin, 1979.
2. W. E. Spear and P. G. LeComber, J. Non-Crystalline Solids, *8–10*, 727, 1972.
3. M. J. Powell, Phil. Mag., B *43*, 93, 1981.
4. R. L. Weisfield and D. A. Anderson, Phil. Mag., B *44*, 83, 1981.
5. M. H. Cohen, H. Fritzsche and S. R. Ovshinsky, Phys. Rev. Lett., *22*, 1065, 1969.
6. J. Gazsó, Phys. Stat. Sol. (a), *68*, 675, 1981.
7. J. Gazsó, Phys. Stat. Sol. (a), *70*, K181, 1982.
8. Handbook of Mathematical Functions. Editors: M. Abramowitz and I. A. Stegun, Dover, New York, 1968.

Acta Physica Hungarica 56 (1—4), pp 217—243 (1984)

RELATIVISTIC HYDRO- AND THERMODYNAMICS IN NONLINEAR SCALAR FIELD

G. DÁVID

Department of Atomic Physics, Roland Eötvös University
1088 Budapest, Hungary

(Received 12 July 1983)

A classical relativistic theory is proposed describing the hydrodynamics and thermodynamics of fermions in the presence of a nonlinear scalar field, which contributes to the rest mass of particles. The macro and microdynamics (i.e. hydrodynamics and Fermi motion) are separated in a covariant way. The obtained equations of motion, of field and of state are consistent with thermodynamics and with the conventional formulation of relativistic hydrodynamics. Static solutions can describe e.g. cosmological domain walls or scalar bags. The acoustic and scalar waves propagating in the medium have been investigated.

Introduction

The scalar fields, having been frequently discussed in the forties and the fifties [1]–[7] appeared again in particle physics: the non-vanishing vacuum expectation value of a scalar field serves as a background of the motion of other particles and gives them masses via the Higgs mechanism. But at sufficiently high energy the scalar fields occur as independent degrees of freedom. They may play an important role in the formation processes and in the equilibrium state of macroscopic objects on astrophysical and cosmological scale (quark stars, vacuum domains, etc.). It justifies the effort to investigate the interactions of scalar fields with other fields and particles in the frame of classical physics. The results and solutions, the possible structures can serve as guides to the non-perturbative investigations in the nonlinear quantum field theory.

The basic phenomenon of the Higgs mechanism is the contribution of scalar field to the masses of other particles. This phenomenon already occurs in the classical relativistic physics [1]–[4]. This fact motivated the choice of methods used in the present paper: the treatment is all along relativistic, but quantum phenomena are neglected. The only exceptions are zero point energy and pressure of fermion systems, occurring already on macroscopic level in the thermodynamics of fermion matter.

Earlier papers (e.g. [7], [8], [9]) dealing with the interaction of fermions and scalar fields on semi-classical level averaged the zero point Fermi motion and investigated the thermostatic equation of state, seeking for possible phase transitions and anomalous states.

But the large size (e.g. quark star) or fast variations (e.g. transition complex formed in heavy-ion collision) of the realistic fermion-scalar systems make the static treatment insufficient and require the description of spatial structures and of dynamical processes.

The present paper attempts the consistent development of the classical relativistic hydrodynamics and thermodynamics of fermion systems interacting with nonlinear scalar fields. After defining the previous hydrodynamical theory the main step is the consequent covariant separation of fluctuations and macroscopic flow. According to the thermodynamical discussion this separation process works on a sufficiently broad class of averaging methods. The theory obtained has static solutions describing spatial structures which may be suitable to model the realistic objects mentioned above. After discussing some hydrodynamical aspects of the theory we investigate different types of waves propagating in the fermion-scalar system.

1. Motion of a mass point in a scalar field

Let us consider a $(D+1)$ dimensional space-time with metrics and notations:

$$i, k, \ldots = 0, 1, \ldots, D;$$

$$\alpha, \beta, \ldots = 1, \ldots, D;$$

$$c = 1;$$

$$x_0 = it;$$

$$\Box = \partial_k \partial_k = \nabla^2 - \partial_t^2;$$

$$d\tau = (-dx_k dx_k)^{1/2} = dt\sqrt{1-v^2}.$$

The norm of the Minkowski velocity $U_i = \dfrac{dx_i}{d\tau}$ is

$$U_i U_i = -1. \tag{1.1}$$

The covariant equation of motion for a mass point of rest mass M, interacting with a scalar field φ via a coupling constant g is [3]:

$$\frac{d}{d\tau}(MU_i) = -g\partial_i\varphi. \tag{1.2}$$

The projection of Eq. (1.2) on the direction of U_i gives

$$\frac{d}{d\tau}(M - g\varphi) = 0, \tag{1.3}$$

thus the rest mass M is not constant but varies from point to point with the scalar field as

$$M = M_0 + g\varphi .$$

This is the most characteristic feature of relativistic motion in a scalar field [1], [2].

Because of the close connection of φ and M one can consider M as the physical quantity describing the scalar field with an appropriate shift and change of the scale.

The derivatión with respect to the proper time τ will be written in the form

$$\frac{d}{d\tau} \equiv U_k \partial_k ,$$

thus the equation of motion is

$$U_k \partial_k (M U_i) + \partial_i M = 0 . \tag{1.4}$$

2. Hydrodynamics of an incoherent fluid in a scalar field

Let the Lagrangian describing the fluid and scalar field be a sum of three terms:

$$L_0 = L_M + L_V + L_f , \tag{2.1}$$

where

$$L_M = -\frac{1}{2} \partial_k M \partial_k M \tag{2.2}$$

represents the kinetics of the scalar field;

$$L_V = -V(M) \tag{2.3}$$

describes the self-energy and nonlinear self-interaction of scalar field (where V is a positive semi-definite function of M, in the renormable case a polynomial of fourth order at most); and

$$L_f = -M\rho_0 \tag{2.4}$$

gives the rest and kinetic energy of fermions: ρ_0 denotes the density of particle number measured in the local co-moving frame, called "particle frame".

Varying L_0 with respect to M one gets the equation of field:

$$\Box M = \rho_0 + V'(M) \equiv Z_0 . \tag{2.5}$$

The rest of equations can be derived from an energy-momentum tensor. By using Hilbert's definition and formulas of Appendix A one gets the term T^f_{ik} corresponding to L_f:

$$T^f_{ik} = -M\rho_0 g_{ik} - 2\frac{\partial L}{\partial \rho_0}\frac{\rho_0}{2}(g_{ik} + U_i U_k) = M\rho_0 U_i U_k . \tag{2.6}$$

L_M can be written in the form

$$L_M = -\frac{1}{2} g^{ik} \partial_i M \, \partial_k M ,$$

thus the corresponding term of the energy-momentum tensor is

$$T_{ik}^M = \partial_i M \, \partial_k M - \frac{1}{2} \delta_{ik} \, \partial_l M \, \partial_l M , \tag{2.7}$$

with the divergence

$$\partial_k T_{ik}^M = \Box M \cdot \partial_i M . \tag{2.8}$$

The third term is

$$T_{ik}^V = -V(M) \, \delta_{ik} . \tag{2.9}$$

The divergence of $(T_{ik}^M + T^{Vik})$ can be written as follows, using the field equation (2.5):

$$\partial_k (T_{ik}^M + T_{ik}^V) = [\Box M - V'(M)] \, \partial_i M = \rho_0 \, \partial_i M . \tag{2.10}$$

The total energy-momentum tensor of the hydrodynamical theory is given by

$$T_{ik}^0 = M \rho_0 U_i U_k + T_{ik}^M - V \delta_{ik} . \tag{2.11}$$

Its vanishing divergence gives the equations of motion:

$$\partial_k T_{ik}^0 \equiv \partial_k (M \rho_0 U_i U_k) + \rho_0 \, \partial_i M = 0 , \tag{2.12}$$

where we have used Eq. (2.10). This is the relativistic Euler equation [5], [14]. Its projection to the direction of U_i leads to the equation of continuity:

$$\partial_k (\rho U_k) = 0 , \tag{2.13}$$

and the transversal components are identical with the equations of motion (1.4) for the particles forming the fluid. The complete set of the equations (1.1), (2.5) and (2.12) contains 6 equations for the 6 variables (M, ρ_0, U_i).

Let us investigate the static limit. (2.13) and the 0^{th} component of (1.4) are satisfied as $0 = 0$. The space components of (1.4) give

$$\partial_\alpha M = 0 . \tag{2.14}$$

Substituting it into the static form of Eq. (2.5) one gets

$$Z_0 = \rho_0 + V'(M) = 0 , \tag{2.15}$$

which is not a differential equation but an algebraic "equation of state" for the physical quantities M and ρ_0, characterizing a homogeneous phase of matter and field. There are no static spatial structures among the solutions.

3. Covariant separation of micro and macrodynamics

The macroscopic behaviour of a system composed of microscopic particles can be obtained by averaging over microscopic motions. So the fluid flow described by hydrodynamical equations does not give exact trajectories but the average of random motion of particles.

The critical point of statistical theories is the separation of macro and microdynamics, the well-defined separation of macro and microdynamics, the well-defined separation of macroscopically observable processes and ones to be averaged.

Let the Minkowski velocity U_i be decomposed to a slow macroscopic hydrodynamical motion varying smoothly and to fast stochastic fluctuations. This decomposition has to be made according to the relativistic addition of velocities.

Let us fix a point of the space-time. Let the vector of nonrelativistic velocity of particles be denoted by $\mathbf{V}$, and the vector of macroscopic observable fluid velocity by $\mathbf{v}$. The velocity of the examined particle is $\mathbf{w}$ in the frame called "*fluid frame*" co-moving with the fluid of velocity $\mathbf{v}$. The Minkowski vectors of $(D+1)$ dimension corresponding to the space vectors $\mathbf{V}$, $\mathbf{v}$ and $\mathbf{w}$ of D dimension are denoted by U_i, u_i and ω_i, respectively.

The velocity $\mathbf{V}$ of the moving particle, measured in the labor frame can be obtained by Lorentz boosting the velocity $\mathbf{w}$ measured in the fluid frame. The parameters of the Lorentz transformation are the components of the velocity $(-\mathbf{v})$ of labor frame, measured in the fluid frame:

$$U_i = \Lambda_{ik}(-\mathbf{v})\,\omega_k\,. \tag{3.1}$$

Properties of Lorentz matrices Λ_{ik} are summarized in Appendix B.

Let us investigate the density of particle number ρ_0, which is defined in the particle frame. After the averaging any information concerning the particle frame will vanish, but quantities related to the fluid frame will survive. Therefore ρ_0 must be changed to the density ρ defined in fluid frame:

$$\rho = \frac{\rho_0}{\sqrt{1-w^2}}\,. \tag{3.2}$$

Let us substitute (3.2) to each formula to be averaged.

The term T^f_{ik} of T^0_{ik} can be written in the following form, using the quantities ρ, $\mathbf{w}$, and $(-\mathbf{v})$ defined in the fluid frame:

$$T^f_{ik} = M\rho_0 U_i U_k = M\rho\,\Lambda_{il}(-\mathbf{v})\,\Lambda_{km}(-\mathbf{v})\,(\sqrt{1-w^2}\,\omega_l\omega_m)\,. \tag{3.3}$$

The factors outside the parenthesis will survive the averaging. Let us denote the quantities averaged over the fluctuation velocity $\mathbf{w}$ by brackets: $\langle f(\mathbf{w})\rangle$. The method of averaging will be fixed later.

Let us define:

$$G_{lm}=\langle\sqrt{1-w^2}\,\omega_l\omega_m\rangle=\left\langle\frac{w_l w_m}{\sqrt{1-w^2}}\right\rangle, \tag{3.4}$$

so the average of T^f_{ik} is:

$$\langle T^f_{ik}\rangle=M\rho\,\Lambda_{il}\,\Lambda_{km}\,G_{lm}\,. \tag{3.5}$$

Knowing the distribution of fluctuations in the labor frame we can calculate G_{lm}, using $\mathbf{w}$ given by Lorentz boost parametrized by arbitrary $\mathbf{v}$. Now let us require the mixed components of G_{lm} to satisfy:

$$G_{\alpha 0}=0\,. \tag{3.6}$$

These are 3 independent requirements for 3 component of $\mathbf{v}$. Therefore Eq. (3.6) can be used to fix the fluid frame.

Let us decompose the energy-momentum tensor (3.5) according to the space and time-like components of G_{lm}, by using Eq. (3.6). The space components $G_{\alpha\beta}$ can be further decomposed to diagonal and trace-less components. (Forming the trace of $G_{\alpha\beta}$ the number of spatial dimensions, D appears explicitly in our equations.)

$$\langle T^f_{ik}\rangle=M\rho\,\Lambda_{i0}\Lambda_{k0}G_{00}+M\rho\,\Lambda_{i\alpha}\Lambda_{k\alpha}\frac{1}{D}G_{\gamma\gamma}+$$

$$+M\rho\,\Lambda_{i\alpha}\Lambda_{k\beta}\left(G_{\alpha\beta}-\delta_{\alpha\beta}\frac{1}{D}G_{\gamma\gamma}\right). \tag{3.7}$$

Using formulas of Appendix B one can transform (3.7) into the following form:

$$\langle T^f_{ik}\rangle=-M\rho\,G_{00}\,u_iu_k+M\rho\frac{1}{D}G_{\gamma\gamma}(\delta_{ik}+u_iu_k)+$$

$$+M\rho\,\Lambda_{i\alpha}\,\Lambda_{k\beta}\left(G_{\alpha\beta}-\delta_{\alpha\beta}\frac{1}{D}G_{\gamma\gamma}\right). \tag{3.8}$$

Let us compare (3.8) with the conventional form of the energy-momentum tensor used in relativistic hydrodynamics (see e.g. [14]):

$$T_{ik}=eu_iu_k+p\,(\delta_{ik}+u_iu_k)+\theta_{ik}\,, \tag{3.9}$$

where e is the energy density of fluid and p is the hydrostatic pressure. The symmetric, trace-less tensor θ_{ik}, describing the dissipative phenomena, is orthogonal to u_i:

$$\theta_{ik}u_k=0\,. \tag{3.10}$$

A simple comparison shows that (3.8) corresponds to (3.9) and (3.10) has been satisfied.

In the rest of this paper we neglect the dissipative phenomena, i.e. assume that the distribution of fluctuations is isotropic in the fluid frame, thus

$$G_{\alpha\beta}=\frac{1}{D}G_{\gamma\gamma}\,\delta_{\alpha\beta}\,,$$

which leads to

$$\theta_{ik}=0\,. \tag{3.11}$$

In the first term of (3.8)

$$e=-M\rho G_{00}=-M\rho\,\langle\omega_0\omega_0\sqrt{1-w^2}\rangle=M\rho\left\langle\frac{1}{\sqrt{1-w^2}}\right\rangle=M\rho\,\langle\mathrm{ch}\omega\rangle \tag{3.12}$$

represents the intrinsic and kinetic energy densities of fluid, involving the contribution of fluctuations, but not involving the energy density of scalar field, occurring in T^{M}_{ik} and T^{V}_{ik}.

At the last transformation of (3.12) we have introduced the usual notation

$$\omega=\mathrm{arth}\,|\mathbf{w}|\,. \tag{3.13}$$

In the second term of Eq. (3.8)

$$p=\frac{1}{D}M\rho\,G_{\gamma\gamma}=\frac{1}{D}M\rho\,\langle\omega_\gamma\omega_\gamma\sqrt{1-w^2}\rangle=\frac{1}{D}M\rho\left\langle\frac{w^2}{\sqrt{1-w^2}}\right\rangle=\frac{1}{D}M\rho\left\langle\frac{\mathrm{sh}^2\omega}{\mathrm{ch}\omega}\right\rangle \tag{3.14}$$

means the hydrostatic pressure induced by the fluctuations in the continuum which was originally incoherent.

The average of the total energy-momentum tensor T^{0}_{ik} is

$$\begin{aligned}T_{ik}=\langle T^{0}_{ik}\rangle&=eu_iu_k+p(\delta_{ik}+u_iu_k)-V\delta_{ik}+T^{M}_{ik}=\\&=(e+p)\,u_iu_k+(p-V)\delta_{ik}+T^{M}_{ik}\,.\end{aligned} \tag{3.15}$$

It is manifest that the potential $V(M)$ of scalar field acts as a negative pressure. Therefore let us introduce the total pressure P:

$$P=p-V(M) \tag{3.16}$$

and the following quantity:

$$\varepsilon=e+V(M)\,. \tag{3.17}$$

The enthalpy density $(e+p)$ transforms to $(\varepsilon+P)$. Using the new notations (3.15) gives:

$$T_{ik}=(\varepsilon+P)\,u_iu_k+P\delta_{ik}+T^{M}_{ik}\,. \tag{3.18}$$

Let us consider the total energy density:

$$\begin{aligned}-T_{00}&=(\varepsilon+P)\frac{1}{1-v^2}-P+\frac{\dot{M}^2}{2}+\frac{(\nabla M)^2}{2}=\\&=\frac{\varepsilon}{1-v^2}+P\frac{v^2}{1-v^3}+\frac{\dot{M}^2}{2}+\frac{(\nabla M)^2}{2}\,.\end{aligned} \tag{3.19}$$

In the static case it is simplified to

$$-T_{00}=\varepsilon\,,$$

thus the physical meaning of ε introduced by (3.17) is the total energy density in the homogeneous static states of our system.

Substitution of (3.2) into the right side of field equation (2.5) to be averaged leads to a new averaged quantity, which is not independent from the former ones, thus $\langle\rho_0\rangle$ can be expressed by e and p:

$$z=\langle\rho_0\rangle=\langle\rho\sqrt{1-w^2}\rangle=\rho\left\langle\frac{1}{\mathrm{ch}\,\omega}\right\rangle=$$

$$=\rho\left\langle\mathrm{ch}\,\omega-\frac{\mathrm{sh}^2\omega}{\mathrm{ch}\,\omega}\right\rangle=\frac{1}{M}(e-Dp)\,. \tag{3.20}$$

Let us denote the averaged right side of (2.5) by Z. Therefore the new form of scalar field equation is

$$\Box M=Z\,, \tag{3.21}$$

where

$$Z=z+V'(M)=\frac{e-Dp}{M}+V'(M)\,. \tag{3.22}$$

4. First law of thermodynamics in the presence of scalar field

The usual form of the First Law of thermodynamics concerning densities is [15]:

$$d\varepsilon=T d\sigma+\mu d\rho\,. \tag{4.1}$$

Here ε is the energy density (it may be identified with the quantity defined by Eq. (3.17)), ρ is the particle density (3.2), T, σ, and μ are the absolute temperature, the entropy density and the chemical potential, respectively.

This form of the first law has to be completed because of the presence of a new degree of freedom, the value M of the scalar field. The energy density depends on M as well.

Before averaging, the total energy density ε_0 of the static case was given by $(-T_{00})$ (see Eq. (2.11)):

$$\varepsilon_0=M\rho_0+V(M)\,.$$

Its variation according to M is

$$\delta\varepsilon_0=(\rho_0+V'(M))\,\delta M=Z_0\,\delta M\,,$$

where Z_0 is the right side of the field equation (2.5). This expression has to be changed to

its average Z, which stands in the right side of Eq. (3.21). So the completed differential form of the First Law is

$$d\varepsilon = Td\sigma + \mu d\rho + ZdM\,. \tag{4.2}$$

According to Eq. (4.2) the proper variables of ε are the densities of two extensive quantities (the entropy S and the particle number N) and an intensive parameter, M. Thus ε cannot be identified with the density of the thermodynamical energy, but with one of its Legendre transforms [15]. The quantity Z conjugated to M in Eq. (4.2) is the density of an extensive quantity, (ZV), where V stands now for volume.

Let us perform the inverse Legendre transformation. Let $\tilde{\varepsilon}$ denote the density of the proper thermodynamical energy:

$$\tilde{\varepsilon} = \varepsilon - ZM = \tilde{\varepsilon}(\sigma, \rho, Z)\,.$$

Its differential is

$$d\tilde{\varepsilon} = Td\sigma + \mu d\rho - MdZ\,. \tag{4.3}$$

Passing on to the extensive quantities one gets [15]:

$$\tilde{E} = V\tilde{\varepsilon}\,,$$

and

$$d\tilde{E} = TdS - PdV + \mu dN - Md(ZV)\,,$$

where the thermodynamic pressure P may be identified with the expression (2.16).

According to Euler's theorem on homogeneous functions the differential form of the First Law expressed by differentials of extensive quantities only can be integrated directly [15]:

$$\tilde{E} = TS - PV + \mu N - MZV,$$

thus its density $\tilde{\varepsilon}$ is

$$\tilde{\varepsilon} = T\sigma - P + \mu\rho - MZ\,. \tag{4.4}$$

Using the form (4.3) of the First Law one gets the Gibbs–Duhem relation:

$$0 = \sigma dT - dP + \rho d\mu - ZdM\,. \tag{4.5}$$

Let us perform the Legendre transformation of the finite (4.4) and the infinitesimal (4.3) forms of the First Law:

$$\varepsilon = T\sigma - P + \mu\rho\,, \tag{4.6}$$

$$d\varepsilon = Td\sigma + \mu d\rho + ZdM\,. \tag{4.7}$$

It will be useful to use the specific entropy

$$s = \sigma/\rho \tag{4.8}$$

(instead of the entropy density σ) and the specific enthalpy

$$m=\mu+Ts \tag{4.9}$$

(instead of the chemical potential μ). Substituting (4.8) and (4.9) into the thermodynamical equations (4.5)–(4.7) one gets:

$$\varepsilon=m\rho-P\,, \tag{4.10}$$

$$d\varepsilon=T\rho ds+md\rho+ZdM\,, \tag{4.11}$$

$$dP=-T\rho ds+\rho dm-ZdM\,. \tag{4.12}$$

Subtracting the contributions of the scalar field potential $V(M)$ the equations (4.10)–(4.12) can be expressed by purely hydrodynamical quantities:

$$e=m\rho-p\,, \tag{4.13}$$

$$de=T\rho ds+md\rho+zdM\,, \tag{4.14}$$

$$dp=-T\rho ds+\rho dm-zdM\,, \tag{4.15}$$

where z is the average (3.20) of ρ_0. In the rest of this paper the forms (4.10)–(4.12) and (4.13)–(4.15) of the First Law will be used.

5. Hydrodynamical equations of motion

Let us rewrite the energy-momentum tensor (3.18) using the specific enthalpy (4.9):

$$T_{ik}=m\rho\, u_iu_k+P\delta_{ik}+T^M_{ik}\,. \tag{5.1}$$

The equations of motion can be obtained from the divergence of T_{ik}. The divergence of the term T^M_{ik} can be written by using (2.8) and (3.21) as

$$\partial_k\, T^M_{ik}=\partial_iM\cdot\Box M=Z\partial_iM\,. \tag{5.2}$$

Thus the hydrodynamical equations of motion are

$$\partial_k\, T_{ik}\equiv\partial_k(m\rho\, u_iu_k)+\partial_iP+Z\,\partial_iM=0\,. \tag{5.3}$$

Calculating the expression (5.3) one gets

$$mu_i\,\partial_k(\rho u_k)+\rho[u_k\partial_k(mu_i)+\partial_im]=\rho\partial_im-\partial_iP-Z\partial_iM\,. \tag{5.4}$$

The multiplication of Eq. (5.4) by $(u_id\tau)$ and the substitution of (4.12) lead to

$$-m\partial_k(\rho u_k)\,d\tau=\rho dm-dP-ZdM=T\rho\, ds\,.$$

Thus the equation of continuity has the form

$$m\,\partial_k(\rho u_k)=-T\rho\, u_k\partial_ks\,. \tag{5.5}$$

Substituting Eq. (5.5) into Eq. (5.4) one gets the projection of Euler equation, orthogonal to u_i:

$$u_k \partial_k (m u_i) + \partial_i m = (u_i u_k + \delta_{ik})\, T \partial_k s\,. \tag{5.6}$$

The equations (5.5) and (5.6) are identical with the corresponding formulas of the conventional relativistic hydrodynamics (see [14]).

There is a need for further assumptions about the mechanism of dissipative processes to complete the set of equations. The most simple assumption is that of isentropy, i.e. the fluid is assumed to be ideal:

$$\frac{ds}{d\tau} = u_k \partial_k s = 0\,. \tag{5.7}$$

By using this (oversimplifying) assumption one gets the set of equations, describing the system of ideal fluid and scalar field:

$$\Box M = Z\,, \tag{5.8}$$

$$\partial_k (\rho u_k) = 0\,, \tag{5.9}$$

$$u_k \partial_k (m u_i) + \partial_i m = 0\,. \tag{5.10}$$

By using Eqs (3.22) and (4.13) Z can be expressed by e, M, ρ and m:

$$\Box M = Z = V'(M) + \frac{1}{M}\left[(D+1)\, e - m\rho\right]. \tag{5.11}$$

The set of equations is not closed: one has 7 variables (M, ρ, m, e and 3 independent components of u_i) and 5 equations ((5.9), (5.11) and 3 independent components of (5.10)). (The situation is more complicated in the case of non-ideal flow: in the general case further thermodynamical quantities (T and s) appear in the hydrodynamical equations.) The missing equations characterize the examined state ("phase") of system. They can be found by fixing the method of averaging, seeking for connections among the quantities occurring. These equations serve as equations of state, e.g. in the form:

$$e = e(M, \rho)\,, \tag{5.12}$$

$$m = m(M, \rho)\,. \tag{5.13}$$

This question will be discussed in detail later.

6. Static solutions

Let us compare the new set of equations (5.9)–(5.11) to the old ones ((1.4), (2.5), (2.13)). The individual velocity of particles, U_i has been replaced by u_i, the velocity of the fluid, which is the average of U_i. The quantity M has been splitted to M, representing the scalar field in the field equation (5.11) and to the specific enthalpy m,

taking the original role of M in the Euler equation (5.10). The particle density ρ_0 has been replaced by ρ (its Lorentz transformed value) in the equation of continuity (5.9) and by z (its average) as a source of scalar field in Eq. (5.11).

Let us consider the static limit of the set of Eqs (5.9)–(5.11) and compare to the corresponding results of Chapter 2. Eq. (5.9) and the time component of (5.10) are satisfied identically, but the space components of (5.10) give

$$\partial_\alpha m = 0\,, \tag{6.1}$$

i.e. the specific enthalpy m is to be constant. Contrary to (2.14) there is no requirement for the scalar field M to be homogeneous. In the averaged form of the theory the acceleration of fluid is due to the gradient of m instead of the gradient of M. Therefore the static form of field equation (5.11)

$$V^2 M = Z = V'(M) + \frac{1}{M}\left[(D+1)\,e - m\rho\right], \tag{6.2}$$

the equations of state (5.12) and (5.13), and the requirement (6.1) form a complete set of equations for the quantities M, ρ, m, e, which has spatially structured solutions. The results of detailed numerical investigation and classification of static structures described by Eq. (6.2) (e.g. periodic scalar fields, domains, domain walls, scalar bag) will be published elsewhere.

7. Specific averages

The quantities e and p were defined by the averages (3.12) and (3.14), but at the same time they appear as thermodynamical variables in the Eqs (4.13)–(4.15). The correspondence of these two roles of quantities leads to requirements concerning the averaging method.

Identical transformations of the thermodynamical equations (4.13)–(4.15) give

$$d\left(\frac{p}{M\rho}\right) - \frac{p}{M\rho}\left(\frac{e - zM}{p}\,\frac{dM}{M} - \frac{d\rho}{\rho}\right) = \frac{1}{y}(d\alpha - \varkappa\, dy), \tag{7.1}$$

where we have introduced the notations

$$\alpha = \frac{\mu}{T}, \qquad y = \frac{M}{T}, \qquad \varkappa = \frac{m}{M}. \tag{7.2. a, b, c}$$

Thus by using Eqs (4.9) and (4.13) one gets

$$\alpha = y\varkappa - s. \tag{7.3}$$

The right side of Eq. (7.1) can be transformed by using Eq. (7.3):

$$\frac{1}{y}(d\alpha - \varkappa\, dy) = d\varkappa - \frac{ds}{y}. \tag{7.4}$$

Let us now utilize the form of z given by Eq. (3.20) and let us introduce the new quantity x:

$$x = M^{-1}\rho^{1/D}. \tag{7.5}$$

Substituting (3.20) and (7.5) into (7.1) one gets:

$$d\left(\frac{pyx^D}{M\rho}\right) = x^D\left(d\alpha - \frac{e}{M\rho}dy\right). \tag{7.6}$$

Let us substitute the definitions of e and p, given by averages in Eqs (3.12) and (3.14), respectively:

$$d\left(yx^D\left\langle\frac{\mathrm{sh}^2\,\omega}{D\,\mathrm{ch}\,\omega}\right\rangle\right) = x^D(d\alpha - \langle\mathrm{ch}\,\omega\rangle dy). \tag{7.7}$$

Eq. (7.7) shows that the quantity occurring on the left side, including an averaged quantity over the individual velocity parameter ω of particles, can be considered as a function of two thermodynamical parameters: α and y. Therefore one can choose α and y for the averaging parameters, occurring in the weight function, which defines the averages over ω:

$$\langle F(\omega)\rangle = \int_0^\infty F(\omega)\, W(\omega;\alpha,y)\, d\omega = \langle F\rangle(\alpha, y). \tag{7.8}$$

It can be shown [17] that the thermodynamical requirement (7.7) can be satisfied by specifying the weight function as follows:

$$\langle F(\omega)\rangle = \frac{\int_0^\infty d\omega\, F(\omega)\,\beta(\omega)\,\varphi(b(\omega,\alpha,y))}{\int_0^\infty d\omega\,\beta(\omega)\,\varphi(b(\omega,\alpha,y))}, \tag{7.9}$$

where

$$\beta(\omega) = D\,\mathrm{sh}^{D-1}\omega\,\mathrm{ch}\,\omega = \frac{d}{d\omega}(\mathrm{sh}^D\omega), \tag{7.10}$$

$$b(\omega,\alpha,y) = y\,\mathrm{ch}\,\omega - \alpha, \tag{7.11}$$

and identifying x^D with the denominator of Eq. (7.9):

$$x^D = \int_0^\infty d\omega\,\beta(\omega)\,\varphi(b(\omega,\alpha,y)). \tag{7.12}$$

The function $\varphi(b)$ is arbitrary, there is only the restriction of the convergence of integrals in Eq. (7.9). Direct substitution and partial integration shows that (7.7) is satisfied. It can be proved [17] that Eq. (7.12) does not contradict to other thermodynamic equations.

Let some special cases be mentioned. If one specifies the arbitrary function $\varphi(b)$ as

$$\varphi(b)=(e^b+k)^{-1}, \tag{7.13}$$

one gets the finite temperature Fermi, Bose, or Maxwell distributions in a relativistic velocity space of dimension D, by putting $k=1$, $k=-1$, and $k=0$, respectively.

Specifying $\varphi(b)$ as

$$\varphi(b)=\theta(-b), \tag{7.14}$$

where $\theta(x)$ is Heaviside's unit step function, Eq. (7.9) can be rewritten as

$$\langle F(\omega)\rangle=\frac{1}{\mathrm{sh}^D\Omega}\int_0^{\Omega} F(\omega)\, d(\mathrm{sh}^D\omega), \tag{7.15}$$

where

$$\Omega=\mathrm{arch}\frac{\alpha}{y}=\mathrm{arch}\frac{\mu}{M}. \tag{7.16}$$

This is the zero temperature Fermi distribution: Eq. (7.15) indicates averaging over the filled Fermi sphere of dimension D. The radius of Fermi sphere,

$$x=\mathrm{sh}\,\Omega \tag{7.17}$$

is the relativistic Fermi velocity,

$$\mathrm{th}\,\Omega=\frac{x}{\sqrt{1+x^2}}=\frac{x}{\varkappa} \tag{7.18}$$

is the nonrelativistic Fermi velocity,

$$\rho^{1/D}=Mx=M\,\mathrm{sh}\,\Omega=p_F \tag{7.19}$$

means the Fermi momentum, and

$$m=\mu=M\,\mathrm{ch}\,\Omega=\sqrt{M^2+p_F^2}=E_F \tag{7.20}$$

defines the Fermi energy, which is now equal to the specific enthalpy m and the chemical potential μ. In this case the averages in Eq. (7.7) and the quantities (7.16)–(7.20) can be calculated analytically [17], [18].

8. Effective Lagrange theory of ideal flow

Substituting the definitions of e (3.12) and p (3.14) into (4.13) and using (7.2. c) we can express $\varkappa$ as an average:

$$\varkappa=\left\langle \mathrm{ch}\,\omega+\frac{1}{D}\frac{\mathrm{sh}^2\,\omega}{\mathrm{ch}\,\omega}\right\rangle, \tag{8.1}$$

i.e. (fixing the weight function) as a function of y and α. By using (8.1), (7.3) and the expression of x (7.12) as functions of y and α one can express the thermodynamical parameters y and α by x and s. We can consider every averages $\langle f(\omega)\rangle$ as functions of x and s.

Investigating the ideal flow, s is only a constant parameter. Thus the averages are functions of x only. Let us introduce a function

$$\Phi(x)=\langle \mathrm{ch}\,\omega\rangle. \tag{8.2}$$

It can be shown [17] that specifying $\Phi(x)$ is equivalent to the fixing the weight function $\varphi(b)$, and $\Phi(x)$ contains all the information one needs about the microscopic motion.

Other quantities can be defined by $\Phi(x)$ and its derivative $\Phi'(x)$:

$$e=M\rho\,\Phi(x)=M\rho\,\Phi(x(M,\rho))=e(M,\rho), \tag{8.3}$$

$$p=M\rho\frac{x}{D}\Phi'(x)=p(M,\rho), \tag{8.4}$$

$$m=M\varkappa=M\left(\Phi+\frac{x}{D}\Phi'\right)=\frac{\partial}{\partial\rho}e(M,\rho)=m(M,\rho), \tag{8.5}$$

$$z=\frac{1}{M}(e-Dp)=\rho(\Phi-x\Phi')=\frac{\partial}{\partial M}e(M,\rho)=z(M,\rho). \tag{8.6}$$

At the next transformations in (8.5) and (8.6) we used the definition of x (7.5). The definitions (8.3)–(8.6) are consistent with the thermodynamical requirements of Chapter 7. Substituting (8.3)–(8.6) into (7.1), using (7.4) and utilizing the assumption of ideal flow ($ds=0$) one can prove, that (7.1) is satisfied identically.

We note that Eqs (8.3) and (8.5) can serve as the missing equations of state mentioned in Chapter 5.

Let us now define an effective Lagrange theory of ideal flow. The new Lagrangian is

$$L_\varepsilon=-\varepsilon(M,\rho)+L_M, \tag{8.7}$$

where L_M is defined by (2.2), ε by (3.17), and the quantity e is identified with (8.3):

$$\varepsilon=e+V(M)=M\rho\,\Phi(x(M,\rho))+V(M)=\varepsilon(M,\rho). \tag{8.8}$$

As consequences of (8.5), (8.6) and (3.22), derivatives of $\varepsilon(M,\rho)$ with respect to M and ρ give Z and m, respectively:

$$\frac{\partial\varepsilon}{\partial M}=Z=z+V'(M),\qquad \frac{\partial\varepsilon}{\partial\rho}=m. \tag{8.9}$$

Thus the variation of M in L_ε leads to the field equation (5.11). The energy-momentum tensor belonging to L_ε is identical with (5.1). (Deriving it one has to make use of the remark after (A.7) in Appendix A.) Therefore the corresponding equations of motion

and of continuity are identical with (5.10) and (5.9). The effective Lagrangian (8.7) containing the arbitrary function $\Phi(x)$ has reproduced the hydrodynamical and field equations, has given the equations of state (8.3) and (8.5), leading to a complete set of equations for quantities M, ρ, m and u_i.

9. Potential flow

The equation of motion (5.10) can be satisfied identically by the assumptions [5]

$$u_i = \frac{\partial_i \psi}{m}, \tag{9.1}$$

$$m = \sqrt{-\partial_k \psi \partial_k \psi}, \tag{9.2}$$

where ψ will be called relativistic momentum potential. These flows form a subset of solutions of Eq. (5.10): the class of potential flows. The condition of a flow to have potential is

$$\partial_i(mu_k) - \partial_k(mu_i) = 0. \tag{9.3}$$

The equation of continuity now has the form:

$$\partial_k\left(\frac{\rho}{m}\partial_k \psi\right) = 0. \tag{9.4}$$

Eq. (9.2) can be considered as a relativistic Bernoulli equation [5]:

$$\partial_k \psi \partial_k \psi = -m^2(M, \rho), \tag{9.5}$$

where m is expressed by basic quantities M and ρ via Eq. (8.5).

To construct a Lagrange formalism for potential flows it is suitable to exchange the roles of the basic quantity ρ and the derived quantity m. Considering Eqs (4.10)–(4.12) one can see that in the isentropic case the proper variables of ε are M and ρ, but those of P are M and m.

Let us define a new Lagrangian for potential flows. Its basic variables are ψ and M:

$$L_\psi = P(M, m(\partial_k \psi)) + L_M, \tag{9.6}$$

where $P(M, m)$ can be derived from functions $m(M, \rho)$ (8.5) and $p(M, \rho)$ (8.4) using (3.16), L_M is defined by (2.2), and $m(\partial_k \psi)$ refers to Bernoulli equation (9.5).

Varying L_ψ with respect to M and by taking the consequence of (4.12)

$$\frac{\partial P(M, m)}{\partial M} = -Z \tag{9.7}$$

into account one gets the field equation (5.11).

L_ψ gives the equation of continuity directly, without the roundabout of Hilbert's T_{ik}. L_ψ does not depend on ψ, thus one gets a conserved current:

$$j_k = \frac{\partial L_\psi}{\partial \partial_k \psi} = \frac{\partial P}{\partial m} \frac{\partial m}{\partial \partial_k \psi} = -\rho \frac{\partial_k \psi}{m}. \tag{9.8}$$

We used (4.12) to get the derivative of P:

$$\frac{\partial P}{\partial m} = \rho. \tag{9.9}$$

The conservation of j_k gives the equation of continuity (9.4).

The velocity of fluid can be defined by (9.1) and (9.2):

$$u_i = \frac{\partial_i \psi}{\sqrt{-\partial_k \psi \partial_k \psi}}. \tag{9.10}$$

Thus u_i obeys the condition

$$u_i u_i = -1. \tag{9.11}$$

One can derive the energy-momentum tensor corresponding to L_ψ: according to Appendix A, it is identical with (5.1).

By using the remark made after (A.8) one may start from a Lagrangian L_P containing an arbitrary function $P(M, m)$, without the assumption of potential flow:

$$L_P = P(M, m) + L_M. \tag{9.12}$$

Eqs (9.7) and (9.9) are now used as definitions of quantities Z and ρ. The field equation and energy-momentum tensor corresponding to L_P are identical with (5.11) and (5.1), respectively. (One can use the results of Appendix A to get the metric derivative of m.)

This description of a non-potential flow will be especially useful while discussing the wave phenomena propagating in the system.

10. Wave phenomena

The set of Eqs (5.8)–(5.11) has homogeneous static solutions characterized by

$$\begin{aligned} u_k &= i\delta_{k0}, \\ Z_0 &= Z(M_0, \rho_0) = 0, \\ m_0 &= m(M_0, \rho_0), \end{aligned} \tag{10.1. a–c}$$

where M_0, ρ_0 and m_0 are now constants.

We shall investigate here small perturbations of these solutions, using the way of description of the system by the function $P(M, m)$. Let us introduce some notations:

$$P''_{MM} = -Z'_M = -Q, \tag{10.2}$$

$$P''_{mm}=\rho'_m=\frac{\rho_0}{m_0}\frac{1}{c^2}, \tag{10.3}$$

$$P''_{Mm}=\rho'_M=-Z'_m=-\frac{\rho_0}{M_0c^2}\frac{1}{q^2}. \tag{10.4}$$

These equations serve as definitions of Q, c^2 and q^2. We introduce a further quantity a which will set a scale of the frequency space:

$$a^2=\frac{\rho_0 m_0}{M_0}\frac{1}{c^2q^4}. \tag{10.5}$$

Let us write the perturbations of the state (10.1) in the following form:

$$\begin{aligned} M(\mathbf{r},t)&=M_0[1+\mu(\mathbf{r},t)],\\ \rho(\mathbf{r},t)&=\rho_0[1+\eta(\mathbf{r},t)],\\ m(\mathbf{r},t)&=m_0[1+\nu(\mathbf{r},t)],\\ u_\alpha&=\xi_\alpha(\mathbf{r},t),\\ u_0&=i. \end{aligned} \tag{10.6. a–e}$$

The products and powers of the dimensionless, time and space dependent quantities μ, η, ν, and ξ_α will be neglected. (The above form of u_i obeys Eq. (9.11)).

The linearization of the equation of continuity (5.9) gives

$$\dot\eta=-\partial_\alpha\xi_\alpha. \tag{10.7}$$

The linearized form of time component of (5.10) leads to an identity. Its space components give

$$\dot\xi_\alpha=-\partial_\alpha\nu. \tag{10.8}$$

Eqs (10.7) and (10.8) can be contracted:

$$\ddot\eta=\nabla^2\nu. \tag{10.9}$$

By using the definitions (10.2)–(10.5) one gets the linearized form of field equation (5.11):

$$\frac{1}{M_0}\Box M=\Box\mu=\frac{z}{M_0}=Q\mu+a^2c^2\nu, \tag{10.10}$$

and that of the equation of state (8.5):

$$\nu=c^2\eta+\frac{1}{q^2}\mu. \tag{10.11}$$

Let us take the plane wave solutions of the linearized set of Eqs (10.9)–(10.11). One gets the algebraic set of equations:

$$(\omega^2-k^2-Q)\mu-a^2q^2\nu=0, \tag{10.12a}$$

$$v - c^2\eta - \frac{1}{q^2}\mu = 0, \tag{10.12b}$$

$$k^2 v - \omega^2 \eta = 0. \tag{10.12c}$$

The condition of getting nontrivial solutions is the vanishing determinant:

$$(\omega^2 - k^2 - Q)(\omega^2 - c^2 k^2) - \omega^2 a^2 = 0. \tag{10.13}$$

This is the dispersion relation for the plane waves. Let us scale the frequency space with a (10.5). By introducing

$$X = \frac{k^2}{a^2}, \qquad Y = \frac{\omega^2}{a^2}, \qquad K = \frac{Q}{a^2} \tag{10.14. a–c}$$

the dispersion relation gets the form

$$(Y - X - K)(Y - c^2 X) = Y. \tag{10.15}$$

This is the equation of a hyperbola going through the origin. The points of the hyperbola in the quarter $X > 0$, $Y > 0$ represent travelling plane waves, those of quarter $X < 0$, $Y > 0$ refer to unbounded solutions, which cannot be considered as perturbations. Points of quarter $X > 0$, $Y < 0$ form the instability region.

The physical criterion of stability of homogeneous static solutions (10.1) requires that the hyperbola (10.15) should not enter into this quarter. The placing of hyperbola depends on the parameter K. The only stable placing is characterized by the requirement

$$K \geq 0, \tag{10.16}$$

that is

$$Q \geq 0. \tag{10.17}$$

Based on the set of Eqs (10.12) the relative magnitudes of oscillating perturbations can be estimated:

$$\xi/v \sim k/\omega = \sqrt{X/Y}, \qquad \eta/v \sim k^2/\omega^2 = X/Y,$$

$$\frac{\mu}{v} \sim q^2 \frac{v - c^2\eta}{v} = q^2\left(1 - c^2\frac{X}{Y}\right). \tag{10.18. a–c}$$

Fig. 1 shows the dispersion relation of the stable case ($K > 0$), plotted on $\omega - k$ plane. The curve has two branches: an "acoustic branch" starting from origin and a "scalar branch" starting with a gap.

The scalar branch in the long wavelength limit has the dispersion relation

$$\omega^2 = \omega_0^2 + v_1^2 k^2, \tag{10.19}$$

where

$$\omega_0^2 = Q + a^2, \qquad v_1^2 = 1 + \frac{c^2}{K+1}. \tag{10.20}$$

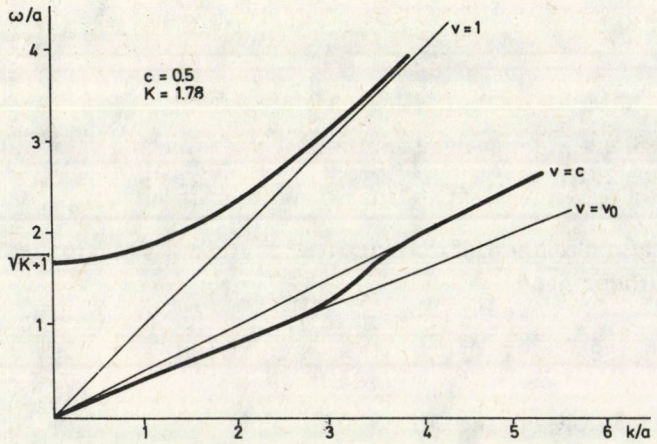

Fig. 1. Plot of the dispersion relation (10.13). Acoustic and scalar branches and their asymptotics are shown

The relative magnitudes are now:

$$k \ll 1, \qquad \omega \sim \omega_0,$$
$$\xi/v \sim k/\omega_0 \sim 0, \qquad \eta/v \sim k^2/\omega_0^2 \sim 0, \tag{10.21}$$
$$\mu/v \sim q^2.$$

At long waves the perturbation of the density and velocity can be neglected: the phenomenon is practically a pure scalar wave obeying the dispersion relation (10.19).

In the short wavelength limit the curve of scalar branch fits to the line $Y = X$, thus both the phase and group velocities converge to 1, to the speed of light in vacuum. The relative magnitudes are now:

$$k \gg 1, \qquad \omega \sim k,$$
$$\eta/v \sim \xi/v \sim 1, \tag{10.22}$$
$$\mu/v \sim q^2(1-c^2).$$

Fig. 2 shows the velocities, Fig. 3 the relative magnitudes of perturbations against the frequency ω scaled by a.

The dispersion relation of the acoustic branch near the origin gives a straight line, thus the phase and group velocities are equal:

$$V_{ph}^a = V_g^a = V_0 = c\sqrt{\frac{K}{K+1}} < c. \tag{10.23}$$

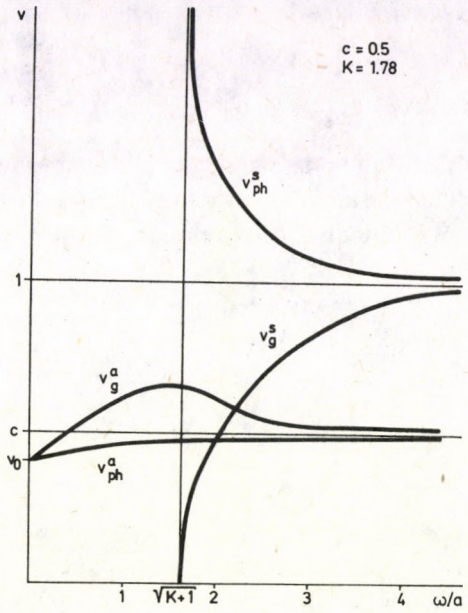

Fig. 2. Plot of phase (subscript *ph*) and group (subscript *g*) velocities of acoustic (superscript *a*) and scalar (superscript *s*) waves against scaled frequency ω/a

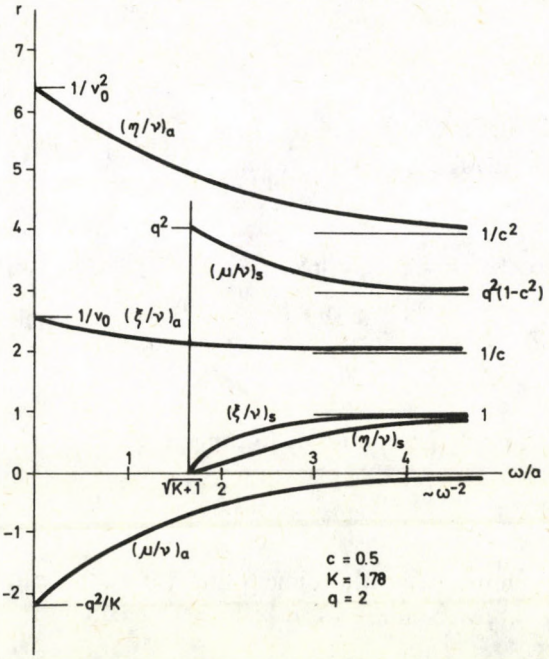

Fig. 3. Relative magnitudes of perturbations in the case of acoustic (subscript *a*) and scalar (subscript *s*) waves as functions of frequency ω. Asymptotic ($\omega\sim\infty$) and initial ($\omega\sim 0$ or $\omega\sim\omega_0$) values are indicated

The relative magnitudes are

$$\xi/\nu \sim 1/V_0, \qquad \eta/\nu \sim 1/V_0^2,$$
$$\mu/\nu \sim q^2(1-c^2/V_0^2) = -q^2/K. \tag{10.24}$$

In the short wavelength limit the phase and group velocities both converge to c (see Fig. 2). It can be proved that the maximum value of group velocity is less than 1. Using the accurate form (10.15) of the dispersion relation one gets that in this limit

$$Y - c^2 X \sim -\frac{c^2}{1-c^2}, \tag{10.25}$$

thus the relative magnitudes are

$$\xi/\nu \sim 1/c, \qquad \eta/\nu \sim 1/c^2,$$
$$\mu/\nu \sim -\frac{q^2 c^2}{1-c^2} \cdot \frac{1}{\omega^2}. \tag{10.26}$$

One can see that at high frequencies the amplitude μ of the perturbation of scalar field M is repressed by ω^{-2}: the scalar field is practically constant, but the density ρ, the velocity u_i and the specific enthalpy m oscillate with comparable amplitudes η, ξ and ν, respectively. This phenomenon is the sound in fermion matter in the presence of scalar field. Comparing the speed of sound c, defined by (10.3) to the classical non-relativistic speed of sound c_0 (defined as square root of derivative of pressure with respect to the density of mass) one gets:

$$c_0^2 = \left.\frac{\partial P}{\partial(M\rho)}\right|_M = \frac{1}{M}\left(\frac{\partial P(M,m)}{\partial m}\right)_M \left(\frac{\partial \rho}{\partial m}\right)_M^{-1} = \frac{m}{M} c^2 = \varkappa c^2. \tag{10.27}$$

According to Eq. (8.1) $\varkappa$ is an average of a quantity larger than 1, thus the relativistic speed of acoustic waves is smaller than the classical one [5]:

$$c^2 = \frac{c_0^2}{\varkappa(x(M,\rho))} < c_0^2. \tag{10.28}$$

The theory of relativity gives bounds to the speed of sound:

$$0 < c^2 < \frac{1}{D}, \tag{10.29}$$

where D is the number of spatial dimensions. By using definitions of c (10.3) and $\varkappa$ (7.2. c), (8.1), the above condition can be transformed to

$$0 < \frac{d \ln \varkappa(x)}{d \ln x} < 1. \tag{10.30}$$

We note, that in the case of zero temperature Fermi averaging

$$\varkappa(x)=\sqrt{1+x^2}, \qquad \frac{d\ln\varkappa(x)}{d\ln x}=\frac{x^2}{1+x^2}<1. \tag{10.31}$$

Eq. (10.30) can be rewritten by using directly the function $\Phi(x)$ (8.2):

$$\frac{x^2}{D}\Phi''<\Phi-x\Phi'. \tag{10.32}$$

The requirement (10.32) restricts the allowed class of functions $\Phi(x)$ for the Lagrangian (8.7).

Further and detailed investigations on wave propagation, on the stability of static solutions (10.1) and of spatial structures mentioned in Chapter 6 will be published later [18].

Conclusion

Following and extending the previous investigations of [5], [7], [8] and introducing a covariant method for the separation of macro and microdynamics a relativistic hydrodynamical theory of fermions moving in a scalar field has been presented. The theory works successfully under a sufficiently broad class of averaging instructions (including Fermi, Bose and Maxwell statistics), it is consistent with the thermodynamics and with the conventional relativistic hydrodynamics. This theory can be derived from effective Lagrangians. Static solutions can describe e.g. domain walls or scalar bags. The dynamical theory enables the investigation of wave phenomena and stability problem.

The theory can be extended to non-isotropic local velocity distributions and to non-equilibrium statistics. By dropping the assumption of isentropy one can give the description of viscosity phenomena. The contribution of antifermions to the equilibrium can also be taken into consideration. Detailed numerical calculations may clarify the question of phase equilibrium in this model. The behaviour of perturbations, shock waves in a macroscopic configuration (e.g. quark star) or their scattering on the inhomogeneities of scalar field can also be approached by the theory presented. These problems may be subject of further work.

Acknowledgement

I am grateful to Professor G. Marx for stimulating this work and for his fruitful suggestions and comments.

Appendix A

Properties of physical quantities during the variation of metrics

Hilbert's definition of energy-momentum tensor (see [6], [12], [13]) makes use of the variation of the metrical tensor:

$$\delta \int \sqrt{g}\, L\, dx^{D+1} = -\frac{1}{2} \int T_{ik}\, \delta g^{ik} \sqrt{g}\, dx^{D+1}. \tag{A.1}$$

Here g_{ik} is the metrical tensor, g^{ik} is its inverse and g is its determinant. The definition of determinant leads [13] to

$$\delta \ln \sqrt{g} = -\frac{1}{2} g_{ik} \delta g^{ik}. \tag{A.2}$$

So (A.1) can be written in the form:

$$T_{ik}\delta g^{ik} = -\frac{2}{\sqrt{g}} \delta(L\sqrt{g}) = \left(L g_{ik} - 2\frac{\partial L}{\partial g^{ik}} \right) \delta g^{ik},$$

thus [6]

$$T_{ik} = \left(L g_{ik} - 2\frac{\partial L}{\partial g^{ik}} \right)\Bigg|_{g_{ik}=\delta_{ik}}. \tag{A.3}$$

Let us consider the proper time interval $d\tau$. Its definition is

$$d\tau = \sqrt{-g_{ik} dx^i dx^k},$$

where dx^i is independent of the variation of g_{ik}. Thus

$$\delta \ln d\tau = -\frac{1}{2} \frac{1}{d\tau^2} dx^i dx^k \delta g_{ik} = \frac{1}{2} u_i u_k \delta g^{ik}, \tag{A.4}$$

where the Minkowski velocity

$$u^i = \frac{dx^i}{d\tau}$$

obeys the condition

$$g_{ik} u^i u^k = -1.$$

The metric properties of physical quantities in the Lagrangian can be traced back to those of the auxiliary quantities discussed above in (A.2) and (A.4).

The quantities like the proper density of mass or particle number are defined [5] by the their invariant integral with respect to the volume element of the rest frame:

$$I = \int \rho dV_0 = \text{inv.} \tag{A.5}$$

Since

$$\sqrt{g} dx^{D+1} = \sqrt{g} dV dt = dV_0 d\tau = \text{inv.},$$

g_{ik}, therefore T_0 transforms like $1/d\tau$. The specific entropy s is invariant [15], thus the entropy density σ behaves like ρ. Therefore the metric variation of quantity

$$(T_0\sigma\sqrt{g})$$

vanishes: the Lagrangian containing free energy density leads to the same energy-momentum tensor as L_ε and L_p containing energy density or pressure.

Appendix B

Some useful properties of matrix of Lorentz boosts

The general form of a Lorentz transformation matrix containing no spatial rotation, corresponding to the boost of velocity $(-\mathbf{v})$ and written by the metrics defined in Chapter 1 is [16]:

$$\Lambda = \begin{pmatrix} \mathbf{1}\sqrt{1-v^2}+(1-\sqrt{1-v^2})\mathbf{v}\circ\mathbf{v} & -i\mathbf{v} \\ i\mathbf{v} & 1 \end{pmatrix} \cdot \frac{1}{\sqrt{1-v^2}}, \tag{B.1}$$

where $\mathbf{1}$ denotes the unit matrix of dimension D and $\circ$ indicates diadic product.

Orthogonality of Lorentz transformation gives

$$\Lambda_{il}\Lambda_{kl} = \Lambda_{li}\Lambda_{lk} = \delta_{ik}. \tag{B.2}$$

One can recognize that the 0^{th} column of Λ (B.1) is proportional to u_i:

$$\Lambda_{i0} = -iu_i. \tag{B.3}$$

The space-like elements of the 0^{th} row of matrix are:

$$\Lambda_{0\alpha} = iu_\alpha = -\Lambda_{\alpha 0}. \tag{B.4}$$

We shall need the product of vector u_i and matrix Λ_{ik}. Substituting (B.1) we get:

$$u_i\Lambda_{ik} = i\delta_{k0}. \tag{B.5}$$

The physical meaning of (B.5) is clear: the Lorentz boost of velocity parameter $(-\mathbf{v})$ transforms the Minkowski vector u_i belonging to the velocity $\mathbf{v}$ to the "standing" velocity vector $(\mathbf{0}, i)$.

The important expression

$$\Lambda_{i\alpha}\Lambda_{k\alpha}$$

can be written using Eqs (B.2) and (B.3) as follows:

$$\Lambda_{i\alpha}\Lambda_{k\alpha} = \Lambda_{il}\Lambda_{kl} - \Lambda_{i0}\Lambda_{k0} = \delta_{ik} + u_i u_k. \tag{B.6}$$

There is a consequence of (B.5) or (B.6)

$$\Lambda_{i\alpha}\Lambda_{k\alpha}u_k = 0. \tag{B.7}$$

References

1. G. Marx, Acta Phys. Hung., *6*, 353, 1956.
2. K. F. Novobátzky, Ann. Phys. VI., *11*, 285, 1953.
3. G. Szamosi and G. Marx, Acta Phys. Hung., *4*, 221, 1955.
4. G. Szamosi, G. Marx, Ann. Phys., *15*, 182, 1955.
5. G. Marx, Bull. Polon. Acad. Sci. Cl. III. *4*, 29, 1956.
6. G. Marx, P. Román, MTA III. Oszt. Közl., *6*, 269, 1956 (in Hungarian).
7. G. Marx, Nucl. Phys., *1*, 660, 1957.
8. G. Marx and J. Németh, Acta Phys. Hung., *18*, 77, 1964.
9. T. D. Lee and M. Margulies, Phys. Rev., *D11*, 1591, 1975.
10. G. Marx, Acta Phys. Austr., *42*, 251, 1975.
11. G. Marx, Spontaneously Broken Symmetry and Vacuum Domains, manuscript, Budapest, 1974.
12. L. D. Landau and E. M. Lifshitz, The Classical Theory of Fields, Addison-Wesley Press, Cambridge, 1951.
13. K. F. Novobátzky, The Theory of Relativity, Tankönyvkiadó, Budapest, 1963 (in Hungarian).
14. L. D. Landau and E. M. Lifshitz, Fluid Mechanics, Pergamon Press, London, 1963.
15. I. Fényes, Thermostatics and Thermodynamics, Műszaki Kiadó, Budapest, 1968 (in Hungarian).
16. L. Jánossy, P. Tasnády, Vector Calculus, Vol. 1., Tankönyvkiadó, Budapest, 1980 (in Hungarian).
17. G. Dávid, Relativistic Hydrodynamics of Fermions in Scalar Field, Thesis, Budapest, 1981 (in Hungarian).
18. G. Dávid, to be published.

Acta Physica Hungarica 56 (1—4), pp 245—250 (1984)

ON THE DOPPLER EFFECT AND UNIVERSAL FIELDS: AN ANSWER TO WILCZYŃSKI

M. F. PODLAHA

Wilhelm-Riehlstrasse 41, D-8000 München 21, FRG

and

T. SJÖDIN

T. E. N. A., Fakulteit der Wetenschappen, V. U.B., Pleinlaan 2, B-1050 Brussel, Belgium

(Received 20 July 1983)

Wilczyński's criticism of our derivation of the "relativistic" Doppler formula is repudiated. Some clarifications intended to facilitate the understanding are made. The main points of the aether approach are summarized stressing the importance of the concept of "universal field".

In a recent article [1] Wilczyński criticizes our derivation of the "relativistic" Doppler formula in a class of aether theories [2] characterized by the assumption that the ratio between the longitudinal and transversal contraction of moving bodies is given by the relation $\Phi(w)/\Psi(w)=\sqrt{1-w^2/c^2}$. He makes however several obvious mistakes which invalidate his criticism.

In our answer to Wilczyński's criticism we shall restrict ourselves to a few principal points, the clarifying of which we hope to be of use for a better understanding of the physics related to the Doppler effect. At the end of the paper we shall also make some general remarks concerning the aether approach and the importance of universal fields.

Wilczyński's criticism centres on our formula

$$\nu=\nu_0\frac{\Omega(w_S)}{\Omega(w_B)}\frac{1-\frac{w_B}{c}\cos\beta}{1-\frac{w_S}{c}\cos\alpha}. \tag{1}$$

ν is here the frequency measured by the observer B (at rest in F_B). ν_0 is the proper frequency of the oscillator acting as source. (By 'proper frequency' of an oscillator we understand its frequency as measured in the preferred frame F_P when it is at rest with respect to F_P. Note that, due to our choice of units in moving frames "preserving matter-geometry" [3], which is the choice that most authors (implicitely) prefer we obtain a de facto equivalent definition if we substitute an arbitrary moving frame F_M

for F_P.) w_S and w_B are the velocities of the source and the observer, respectively. α and β are the angles between the velocity vectors and the straight line between the source and the observer.

Let us now show in detail how we obtained the formula (1). We consider two oscillators with the same proper frequency ν_0, moving with respect to F_P at the respective velocities w_S and w_B. The oscillator S is the source of waves and the oscillator B the receiver.

In classical physics the frequencies of moving oscillators are not changed due to their motion. The frequency of S as observed by B is then given by the classical Doppler formula. (This formula is immediately obtained from (1) by setting $\Omega(w) \equiv 1$.)

In our actual world, however, the frequencies of moving oscillators depend on their velocities. We assume the change of frequency to be given by the factor $\Omega(w)$, i.e. an oscillator with the proper frequency ν_0 will have the frequency $\nu_w = \nu_0 \Omega(w)$, when moving at the velocity w with respect to the preferred reference frame F_P. This must evidently be taken into account in the derivation of the "relativistic" Doppler formula.

i) In the case that the observer is at rest and the source is moving, the frequency of the source will be $\nu_0 \Omega(w_S)$. Since B's frequency standard will not have changed but will still be ν_0, he will observe the frequency

$$\nu = \nu_0 \Omega(w_S) \left(1 - \frac{w_S}{c} \cos \alpha\right)^{-1}. \tag{2}$$

ii) In the case of the source at rest and the observer moving the emitted frequency will be ν_0. However, since the frequency standard of the observer has changed and is here $\nu_0 \Omega(w_B)$, he does not measure the "right" frequency as given by the classical Doppler formula but instead measures the frequency

$$\nu = \nu_0 \Omega(w_B)^{-1} \left(1 - \frac{w_B}{c} \cos \beta\right). \tag{3}$$

iii) In the case that both the source and the observer are moving we of course have to combine the formulae (2) and (3) and obtain immediately the formula (1).

It is evident that the formula (1) is in general valid only in F_P since the slowing down of moving clocks in a moving frame F_M in general is given by a function $\Omega_{F_M}(v) \neq \Omega(v)$ (cf. [4]). Presupposing standard Poincaré–Einstein synchronization, the function Ω_{F_M} is independent of F_M only in the Lorentzian world, i.e. when

$$\Omega = \Phi = \sqrt{1 - w^2/c^2} \qquad \text{and} \qquad \Psi \equiv 1.$$

In fact, in the first paragraph of his introduction Wilczyński claims that we in our derivation of the Doppler formula assume $\Omega(w) = \sqrt{1 - w^2/c^2}$. This is wrong. We make no assumption on the form of the function Ω at the derivation of the Doppler formula. Only in Section 4 do we point out that experiments have "shown" that $\Omega = \sqrt{1 - w^2/c^2}$. This mistake of Wilczyński's also explains why he does not see the important difference

between Ives' formula (5) and ours (his Sect. 2.1). Ives' formula is valid only in the Lorentzian world, so it can be used in any inertial frame.

In the second paragraph of his Section 2.1 Wilczyński criticizes the fact that from formula (1) follows that for $w_S = w_B$ it holds $\nu = \nu_0$. – An obvious consequence of $w_S = w_B$ is that the "source oscillator" and the "receiver oscillator" have the same frequency. B's measurement of the frequency of the source will therefore, in this special case, give the same result as if both B and S were at rest in F_P.

Wilczyński derives a formula (number 5 in his article) which he claims to be the correct Doppler formula in the aether world. Apart from the fact that he only considers the Lorentzian world, so his formula is less general than ours, there is a very important difference: he writes ν_B instead of ν_0, where ν_B is given by $\nu_B = \nu_0 \sqrt{1 - w^2/c^2}$. Such a "revaluation", as Wilczyński calls it, it is possible to do. It is, however, very important to know what it means, since every revaluation will have consequences at the process of measurement. If one does not take account of this, it can happen as in Great Britain at the change from Fahrenheit to Centigrades (Celsius): People thought that it was colder since the thermometers showed "less".

In Wilczyński's case the revaluation means that the units in the observer's frame are not chosen in the usual way ("preserving matter-geometry" [3]) but so that all observers agree about the frequencies of moving clocks. (We therefore suggest to call this choice "absolute".) This means that an oscillator at rest in F_B, which has the frequency $\nu_0 \Omega(w_B)$ as measured in F_P, will per definition have the frequency $\nu_0 \Omega(w_B)$ as measured in F_B, too. If one takes account of this change of the units of measurement used in F_B, Wilczyński's formula (5) is physically equivalent to our formula in the Lorentzian world. Let us note, however, that not only practical reasons speak against Wilczyński's formula but also theoretical: the "absolute" choice of units presupposes the knowledge of absolute velocities, what is forbidden by Poincaré's principle [4, 6].

In the third paragraph of his introduction Wilczyński makes a rather cryptic statement about the velocity of light in a moving frame. The correct statement is that, presupposed that the units in the moving frame are chosen "preserving matter-geometry" [3], which is the way in which they are usually (implicitly) chosen, the measured round trip velocity of light in a frame moving at the velocity w_M is given by the following expression:

$$c' = \frac{1 - w_M^2/c^2}{\Omega(w_M)\, \Phi(w_M)}\, c\,, \tag{4}$$

where c is the velocity of light in the preferred frame F_P. If we choose standard synchronization, also the one-way velocity will be given by this expression.

In his Section 2.5 Wilczyński writes "Podlaha and Sjödin propose a new modification of the rotor experiment to state the value of Γ". He has here completely misunderstood the purpose of our proposed experiment: we do neither propose to measure any absolute velocities nor the ordinary velocity dependence of the rates of moving clocks. In fact, a prerequisite for our experiment is the validity of Poincaré's

principle about the impossibility to measure absolute velocities [4, 7] and hence also the relation $\Omega = \sqrt{1 - w^2/c^2}$. We suggest a precision experiment to test the possible *acceleration dependence* of the rates of clocks.

At the time when we wrote the paper [2], we had no reason to suspect that there would exist any acceleration dependence, so our experiment was mainly intended as a proof that the hitherto observed effects at the rotor experiments are due to the velocity dependence of the rate of moving clocks and not to any acceleration dependence as sometimes erroneously asserted [8]. In the meantime, however, theoretical considerations [9] have given us reason to suppose that, contrary to the common opinion [10], there exists an additional acceleration influence on the rates of moving clocks and that it is proportional to $1/c^4$. The influence of the usual transversal Doppler effect (classical part eliminated) is proportional to $1/c^2$. If this effect is not eliminated, the measurement of the influence of acceleration is practically impossible. Our proposed experiment is a 'null experiment' in the sense that if the rates of moving clocks do not depend on acceleration, no effect should be observed. *Any* observed effect must hence be due to the acceleration dependence. As far as we know, our experiment is the first one offering the possibility to measure the possible acceleration effect with some precision.

*

At this occasion we would like to summarize the main points of the aether approach. The basic idea is that the "aether", or "physical vacuum" which is just another name for the same thing, is a *material physical entity* which is everywhere and can have three forms: 1) the "amorphous" or "primal" aether, 2) radiation, 3) mass substance (or "body", not to be mixed up with the *measure* of mass). All different kinds of observed elementary particles are considered as created of the amorphous aether at its conversion into mass substance.

A very important property of particles is their wave nature as described by de Broglie's waves [11]. As we have found elsewhere, associated to each particle there exist two different kinds of material waves, to be called de Broglie's waves of first and second order respectively [12]. Let us note, however, that the existence of two kinds of material waves does not contradict the notion of one physical reality. Both the considered kinds of waves are waves of the same material entity. Since further the "amorphous aether", the mass substance, and the radiation are only different forms of matter in this theory, we consider the whole cosmos as consisting of only *one physical reality* for which a "primary conservation law" is valid.

The most important feature of the aether concept is that the space between the elementary particles is not "void" but filled with the material amorphous aether. So for example, the amorphous aether around a body with mass M has a density [13]

$$\rho(r) \approx \rho_0 (1 + 2GM/rc^2), \tag{5}$$

which is the real physical cause of the observed bending of light in the gravitational field

around the Sun [14, 13]. It is also the inhomogeneity of the aether around masses which is the *real cause of the gravitational forces* [14].

Gravitation-free space, i.e. the space of the theory of special relativity, is in the aether theory considered to have an aether density

$$\rho = \rho_0 = \text{const.} \tag{6}$$

We may therefore define the gravitation-free space as a homogeneous aether field. Since the inhomogeneous aether field is a *universal field*, so is also the homogeneous field, being just a special case of the inhomogeneous one.

The universality of a field is defined by the statement that it cannot be detected locally, and therefore the "absolute value" of ρ remains unknown. It is, however, possible to measure $(\text{grad}\,\rho)/\rho$ and $\left(\frac{\partial\rho}{\partial t}\right)\Big/\rho$. The impossibility to detect the aether field locally is equivalent to the impossibility to measure the one-way velocity of light. This impossibility is further equivalent to the impossibility to measure absolute velocities ("Poincaré's principle of relativity"). Reichenbach [15] characterized a universal field by the following two properties: i) It affects all materials in the same way. ii) There are no insulating walls. It is, however, easily seen that they are not sufficient for a complete characterization for which instead one of the above equivalent principles is needed. Reichenbach's properties then become testable *consequences*. For the case of gravitation these consequences have been tested, the first one already by Galileo Galilei in his experiments with falling bodies on the leaning tower of Pisa. The second statement was experimentally verified by Austin and Thwing [16]. The two statements have also been tested together, namely by Fekete, Eötvös, and Pekar [17]. All these experiments can hence be considered as tests of the universality of the inhomogeneous aether field.

The Michelson–Morley, Trouton–Noble, Kennedy–Thorndike, and Ives–Stilwell experiments as well as the experiments of the Champeney and Moon type can be considered as tests of the universality of the homogeneous aether field.

From this point of view the resulting formula for the Doppler effect can be considered as a logical consequence of both the validity of the very general formula (1) *and* the universality of the homogeneous aether field which guarantees that $\Omega(w) = \sqrt{1-w^2/c^2}$, and that therefore the absolute velocity w cannot be measured.

References

1. J. Wilczyński, Acta Phys. Hung., 54, 361, 1983.
2. M. F. Podlaha and T. Sjödin, Acta Phys. Hung., *48*, 69, 1980.
3. T. Sjödin, Nuovo Cimento, *51B*, 229, 1979.
4. P.-A. Ivert and T. Sjödin, Acta Phys. Hung., *48*, 439, 1980.
5. H. E. Ives, J. Opt. Soc. Am., *27*, 177, 1937.
6. T. Sjödin, Z. Naturforsch., *35a*, 997, 1980; *37a*, 671, 1982.
7. H. Poincaré, L'Eclairage Electrique *5*, 5, 1895; cf. also G. H. Keswani, Brit. J. Phil. Sci., *15*, 286, 1964.
8. W. Kündig, Phys. Rev., *129*, 2371, 1963.
9. M. F. Podlaha, Spec. Sci. Tech., to be published.
10. A. Einstein, Ann. d. Phys., *17*, 1905; C. Møller, The Theory of Relativity, Oxford Clarendon Press, 1952; W. G. V. Rosser, Brit. J. Phil. Sci., *29*, 349, 1978.
11. L. de Broglie, Matière et Lumière, Albin Michel, Paris, 1937.
12. M. F. Podlaha and T. Sjödin, submitted for publication.
13. T. Sjödin, Z. Naturforsch., *37a*, 401, 1982.
14. M. F. Podlaha, Indian J. Theor. Phys., *28*, 19, 1980.
15. H. Reichenbach, Philosophie der Raum-Zeit Lehre, Walter de Gruyter Verlag, Berlin, 1928.
16. L. W. Austin and C. B. Thwing, Phys. Rev., *5*, 294, 1897.
17. E. Fekete, R. V. Eötvös, and D. Pekar, Ann. d. Phys., *68*, 11, 1922.

Acta Physica Hungarica 56 (1—4), pp 251—254 (1984)

SHORT COMMUNICATIONS

EFFECT OF Cu-DOPANTS ON THE BIREFRINGENCE OF TGS CRYSTALS

L. MALICSKÓ

Research Laboratory for Crystal Physics of the Hungarian Academy of Sciences 1502-Budapest, Hungary

and

R. SCHALGE

Central Institue for Optics and Spectroscopy of the Academy of Sciences of GDR GDR-1199 Berlin

(Received 24 May 1983)

Complementing a recent work published in this journal [1] this note reports on some supplementary investigations of birefringence carried out on undoped and Cu-doped triglycine sulphate (TGS) crystals.

Samples and measurements

For the investigations orthogonal parallelepipeds of sizes between 5 and 15 mm in the X, Y and Z directions were prepared from undoped and 0.1 mole% Cu-doped TGS single crystals grown from solutions. The Y-axes of the samples corresponded to the $\langle 010 \rangle$ and the Z ones to the $\langle 001 \rangle$ crystallographic directions of the TGS crystals. The angles between the X-axes and the crystallographic $\langle 100 \rangle$ directions amounted to 15 degrees.

The temperature dependence of the change of birefringence was measured in the three orthogonal directions on heating and cooling between 308 and 340 K by means of an orthoscopic set-up described earlier [2]. The crystal samples were placed in a small furnace between crossed polarizers and illuminated with collimated light of the wavelength of 535 nm. The polarizers were rotated to $\pm 45°$ opposite to the direction of extinction. The intensity of the transmitted light measured behind the analyzer by a photomultiplier changes sinusoidally; this corresponds to the actual path difference given by the birefringence change during the variation of the temperature. The birefringence changes could be determined from the points of minimum transmissions which corresponded to path differences of integer numbers of the used wavelength. The heating and cooling cycles were performed by a temperature program controller at a rate of 0.5 K/min.

Results and discussion

Fig. 1 shows orthoscopic photographs of a homogeneous sample from an undoped TGS crystal (a) and of an inhomogeneous sample from a Cu-doped crystal (b). In Fig. 1b the shifts in the fringes mark the boundaries between neighbouring growth pyramids of the crystal. At the intersection of the boundary lines a large defect is also visible.

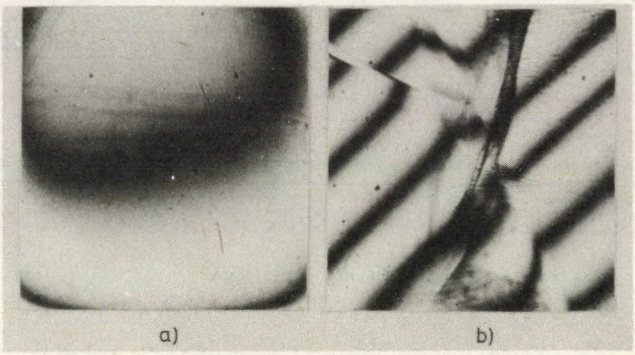

Fig. 1. Orthoscopic photographs of a homogeneous undoped TGS crystal sample (a) and of an inhomogeneous Cu-doped sample (b).

The changes of the birefringence $\delta_x = \delta(n_z - n_y)$, $\delta_z = \delta(n_x - n_y)$ and $\delta_y = \delta(n_z - n_x)$ for a light beam propagating in the three orthogonal directions are shown in Fig. 2 as functions of the temperature. Fig. 2a demonstrates that on heating the δ_x decreases in the case of the undoped as well as of the Cu-doped crystals. The ferroelectric phase transition around 322 K appears somewhat diffuse at first heating after long-term storage of the crystal, but on cooling and also during subsequent temperature cycles the phase transition is indicated by a sharp kink. During a heating and subsequent cooling cycle a small hysteresis can be observed. The hysteresis is more distinct for Cu-doped crystals than for undoped ones (see curves 1 and 2 in Fig. 2a).

In the case of light propagating in the Z-direction δ_z shows similar main courses as before the δ_x, though the Cu-dopants cause only small shifts as compared with those at δ_x, (see curves 1 and 2 in Fig. 2b and in the enlarged inset). The hystereses are also smaller than those for δ_x.

It should be mentioned that both for δ_x and for δ_z, the differences between the ferroelectric legs of the curves and the straight lines extrapolated from the corresponding paraelectric legs show similar courses with the temperature as does the spontaneous polarization measured earlier [1].

Contrary to the δ_x and δ_z for the light propagating in the Y-direction the change of birefringence δ_y slightly increases in the ferroelectric phase. After reaching a sharp maximum it decreases again in the paraelectric phase as demonstrated in Fig. 2c. The

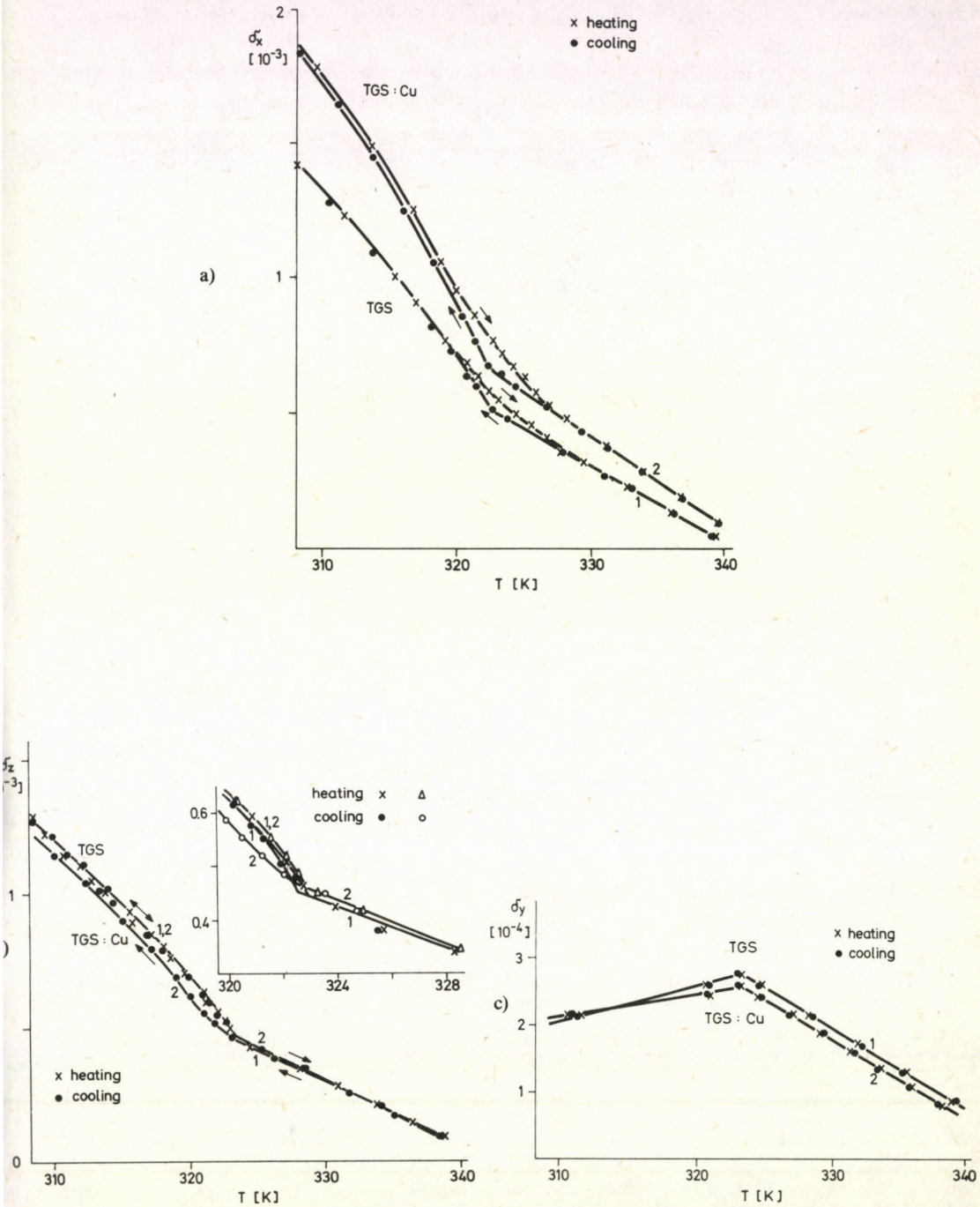

Fig. 2. Changes of birefringence versus temperature in undoped (curves 1) and 0.1 mole% Cu-doped (curves 2) TGS crystal samples for light propagating in the orthogonal directions X (a), Z (b) and Y (c).

Cu-dopants cause only a small shifting but no hysteresis can be observed (see curves 1 and 2).

Some characteristic data concerning the ferroelectric (f)-paraelectric (p) transition points (T_i) on heating (h) and cooling (c), and the slopes (s) of the curves are listed in Table I. Comparing the curves and their slopes in Table I one can conclude that the birefringence and the slopes, furthermore the hystereses in a heating–cooling cycle are generally increased by the Cu-dopants.

Table I

Characteristic data for the temperature dependence of the change of birefringence found in undoped and Cu-doped TGS crystals.

Direction	Course	TGS			TGS : Cu		
		T_i[K]	$s/10^{-5}$[K]		T_i[K]	$s/10^{-5}$[K]	
			f	p		f	p
X	h	324.4	−5.4	−3.12	323.4	−7.8	−3.29
	c	322.3			322.1		
Z	h	323.5	−5.4	−2.30	323.3	−5.2	−2.50
	c	323.1			322.9		
Y	h	323.3	+0.55	−1.20	323.3	+0.38	−1.19
	c						

The results can be summarized as follows: The main characteristics of the birefringence-temperature curves correspond to those known from the literature for undoped TGS crystals only [3]. The fine differences in the characteristic data listed in Table I point to the influence of Cu-dopants on the formation and structure of ferroelectric domains at phase transition, thus supporting earlier conclusions [1].

Acknowledgement

The authors wish to express their thanks to Prof. R. Voszka and Dr. L. W. Wieczorek for their stimulating interest in this work. Part of this work was supported by the State Office for Technical Development (OMFB), in Hungary.

References

1. L. Malicskó, L. Jeszenszky, E. Hartmann, L. Kovács, Á. Péter and B. Vajna, Acta Phys. Hung., *53*, 67, 1982.
2. R. Schalge and Č. Barta, in Symp. on Mercury (I) Halides, Liblice, 17–19. Nov. 1976. Publ. by Ustav Fyziki Pevnych Látek ČSAV, pp. 31–36.
3. A. A. Sonin and A. S. Vasilevskaya, Electrooptical Crystals (in Russian), Atomizdat, Moscow, 1971, pp. 191–192.

Acta Physica Hungarica 56 (1—4), pp 255—256 (1984)

EXPERIMENTAL APPLICATION OF THEORETICALLY DERIVED ANALYTICAL EXPRESSIONS OF THE Λ-TYPE DOUBLING OF THE $^5\Pi$ STATE BELONGING TO THE INTERMEDIATE CASE BETWEEN HUND'S CASES a) AND b).

I. KOVÁCS

Department of Atomic Physics, Technical University
1521 Budapest, Hungary

and

J. ANTAL

Physical Department, Technical University
1521 Budapest, Hungary

(Received 24 May 1984)

Cheung et al [1] have analysed the $A\,^5\Sigma - X\,^5\Pi(0,0)$ electronic transition of the CrO molecule. Recently the following explicit expression valid for all values of Y intermediate between Hund's cases a) and b) has been given by one of us [2] for the width of the Λ-type doubling of a $^5\Pi$ state:

$$\Delta\nu(^5\Pi_N) = \frac{f_N g_N}{C_N(J)} J(J+1)\{2C_0 V_N + C_1[2X_N(J-1)(J+2)+3Y_N]+ \tag{1}$$

$$+C_2[4Z_N(J-1)(J+2)+M_N f_N g_N]\} \qquad (N=J+2, J+1, \ldots, J-2)$$

where

$$C_0 = 12\sum_K \frac{(-1)^\Sigma(\xi+2\eta)^2}{\nu(^5\Pi\,^5\Sigma_K)} = 6(o+p+q),$$

$$C_1 = 32\sum_K \frac{(-1)^\Sigma(\xi+2\eta)\eta}{\nu(^5\Pi\,^5\Sigma_K)} = 4(p+2q), \tag{2}$$

$$C_2 = 8\sum_K \frac{(-1)^\Sigma\eta^2}{\nu(^5\Pi\,^5\Sigma_K)} = q$$

$$M_{J+2} = M_{J+1} = M_{J-1} = M_{J-2} = 3, \qquad M_J = 1$$

and $\xi = (AL_\xi)\,(^5\Pi\,^5\Sigma)$, $\eta = (BL_\xi)\,(^5\Pi\,^5\Sigma)$ and $L_\xi(^5\Pi\,^5\Sigma)$ denotes the matrix element of the component of the electronic orbital angular momentum in the ξ direction, perpendicular to the molecular axis for the stationary molecule. (The three parameters o, p, and q are named following the usage of Mulliken and Christy.) In the middle part of

Eqs (2) in the exponent $\Sigma = 0$ or 1 according as the perturbing $^5\Sigma$ term is Σ^+ or Σ^-, C_N, V_N, X_N, Y_N, Z_N, f_N, g_N are complicated functions of the coupling constant $Y = A/B$ (where A is the multiplet splitting constant and B is the rotational constant) and of the rotational quantum number J and are given explicitly in the paper [2].

Using the values of the rotational lines of the branches and the value $Y = 120.56\ \mathrm{cm}^{-1}$ given in Ref. [1] we obtain for the width of the Λ-type doubling of the

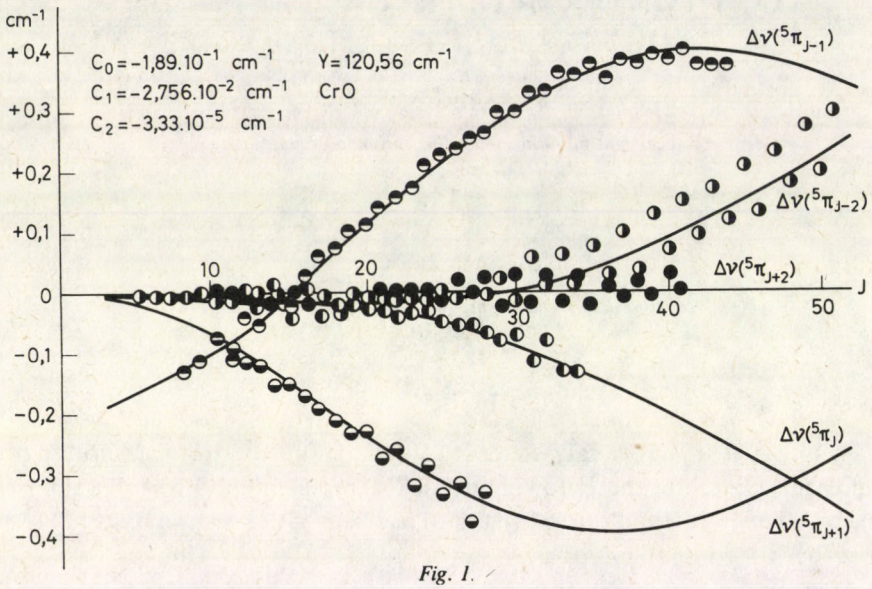

Fig. 1.

$X\ ^5\Pi(v=0)$ (Fig. 1) with $C_0 = -1.89 \cdot 10^{-1}\ \mathrm{cm}^{-1}$, $C_1 = -2.756 \cdot 10^{-2}\ \mathrm{cm}^{-1}$ and $C_2 = 3.33 \cdot 10^{-5}\ \mathrm{cm}^{-1}$. The solid line curves and the circles indicate the calculated and the observed values, respectively. The agreement between the observed and calculated values is excellent.

It is remarkable that in order to theoretically interpret the Λ-type doubling it was not necessary to use in addition to the first order spin-orbit interaction and the matrix element neglected at the separation of the wave equation other interactions such as the spin–spin, the spin–rotation interactions and the centrifugal distortion corrections.

References

1. A. S-C. Cheung, W. Zyrnicki, A. J. Merev, J. Mol. Spectr., *104*, 315, 1984.
2. I. Kovács, J. Mol. Spectr., *98*, 41, 1983.

Acta Physica Hungarica 56(1—4), pp 257—260 (1984)

BOOK REVIEWS

Lectures on Lepton Nucleon Scattering and Quantum Chromodynamics

Edited by: A. Jaffe and D. Ruelle, Birkhäuser, Boston—Basel, 1982, pp. 561

Quantum chromodynamics is certainly the most feverishly developing chapter of fundamental physics in our days. The essential points are far from everyday experiences, the experiments are indirect, the calculations are complex. The science journals print only short letters about the work of dozens of scientists and with a huge computation in the background. The essential flow of information goes another way: through informal workshops, hardly accessible for those living far from world centers.

This volume contains four lectures, given at the 1982 Stanford Linear Accelerator Center's Summer Institute by four staff members: W. B. Atwood, J. D. Bjorken, S. J. Brodsky, R. Stroynowski. They offer an introduction to QCD and also a status report of the theory, based on calculations and experiments. So the book is a valuable help for everyone working in this field in the early eighties. It is comprehensive, readable and up-to-date. But you have to rush to study it in time!

G. Marx

WALTER THIRRING: *Quantum Mechanics of Large Systems*

A Course in Mathematical Physics Vol. 4. Springer Verlag, Wien, New York 1983, pp. 290, 39 figures

"Take 10 clocks with hands moving at different rates. The question is: how long it takes for the initial configuration of clock faces to reappear within an angular accuracy of 1%?" A simple question allowing exact evaluation. The answer is shocking: "Longer than the age of the Universe." This start illustrates the ars poetica of the author: exactness does not contradict simplicity but it makes simplicity possible. This has been the goal of the whole textbook series but it has been realized in the most convincing way in this volume. It is based on the density matrix formalism of quantum mechanics. "The ordinary perturbation-theoretic calculations are not very useful here. Those methods have never led to propositions of much substance"—writes the author in the preface. He restricts himself to a few models which can be treated with rigour and which illustrate the thermal behaviour of realistic systems (like gases, atoms, metals, stars, radiation, even living organisms).

G. Marx

Third Workshop on Grand Unification

University of North Carolina, Chapel Hill, April 15–17, 1982. Edited by: P. H. Frampton, S. L. Glashow and H. van Dam, Progress in Physics, No. 6. Edited by: A. Jaffe and D. Ruelle, Birkhäuser Boston, Inc., 1982, pp 374

In this book the status of grand unified theories and their connection to experiment are discussed, based on 27 talks given at the Third Workshop on Grand Unification, Chapel Hill, April 1982. Each of the 14 experimental contributions follows after a theoretical one. 8 experimental talks treat the status of proton decay experiments. Two talks discuss experiments on the neutrino mass, furthermore, searches of neutrino oscillations are described in two papers. Neutron-antineutron oscillation, and the magnetic monopole search at Stanford are dealt with in two reports.

On the theoretical side, various aspects and problems of the supersymmetry are described in 6 reports. In particular, S. Weinberg examines the problem of supersymmetry breaking. Grand unified theories are discussed in three papers. Possible origins for the monopole flux, a novel approach to the gauge hierarchy problem, the invisible axion and the top quark mass are treated in further talks.

The volume provides the reader with a clear overall picture of the present status of grand

unification. Its authors are experts of this field, such as S. L. Glashow, S. Weinberg, P. H. Frampton, B. A. Ovrut, S. Dimopoulos, S. Miyake, H. Georgi, S. Rudaz, P. Langacker, A. de Rujula, D. Cundy, S. Pakvasa etc.

This book is valuable first of all to professional researchers in the field, and also to the wide community of particle physicists.

G. Pócsik

Physics in Collision. High Energy ee(pp) Interactions

Volume 2. Proceedings of an International Conference on Physics in Collision, June 2–4, 1982, Stockholm. Edited by: P. Carlson and W. P. Trower. Plenum Press, New York and London, 1983, pp. 432

This volume contains 18 papers of main speakers presented at the Second International Conference on Physics in Collision, held in Stockholm, Sweden, June 2–4, 1982. The motivation of the Conference was to provide an up-to-date review of the most exciting results of experimental particle physics obtained since the first Conference in 1981.

Thus, 6 papers deal with the physics of $p\bar{p}/pp$ collisions. Not only hard scattering at ISR energies is treated, but also quite new results on $p\bar{p}$ collisions at a centre of mass energy of 540 GeV (Proton-Antiproton Collider) are included (Section I).

In Section II (4 papers) promising aspects of e^+e^- collisions are reviewed. In particular, two-photon physics, the J/ψ region, Upsilon resonances and electroweak effects are discussed.

Experimental results on jets at PETRA and PEP are described in Section III (3 papers).

Section IV is devoted to studying structures in hadronic interactions and heavy flavours (4 papers).

Llewellyn Smith's overview (Section V) is a far-seeing conclusion of this excellent volume.

Since the book contains very important new results in experimental particle physics, it is highly recommended to particle physicists, both theoreticians and experimentalists.

G. Pócsik

ORAZIO SVELTO: *Principles of Lasers*

Second Edition, Plenum Publishing Corporation, New York and London, 1982

An excellent introductory text on the theory and practice of lasers that has been needed since long. It gives the reader a fairly complete still deep insight into the field and provides an excellent basis for further theoretical or experimental work, or further studies of the specialized literature.

The short and clear explanations of the basic physical ideas, specifying limitations of different models describing the operational mechanisms of lasers are followed by practical chapters: on the types of lasers, properties of laser beams, transformation of laser beam in space, amplitude or frequency, and applications of lasers.

Since the book contains recent results as well (up to 1980) it provides the reader a good survey over the results of the last 20 years. It gives a very good physical insight into laser science and technology therefore it can be highly recommended for students at the upper undergraduate level, as a textbook as well.

Peter Richter

The Dissipation of Electromagnetic Waves in Plasmas

Consultants Bureau, New York and London, a Division of Plenum Publishing Corporation, New York, 1982. Translated from Russian by H. McNeill

The anthology contains four papers on experiments with the interaction between high-power electromagnetic waves and collisionless plasmas or electrons. In particular, these are special reports on the non-linear interaction of waves with plasmas, investigated both under free space conditions and in waveguides. Secondary-emission discharges were studied in order to ascertain their possible effects on measurements in waveguides.

The original Russian text as Volume 92 of the Proceedings in "The Lebedev Physics Institute Series" edited by Academicians D. V. Skobel'tsyn and N. G. Basov, was published in 1977 by Nauka Press, Moscow, for the Academy of Sciences of the USSR.

The results presented are of interest to physicists and engineers concerned with a wide range of problems of the interaction of electromagnetic radiation with plasmas, microwave heating of plasmas and laser fusion included.

The summaries of the four papers are as follows:

An experimental investigation of nonlinear dissipation of electromagnetic waves in inhomogeneous collisionless plasmas. (G. M. Batanov and V. A. Silin)

The methods of transferring energy from an electromagnetic wave to the electrons of a plasma by exciting various types of parametric instabilities are examined. Data are presented from an experimental study of the reflection and penetration of microwaves at an inhomogeneous collisionless plasma layer. Measurements of the energy of fast electrons, a determination of the combination frequencies, and modulation of the plasma density suggest that a t—

—L+s instability arises. It is established that the energy density of the plasma is not constant in time. This is manifested in the form of an almost periodic modulation in the fast-electron current, which exists throughout the time a microwave field is acting on the layer.

Collisionless absorption of electromagnetic waves in plasmas and "SLOW" nonlinear phenomena. (V. I. Barinov, I. R. Gekker, V. A. Ivanov and D. M. Karfidov)

An experimental study is made of the interaction of pulsed microwaves in the 10 cm range with collisionless plasma flows ($\omega \gg v$) in a waveguide under both favourable ($\Delta n \parallel E, \omega \approx \omega Le$) and unfavourable initial conditions for plasma resonance of the waves. It is shown that in the first case over the interval $v_E/v_{Te} = 10^{-5} - 5$ the absorption coefficient D^2 changes little while absorption sets in almost immediately ($t < 0{,}01$ μs) and is accompanied by the rapid decay of the plasma and the production of fast electrons. In the second case ($\nabla n \perp E$) anomalously strong absorption sets in after a time delay ($t_{delay} = 1 - 3$ μs) related to the time for the leading edge of the plasma to become deformed when wave pressure exceeds plasma pressure ($E_0^2 8\pi \gtrsim n_e T_e$).

Nonlinear effects in the propagation of electron plasma waves in an inhomogeneous plasma layer. (V. A. Silin)

A review is given of some experiments on the dynamics of electron Langmuir oscillations and plasma waves in weakly inhomogeneous collisionless plasmas. Field amplification at a plasma resonance, collapse, and nonlinearities in the collisionless damping of waves are discussed. Experimental data on the deformation of the field distribution in the neighbourhood of a plasma resonance are presented. It is established that, at high field amplitudes, in an inhomogeneous layer plasma waves fill the region from the critical density point n_c to $\sim 1/4n_c$.

A study of secondary-emission microwave discharges with large electron transit angles. (L. V. Grishin, A. A. Dorofeyuk, I. A. Kossyi, G. S. Luk'yanchikov and M. M. Savchenko)

The conditions for the production of a secondary-emission microwave discharge in systems with a large distance between the walls (cavity resonators, waveguides, etc.) and in free space are analyzed. The traditional theory of a resonance discharge is shown to be invalid for these cases and a new method is proposed for determining the thresholds for the discharge. The discussion takes into account the contribution to the discharge current from electrons emitted at all phases of the field. The theoretical calculations are compared with experimental results.

J. Bitó

D. PAPOUŠEK and M. R. ALIEV:
Molecular Vibrational/Rotational Spectra

Czechoslovak Academy of Sciences, Academia, Prague, 1982, pp. 323, Kčs 145

Research workers dealing with the theory and analysis of the vibration-rotation spectra of small polyatomic molecules in the gaseous phase must note this book with particular interest. Experimental techniques in the field of high-resolution molecular spectroscopy have developed very fast in recent years. Albeit a number of excellent, older treatments of the theory for the accurate interpretation of such spectra are available, the theoretical apparatus for the needs of the working spectroscopist is rather scattered. A significant portion of important developments, including the authors' own work, has up till now been available in the form of original papers only. The authors have therefore attempted to collect and organize the up-to-date theory of vibrational-rotational spectroscopy into a compact volume of 323 pages. As the authors belong to today's active theoreticians this goal has certainly been achieved.

The book contains four main chapters, each structured to several subdivisions. References are grouped for each subdivision independently. The first chapter discusses the vibrational-rotational Hamiltonian of semi-rigid molecules, the second contains the description of the modern, permutation-inversion concept of molecular symmetry and its applications in the classification of vibrational-rotational states, and the optical selection rules among them. The third chapter covers various forms of interactions between vibrations and rotations, including Coriolis interactions, while the final chapter describes non-rigid molecules possessing large-amplitude motions, in particular molecular inversion and internal rotation. There are ten interesting Appendices, containing for example the sum-rules for vibration-rotation interaction coefficients, the description of the adiabatic approximation for separating dynamical degrees of freedom in a molecule, character tables for the irreducible representations of some point groups, and symmetry relations among molecular spectroscopic parameters.

The Subject Index is detailed, but—alas—no Author Index is given. The treatment is strictly theoretical throughout, but as it progresses from fundamentals to advanced ideas it should enable the practically minded, chemically-oriented infrared, Raman and microwave spectroscopists to understand and develop their problems deeper and further. By the same token this book is recommended for advanced courses on molecular spec-

troscopy. In addition the rapidly advancing field of infrared laser physics necessitates the kind of understanding of molecular vibrational — rotational levels that this book fosters.

The Publishing House of the Czechoslovak Academy of Sciences, Academia/Prague has produced a cloth-bound book of good material quality, careful printing and low price (145 Czech Crowns). To the knowledge of the reviewer there will be another publication of the same book to supply a wider market by Elsevier Scientific Publishing Co. Amsterdam.

László Nemes

W. PETZOLD: *Strahlenphysik, Dosimetrie und Strahlenschutz*

B. G. Teubner Verlag, Stuttgart, 1983

Dieses Buch enthält eine gute und klare Zusammenfassung über Strahlenphysik, Dosimetrie und Strahlenschutz für Röntgentechniker, medizinische und technische Studenten und beginnende Fachleute. Der Autor schreibt im Vorwort des Buches: "Für die Niederschrift des Buches haben mir viele Diskussionen mit Studenten, Kollegen des Physikalischen Instituts und Kursteilnehmern wertvolle Anregungen gegeben."

Diese Arbeit war erfolgreich, weil der Leser ein Buch mit vielen guten, in der Praxis anwendbaren Informationen über die Strahlenphysik und den Strahlenschutz erhält.

In den ersten 6 Kapiteln der Zusammenstellung sind die Grundgesetze von Radioaktivität und Röntgenstrahlung bzw. die Wechselwirkungen von Röntgen- und Gammastrahlen mit der Materie zusammengefasst.

In Kapitel 7 (Dosimetrie) werden die Grundbegriffe der Dosimetrie: die Dosiseinheiten, die verschiedenen Messverfahren in der Dosimetrie und die grundsätzlichen Berechnungen der Ortsdosis beschrieben.

In Kapitel 8 (Strahlenschutz) sind die nächsten Themenkreise zusammengefasst: die schädigende Wirkung ionisierender Strahlung, natürliche und zivilisatorische Strahlenbelastung des Menschen, Strahlenschutzbereiche und Schutzzonen, Röntgen- und Strahlenschutzverordnung, praktischer Strahlenschutz.

Im Anhang befinden sich viele Zahlenbeispiele und Tabellen, die in der Praxis gut verwendbar sind.

Das Buch des B. G. Teubner Verlages ist zu empfehlen als eine praxisorientierte Einführung in die Grundlagen der Dosimetrie und des Strahlenschutzes für medizinisch-technische Assistenten, sowie für Studierende der Naturwissenschaften und der Medizin.

E. Virágh

HANS-JÜRGEN TREDER: *Grosse Physiker und ihre Probleme*

Studien zur Geschichte der Physik, Akademie-Verlag, Berlin, 1983

Die geistreiche Grundidee der Artikel und Vorträge des Verfassers zu dem, im Titel angedeuteten Thema ist folgende: Würde sich die Physik nur aufgrund der Ansammlung ihrer inneren Kenntnisse entwickeln, so wäre es schwer zu verstehen, warum nicht einige Generationen nach Axiomatisierung der Statik von Archimedes ein Galilei zur Gründung der Dynamik gelangte und weshalb 2000 Jahre zwischen Archimedes und Galilei in Wirklichkeit vergehen mussten. Da die Denkweise und die Möglichkeiten der Physiker nicht nur vom Niveau der physikalischen Kenntnisse, sondern auch von den gesellschaftlichen Verhältnissen und Produktivkräften, d. h. von dem Entwicklungsstand der Technik und andererseits von den philosophischen Anschauungen der gegebenen Zeit bestimmt werden, ist es empfehlenswert, all diese Verhältnisse in der Tätigkeit eines Physikers konkret zu analysieren. Der wissenschaftliche Lebenslauf von grossen Physikern ist kein anekdotischer Beitrag zur Geschichte der Physik, sondern ein wesentliches Element der Entwicklung, d. h. der Geschichte der Physik.

Das Buch enthält insgesamt 29 Artikel und umfasst eine ganze Reihe von Wissenschaftlern von Aristoteles über Descartes, Helmholtz und Boltzmann bis zu Einstein und Planck. Die grossen Physiker werden im Spiegel eines speziellen Problems und die grossen Probleme durch die Tätigkeit der Wissenschaftler dargestellt. Unter den schöpferischen Persönlichkeiten sind nicht nur die grossen Personen der Geschichte und Vorgeschichte der Physik zu finden, sondern auch Kant, Hegel, Engels und Lenin sind im Zusammenhang mit einem Problem der Naturwissenschaften oder der Physik vertreten.

Das Werk will natürlich keine "Gesellschaftsgeschichte" der Physik im weiten Sinne des Wortes anbieten, aber der Verfasser als theoretischer Physiker gibt lehrreiche Beiträge dazu. Die Studiensammlung kann sowohl für Physiker als auch Philosophen und Historiker von Interesse sein.

G. Biró

NOTES TO CONTRIBUTORS

I. PAPERS will be considered for publication in Acta Physica Hungarica only if they have not previously been published or submitted for publication elsewhere. They may be written in English, French, German or Russian.

Papers should be submitted to

Prof. I. Kovács, Editor
Department of Atomic Physics, Technical University
1521 Budapest, Budafoki út 8, Hungary

Papers may be either articles with abstracts or short communications. Both should be as concise as possible, articles in general not exceeding 25 typed pages, short communications 8 typed pages.

II. MANUSCRIPTS

1. Papers should be submitted in three copies.
2. The text of papers must be of high stylistic standard, requiring minor corrections only.
3. Manuscripts should be typed in double spacing on good quality paper, with generous margins.
4. The name of the author(s) and of the institutes where the work was carried out should appear on the first page of the manuscript.
5. Particular care should be taken with mathematical expressions. The following should be clearly distinguished, e.g. by underlining in different colours: special founts (italics, script, bold type, Greek, Gothic, etc.); capital and small letters; subscripts and superscripts, e.g. x^2, x_3; small *l* and l; zero and capital O; in expressions written by hand: *e* and *l*, *n* and *u*, *v* and v, etc.

A List of Symbols on a separate sheet should be attached to each paper.

6. References should be numbered serially and listed at the end of the paper in the following form: J. Ise and W. D. Fretter, Phys. Rev., *76*, 933, 1949.

For books, please give the initials and family name of the author(s), title, name of publisher, place and year of publication, e.g.: J. C. Slater, Quantum Theory of Atomic Structures, I. McGraw-Hill Book Company, Inc., New York, 1960.

References should be given in the text in the following forms: Heisenberg [5] or [5].

7. Captions to illustrations should be listed on a separate sheet, not inserted in the text.
8. In papers submitted to Acta Physica all measures should be expressed in SI units.

III. ILLUSTRATIONS AND TABLES

1. Each paper should be accompanied by three sets of illustrations, one of which must be ready for the blockmaker. The other sets attached to the copies of the manuscript may be rough drawings in pencil or photocopies.
2. Illustrations must not be inserted in the text.
3. All illustrations should be identified in blue pencil by the author's name, abbreviated title of the paper and figure number.
4. Tables should be typed on separate pages and have captions describing their content. Clear wording of column heads is advisable. Tables should be numbered in Roman numerals (I, II, III, etc.).

IV. RETURN OF MATERIAL

Owing to high postage costs, the Editorial Office cannot undertake to return *all* material not accepted for any reason for publication. Of papers to be revised (for not being in conformity with the above Notes or other reasons) only *one* copy will be returned. Material rejected for lack of space or on account of the Referees' opinion will not be returned to authors outside Europe.

Periodicals of the Hungarian Academy of Sciences are obtainable at the following addresses:

AUSTRALIA
C.B.D. LIBRARY AND SUBSCRIPTION SERVICE
Box 4886, G.P.O., *Sydney N.S.W. 2001*
COSMOS BOOKSHOP, 145 Ackland Street
St. Kilda (Melbourne), Victoria 3182

AUSTRIA
GLOBUS, Höchstädtplatz 3, *1206 Wien XX*

BELGIUM
OFFICE INTERNATIONAL DE LIBRAIRIE
30 Avenue Marnix, *1050 Bruxelles*
LIBRAIRIE DU MONDE ENTIER
162 rue du Midi, *1000 Bruxelles*

BULGARIA
HEMUS, Bulvar Ruszki 6, *Sofia*

CANADA
PANNONIA BOOKS, P.O. Box 1017
Postal Station "**B**", *Toronto, Ontario M5T 2T8*

CHINA
CNPICOR, Periodical Department, P.O. Box 50
Peking

CZECHOSLOVAKIA
MAD'ARSKÁ KULTURA, Národní třida 22
115 66 Praha
PNS DOVOZ TISKU, Vinohradská 46, *Praha 2*
PNS DOVOZ TLAČE, *Bratislava 2*

DENMARK
EJNAR MUNKSGAARD, Norregade 6
1165 Copenhagen K

FEDERAL REPUBLIC OF GERMANY
KUNST UND WISSEN ERICH BIEBER
Postfach 46, *7000 Stuttgart 1*

FINLAND
AKATEEMINEN KIRJAKAUPPA, P.O. Box 128 *SF- 00101 Helsinki 10*

FRANCE
DAWSON-FRANCE S. A., B. P. 40, *91121 Palaiseau*
EUROPÉRIODIQUES S. A., 31 Avenue de Versailles, *78170 La Celle St. Cloud*
OFFICE INTERNATIONAL DE DOCUMENTATION ET LIBRAIRIE, 48 rue Gay-Lussac
75240 Paris Cedex 05

GERMAN DEMOCRATIC REPUBLIC
HAUS DER UNGARISCHEN KULTUR
Karl Liebknecht-Straße 9, *DDR-102 Berlin*
DEUTSCHE POST ZEITUNGSVERTRIEBSAMT Straße der Pariser Kommüne 3–4, *DDR-104 Berlin*

GREAT BRITAIN
BLACKWELL'S PERIODICALS DIVISION
Hythe Bridge Street, *Oxford OX1 2ET*
BUMPUS, HALDANE AND MAXWELL LTD.
Cowper Works, *Olney, Bucks MK46 4BN*
COLLET'S HOLDINGS LTD., Denington Estate *Wellingborough, Northants NN8 2QT*
WM. DAWSON AND SONS LTD., Cannon House *Folkstone, Kent CT19 5EE*
H. K. LEWIS AND CO., 136 Gower Street
London WC1E 6BS

GREECE
KOSTARAKIS BROTHERS INTERNATIONAL BOOKSELLERS, 2 Hippokratous Street, *Athens-143*

HOLLAND
MEULENHOFF-BRUNA B. V., Beulingstraat 2,
Amsterdam
MARTINUS NIJHOFF B.V.
Lange Voorhout 9–11, *Den Haag*
SWETS SUBSCRIPTION SERVICE
347b Heereweg, *Lisse*

INDIA
ALLIED PUBLISHING PRIVATE LTD., 13/14
Asaf Ali Road, *New Delhi 110001*
150 B-6 Mount Road, *Madras 600002*
INTERNATIONAL BOOK HOUSE PVT. LTD.
Madame Cama Road, *Bombay 400039*
THE STATE TRADING CORPORATION OF INDIA LTD., Books Import Division, Chandralok 36 Janpath, *New Delhi 110001*

ITALY
INTERSCIENTIA, Via Mazzé 28, *10149 Torino*
LIBRERIA COMMISSIONARIA SANSONI, Via Lamarmora 45, *50121 Firenze*
SANTO VANASIA, Via M. Macchi 58
20124 Milano
D. E. A., Via Lima 28, *00198 Roma*

JAPAN
KINOKUNIYA BOOK-STORE CO. LTD.
17-7 Shinjuku 3 chome, Shinjuku-ku, *Tokyo 160-91*
MARUZEN COMPANY LTD., Book Department, P.O. Box 5050 Tokyo International, *Tokyo 100-31*
NAUKA LTD. IMPORT DEPARTMENT
2-30-19 Minami Ikebukuro, Toshima-ku, *Tokyo 171*

KOREA
CHULPANMUL, *Phenjan*

NORWAY
TANUM-TIDSKRIFT-SENTRALEN A.S., Karl Johansgatan 41–43, *1000 Oslo*

POLAND
WĘGIERSKI INSTYTUT KULTURY, Marszalkowska 80, *00-517 Warszawa*
CKP-I W, ul. Towarowa 28, *00-958 Warszawa*

ROUMANIA
D. E. P., *Bucuresti*
ILEXIM, Calea Grivitei 64–66, *Bucuresti*

SOVIET UNION
SOJUZPECHAT — IMPORT, *Moscow*
and the post offices in each town
MEZHDUNARODNAYA KNIGA, *Moscow G-200*

SPAIN
DIAZ DE SANTOS, Lagasca 95, *Madrid 6*

SWEDEN
GUMPERTS UNIVERSITETSBOKHANDEL AB
Box 346, *401 25 Göteborg 1*

SWITZERLAND
KARGER LIBRI AG, Petersgraben 31, *4011 Basel*

USA
EBSCO SUBSCRIPTION SERVICES
P.O. Box 1943, *Birmingham, Alabama 35201*
F. W. FAXON COMPANY, INC.
15 Southwest Park, *Westwood Mass. 02090*
READ-MORE PUBLICATIONS, INC.
140 Cedar Street, *New York, N.Y. 10006*

YUGOSLAVIA
JUGOSLOVENSKA KNJIGA, Terazije 27, *Beograd*
FORUM, Vojvode Mišića 1, *21000 Novi Sad*

Index: 26.022